Durham E-Theses

Surface photometry of early-type galaxies in rich clusters

Steel, James

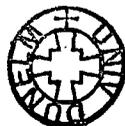# Surface Photometry of Early-Type Galaxies in Rich Clusters

James Steel

A thesis submitted to the University of Durham
in accordance with the regulations for
admittance to the Degree of Doctor of Philosophy.

Department of Physics
University of Durham
August 1998

Preface

The work described in this thesis was undertaken between 1992 and 1997 whilst the author was a research student under the supervision of Dr. J.R. Lucey in the Department of Physics at the University of Durham. This work has not been submitted for any other degree at the University of Durham or at any other University.

The work contained in this thesis is entirely the authors own work (the observing run at the Isaac Newton Telescope, La Palma, in March 1994, was carried out in collaboration with John Lucey and Dave Carter). It is expected that some of the work contained in this thesis will be published in the scientific press during 1998.

Acknowledgements

Abstract

This thesis investigates the morphology of early-type galaxies in two rich clusters using 2D surface photometry. In particular, the amount of light in the 'disk' component is focussed upon, as the presence of a disk is the main morphological criterion in distinguishing between the traditional 'elliptical' and 'S0' classes. Extensive and photometric R-band CCD observations of continuous areas of the Coma and Abell 1367 clusters were obtained at the 2.5 m Isaac Newton telescope, La Palma during March 1994. A subset of this large data-set has been used in this study, comprising a magnitude-limited (to $R = 15.6$) sample of 153 galaxies in the two clusters.

Surface photometry measurements, including surface brightness profiles and isophotal shapes, have been made for the sample. Atmospheric seeing is a major problem when measuring light profiles at the distance of Coma from ground-based telescopes. Typical seeing at La Palma ($FWHM \sim 1.2''$) is a significant fraction of the effective radius of many Coma/Abell 1367 galaxies ($r_e \sim 3''$ for small ellipticals). An iterative algorithm was developed to deconvolve the effects of seeing from surface brightness profiles. The result of the algorithm is to extend the range of useful surface photometry inwards to within 2 times the $FWHM$. In order to parametrise the surface brightness profiles and discriminate between different profile-types, further software was developed to fit one- and two-component model profiles to the seeing-corrected data. The following parameters were measured and tabulated for each of the 153 galaxies: total magnitude M_t; half-light parameters $r_{1/2}$ and $\langle \mu \rangle_{1/2}$; SB at half-light radius $\mu(r_{1/2})$; photometric diameter $D_{19.23}$ (equivalent to D_n); ellipticity at $R = 21.5$ isophote $\epsilon_{21.5}$; averaged isophote high-order terms $\langle c_3 \rangle$, $\langle s_3 \rangle$, $\langle c_4 \rangle$ and $\langle s_4 \rangle$; effective radii and surface brightnesses of 5 single power-law $r^{\frac{1}{n}}$ models, $r^n{}_e$ and $\langle \mu \rangle^n{}_e$ ($n = 1, 2, 3, 4, 5$); best-fitting power-law index n; bulge effective radii and surface brightnesses from the two-component fit $r^b{}_e$ and $\langle \mu \rangle^b{}_e$; disk effective parameters $r^d{}_e$ and $\langle \mu \rangle^d{}_e$; and disk-to-bulge luminosity ratio D/B.

The measured parameters have been used to investigate various aspects of early-type galaxy morphology. The conclusions are outlined below. Firstly, a two-component $r^{\frac{1}{4}}$ plus exponential model is a better fit to most galaxies than a single component $r^{\frac{1}{n}}$ law fit. Secondly, the traditional division of early-type galaxies into 'elliptical' and 'S0' classes is severely biased by the viewing angle. In fact, it appears that early-type galaxies comprise a population of objects with smoothly varying bulge-to-disk ratio - although a few ellipticals (less than 13%) do not appear to have a exponential component. Finally, there is a general correlation (with much scatter) between the size and the profile shapes of early-type galaxies. The interpretation is that smaller galaxies are more disk-dominated than larger galaxies, which can be linked to the merging process in rich clusters.

Contents

Chapter 1

Introduction - Early-type Galaxies in Clusters

1.1 Overview

This thesis reports a study of the photometric and isophotal properties of early-type galaxies in rich clusters, investigating their relation to morphology, environment and the formation/evolution of galaxies. A picture seems to be emerging of a dichotomy in the population of bright early-type galaxies, based on their kinematics and isophote-shapes. Fast rotators often have disky isophotes, while slow rotators (flattened by velocity anisotropy) usually have regular or boxy isophotes. A main aim of this study is to investigate the relationships between early-type galaxies. Do S0's and disky ellipticals belong physically to a single class of objects, which have a smooth range of bulge-to-disk ratio's, seen at random viewing angles? It is probable that the dichotomy between disky and non-disky galaxies results from differences in the formation histories of the individual galaxies. By studying ellipticals and S0's in the rich cluster environment, we can put constraints on different models of galaxy formation.

The observations on which this study is based were made during March 1994 with the Isaac Newton Telescope, La Palma. The following sections will review the major observations of galaxies in clusters which are relevant. At the end of this introduction, the aims and purposes of this study are outlined in more detail. The remainder of the thesis is then organised as follows. An overview of the observation program and the sample selection for the two observed clusters - Coma and Abell 1367 - is presented in Chapter 2. The data

preparation and photometric calibration is described in Chapter 3. Chapter 4 outlines the methods used to obtain total magnitudes and global parameters for the sample, plus internal and external comparisons. Chapter 5 covers the surface photometry investigation, with a description of the method which has been developed to deconvolve the effects of seeing from radial profiles of intensity, ellipticity, position angle and isophotal shapes. Included in Chapter 6 is a method of fitting parametric forms to the data (a full data-set of deconvolved profiles and derived parameters is given in the appendices). Chapter 7 gives the analysis and discussion of the most important results from the data-set. Finally, a conclusion is given in Chapter 8.

1.2 Galaxy Morphology

Observationally, galaxies present to us a huge range of shapes, sizes, and appearances. In order to understand how galaxies evolved into the complex variety of objects we see today, the first stage is always to look for similarities and patterns which can be used to group galaxies into classes. The Hubble system (see figure 1.1) is the simplist and most widely used classification scheme (Hubble 1936, Sandage 1961). The most obvious distinction is between the elliptical (E) and spiral (S) classes. Ellipticals (or 'early-types') are smooth, featureless and spheroidal in appearance. Their stellar population is red ($B - V \sim 1$), and they were once thought to be completely deficient in interstellar dust, cool gas or recent star-formation. The spirals (or 'late-types'), on the other hand, comprise two components - an elliptical-like central bulge plus a flattened stellar disk superimposed with a spiral-pattern of dust, HII regions, and young blue stars. Hubble also recognised an intermediate type of galaxy - the S0 or lenticular. Like spirals, S0's possess both bulge and disk components. However, the disks are smooth with no spiral structure, little evidence of dust-lanes and presumably no young stars. The two components (bulges and disks) which exist in galaxies must represent strikingly different formation mechanisms. Thus their relative importance in galaxies must provide vital clues in unravelling the processes of galaxy formation.
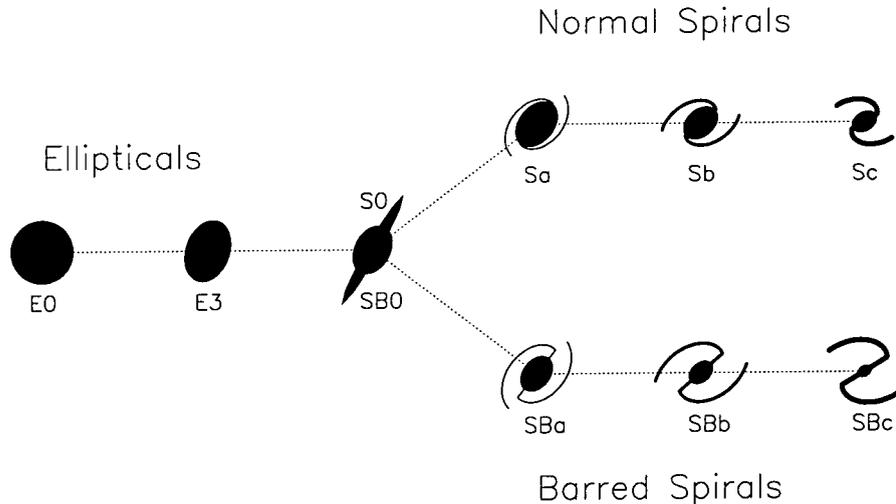
Figure 1.1: The classic Hubble 'tuning-fork' diagram of galaxy morphological types.

1.3 The Cluster Environment

Any theory of galaxy formation will have to explain how we end up with the mixture of morphological types which we observe today. Was the eventual morphology of a particular galaxy uniquely determined by its initial conditions? Alternatively, has the morphology of galaxies been largely determined by their subsequent evolution - in particular through interactions with other galaxies or the intra-cluster medium?

A significant fraction of galaxies (~5%) in the present-day Universe occupy environments where the number density of galaxies is considerably greater than the average (by a factor of ~100 or more). These aggregations of galaxies - the clusters - display a great range of morphologies, like the galaxies themselves. They include populous, centrally-concentrated, and symmetrical systems such as the Coma cluster - which are interpreted as dynamically-relaxed systems (Peebles 1970, Butcher and Oemler 1978). Other clusters are less symmetrical, less dense, and show significant sub-clustering - presumably these clusters have not yet virialized. We are perhaps fortunate that Coma, one of our nearest neighbours, at a distance[1] of about 145 Mpc, is also one of the richest clusters known - richer than 95% of clusters in the Abell (1958) catalogue. Coma is, in effect, a natural laboratory where one can study the effects of an extreme environment on the evolution of

---

[1]The Hubble Constant H_0 is assumed to equal 50 $kms^{-1}Mpc^{-1}$ throughout this work.

galaxies - if it has happened anywhere, it must have happened in Coma!

Although all morphological types are represented at all local densities, it has long been realised that the cluster and field populations are quite different (Hubble and Humason 1931, Morgan 1961, Abell 1965, Oemler 1974). While the field population is dominated by late-type galaxies (spirals and irregulars), the richest clusters contain mainly early-type objects (ellipticals and S0's). The core of Coma, in fact, is almost entirely devoid of spiral galaxies. These observations were taken further by Dressler (1980a), who showed that a smooth, monotonical relationship exists between the morphological fractions and local density. The morphology-density relation is very slow - virtually logarithmic - and extends all the way down to the low-density field, some five orders of magnitude in local space density. This fundamental observation does not rule out the possibility that initial conditions, such as angular momentum (e.g. Sandage *et al.* 1970) and local density (e.g. Gott and Thuan 1976), dominate the eventual morphology of the galaxies. However, to explain the morphology-density relationship we would require these initial conditions to correlate with where the galaxy is forming - i.e. in a proto-cluster region or a proto-field region. Depending on the cosmological model used, such correlations may indeed exist. At present, however, these scenarios do not provide us with predictions which we can test observationally.

The alternative to an 'initial conditions' type explanation for galaxy morphology is later, environment-dependent evolution. In the virialized core of Coma, which relaxed several cluster-crossing times ago, we expect mergers, collisions, and tidal interactions between galaxies to have been significant at the very least. The cores of rich clusters are bathed in a hot X-ray emitting gas. The deep ROSAT image of Coma (White *et al.* 1993) shows the extent of this gas (and incidently also shows significant sub-concentrations of X-ray gas within the cluster - associated with remnants of smaller clusters and groups accreted by Coma). Thus rich clusters possess a significant intra-cluster medium (ICM), which is likely to be an additional factor in galaxy evolution.

1.4   Causes of the Morphology-Density Relation

There are several mechanisms by which *galaxy-galaxy* and *galaxy-cluster* interactions in clusters can potentially explain morphology-gradients (see Dressler 1984 for review). These

are in general better understood than 'initial conditions' and can be tested by observation. It was long believed, for example, that sweeping of gas from spirals by various mechanisms - galaxy collisions (Spitzer and Baade 1951), ram-pressure stripping (Gunn and Gott 1972), and gas evaporation by the hot ICM (Cowie and Songaila 1977) - was responsible for the creation of S0's in rich clusters. Dressler (1980a) largely showed that this was unlikely to be a significant mechanism as S0's exist at *all* local densities, and have a higher bulge-to-disk ratio than spirals at any given local density, as well as more luminous bulges. In addition, S0's sometimes possess a 'third-component', often described as a lens or a thick disk (Burstein 1979), which is not observed in spirals. It is, of course, possible that anemic spirals - i.e. spirals with depleted gas (van den Bergh 1976) - do form in this way (e.g. Strom and Strom 1979, Sullivan *et al.* 1981). Also, Bothun (1981) claims a population of small-bulge S0's in the very core of Coma - perhaps these are the remnants of genuinely stripped spirals. Similarly, excesses of S0's have been found in the most X-ray luminous clusters, which are believed to be in the process of virialisation. However, a large number of S0 galaxies are to be found in the field - around 10% of field galaxies are S0's according to Dressler (1980a). For these objects at least, it seems very unlikely that S0 galaxies were formed by stripping gas from spirals galaxies (through interactions with other galaxies or the cluster environment).

So why are there more S0's than spirals in clusters today? The important distinction between the disks of S0's and spirals is that spiral disks are still actively forming stars today. Larson *et al.* (1980) have suggested that to prevent gas exhaustion through star-formation, spirals must be continuously refuelled by infall from huge, tenuous, gas halo's. In dense regions, tidal encounters will easily 'strip' these loosely-bound envelopes, thus depriving the spirals of their gas supply, fading their disks, and turning them into S0's. Kent (1981) has shown that the morphology-density relation of Dressler can be reproduced by fading the disks of spirals by an amount which is a function of local density, plus various selection effects. The problem with these models is that the turnover of the LF's of spirals and S0's in clusters would be very different, which is not observed (Sandage *et al.* 1985). Processes in clusters are, therefore, increasing the masses of bulges as well as fading disks - the total light being roughly conserved.

Another process by which the properties of cluster galaxies can be changed is through *merging*. A special feature of dense environments is the existence of 'supergiant' cD galaxies.

The massive elliptical-like systems have extended, low surface-brightness stellar envelopes up to 2 Mpc across. They seem to occur at peaks of local density - often at the kinematical centres of rich clusters (Quintana and Lawrie 1982), and also sometimes in smaller, but dense, groups of galaxies. Since cD's have never been found in a field environment, it is clear that they do not represent the extreme bright end of the elliptical LF, but rather the end product of a process which specifically occurs at high density. The high incidence of multiple nuclei (Schneider *et al.* 1983), and other observations, have led astronomers to believe that cD galaxies have grown by early mergers of other cluster galaxies, plus cannibalism of smaller galaxies and tidal stripping.

Have other galaxies undergone mergers during their evolution too? The formation of ellipticals from merging spirals (e.g. Toomre and Toomre 1972) could partly explain the increasing proportion of ellipticals with higher density. Brighter ellipticals ($M < -21$) tend to be slow rotators (Davies *et al.* 1983). Slow rotation is difficult to produce from models of dissipative collapse of gaseous halo's believed to be responsible for disk formation (Fall 1983). Are we, therefore, to identify larger ellipticals (and possibly bulges) with the products of mergers?

These last three sections have reviewed qualitatively the evidence of morphology for galaxy evolution in clusters. The next section summarises the more quantitative approach to morphology, using surface photometry.

1.5   Early-type Galaxies - Surface Photometry

Surface photometry of galaxies - the quantification of the 2D light distribution - is a powerful tool in the study of morphology of galaxies. Although surface photometry requires better signal-to-noise definition than aperture or integrated photometry, it allows us to see, and measure, morphological detail that is otherwise hidden. Elliptical galaxies were once thought to be completely regular and amorphous objects, with no detailed or complex structure. In fact, surface photometry over the years has revealed a whole range of detailed structures in elliptical galaxies. These include shells, ripples, dust, bars and disks, all of which give clues to the evolutionary history of these galaxies.

One of the earliest results of surface photometry of elliptical galaxies was that the shape of the surface brightness to radius function was remarkably uniform from galaxy to galaxy.

This function was, of course, the $r^{\frac{1}{4}}$-law (de Vaucouleurs 1948). Expressed in its usual form:-

$$I(r) = I_e \exp\left(-c\left[\left(\frac{r}{r_e}\right)^{1/4} - 1\right]\right) \tag{1.1}$$

It can be shown by simple integration that if constant c has the value 7.6692, then scale-parameter r_e has the physical interpretation of being the radius enclosing half the total light - the effective radius. Throughout this work, I will use the the convention r_e to mean the effective (half-light) radius of a model profile (such as $r^{\frac{1}{4}}$), while I reserve $r_{1/2}$ to mean the *actual* half-light radius of a galaxy. Only when a model perfectly fits a galaxy from $r = 0$ to $r = \infty$ does $r_e = r_{1/2}$. The effective surface brightness $\langle\mu\rangle_e$ is defined as the mean surface brightness within the isophote of effective radius r_e. Again, I distinguish $\langle\mu\rangle_e$ for a fitted model from $\langle\mu\rangle_{1/2}$ for the *actual* galaxy.

The use of the de Vaucouleurs law to fit the surface photometry of ellipticals, and derive global parameters, has been a valuable tool in the study of the nature of elliptical galaxies. Much has been learned from parameter correlations. Ellipticals were once thought to be a homogeneous single-parameter family - with all properties correlating only with mass or luminosity. This was supported by the correlation between luminosity and velocity dispersion (Faber & Jackson 1976):-

$$L \propto \sigma^4 \tag{1.2}$$

Other correlations between photometric parameters were soon discovered. Kormendy (1977,1980,1982) showed that the effective surface brightness and effective radius were correlated - more luminous galaxies had higher r_e, but lower I_e. The large amount of scatter in the Faber-Jackson relation was recognized as an indication of a second parameter (Terlevich *et al.* 1981). Eventually, it was realised that the variance of global properties was exhausted by two free parameters - the so-called *Fundamental Plane* (Djorgovski & Davis 1987, Dressler *et al.* 1987) relates the photometric parameters r_e and I_e to the velocity dispersion σ:-

$$\log r_e = \alpha\log\sigma + \beta\log I_e + \gamma \tag{1.3}$$

The Faber-Jackson and Kormendy relations are thus projections of the fundamental plane. Because the fundamental plane relates a distance-dependent parameter (r_e) to distance-independent parameters (σ and I_e), it has been used extensively in the field of distance indicators/peculiar velocities. The interpretation of the fundamental plane is that it derives

from the virial theorem, plus a dependence of mass-to-light ratio with mass. It is believed to originate from the formation and evolution processes.

The de Vaucouleurs law has been by far the most popular tool used to parametrise and classify elliptical galaxies. Although there there has never been a rigorous physical justification of the law, numerical models of violent relaxation (van Albada 1982), merging (Barnes 1988) and tidal stripping (Aguilar & White 1986) do produce or preserve $r^{\frac{1}{4}}$-like profiles. However, the increasing improvements in CCD photometry over the past two decades has led to a questioning of the 'universality' of the de Vaucouleurs $r^{\frac{1}{4}}$-law, with many studies concluding that ellipticals have a wide-variety of shapes. Michard (1985) noted that systematic deviations from an $r^{\frac{1}{4}}$-law fit seem to correlate with luminosity. Capaccioli (1985) showed that while the best match to an $r^{\frac{1}{4}}$-law occurred for galaxies with $M_B \sim -21$, galaxies brighter than this had more light at large radii (and vice-versa for fainter galaxies).

This approach is taken further by Caon *et al.* (1993) and D'Onofrio *et al.* (1994), who fit a generalised $r^{\frac{1}{n}}$-law to a sample of Virgo and Fornax early-type galaxies. The generalised $r^{\frac{1}{n}}$-law (first derived by Sersic 1968), can be expressed as:-

$$I(r) = I_e \exp\left(-c_n\left[\left(\frac{r}{r_e}\right)^{1/n} - 1\right]\right) \tag{1.4}$$

Where the constant c_n is chosen to define r_e as the half-light radius of the model fit. The conclusion of Caon *et al.* (1993) and D'Onofrio *et al.* (1994) was that the best-fitting power-law index n is correlated with galaxy size in the sense that brighter/larger objects have higher n. They identify two groupings of galaxies from the $n - r_e$ diagram - 'ordinary' ellipticals and 'bright' ellipticals - with $n < 4$ and $n > 4$ respectively. They associate the 'bright' ellipticals with the products of merging, and suggest that merging not only inflates the galaxy (increases r_e), but also changes the shape of the light-distribution (increases n).

An alternative explanation for the deviations of surface photometry from an $r^{\frac{1}{4}}$-law is the presence of a disk-component. The surface brightness profiles of disks in spiral and S0 galaxies have long been described by the exponential-law (Freeman 1970):-

$$I(r) = I_0 \exp\left(-\frac{r}{\lambda}\right) \tag{1.5}$$

Where I_0 is central intensity and λ is the disk scale-length. The exponential-law is in fact

a special case of the generalised $r^{\frac{1}{n}}$-law with $n = 1$:-

$$I^d(r) = I_e^d \exp\left(-c_1 \left[\frac{r}{r_e^d} - 1\right]\right) \tag{1.6}$$

The disk parameters can thus be expressed in terms of 'half-light' or effective radius and surface brightness - this convention is followed throughout this work, so that disk parameters are easily comparable to parameters from other model fits.

If the disks of spirals and S0's follow an exponential-law, there is no reason to assume that any disks found in elliptical galaxies can not be approximated in the same way. Disks in elliptical galaxies were first discovered not from the surface brightness profile, but from deviations of the isophotes from a perfect ellipse. These deviations can be parametrised by the amplitude c_4 of the $\cos(4\theta)$-term in a Fourier expansion of the isophote radius in polar coordinates (Carter 1978). Positive values of c_4 produce isophotes which are 'pointy' or 'lemon-shaped' - these are termed *disky*. Negative values of c_4 can also occur - these produce *boxy* isophotes. Typically c_4 for ellipticals equals about 1% of the radius of the isophotes (Bender 1988). The usual (though not unique) explanation of disky isophotes is the presence of a weak, nearly edge-on, stellar disk (Carter 1987, Rix & White 1990). This makes disky ellipticals very similar to S0 galaxies. This is backed by Bender *et al.* (1989), who found strong correlations between isophote shapes and other properties. The kinematics show that whereas boxy ellipticals are supported by a mixture of rotation (including minor-axis rotation) and anisotropic velocity dispersion ($0 < V/\sigma < 1$), disky ellipticals appear to be strongly rotation-supported ($V/\sigma \sim 1$, like S0's). Both boxy and disky ellipticals are more flattened than regular ellipticals with $c_4 \sim 0$. Boxy ellipticals can have high X-ray and radio luminosity, whereas disky ellipticals are X-ray and radio quiet (again, like S0's). It has long been known from kinematical studies that bright ellipticals are rotating too slowly to explain their flattening (Bertola & Capaccioli 1975), whilst fainter ellipticals are more rotationally supported (Davies *et al.* 1983). Thus we seem to have either a dichotomy or a trend in elliptical properties between fainter/disky/fast-rotating objects and brighter/boxy/slow-rotating objects. In the next section (1.6), we look at a possible causes of this trend/dichotomy from galaxy evolution in clusters. Using the evidence from surface photometry alone, can we verify whether a continuous range of disk/bulge ratio, c_4 or other properties is giving the sequence $E(Boxy/Bright) \to E(Disky) \to S0$, or are the different classes physically distinct?

1.6 Aims of This Study

The morphology and structure of elliptical and S0 galaxies in rich clusters can provide a vital constraint on theories of galaxy formation and evolution, as the review above demonstrates. Recently, many studies have looked at the differing properties of disky and boxy ellipticals. A picture seems to be emerging of a dichotomy in the elliptical population. Boxy (brighter) ellipticals are supported by anisotropic velocity dispersion, while disky (fainter) ellipticals are flattened by rotation. Boxy ellipticals have higher X-ray and radio luminosities than disky ellipticals. The kinematics of boxy ellipticals suggests, possibly, a lower M/L ratio for these systems, at a given luminosity. Recently, HST data has extended this dichotomy to the cores of ellipticals, suggesting that disky/fainter systems have unresolved cores, whereas boxy/brighter ellipticals show a power-law break in their core intensity profiles. All this evidence points to there being two different formation processes for early-type galaxies. Bender, Burstein and Faber (1992) have proposed a scenario whereby the degree of gaseous dissipation occurring in the last merger determines the eventual characteristics of the galaxy. The first ellipticals are formed by gaseous mergers, producing disky, rapidly-rotating systems. As larger systems are formed by increasingly stellar mergers, galaxies are produced which are slow-rotating (and boxy). This is termed the gas/stellar (GS) continuum. There should obviously be an environmental dependance as to how far the GS continuum has proceeded, with the relaxed central regions of rich clusters showing the greatest evidence of stellar mergers.

All of the older surveys of nearby clusters were based on photographic plates (e.g. Godwin and Peach 1977, Dressler 1980b, Binggeli *et al.* 1985). While this was adequate for LF and morphological studies, much more detail, such as structural and isophotal parameters of galaxies can be accurately measured from CCD data (although, of course, smaller fields of view make it harder to observe large samples). Recent studies such as Jorgensen and Franx (1994), using CCD data, have demonstrated the value of such an approach. Jorgensen and Franx showed that the distribution of isophotal shapes and ellipticities for ellipticals (fainter than $M_B \sim -22$) and S0's in Coma can be adequately modelled by a population which comprises 10% diskless systems and the remaining 90% with a uniform distribution of disk fraction L_d/L_{tot} between 0 and 1. Saglia, Bender & Dressler (1993) showed that c_4 is correlated with residuals from the fundamental plane - explaining that

projection of stellar disks plus unresolved rotation (adding to σ) is causing the effect.

A large CCD-based survey of two rich clusters (Coma and Abell 1367) has been under-taken. The observations were made during March 1994, on the Isaac Newton Telescope, La Palma. A continuous area was imaged in the centres of both clusters, plus selected fields out to over half the turnaround radius for Coma (see Chapter 2 for full details). Rich clusters provide large samples of galaxies at a common distance, and hence they are ideal laboratories for studying the statistical properties of galaxies. Radial profiles of surface brightness, ellipticity, position angle, and isophotal shapes have been measured for a magnitude-limited sample. Seeing is a big problem when trying to extract radial profiles from galaxy images at the distance of Coma or Abell 1367 - typical effective radii are in the range 3"→7" compared to a typical seeing resolution of 1.3". Extensive deconvolution software to remove these effects has been developed. This has been a major part of this study, and is described in detail in Chapter 5. Global parameters such as effective radius, surface brightness and total magnitude (see definition above, Section 1.5) have also been measured.

The principle aim to this project is to study the dichotomy of non-disky/disky ellipticals and the relationship between disky ellipticals and S0's. Do the disky ellipticals and the S0's belong to a single class, as Jorgensen and Franx suggest? Both the isophote shapes and the shape of the intensity profile will be used to answer this. The profile-shape should provide an inclination independent measurement of disk-fraction L_d/L_{tot} - especially useful when the galaxy is near face-on. The 'missing' S0's which have low inclination and have been classed as elliptical (Rix and White 1990) have never been convincingly identified - a problem which this study aims to at least partially resolve. The effect of an extreme high-density environment upon the early-type galaxy population will be investigated. The distribution of galaxies in the central 1° area of Coma (which has been covered continuously) indicates that the core is dynamically relaxed, with the galaxies having interacted with each other frequently. This environment is devoid of cool gas and late-type galaxies. Selected fields out to over half the turnaround radius ($r \sim 3°$) were imaged in the INT March 1994 observations - galaxies here will have not yet visited the cluster core, and will therefore have had much less opportunity to interact, accrete material or merge. Unfortunately, due to time constraints on the project, this part of the INT March 1994 data-set has not yet been processed (though it may form part of a future study). 26 galaxies from the cluster

Abell 1367 (which is more spiral-rich and less-relaxed than Coma) have been included in the sample. However, this number is too small to provide a realistic environmental comparison with Coma. The environment that is sampled in Coma is extreme, therefore the effects of galaxy mergers and interactions should be dramatic. Can the observed trends of profile shape and diskyness with luminosity indicate the degree of merging which has taken place? Relating the isophotal class of ellipticals to the type of merger last experienced (gaseous and dissipative, or stellar and dissipationless) could provide an important picture of how environment affects the merging process.

Chapter 2

Sample and Observations

2.1 Observational Overview

The observations relevant to this study were undertaken with the 2.5 m Isaac Newton Telescope (INT) at the Observatario del Roque de los Muchachos, La Palma, Canary Islands, during the period between March 15th and March 21st 1994. The instrument used was the EEV5 CCD, positioned at the prime focus of the telescope. The EEV5 chip comprises an array of 1280×1180 pixels. Given a pixel-scale of $0.55''/pixel$, this produces a relatively large field-size of $11'23'' \times 10'32''$. All observations were made using the standard R-band filter, which provides the best contrast of galaxy surface brightness over sky surface brightness for this set-up - important for isophotal analysis. Also, observing in the R-band (compared to B or V) de-emphasises the effects of dusty structure such as dust-lanes, which are often present in disky ellipticals or S0's.

The photometric conditions and seeing throughout the 7-night run were consistently very good. Typically, the residual RMS scatter of standard stars was around 0.01-0.02 mag. Only on the first and last nights of the run was the seeing poor ($FWHM\sim 3.0''$ and $\sim 2.0''$ respectively). Additionally, very little usable data was obtained on the final night (due to problems with the telescope pointing and tracking). The $FWHM$ for the remaining 5 nights typically varied between $0.9''$ and $1.4''$. This left 5 nights (about 48 hours) worth of extensive and high quality photometric data. In order to calibrate the data photometrically, several multiple standard star fields (taken from Landolt 1992) were observed every two to three hours. At each occasion, the fields were selected to provide a good range in airmass (see Section 3.3). Twilight exposures were taken at each dusk and dawn to provide evenly-

illuminated CCD frames for flat-field calibration. Also, zero-exposure (bias) frames and dark-current exposures were taken for future calibration.

A total of 398 science exposures were taken, covering the Coma and Abell 1367 clusters. A grid system was set-up to identify and locate each frame. The separation between neighbouring grid-points was 8′, which provides considerable overlap between CCD fields (see Sections 2.2 and 2.3). The Coma grid covered a continuous area of 6° × 6°, with 2025 individual grid-points. It would obviously have taken several months on the INT to observe every grid-point, so it was necessary to be selective. The priorities for the Coma part of the project were as follows:-

- A continuous 1° × 1° square area, centred on the central cD galaxy NGC 4874

- Selected grid-points between 1° and 3° from the centre of Coma. These points were pre-selected in the knowledge that the CCD image would contain at least one Coma galaxy (from various sources, including NED - Nasa/IPAC Extragalactic Database)

- A extension to the central area, surrounding the large (possibly cD) elliptical NGC 4839 - this area is interesting because it may represent a separate cluster which was captured by Coma

- If time allows, enlarge the central (continuous) area by exposing neighbouring frames

All of the above priorities were achieved during the 5 (good seeing) nights. Almost every field was exposed at least twice - once at 60 seconds and once at 300 seconds. The reason for the two different exposure times is as follows. The shorter exposure ensures that the central pixel(s) are not saturated - typically highest counts are in the range 10000 to 25000 - this is very important for profile-fitting and seeing deconvolution. The longer exposure times, whilst saturating the central pixel(s), provide higher S/N ratios further out in the galaxy, thus extending the range over which isophotal analysis is reliable. A similar observing program was devised for Abell 1367. However, the grid was smaller, covering only the central 0.7° × 0.7° area of the cluster. Also, the exposure times used were different from Coma. All the data from Abell 1367 which was used in this study was observed with a single exposure time (120 seconds - sufficient to get reasonable S/N in the outer regions without saturating the core). Unfortunately, due to time limitations, only the data obtained on the night of March 16-17 has been used for this project. This data-set

comprises about two-thirds of the central Coma area and around half the Abell 1367 area covered (the remaining 4 nights of quality data, comprising mainly galaxies in the outer core of Coma, will be included in a future study).

2.2 Sample Selection - Coma (Abell 1656)

The intention of this study is to provide an approximately magnitude-limited sample of early-type galaxies within a volume-limited region of the central Coma Cluster. The continuous area observed on the night of March 16-17 1994 forms the basis of the sample. This is a roughly rectangular region (approximately $1° \times 0.5°$) centred on the cD galaxy NGC 4874. The sample was initially identified using the catalogue of Godwin, Metcalfe & Peach (1983), selecting only galaxies with an isophotal magnitude $b_{26.5}$ brighter than 17.3 (giving a magnitude-limit for early-type galaxies of approximately $R{\simeq}15.7$). With the magnitude-limit chosen as such, almost all galaxies in the Dressler (1980) catalogue within this region are included in the sample. The total number of galaxies (all morphological types) is 129, of which two (Dressler #'s 138 & 219) are immediately rejected as background objects (recession velocities greater than $20000 \, \mathrm{km \, s^{-1}}$, from NED), bringing the total down to 127. The area covered by the survey, and the distribution of GMP galaxies $(b_{26.5} < 17.3)$, is shown in Figure 2.1. It is clear that the sample covers the densest part of the relaxed Coma core, where we can safely assume that galaxy-galaxy and galaxy-cluster interaction has been at least a significant factor in galaxy evolution.

The observed area of Coma was covered by 23 CCD fields, each of dimensions $11'23'' \times 10'32''$ (after trimming). As explained in the *observations* section 2.1, each CCD field was observed twice with different exposure times - 60 seconds (to ensure the galaxy cores aren't saturated) and 300 seconds (to increase S/N in the outer galaxy regions). When combined with the large overlaps between neighbouring CCD fields, it is clear that each galaxy is observed 2, 4 or sometimes 8 times - thus providing a large scope for internal photometric consistency checks. In total, there are 174 short exposure and 169 long exposure images of the 127 sample galaxies. The slight difference in the numbers of short and long exposures is due to the fact that 3 of the CCD fields were observed only with the short exposure (see Figure 2.1), which is partly compensated by the accidental repeat of a long exposure field.

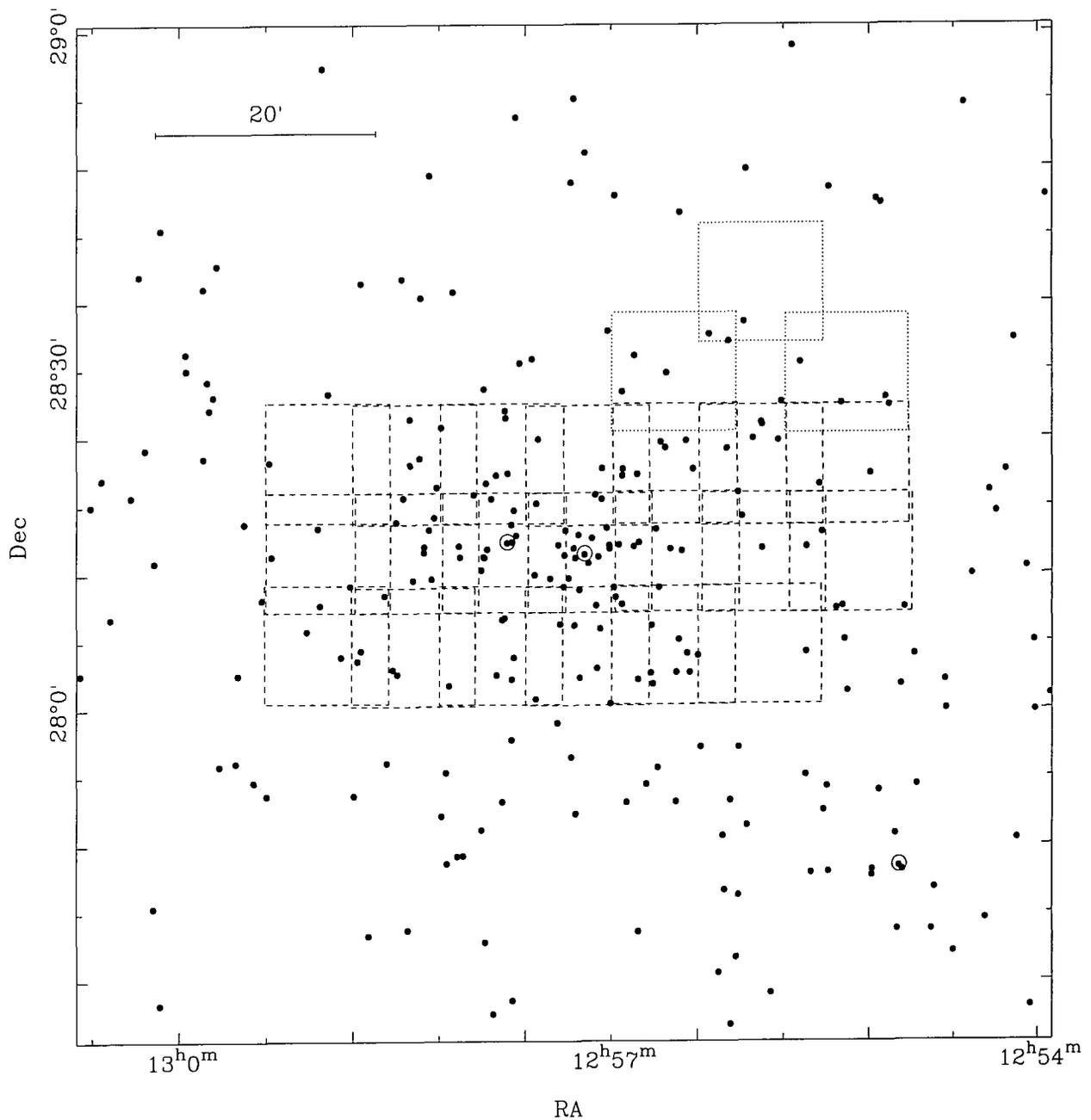Simple morphological typing was then performed, using preferentially the long exposure

Figure 2.1: A map of the central region of Coma showing the locations of the galaxies in the Godwin, Metcalfe & Peach (1983) survey brighter than $b_{26.5} = 17.3$, relative to the area surveyed in this study. The rectangles represent the CCD fields - note the considerable overlap between neighbouring fields. The dashed rectangles show those CCD fields observed with two different exposure times ($60s$ and $300s$), while the three fields shown with dotted lines have only been observed with the short exposure (because of increasing sky-brightness before dawn). The three cD galaxies (NGC 4889, NGC 4874 and NGC 4839) are circled.
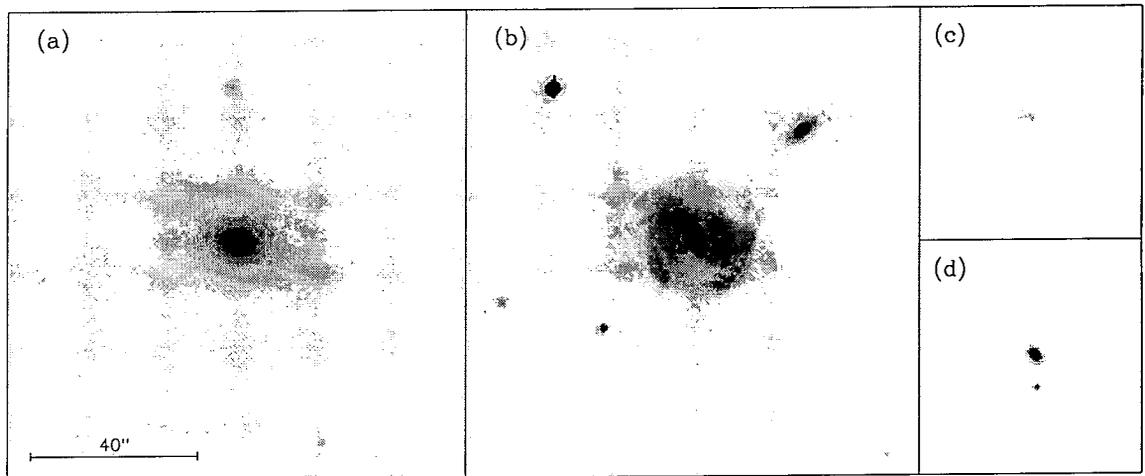
Figure 2.2: Examples from the sample of the four different morphological types used. (a) shows IC 4051, a typical E (early-type) - these account for more than 72% of the data-set. (b) shows NGC 4911, classed S (late-type). (c) shows Dressler #183, classed I (irregular). (d) shows GMP #3133, which is unclassifiable (U) due to its small size, but probably a compact elliptical. All images are to the same scale.

frames. Only 4 types were assigned - E for early-type systems (including S0's and SB0's), S for late-type regular systems, I for irregular or peculiar systems, and U for unclassified. The criterion for classification is described as follows: E galaxies are smooth, amorphous and regular in appearance; S galaxies are round or elliptical in shape but have noticeable substructure (spiral arms, dust lanes); I galaxies are irregular in shape and often have no well-defined core; U galaxies are generally small or faint and cannot convincingly be resolved between types E and S (but are most likely compact ellipticals which have entered the sample because of their high surface brightness). Figure 2.2 displays good examples of the four basic types, taken from the sample. The final breakdown of types is 92 E's, 20 S's, 7 I's and 8 U's. As expected in this high-density environment, the dominant population is early-type - at least 72% of the total. Table 2.1 gives names, positions, redshifts, magnitudes, morphological type and numbers of exposures used for each galaxy in the sample.

2.3 Sample Selection - Abell 1367

In addition to the magnitude-limited Coma sample, observations were also made of a second cluster, Abell 1367. Unlike Coma, Abell 1367 is a relatively spiral-rich irregular cluster - thus providing a contrast with the high-density environment of the relaxed Coma core. As

Table 2.1: Table of the complete Coma galaxy sample, giving names, type, position, redshift, magnitude and number of exposures used. The table is divided into 4 blocks corresponding to the 4 basic morphological types allocated. Names are taken from the D80 (Dressler 1980) and GMP (Godwin, Metcalfe & Peach 1983) catalogues. These are cross-referenced, where applicable, to the NGC, IC and RB (Rood & Baum 1967) catalogues. Positions and redshift are taken from NED (NASA/IPAC Extragalactic Database).

Name of Galaxy			Type	Position (B1950.0)		cz	$b_{26.5}$	# of Exp	
D80 #	GMP #	Other	(D80)	RA	Dec	(km/s)	(GMP)	N_s	N_l
Early-type (E) Galaxies									
62	2393	...	S0	$12^h58^m29.1^s$	$28°03'09''$	8279	16.51	1	1
63	2615	...	S0/a	$12^h58^m07.7^s$	$28°02'07''$	6708	16.97	2	2
64	2866	...	E	$12^h57^m47.6^s$	$28°03'03''$	6992	16.90	1	1
65	2945	...	S0	$12^h57^m41.3^s$	$28°02'40''$	6092	16.15	1	1
68	3660	IC 3963	S0	$12^h56^m48.6^s$	$28°02'38''$	6812	15.76	2	2
69	3730	IC 3959	E	$12^h56^m43.1^s$	$28°03'13''$	7053	15.27	1	1
70	3739	IC 3957	E	$12^h56^m42.6^s$	$28°02'14''$	6345	15.88	1	1
71	3882	RB 214	S0	$12^h56^m32.5^s$	$28°03'18''$	6894	16.97	1	1
72	3958	IC 3947	E	$12^h56^m27.1^s$	$28°03'16''$	5702	15.94	1	1
78	2000	NGC 4923	E	$12^h59^m07.2^s$	$28°06'58''$	5409	14.78	1	1
79	2157	NGC 4919	S0	$12^h58^m52.9^s$	$28°04'41''$	7282	15.06	1	1
80	2237	...	S0	$12^h58^m46.1^s$	$28°04'18''$	6664	16.26	1	1
81	2252	...	E	$12^h58^m44.6^s$	$28°05'13''$	5976	16.10	2	2
84	2956	...	S0	$12^h57^m40.5^s$	$28°04'36''$	6568	16.20	1	1
87	3403	RB 234	E	$12^h57^m05.9^s$	$28°03'45''$	7811	16.87	1	1
88	3423	IC 3976	S0	$12^h57^m04.4^s$	$28°07'10''$	6817	15.80	1	1
91	3997	IC 3946	S0	$12^h56^m23.5^s$	$28°04'48''$	5916	15.28	1	1
92	4499	...	S0	$12^h55^m38.3^s$	$28°05'05''$	7095	16.10	1	1
101	3178	RB 49	S0	$12^h57^m21.3^s$	$28°07'35''$	8009	16.18	2	2
104	3296	NGC 4875	S0	$12^h57^m13.0^s$	$28°10'36''$	8056	15.88	2	2
105	3510	NGC 4869	E	$12^h56^m58.6^s$	$28°10'51''$	6788	14.97	2	2
106	3522	RB 8	S0	$12^h56^m58.1^s$	$28°09'59''$	5126	16.39	2	2
107	3557	RB 6	E	$12^h56^m55.3^s$	$28°09'20''$	6429	16.35	4	4
108	3782	RB 262	S0	$12^h56^m39.6^s$	$28°10'50''$	6396	16.55	2	2
110	4626	...	S0/E	$12^h55^m25.5^s$	$28°08'58''$	7046	16.60	1	2
111	4653	...	S0	$12^h55^m22.9^s$	$28°09'10''$	5805	15.67	1	2
115	1865	...	S0	$12^h59^m21.6^s$	$28°13'34''$	4706	17.09	1	1
116	2510	RB 113	SB0	$12^h58^m18.1^s$	$28°13'56''$	8366	16.13	1	1
117	2457	RB 119	S0/a	$12^h58^m22.6^s$	$28°11'28''$	8571	16.56	1	1
118	2541	NGC 4906	E	$12^h58^m14.9^s$	$28°11'35''$	7494	15.44	1	1
120	2794	NGC 4898B	E	$†12^h57^m53.3^s$	$†28°13'32''$	6371	16.19	1	1
121	2798	NGC 4898A	E	$12^h57^m52.9^s$	$28°13'28''$	6811	14.85	1	1
122	2815	NGC 4894	S0	$12^h57^m51.7^s$	$28°14'12''$	4634	15.87	1	1
124	3201	NGC 4876	E	$12^h57^m19.5^s$	$28°10'54''$	6629	15.51	2	2
125	3222	RB 43	E	$12^h57^m17.9^s$	$28°11'47''$	6907	16.47	1	1
126	3206	RB 46	S0	$12^h57^m19.2^s$	$28°13'40''$	6892	16.36	1	1
127	3254	RB 42	S0	$12^h57^m15.4^s$	$28°14'16''$	7514	16.57	1	1
128	3269	RB 40	S0	$12^h57^m15.1^s$	$28°13'32''$	8001	16.12	1	1
129	3329	NGC 4874	D	$12^h57^m11.0^s$	$28°13'46''$	7176	12.78	1	1
130	3352	NGC 4872	E/S0	$12^h57^m09.1^s$	$28°12'57''$	7205	14.79	1	1
131	3414	NGC 4871	S0	$12^h57^m05.0^s$	$28°13'31''$	6717	14.89	1	1
132	3487	RB 13	S0	$12^h57^m00.7^s$	$28°14'24''$	7683	16.63	1	1
133	3639	NGC 4867	E	$12^h56^m50.2^s$	$28°14'25''$	4793	15.44	2	2
135	3851	RB 260	E	$12^h56^m35.2^s$	$28°14'13''$	8320	16.98	1	1
136	3914	RB 257	E	$12^h56^m30.4^s$	$28°14'03''$	5631	16.57	1	1
137	4315	NGC 4850	E/S0	$12^h55^m56.8^s$	$28°14'15''$	5994	15.39	1	1

Table 2.1: *Continued...*

Name of Galaxy			Type	Position (B1950.0)		cz	$b_{26.5}$	# of Exp	
D80 #	GMP #	Other	(D80)	RA	Dec	(km/s)	(GMP)	N_s	N_l
Early-type (E) Galaxies continued...									
142	2048	RB 133	E	$12^h59^m02.5^s$	$28°16'05''$	7558	17.06	1	1
143	2390	IC 4051	E	$12^h58^m29.9^s$	$28°16'35''$	4932	14.47	1	1
144	2516	IC 4042	S0/a	$12^h58^m18.1^s$	$28°14'25''$	6363	15.34	1	1
145	2535	IC 4041	S0	$12^h58^m16.1^s$	$28°15'56''$	7056	15.93	1	1
146	2551	RB 110	SB0/a	$12^h58^m14.1^s$	$28°17'00''$	7537	16.85	2	2
148	2921	NGC 4889	D	$12^h57^m43.3^s$	$28°14'44''$	6494	12.62	1	1
150	2940	IC 4011	E	$12^h57^m41.5^s$	$28°16'24''$	7245	16.08	1	1
151	2975	NGC 4886	E	$12^h57^m39.5^s$	$28°15'24''$	6359	14.83	1	1
152	3170	IC 3998	SB0	$12^h57^m21.9^s$	$28°14'35''$	9401	15.70	2	2
153	3213	RB 45	E	$12^h57^m19.2^s$	$28°15'57''$	6665	16.14	1	1
154	3291	RB 38	S0	$12^h57^m13.3^s$	$28°15'23''$	6812	16.41	1	1
155	3367	NGC 4873	S0	$12^h57^m07.7^s$	$28°15'10''$	5848	15.15	1	1
156	3471	RB 18	E/S0	$12^h57^m01.6^s$	$28°16'04''$	6665	16.45	1	1
157	3484	RB 14	S0	$12^h57^m00.9^s$	$28°14'42''$	6082	16.26	1	1
158	3534	RB 7	S0	$12^h56^m56.6^s$	$28°14'35''$	6411	17.20	1	1
159	3664	NGC 4864	E	$12^h56^m48.2^s$	$28°14'47''$	6806	14.70	2	2
160	3761	IC 3955	SB0	$12^h56^m41.1^s$	$28°15'58''$	7650	15.57	1	1
161	4230	RB 241	E	$12^h56^m05.3^s$	$28°17'04''$	7198	15.19	2	2
167	2417	NGC 4908	S0/E	$12^h58^m26.9^s$	$28°18'44''$	8804	14.91	2	2
168	2440	IC 4045	E	$12^h58^m23.9^s$	$28°21'35''$	6896	15.17	1	1
170	2727	IC 4026	SB0	$12^h57^m57.4^s$	$28°18'59''$	8220	15.73	4	4
171	2805	RB 91	S0	$12^h57^m52.3^s$	$28°19'59''$	6141	16.57	1	1
172	2839	IC 4021	E	$12^h57^m50.0^s$	$28°18'38''$	5689	16.01	2	2
173	2861	RB 87	S0	$12^h57^m48.1^s$	$28°20'41''$	7493	16.26	1	1
174	2922	IC 4012	E	$12^h57^m43.2^s$	$28°20'52''$	7196	15.93	1	1
175	3073	NGC 4883	S0	$12^h57^m31.2^s$	$28°18'14''$	8071	15.43	4	4
176	3390	RB 26	S0	$12^h57^m06.3^s$	$28°18'58''$	6832	15.89	2	2
177	3433	RB 22	S0	$12^h57^m04.0^s$	$28°18'35''$	5569	16.56	2	2
178	3439	RB 21	S0	$12^h57^m03.7^s$	$28°21'17''$	3650	16.72	1	1
179	3561	NGC 4865	S0	$12^h56^m54.9^s$	$28°21'14''$	4609	14.54	2	2
180	3656	RB 268	S0	$12^h56^m48.9^s$	$28°20'45''$	7790	15.53	2	2
182	4200	RB 243	S0	$12^h56^m06.9^s$	$28°19'09''$	5705	16.84	2	2
193	3084	RB 155	E	$12^h57^m30.2^s$	$28°23'51''$	7566	16.43	2	2
194	3792	NGC 4860	E	$12^h56^m39.1^s$	$28°23'35''$	7864	14.69	1	1
196	3935	...	E	$12^h56^m28.5^s$	$28°23'44''$	6976	16.59	1	1
198	4308	IC 839	S0	$12^h55^m57.3^s$	$28°25'30''$	6738	16.76	1	1
199	4313	NGC 4851	S0	$12^h55^m56.8^s$	$28°25'06''$	7781	16.00	1	1
200	4379	...	S0	$12^h55^m50.0^s$	$28°23'44''$	7506	16.08	1	1
207	2912	RB 167	E	$12^h57^m44.3^s$	$28°26'22''$	6756	16.07	1	1
208	3553	RB 136	S0	$12^h56^m55.3^s$	$28°28'02''$	9439	16.96	1	0
210	4648	...	Ep	$12^h55^m23.7^s$	$28°27'00''$	7352	15.97	2	1
218	3818	...	S0/a	$12^h56^m36.9^s$	$28°29'41''$	7972	15.44	1	0
...	2201	RB 129	...	$12^h58^m48.9^s$	$28°10'59''$	5852	16.86	1	1
...	2778	RB 94	...	$12^h57^m54.0^s$	$28°12'21''$	5410	16.69	1	1
...	2960	RB 74	...	$12^h57^m40.7^s$	$28°17'37''$	5922	16.78	2	2
...	3554	RB 271	...	$12^h56^m55.4^s$	$28°20'37''$	7125	17.20	2	2
Late-type (S) Galaxies									
82	2374	NGC 4911	Sb	$12^h58^m31.4^s$	$28°03'34''$	7970	13.91	1	-
89	3896	IC 3949	S	$12^h56^m31.4^s$	$28°06'12''$	7378	15.13	1	-
97	2059	NGC 4921	SBb	$12^h59^m01.6^s$	$28°09'17''$	5459	13.53	1	-

Table 2.1: *Continued...*

Name of Galaxy			Type	Position (B1950.0)		cz	$b_{26.5}$	# of Exp	
D80 #	GMP #	Other	(D80)	RA	Dec	(km/s)	(GMP)	N_s	N_l
Late-type (S) Galaxies continued...									
98	2347	RB 124	S0/a	$12^h58^m34.5^s$	$28°10'08''$	6828	15.85	4	-
99	2897	RB 83	S0	$12^h57^m45.4^s$	$28°07'59''$	9902	16.98	1	-
100	2910	RB 82	I	$12^h57^m44.8^s$	$28°08'15''$	5136	16.25	1	-
103	3400	IC 3973	S0/a	$12^h57^m05.8^s$	$28°09'13''$	4692	15.32	2	-
147	2651	RB 100	S0	$12^h58^m03.6^s$	$28°14'29''$	7679	16.19	2	-
149	2946	RB 77	S0	$12^h57^m41.9^s$	$28°14'59''$	7816	16.31	1	-
181	3972	RB 252	S0	$12^h56^m25.7^s$	$28°21'13''$	6018	16.52	1	-
184	4779	...	S0	$12^h55^m11.4^s$	$28°20'49''$	...	17.04	1	-
191	2489	RB 116	S0	$12^h58^m20.4^s$	$28°22'08''$	6628	16.69	1	-
192	2584	...	S0	$12^h58^m10.9^s$	$28°24'55''$	5441	16.14	1	-
197	4130	IC 3943	S0/a	$12^h56^m11.5^s$	$28°22'59''$	6704	15.55	2	-
205	2441	NGC 4907	SBb	$12^h58^m24.3^s$	$28°25'38''$	5879	14.65	1	-
211	4849	...	Sa	$12^h55^m05.0^s$	$28°27'28''$	7069	15.81	1	-
212	4866	...	S0	$12^h55^m03.4^s$	$28°26'46''$	...	16.25	2	-
...	2914	RB 166	...	$12^h57^m44.1^s$	$28°25'44''$	7447	17.18	1	-
...	3298	...	...	$12^h57^m13.0^s$	$28°02'46''$	6554	17.26	1	-
...	4281	...	...	$12^h56^m00.6^s$	$28°23'54''$	8473	17.08	1	-
Peculiar or Irregular (I) Galaxies									
102	3262	RB 41	S0	$12^h57^m15.0^s$	$28°07'26''$	3690	16.77	1	-
123	3068	RB 64	SB0	$12^h57^m32.0^s$	$28°11'58''$	7904	16.47	2	-
162	4570	...	I	$12^h55^m31.7^s$	$28°15'41''$	4649	17.25	2	-
169	2559	IC 4040	Scd	$12^h58^m13.3^s$	$28°19'35''$	7840	15.44	1	-
183	4555	...	I	$12^h55^m32.8^s$	$28°19'51''$	8299	16.07	2	-
195	3816	NGC 4858	SBc	$12^h56^m37.3^s$	$28°23'06''$	9436	15.64	1	-
220	4471	NGC 4848	Scd	$12^h55^m40.7^s$	$28°30'45''$	7049	14.50	1	-
Unclassified (U) Galaxies (mostly compact ellipticals/S0's)									
90	3943	RB 209	S0	$12^h56^m27.9^s$	$28°04'49''$	5496	16.93	1	1
109	3733	IC 3960	S0	$12^h56^m43.1^s$	$28°07'27''$	6650	15.85	1	1
112	4945	...	E	$12^h54^m56.4^s$	$28°09'02''$	7428	16.64	1	2
119	2654	RB 99	S0	$12^h58^m03.2^s$	$28°13'30''$	6984	16.38	2	2
224	4043	...	S0	$12^h56^m19.1^s$	$28°33'08''$	...	17.19	2	0
225	4235	...	S0	$12^h56^m04.2^s$	$28°34'28''$	...	16.80	1	0
...	3133	RB 55	...	$12^h57^m25.3^s$	$28°11'38''$	9833	17.23	2	2
...	3640	...	...	$12^h56^m50.2^s$	$28°31'13''$	7483	17.13	1	0

† NGC 4898B: RA and Dec incorrect in NED (position taken from GMP instead).

with Coma, a continuous area was observed on the second night of the INT 1994 observing run (March 16-17). Unfortunately, the area covered was much smaller - an 'L' shape approximately 0.6° long by 0.4° wide. However, this covered roughly half of the central region of the cluster, including the two bright ellipticals NGC 3862 and NGC 3842. The sample was magnitude-limited using the catalogue of Butcher and Oemler (1985), selecting galaxies with a total magnitude J brighter than 16.5. This gives a magnitude-limit in R of $\sim$ 15.55 - equivalent to the Coma magnitude-limit ($R \sim 15.7$) when an adjustment is made for the slightly smaller redshift of Abell 1367. The total number of galaxies (all morphological types) is 27, of which one (BO85 # 66) is immediately rejected as a background object (recession velocity $\sim 14000\,\mathrm{km\,s^{-1}}$, from NED), bringing the total down to 26. The area covered in this study, and the distribution of Butcher & Oemler (1985) galaxies ($J < 16.5$), is shown in Figure 2.3.

The observations of Abell 1367 comprise 7 large-format CCD fields, each covering an area of $11'23'' \times 10'32''$ (after trimming). Unlike the Coma fields, each Abell 1367 field was observed only once, with an exposure time of 120 seconds. This is long enough to produce a reasonable S/N in the outer regions without saturating the cores. Again, there is a large overlap between neighbouring CCD fields, giving repeat observations for 6 of the 26 galaxies - producing a total of 32 galaxy images. When the Coma and Abell 1367 samples are combined, this study gives a grand total of 208 images of 153 separate galaxies. The Abell 1367 galaxies were assigned basic morphological types (E,S,I and U) on the same basis as Coma (see Figure 2.2). Of the 26 galaxies in the sample, 21 were classified E (early-type), 4 as S (late-type) and 1 as I (irregular) - no galaxies were classed U (unclassifiable). Once again, the majority of galaxies are early-type - though it must be remembered that only a relatively small area of Abell 1367 was covered in this study. Table 2.2 gives names, positions, redshifts, magnitudes, morphological type and numbers of exposures used for each galaxy in the sample.

2.4 The Project Sample

Global parameters ($r_{1/2}$, $\langle\mu\rangle_{1/2}$) and total magnitudes are measured for all 153 galaxies in the sample, irrespective of morphological type (see Chapter 4 for methodology). Since these measurements are taken from aperture photometry, a high signal-noise ratio is achievable
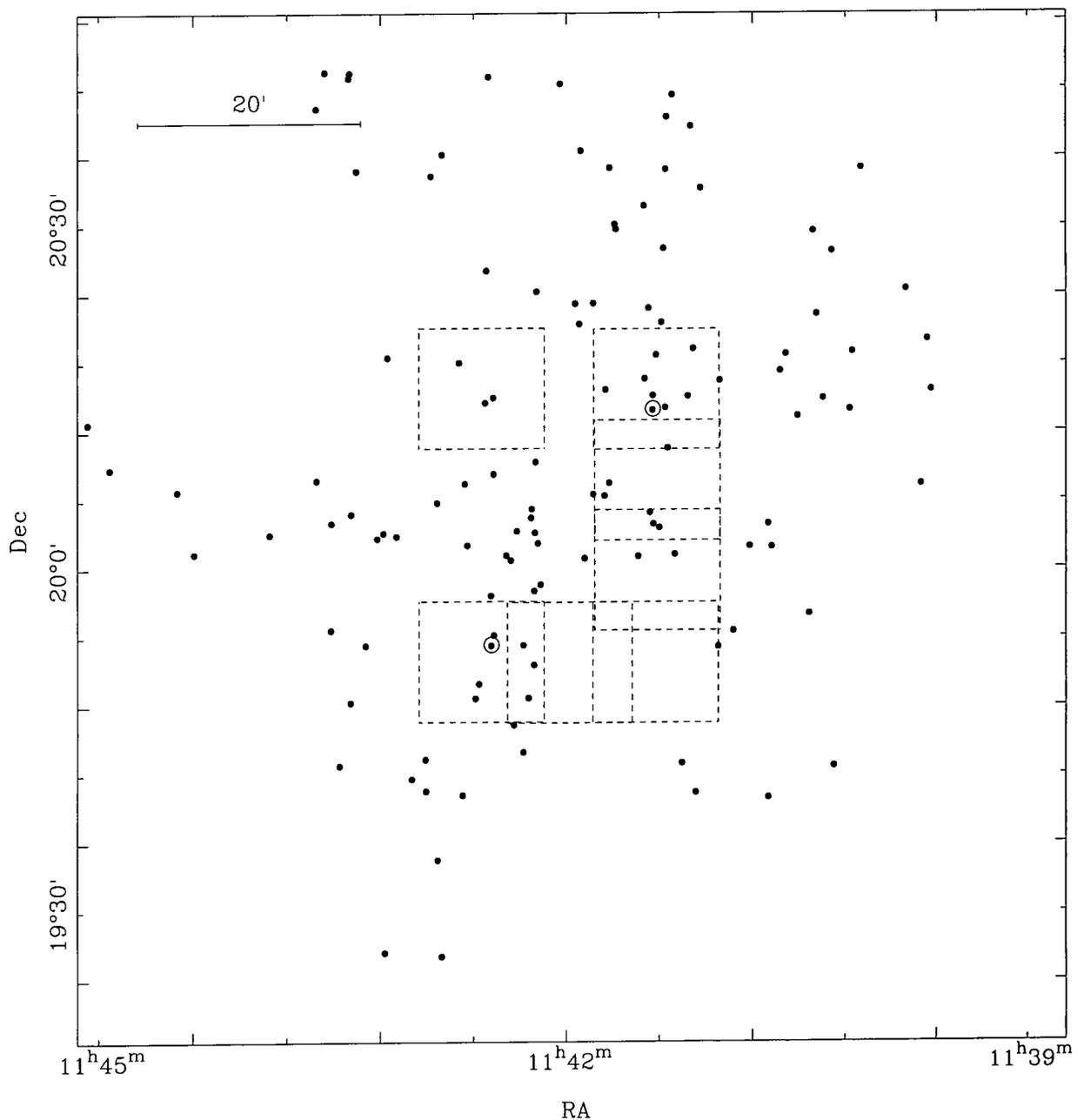
Figure 2.3: A map of the central region of Abell 1367 showing the locations of the galaxies in the Butcher & Oemler (1985) catalogue brighter than $J = 16.5$, relative to the area surveyed in this study. The rectangles represent the CCD fields - note the considerable overlap between neighbouring fields. All CCD fields were observed with an exposure time of $120s$. The two bright elliptical galaxies (NGC 3862 and NGC 3842) are circled.

Table 2.2: Table of the complete Abell 1367 galaxy sample, giving names, type, position, redshift, magnitude and number of exposures used. The table is divided into 3 blocks corresponding to the 3 basic morphological types allocated. Names are taken from the BO85 (Butcher & Oemler 1985) catalogue. These are cross-referenced, where applicable, to the NGC and IC catalogues. Positions and redshift are taken from NED (NASA/IPAC Extragalactic Database).

Name of Galaxy		Type	Position (B1950.0)		cz	J	# of Exp
BO85 #	Other	(BO85)	RA	Dec	(km/s)	(BO85)	N
Early-type (E) Galaxies							
1	NGC 3862	E	$11^h42^m29.5^s$	$19°53'02''$	6462	13.10	1
2	NGC 3842	E	$11^h41^m26.6^s$	$20°13'38''$	6237	13.11	1
10	NGC 3837	E	$11^h41^m20.8^s$	$20°10'20''$	6130	14.05	1
17	NGC 3841	E	$11^h41^m26.6^s$	$20°14'58''$	6363	14.51	1
22	...	S0	$11^h41^m43.4^s$	$20°07'20''$	6454	14.68	1
23	NGC 3844	S0	$11^h41^m25.2^s$	$20°18'25''$	6834	14.69	1
27	NGC 3845	S+	$11^h41^m29.9^s$	$20°16'24''$	5643	14.76	1
28	IC 2955	E	$11^h42^m28.4^s$	$19°53'54''$	6345	14.80	1
33	...	S0	$11^h41^m45.2^s$	$20°06'13''$	5440	14.96	1
38	NGC 3851	E	$11^h41^m44.8^s$	$20°15'30''$	6469	15.08	1
41	...	E	$11^h41^m32.1^s$	$20°00'55''$	7211	15.20	1
45	...	S0	$11^h41^m21.9^s$	$20°13'53''$	6040	15.22	1
46	...	S0	$11^h41^m24.0^s$	$20°03'23''$	5624	15.25	2
52	...	E	$11^h41^m01.4^s$	$19°52'57''$	6564	15.40	1
64	...	S0	$11^h41^m11.1^s$	$20°19'00''$	6399	15.62	1
69	...	E	$11^h41^m27.6^s$	$20°04'43''$	8004	15.78	2
76	...	S0	$11^h42^m16.7^s$	$19°53'15''$	6556	15.93	2
81	...	...	$11^h42^m12.5^s$	$19°51'36''$	...	16.01	2
90	...	...	$11^h42^m35.2^s$	$19°48'41''$	...	16.14	1
107	...	...	$11^h42^m33.8^s$	$19°49'57''$	...	16.36	1
117	...	...	$11^h41^m17.9^s$	$20°01'14''$	...	16.40	1
Late-type (S) Galaxies							
3	NGC 3861	Sbc	$11^h42^m28.4^s$	$20°15'03''$	5082	13.34	1
25	NGC 3857	S0	$11^h42^m14.6^s$	$19°48'38''$	6255	14.71	2
58	...	Sc	$11^h42^m31.5^s$	$20°14'44''$	6009	15.50	1
61	...	Irr	$11^h41^m26.3^s$	$20°03'43''$	4937	15.54	2
Peculiar or Irregular (I) Galaxies							
12	...	S+	$11^h41^m13.2^s$	$20°14'49''$	6903	14.12	1

from the short-exposure fields. The main part of this study is the determination of seeing-corrected $\mu(r)$ profiles, best-fit profile parameters and isophotal shapes for a sample of early-type galaxies (see Chapters 5 and 6). Originally, it was intended to use the long-exposure Coma frames to improve the signal-noise ratio in the outer parts of these galaxies. However, time-constraints have not allowed the problem of merging the short and long-exposure datasets to be resolved (particularly as the long-exposure images of galaxies are saturated in the core). Nonetheless, given the quality of the flat-fielding and the photometry, the objectives of the study can be met using only the short-exposure data-set (see Chapter 7).

Chapter 3

Calibration and Preparation

3.1   Introduction

This chapter outlines the CCD calibration and data-preparation procedures which were carried out on the data of March 16th/17th, in order that data reduction can begin. Section 3.2 describes the CCD calibration procedures, including bias (zero-frame) correction and flat-fielding. Section 3.3 describes the photometric calibration using Landolt standard stars. Finally, Section 3.4 outlines the interactive preparations made for each individual galaxy frame, including the measurement of sky background, seeing *FWHM*, central co-ordinates and the identification of parasitic objects (such as other galaxies, stars and cosmic-ray spikes).

3.2   CCD Calibration - Biasing and Flat-fielding

Before CCD data can be used photometrically, it must be corrected for biasing and flat-field variation. This was done using the packages of the NOAO Image Reduction and Analysis Facility (IRAF).

3.2.1   Bias Removal

The bias was sampled using zero-second exposures of the CCD. A total of 17 bias-frames were taken throughout the INT March 1994 observing run, of which 4 showed evidence of light-leakage and were rejected. To reduce the effect of readout noise on the individual

bias frames (typically 3 ADU per pixel), the 13 zero-exposure frames were averaged into a single master bias-frame. The IRAF routine *zerocombine* subtracts the bias-level (typically 2260 ADU per pixel) from each zero-exposure frame and then averages the residual pixel counts. The master bias-frame thus contains only residual pixel-to-pixel bias structure (up to 15 ADU in one column) and not the bias-level - this is not required, because the IRAF routine *ccdproc* calculates and subtracts the bias-level for each individual image. IRAF does this by fitting a 1D function to the bias overscan strip on each frame - defined by 'pixels' (2-20,3-1150) of the CCD readout. This 1D function, representing the bias-level, is then subtracted by *ccdproc* from the active region of the CCD readout - defined by pixels (23-1264,3-1151) - for each frame (in addition to the master bias-frame).

3.2.2 Flat-fielding

In order to calibrate out the pixel-to-pixel variation in sensitivity on the CCD, it is necessary to expose the CCD to a uniform source of illumination - a flat-field. This was done by exposing the CCD to a patch of twilight sky (chosen from fields known to have relatively few contaminating stars) for enough time to take the pixel count up to about half the saturation value (say 30000 counts). On the night of March 16th/17th, seven flat-fields were observed in the evening twilight and six in the morning twilight. The exposure times varied from 1 second to 16 seconds. After each exposure, the telescope position was skewed by several arc-seconds to avoid co-adding contaminating stars in the master flat-field.

The 13 flat-fields were first de-biased, then examined using IRAF. The flats taken in the dusk sky disagreed with the dawn flats by about 1.5% across the whole CCD. Apart from this, the individual flats agreed with each other to 0.1-0.3%, and there was remarkably little small-scale structure, and no dust rings. A master flat-field for the night was created by the following method:-

1. An evening flat was divided by a morning flat using the IRAF routine *imarith*.

2. A 2-d spline surface was fitted to this residual using the IRAF routine *imsurface*.

3. The spline surface was used to scale the morning flats so that their large-scale structure was identical to the evening flats (to within around 0.2%).

4. All the flats (evening and morning) were scaled and median stacked using IRAF routine *flatcombine* into a master flat-field.

A selection of object frames were then flat-fielded with IRAF using the master flat-field. Inspecting the sky flatness on frames far from the cluster core (i.e. away from the intra-cluster light) showed that the initial flat-fielding was good to 0.8%. It is not certain whether this sky variation is a genuine flat-field (response) error (i.e. should be divided off) or a residual caused by light leakage (i.e. should be subtracted off) or a mixture of both. Certainly, light leakage seems to be present - as only this can explain the difference between the dusk and dawn flat-fields. Looking at frames taken at different times of night, with different mean background levels, seems to suggest than the variation can be subtracted off, as the amplitude seems to depend principally on exposure time only, and not on the background count.

The next step was to try and fit this residual and subtract it from all the object frames. This was done by taking 9 long exposure ($300s$) frames which are far from the central cD's, such that they contain fewer objects and are less contaminated by intra-cluster light. The sky background was interactively measured for each frame, and a constant was subtracted to give the same background on each image (3000 counts). IRAF was then used to perform a clipped median stack on these frames. The resulting frame still had some structure in it (ghosts of galaxies) and pixel-to-pixel variation, which needed to be removed. This structure was removed by fitting a 2D second-order spline to the frame. This surface was subtracted from all 9 object frames, and the sky was seen to be now flat to about 0.3%. There was still a small amount of systematic variation in the frames - the centres of the frames 'dipped' by 10 - 15 counts in the centre. The process outlined above was repeated a second time and a second residual surface was derived. After this had been subtracted there was a modest improvement in the sky flatness. By multiplying this residual frame (for $300s$ exposures) by 0.2 and 0.4, residual frames were produced for $60s$ and $120s$ exposure images respectively.

The conclusion is that a large-scale sky flatness of about 0.2% can be achieved for the night of March 16th/17th. However, the flatness in the photometry itself is not as good - with up to 0.8% variation across the frame. This is equivalent to a photometry error of 0.008 mag from one side of the CCD to the other side - across an individual galaxy (typically 100 pixels), it is clear that the flat-field error becomes negligible (less than 0.06%). Using

the IRAF package *ccdproc*, all the standard star and galaxy images for March 16th/17th were trimmed, de-biased (master bias-frame subtracted) and flat-fielded (divided by master flat-field). Additionally, in order to flatten the sky to 0.2%, the residual frame (for the appropriate exposure time) was subtracted from each Coma and Abell 1367 image.

3.3 Photometric Calibration - Standard Stars

Once all the data has been de-biased and corrected for flat-field variation, it is necessary to calibrate the data for zero-point and atmospheric extinction. After this calibration has been performed it is possible to turn a pixel count into an *above-the-atmosphere* photometric magnitude. In total, 39 images of standard stars from 11 fields were obtained throughout the night of March 16th/17th, all in the R-band and with a range of airmass bracketing the observations. All the stars were chosen from the Landolt (1992) photometric standards, which include multiple fields of standard stars. The advantage of the multiple star fields is that several stars can be observed in a single exposure. The disadvantage is that there is no range in airmass for the groups of stars observed together. Fortunately, all the galaxy observations were made at low airmass, so the requirement for a big range in airmass to bracket the data was diminished.

The first step of the stellar photometry was to measure an instrumental magnitude M_{int} from each standard star image. This was done with John Lucey's *AVIEW* photometry program, which includes a star photometry routine. First the images were displayed and the grey-scale range varied to pick out any obvious contaminating stars, cosmic rays, or defects. These were then removed by interpolating across them. The star photometry routine could then be used on the standard stars. The routine measures the mean background count per arc-second (I_{sky}) within an annulus surrounding the star. Normally, the inner and outer radii used for the annulus were 20″ and 30″ respectively (with a pixel scale[1] of $0.55″pixel^{-1}$, this equates to radii of 36.4 and 54.5 pixels). If this wasn't possible, if the star was too close to edge of the frame for example, then smaller radii were used (such as 13″ and 23″). The total counts within various apertures between radii of 5″ and 21″ centred on the star were integrated. At a given aperture radius $r(″)$, the instrumental magnitude is measured

---

[1]This was measured from positions of stars on an image of star-cluster M67, to an accuracy of less than 1%

as:-

$$M_{int}(r) = 30 - 2.5 \log \left[\frac{L(r) - I_{sky}\pi r^2}{T} \right] \qquad (3.1)$$

Where $L(r)$ is the integrated count within the aperture and T is the exposure time. For each standard star, the photometry measurements were repeated five or six times, each time slightly shifting the origin of the apertures/annuli in a different direction from the centre of the stellar image. This was done in order to get a scatter of a few results and take the mean, rather than rely on one measurement. Also if the different measurements gave totally different results, this might indicate a problem, such a defect or cosmic ray which I had missed. For each star, the instrumental magnitude was taken to be the mean magnitude at an aperture radius of $11''$. Typically, the scatter in the different measurements of $M_{int}(r = 11'')$ was several millimags. M_{int} was not measured at a higher aperture radius than $11''$, because at greater radii the magnitude is affected by pixel noise or flat-field error. On many of the images, the magnitude continued to decline beyond $11''$ (i.e. it appeared as if there was still some starlight beyond $11''$), although on others it stayed constant or even increased. The typical offset between the measured magnitude and the magnitude at the largest sized aperture $(M_{int}(R = 11'') - M_{int}(R = 21''))$ is about $0.01\,\text{mag}$. It cannot be said with certainty whether this is a real offset (due to bad focussing of the telescope) or an artifact of pixel noise or flat-field error adding to the star luminosity. However, if $M_{int}(R = 21'')$ is used to fit the atmospheric absorption and colour term, the RMS scatter of standard stars from the best photometric fit (see Equation 3.2) is doubled compared to the fit using $M_{int}(R = 11'')$. For this reason, it is sensible to choose the magnitude measured within the smaller aperture, although it is realised that there may be a small offset (less than $0.01\,\text{mag}$), which will manifest itself in the zero-point. Table 3.1 gives a list of all the standard stars observed, including the instrumental magnitude measured for each star, the catalogue magnitude and colour index (from Landolt 1992), the time of observation, the airmass and the atmospheric seeing.

The instrumental magnitude in R is a function of the true (above-atmosphere) R magnitude, the atmospheric extinction κ_R, the photometric zero-point ZP (which accounts for the sensitivity of the imaging device), and a colour-term C (which accounts for the difference in spectral response between the filter/CCD and a perfect R-band filter). If the observing conditions are photometric, then the decrement in magnitude due to the atmosphere equals $\kappa_R \sec z$, where κ_R (the atmospheric extinction in R) is a constant during the

Table 3.1: The 39 standard stars observed on the night of March 16th/17th 1994, INT, La Palma.

Name (Landolt)	Time (UT)	Airmass (sec z)	Seeing ($''$)	M_{int} (mag)	R (mag)	$V - R$ (mag)
99Z367	20:44	1.166	2.1	15.954	10.618	0.531
RU149E	20:49	1.147	2.9	18.740	13.397	0.321
RU149F	20:49	1.147	2.9	18.220	12.877	0.594
RU149G	20:49	1.147	2.9	17.842	12.507	0.322
RU149B	20:49	1.147	2.9	17.617	12.268	0.374
RU149A	20:49	1.147	2.9	19.660	14.299	0.196
RU149E	21:54	1.181	1.7	18.752	13.397	0.321
RU149F	21:54	1.181	1.7	18.233	12.877	0.594
RU149G	21:54	1.181	1.7	17.864	12.507	0.322
RU149B	21:54	1.181	1.7	17.622	12.268	0.374
RU149A	21:54	1.181	1.7	19.683	14.299	0.196
RU149E	22:43	1.282	1.4	18.769	13.397	0.321
RU149F	22:43	1.282	1.4	18.243	12.877	0.594
RU149G	22:43	1.282	1.4	17.884	12.507	0.322
RU149B	22:43	1.282	1.4	17.627	12.268	0.374
RU149A	22;43	1.282	1.4	19.693	14.299	0.196
RU149E	23:39	1.509	1.7	18.790	13.397	0.321
RU149F	23:39	1.509	1.7	18.270	12.877	0.594
RU149G	23:39	1.509	1.7	17.910	12.507	0.322
RU149B	23:39	1.509	1.7	17.654	12.268	0.374
RU149A	23:39	1.509	1.7	19.723	14.299	0.196
101327	23:43	1.147	1.4	18.065	12.724	0.717
101326	23:43	1.147	1.4	19.883	14.517	0.406
101330	23:43	1.147	1.4	18.709	13.377	0.346
101262	23:43	1.147	1.4	19.208	13.855	0.440
104339	03:28	1.209	1.2	20.315	14.983	0.476
104336	03:28	1.209	1.2	19.322	13.943	0.461
104334	03:28	1.209	1.2	18.520	13.161	0.323
104330	03:28	1.209	1.2	20.289	14.927	0.369
104325	03:28	1.209	1.2	20.622	15.236	0.345
107626	03:31	1.264	1.3	18.245	12.868	0.600
107627	03:31	1.264	1.3	18.248	12.884	0.465
107626	06:33	1.220	1.4	18.233	12.868	0.600
107627	06:33	1.220	1.4	18.248	12.884	0.465
PG1633D	06:36	1.065	1.4	18.707	13.367	0.324
PG1633C	06:36	1.065	1.4	17.930	12.611	0.618
PG1633B	06:36	1.065	1.4	17.696	12.379	0.590
PG1633A	06:36	1.065	1.4	20.065	14.751	0.505
110230	06:39	1.241	1.3	18.990	13.657	0.624

period of observations, and z is the zenith angle. The colour-term depends on the spectra of the object observed - to the first-order it can be approximated as a linear function of an appropriate colour index, say $V - R$. Putting all this together into the photometric equation:-

$$R - M_{int} + 30 = ZP - \kappa_R \sec z + C_{V-R}(V - R) \tag{3.2}$$

Other (higher-order) colour terms may exist in this expression, but their effect will be very weak and invisible against the random scatter in the measurement of M_{int}. Taking the instrumental magnitudes M_{int} and the catalogue magnitudes R for each standard star, Equation 3.2 can be fitted to yield values for the constants ZP, κ_R and C_{V-R} for the night of March 16th/17th. Once these constants are measured, it is possible to convert any pixel count L into a magnitude R, for any observation of exposure time T, using the following equation:-

$$R = ZP - 2.5 \log \left(\frac{L}{T} \right) - \kappa_R \sec z + C_{V-R}(V - R) \tag{3.3}$$

To fit the photometric constants, a quasi-Newton minimisation algorithm was used to determine the values of the three constants which give the smallest value of RMS scatter in relation 3.2. The results of this fitting are shown in Figures 3.1(a) and (b), which display the separate trends on the photometry of the atmospheric extinction and colour term respectively. The best-fit constants are as follows: $ZP = 24.797$, $\kappa_R = 0.146$ and $C_{V-R} = 0.051$. The RMS scatter to this fit is 0.013 mag. Given the weakness in the trend of the colour-term, and the fact that most of the target objects are ellipticals with $V - R$ close to 0.5, it was decided to drop the colour-term from the photometric equation and add a constant colour-term for $V - R = 0.5$ to zero-point. The new zero-point equals 24.823 (24.797 + 0.5×0.051), and the photometric equation becomes:-

$$R = 24.823 - 2.5 \log \left(\frac{L}{T} \right) - 0.146 \sec z \tag{3.4}$$

The RMS scatter is increased only very slightly to 0.015 mag, and the mean uncertainty on measurements of R, from the quality of the photometric fit, is only 0.002 mag (from $RMS/\sqrt{39}$). Of course, there is likely to be a much larger systematic offset of up to 0.010 mag from the measurement of M_{int}.

It is quite apparent from Figure 3.1 that the night was perfectly photometric. Plots (a) and (b) show that a good fit is achieved with low scatter. Plot (c) is particularly of interest, because it shows atmospheric extinction, calculated for each star *individually*, as
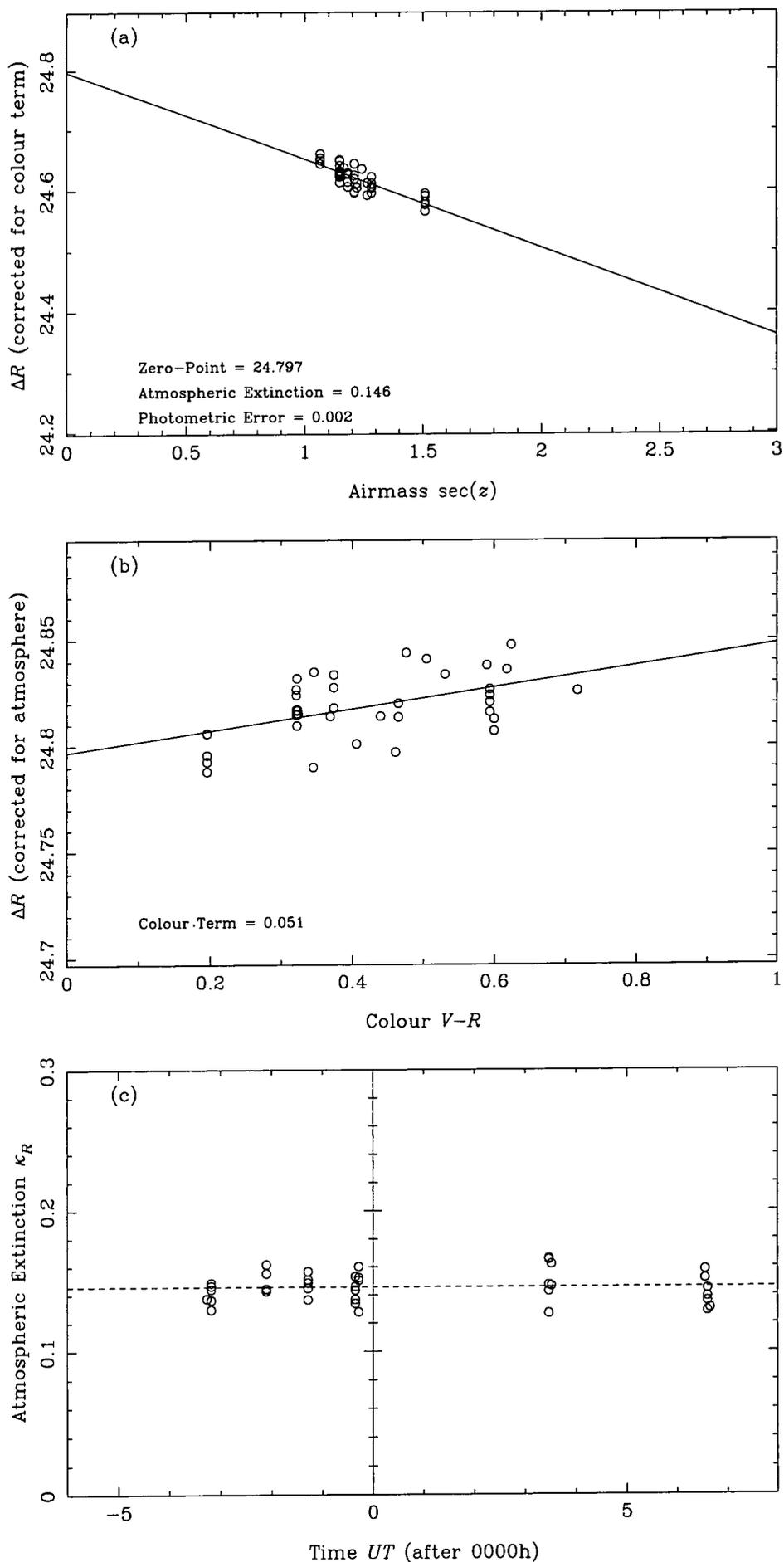
Figure 3.1: The photometric fit to the standard star photometry for the night of March 16th/17th. Plot (a) shows the change in magnitude due to atmospheric extinction versus airmass sec z. Plot (b) shows the change in magnitude due to the colour-term versus colour $V - R$. Plot (c) shows the atmospheric extinction, measured from individual stars, as a function of time, demonstrating that the night was photometric.

a function of time during the night. It is clear that the extinction is, within error, constant for the whole night - from 21:00 UT on March 16th to 07:00 UT on March 17th.

3.4   Data Preparation

After the photometric calibrations for the given night had been completed, it was necessary to prepare each individual galaxy image for the photometric and isophotal data reduction which follows. This involves 'cutting' out a suitable region of the CCD frame containing the galaxy to be studied, and measuring certain parameters from the galaxy which are required by the photometry procedures - specifically the sky background, the FWHM of the stellar PSF and the centroid (central x and y co-ordinates) of the galaxy. Also required is the identification of regions/pixels which are regarded as contaminated - and henceforth excluded from the photometric fitting. All these procedures were undertaken using John Lucey's *AVIEW* software, which contains numerous image-display and photometry algorithms.

The first step to be taken for an individual galaxy is to display the *entire* CCD frame using *AVIEW*. Once the correct galaxy has been identified, the next step is to measure the pixel count of the sky background. The whole frame is used to ensure the region chosen for the sky measurement is sufficiently distant from the galaxy, such that the light from the galaxy is negligible. This causes a problem for the two Coma cD galaxies, as the light from these galaxies is significant right up to, and beyond, their respective CCD frames. The solution is to measure the sky background from neighbouring (overlapping) CCD frames, carefully measuring the background offset between the galaxy CCD frame and the neighbouring frame. The sky background count is measured by placing circular apertures of chosen radius at locations which represent the local sky background for the galaxy in question, carefully avoiding cosmic-rays, stars and neighbouring galaxies. When sufficient apertures have been laid down, *AVIEW* calculates the average sky pixel count from all the pixels in the apertures using a clipped mean. An error on the sky measurement is also calculated using the standard deviation of the pixel counts. A demonstration of the sky measurement procedure using *AVIEW* is shown in figure 3.2.

The next measurement to be undertaken is the FWHM of the stellar PSF. This is required for the seeing deconvolution routines (Chapter 5), and for setting inner radius limits for the galaxy. Again, the whole CCD frame is used - this is because of the scarcity
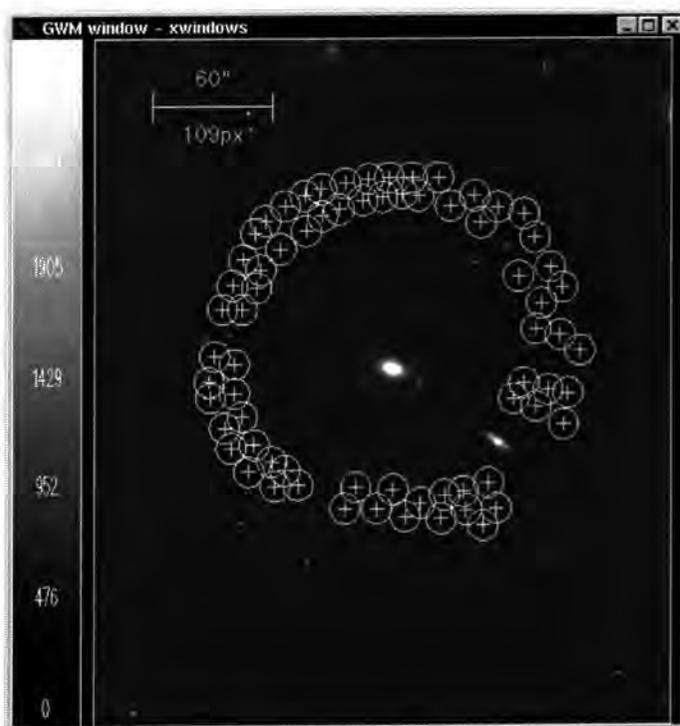
Figure 3.2: Measuring the sky background count for the galaxy IC 4045 in Coma. The circles are manually placed apertures - the pixels within which are used to calculate the sky background and uncertainty.

of stars due to the high galactic latitudes of Coma and Abell 1367. In order to measure the FWHM, a theoretical model for the PSF must be fitted to the stellar images. The PSF model used here is the same as that used by Lucey *et al.* (1991) - a Hankel transform of the combined modulation transfer function of the telescope and atmosphere (see, e.g. Roddier 1981). This gives a much better fit to observed stars than the often-used Gaussian PSF, which does not have enough power at large radii. Using *AVIEW*, several stars with good signal-to-noise (central count $\gtrsim$ 4000) are fitted with the PSF, and the average FWHM calculated. The stars are chosen to be as close as possible to the galaxy, as the FWHM can vary by 10% or more across the CCD frame. The PSF fitting procedure is demonstrated in figure 3.3.

Once the sky background count and FWHM have been successfully measured, the whole area of the CCD frame is no longer needed. A small portion of the CCD frame containing the galaxy is 'chopped' from the image and reloaded into *AVIEW*. The size of the chopped image is chosen to include the outer limits of the galaxy out to where the sky background was measured. This image is saved as it will be used later in the photometry and deconvolution programs. The new image defines a co-ordinate system, and the next step is to define the
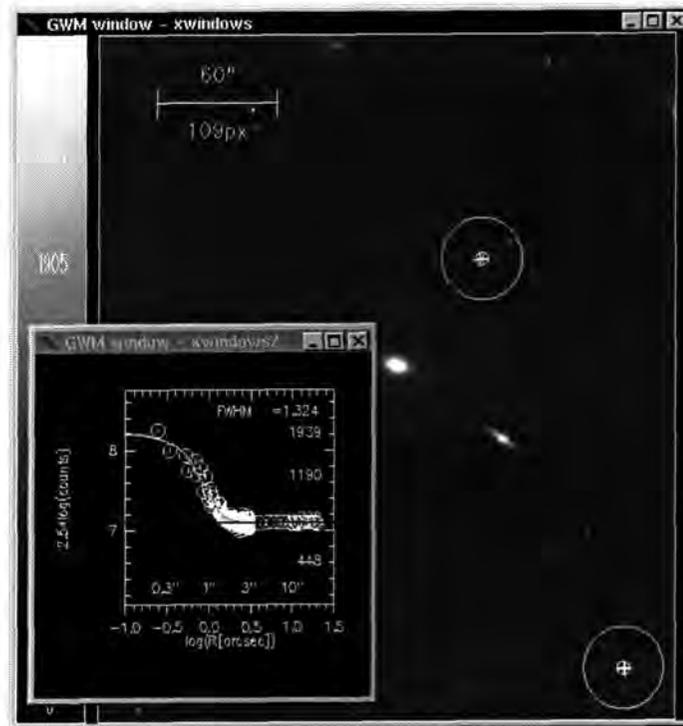
Figure 3.3: The measurement of the FWHM of the stellar PSF. The circles show where a star has been located and chosen for fitting. A theoretical PSF is fitted to each star (small window). The final value for the FWHM is calculated as the average of the FWHM for all stars which are accepted.

centroid (central x and y co-ordinates) for the galaxy. This will be required as a starting point for the ellipse-fitting algorithm. The centroid is calculated using *AVIEW* by laying down a box centred on the brightest pixel - the centroid is calculated as the mean position of the light distribution within the box. The size of the box can be varied according to the seeing and galaxy, but typically 11×11 pixels are used. The centroid fitting procedure is demonstrated in figure 3.4.

The final operation carried out on the data before reduction is the identification of all pixels and regions of pixels which are deemed to be contaminated. This may be due to cosmic-rays, foreground stars or neighbouring galaxies - whatever the case, these pixels need to be recorded so that they can be excluded from all photometry procedures. Included within *AVIEW* is a Starlink algorithm called *PISA*, which identifies and parametrises (as ellipses) all regions of an image where the count exceeds the background by a certain amount across a certain area. The *AVIEW* display for this operation is shown in figure 3.5. Using the cursor, it is possible to 'de-select' ellipses - the obvious one being that fitted to the target galaxy. In addition, *AVIEW* allows extra circles to be manually 'added' to the
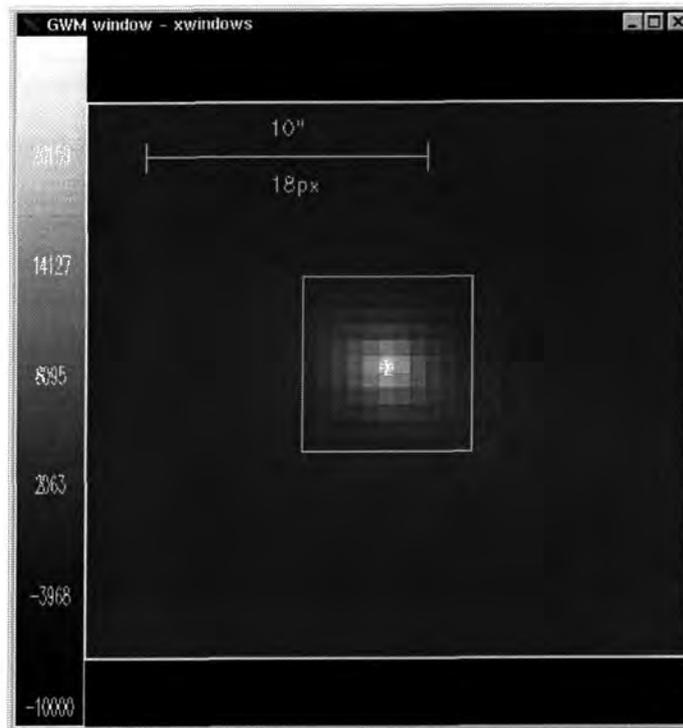
Figure 3.4: Measuring the central co-ordinates of the galaxy IC 4045 in Coma. The galaxy is first zoomed and rescaled to display the central pixels. A variable sized box (typically 11×11 pixels) is placed close to the centre. The central co-ordinates are calculated from the the mean position of the light distribution within the box.
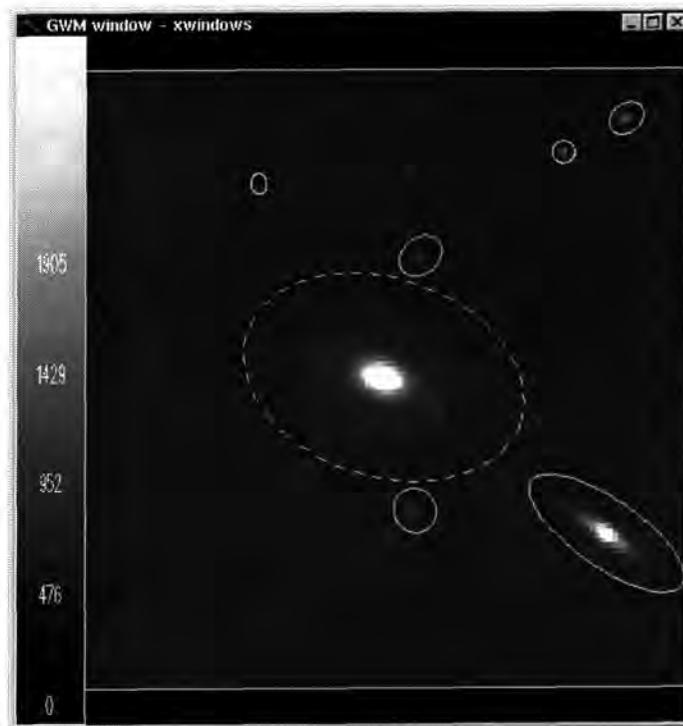
Figure 3.5: The use of *PISA* within *AVIEW* to identify all objects on an image, with the aim of locating all contaminated pixels. In this example, *PISA* has located and parametrised 7 ellipses where the count exceeds a certain level across a certain number of pixels. Using *AVIEW*, the ellipse containing the target galaxy (IC 4045) has been 'de-selected', as obviously these pixels are required - the ellipse now appears as a dashed line.

PISA ellipses, to isolate objects which have been missed by *PISA* - cosmic-rays for instance (see figure 3.6).

Once these preparatory procedures have been successfully undertaken, typically taking 20 minutes per galaxy, *AVIEW* produces two ascii files containing all the information required to perform surface and aperture photometry on the galaxies. The first contains the FWHM, central co-ordinates and sky background count, along with photometric constants (see section 3.3). The second ascii file contains parameters of all *PISA* ellipses, plus any manually added circular apertures. This can easily be turned into a list of 'bad' pixels to be ignored in the surface photometry, or replaced in the aperture photometry.

This chapter has outlined the necessary preparation procedures which must be carried out before data-reduction proper begins. In Chapter 4, the basic galaxy photometry procedures are outlined and comparisons made with other published data.
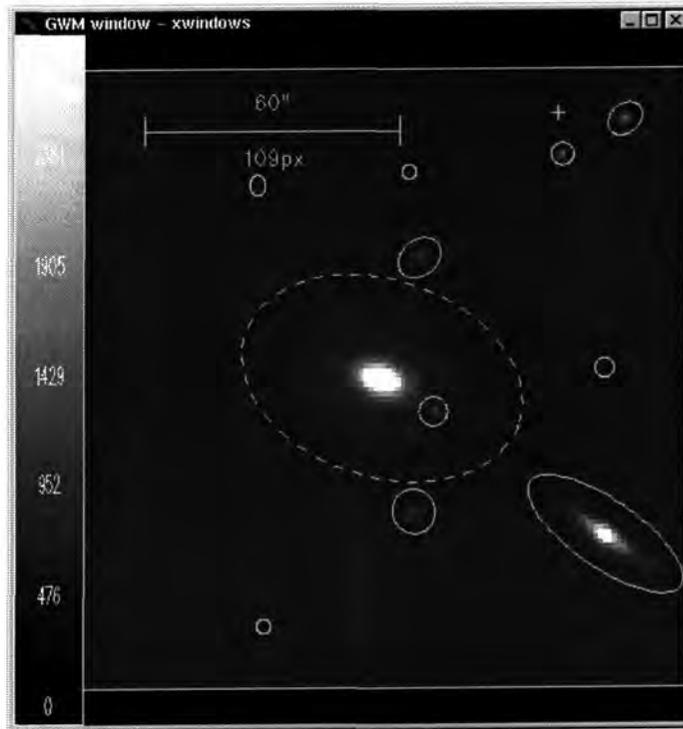
Figure 3.6: Manual identification of objects which were not located by *PISA*. These are typically small and bright (i.e. cosmic-ray streaks), or are blended into the target galaxy. *AVIEW* allows these areas to be identified with a variable radius circle and included with the *PISA* ellipses. In this example, 4 circles have been added to the ellipses in figure 3.5. The cross at the top right hand corner of the image is where a cosmic-ray has been identified - the user now adds a value for the radius and a fifth circle will be added.

Chapter 4

Aperture Photometry and Total Magnitudes

4.1 Introduction

This chapter describes the measurement of model-independent global photometric parameters for the Coma/Abell 1367 sample, and their comparison with other published data (the Coma/Abell 1367 sample is referred to as the *Steel* data-set when comparing with other authors data). Section 4.2 outlines the measurement of elliptical aperture magnitudes and the cosmological corrections applied to these magnitudes. Section 4.3 details how these aperture magnitudes are extrapolated to calculate a total (i.e. asymptotic) R magnitude for each galaxy. Section 4.4 shows how the half-light parameters are now easily measured. Section 4.5 looks at the internal comparisons of photometry from the repeated galaxy images. Finally, Section 4.6 compares the total and aperture magnitudes measured here with other published data.

4.2 Elliptical Aperture Magnitudes

In order to measure the total magnitudes and half-light parameters $(r_{1/2}, \langle \mu \rangle_{1/2})$ of the galaxy sample, it is necessary to perform aperture photometry on their images. It was decided that elliptical apertures (based on fitted ellipses) rather than circular apertures would be used here for the photometry. This was for consistency with the rest of the study - global parameters fitted non-parametrically from the aperture photometry are then com-

parable with scale parameters fitted parametrically from surface photometry profiles (see chapter 6). There is also the consideration that since most galaxies are not circular, then circular aperture photometry is not the most appropriate way to represent the light distribution of real galaxies (admittedly, the difference between circular and elliptical aperture photometry is not great for many objects).

The first task is to fit the objects with elliptical isophotes which are to be used as apertures in the photometry. This is done using a surface photometry routine which is based on *GALPHOT*, created by Marjin Franx (see Franx *et al.* 1989). A full description of this method is given in Section 5.3. The end result is a table containing surface counts, ellipse parameters and higher order isophotal terms as a function of equivalent ellipse radius r $(= \sqrt{ab})$. The range in radius was from 0.3 pixels to the edge of the frame - the size of the radii increase logarithmically, with each radius a factor 1.1 greater than the last. Another useful feature of the ellipse-fitting process is that a $2D$ model of the image can be reconstructed from the output. This can then be used to 'patch' the pixels in the original image which are deemed to be 'bad' (i.e. due to contaminating objects, cosmic-rays and so on). These pixels were defined using *AVIEW*, and are completely ignored by the ellipse-fitting program (see Section 3.4).

Once a table of the fitted ellipse parameters has been obtained, it is a straightforward matter to produce a total aperture count within each ellipse. This is done by summing the counts of the pixels in the 'patched' image which lie within the given ellipse. A small correction is made to each aperture count to account for the difference in area between the summed pixels and the ellipse area (πab) - the surface count of the relevant ellipse is used (from the surface photometry output). Of course, this correction is negligible for aperture radii greater than about 10 pixels. The background (sky) count is subtracted from each of the aperture counts - a discussion about how the sky is measured is included in Section 3.4. Using the calibration for zero-point and atmospheric extinction (Section 3.3), each aperture count can be converted into an above-the-atmosphere aperture magnitude. Thus, if an ellipse of effective radius $r = \sqrt{ab}$ contains N pixels, each with a sky-subtracted count of L_i and an area of A_{pix} (equals $0.3025''^2$ in this case), and $I(r)$ is the sky-subtracted surface count of the ellipse, then the *raw* above-the-atmosphere aperture magnitude R_{raw}

is given by Equation 4.1.

$$R_{raw}(r) = ZP - 2.5 \log \left[\frac{\sum_{i=1}^{N} L_i + (\pi ab - N A_{pix}) I(r)}{T} \right] - \kappa_R \sec z \qquad (4.1)$$

Finally, corrections are made to each aperture photometry point for reduction in measured luminosity due to galactic extinction and K-correction (Equation 4.2).

$$R_{corrected}(r) = R_{raw}(r) - 0.58 A_B - 1.0z \qquad (4.2)$$

Where z is the heliocentric galaxy redshift. The galactic extinction in B is calculated according to the prescription of Burstein & Heiles (1984), and is very small at the high galactic latitudes of Coma and Abell 1367 ($A_B \lesssim 0.05$). The K-correction is to account for the redshifting of the galaxy spectral energy distribution with respect to the R-bandpass, which has approximately the effect of a dimming of value $1.0z$ in magnitude. Additionally, when aperture magnitudes are converted into surface brightness's (e.g. when calculating half-light surface brightness), an additional term $2.5 \log (1 + z)^4$ is subtracted from the photometry to correct for cosmological dimming.

4.3 Magnitude Extrapolation

The calculation of total magnitude from aperture photometry is not a straightforward process. Galaxies do not have a sharp edge - their outer surface brightness profiles merge imperceptibly into the sky background. At some point, the galaxy signal is lost in the sky noise and/or the residual flat-field structure. In order to calculate the asymptotic total magnitude, therefore, it is necessary to extrapolate from a region where the galaxy signal is well-defined. One method is to fit a power-law growth curve to the aperture photometry profiles (e.g. Jorgensen & Franx 1994), which automatically fixes the total magnitude, as well as the scaling parameters ($r_{1/2}$, $\langle \mu \rangle_{1/2}$). However, a growth curve makes the assumption that an $r^{\frac{1}{4}}$-law (or other law) is followed from $r = 0$ to $r = \infty$. This is a not a very good assumption, even for purely elliptical galaxies, and will lead to systematic errors in the derived parameters. The intention here is to obtain total magnitudes (and global parameters) which are as model-independent as possible, and are therefore not biased in any way by the morphology of galaxies.

The method which has been used to measure the total magnitude takes as its base the aperture magnitude measured at an outer radius r_{out}. The total magnitude is then

estimated by calculating how much luminosity lies beyond the ellipse $r = r_{out}$. This is done by performing three least-squares power-law fits ($r^{\frac{1}{4}}$, $r^{\frac{1}{2}}$ and exponential) on the surface brightness data between two limits r_1 and r_2. The fit which gives the smallest χ^2 is a good indicator of the shape of the galaxy profile in its outer regions - this can then be used to calculate the luminosity between $r = r_{out}$ and $r = \infty$. The rules which govern the values of r_1, r_2 and r_{out} are of importance, and are described here:-

- **Outer profile-fitting limit** r_2 is calculated as the radius of the largest ellipse where the pixel count (minus sky) is still greater than 1.5 times the error on the sky measurement. This was chosen to ensure sufficient signal-to-noise for fitting the profiles, but yet far enough out to represent the outer profile of the galaxy. For some galaxies, the surface photometry could not be considered reliable out as far as this - for instance, where a galaxy had be 'chopped out' from a sloping background (such as a cD halo), or if a large parasitic object had to be removed. In these cases, a smaller value of r_2 was obtained by manually inspecting the surface photometry profiles.

- **Inner profile-fitting limit** r_1 is calculated by dividing r_2 by 1.1^{16}, thus generating a range of 17 ellipse photometry points for the profile-fitting. Two exceptions are made to this rule. Firstly, for the four brightest/largest galaxies (i.e. NGC 4874, NGC 4889, NGC 3862 and NGC 3842), the rule is relaxed such that the inner limit r_1 is reduced to the radius of the first ellipse outside $r = 15''$. Secondly, for smaller galaxies, the value r_1 calculated above is smaller than $5''$, where seeing-effects dominate the profile. In such cases, r_1 is set to the radius of the first ellipse outside $r = 5''$ (unless this produces less than 8 ellipse points in the range r_1 to r_2, in which case $r_1 = r_2/1.1^7$).

- **Outer radius for aperture photometry** r_{out} is calculated as the minimum of r_2 and the radius of the last aperture measurement (i.e. the last ellipse fitting entirely within the image).

This procedure is used to measure total magnitudes for all 153 galaxies in the data-set. Also calculated for each galaxy is an extrapolated surface brightness profile. This involves replacing all pixel-count values from $r_2/1.1^2$ (i.e. two ellipses before r_2) to an arbitrarily high radius, using the best-fit surface brightness profile between r_1 and r_2. These profiles are used in the seeing-deconvolution routines (Chapter 5) - this is to reduce the effect

of noise in the outer profile, which can generate instability in the iterative part of the deconvolution algorithm.

4.4 Global Parameters

Once the total magnitude has been measured, it is straightforward to calculate the model-independent half-light parameters. This is done using the *seeing-corrected* aperture and surface photometry profiles with equivalent radius (see Chapter 5, which describes the seeing-correction). The magnitude corresponding to half the luminosity is calculated. The half-light radius $r_{1/2}$ can then be interpolated from the sequence of aperture photometry with radius. The uncertainty on $r_{1/2}$ is calculated from the error on the magnitude (from the sky error) and the slope of magnitude against radius at $r_{1/2}$. The half-light surface brightness $\langle\mu\rangle_{1/2}$ (the mean surface brightness within $r_{1/2}$) is calculated by dividing the half-luminosity by $\pi r_{1/2}^2$. Also calculated is the mean surface brightness $(\mu_{1/2})$ at $r_{1/2}$ - this is simply interpolated from the surface photometry at $r_{1/2}$. In Chapter 7, it is demonstrated that $\mu_{1/2} - \langle\mu\rangle_{1/2}$ can be used to measure the shape n of a galaxy following a generalised $r^{\frac{1}{n}}$-law. The half-light parameters, along with the total magnitudes, measured for each of the 153 galaxies in the sample, are shown in Table A.1 in Appendix A.

4.5 Internal Comparisons

Of the 153 galaxies observed in the Coma & Abell 1367 sample, 41 objects were observed twice and a further 4 were observed four times, giving a total of 53 repeat images. The total (extrapolated) magnitudes for these 53 repeats are unaffected by seeing errors and should provide a useful internal consistency check on the quality of the photometry. Figure 4.1 shows the internal comparison of total magnitudes, by comparing the magnitude of the image processed first with the magnitudes of subsequently processed images. This is plotted as both residual versus magnitude (upper diagram) and as magnitude versus magnitude (lower diagram).

It is apparent that the residual plot shows no trend of increasing scatter with fainter galaxies. The *RMS* scatter is ±0.012 mag. This can be compared with the measured uncertainty, which is $\sim\pm0.037$ mag. This suggests that the errors on the magnitudes,
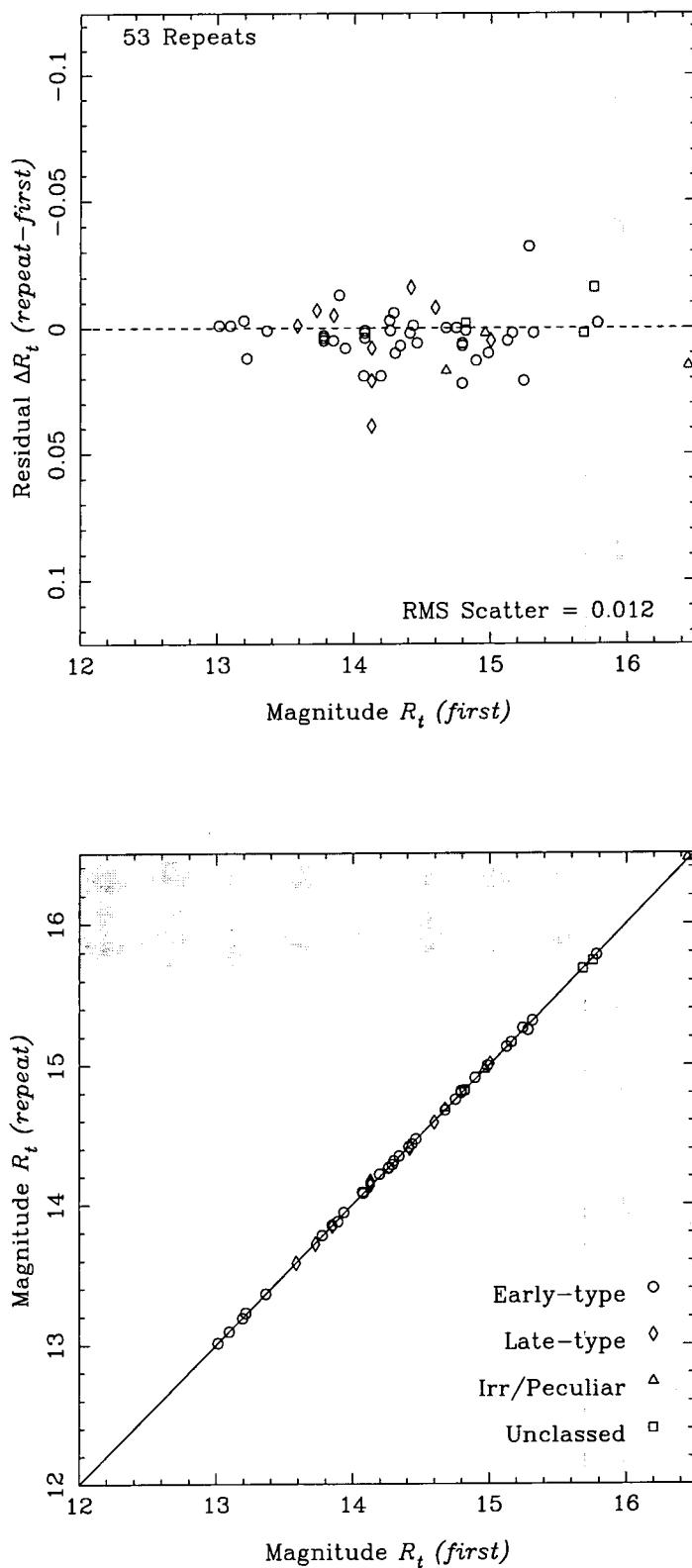
Figure 4.1: Internal comparison of total (asymptotic) magnitudes, comparing first against repeat observations. The upper plot shows the residual against magnitude. The lower plot shows the magnitude against magnitude. The shaded area is beyond the magnitude-limit ($R\sim15.7$ for Steel).

which are derived from the sky errors, are somewhat exaggerated. Additionally, large disagreements between repeat magnitudes were taken into account when fine-tuning the sky-level (see Section 3.4). This may have had the effect of improving the sky measurements for repeat observations relative to single observations.

As an additional internal photometry check, circular aperture magnitudes were measured for all galaxies (diameter equals 20″). In addition to checking the internal photometry, these values can also be used to compare externally with the V-band Coma aperture photometry of Lucey et al. (1991), see Section 4.6. Comparisons between aperture photometry measurements are particularly useful, because they are less affected by sky-error than total magnitudes, and do not involve extrapolation. The internal comparison is shown in Figure 4.2, which has the same layout as Figure 4.1. The RMS scatter is similar to that of the total magnitude measurement at ±0.015 mag. This is somewhat larger than the typical measurement error due to the sky-error (∼±0.007 mag). Thus, other factors may come into play here, including seeing-correction, flat-field errors and pixel-scale errors. The conclusion is that the total and aperture photometry of galaxies is internally consistent to approximately ±0.01 mag.

4.6 External Comparisons

In this section, the total asymptotic magnitudes for Coma are compared with other published data. This is done to confirm the integrity of the photometry. The comparison data-sets are published in Andreon et al. (1996), Jorgensen & Franx (1994), Saglia, Bender & Dressler (1993), Godwin, Metcalfe & Peach (1983), Lobo et al. (1997) and Doi et al. (1995). Each comparison is discussed in detail below:-

1. **Andreon et al. (1996).** R-band CCD photometry of 97 early-type galaxies, brighter than $B = 17.0$ (selected from Godwin, Metcalfe & Peach 1983), within 1° of the centre of Coma. The magnitudes quoted are total (asymptotic), so they should be comparable to the Steel data-set. The comparison is shown in Figure 4.3.

2. **Jorgensen & Franx (1994).** Gunn-r CCD photometry of 171 galaxies magnitude-limited to $r = 15.3$ (selected from Godwin, Metcalfe & Peach 1983), within a rectangular area (somewhat more than 1° square) centred on Coma. The magnitudes
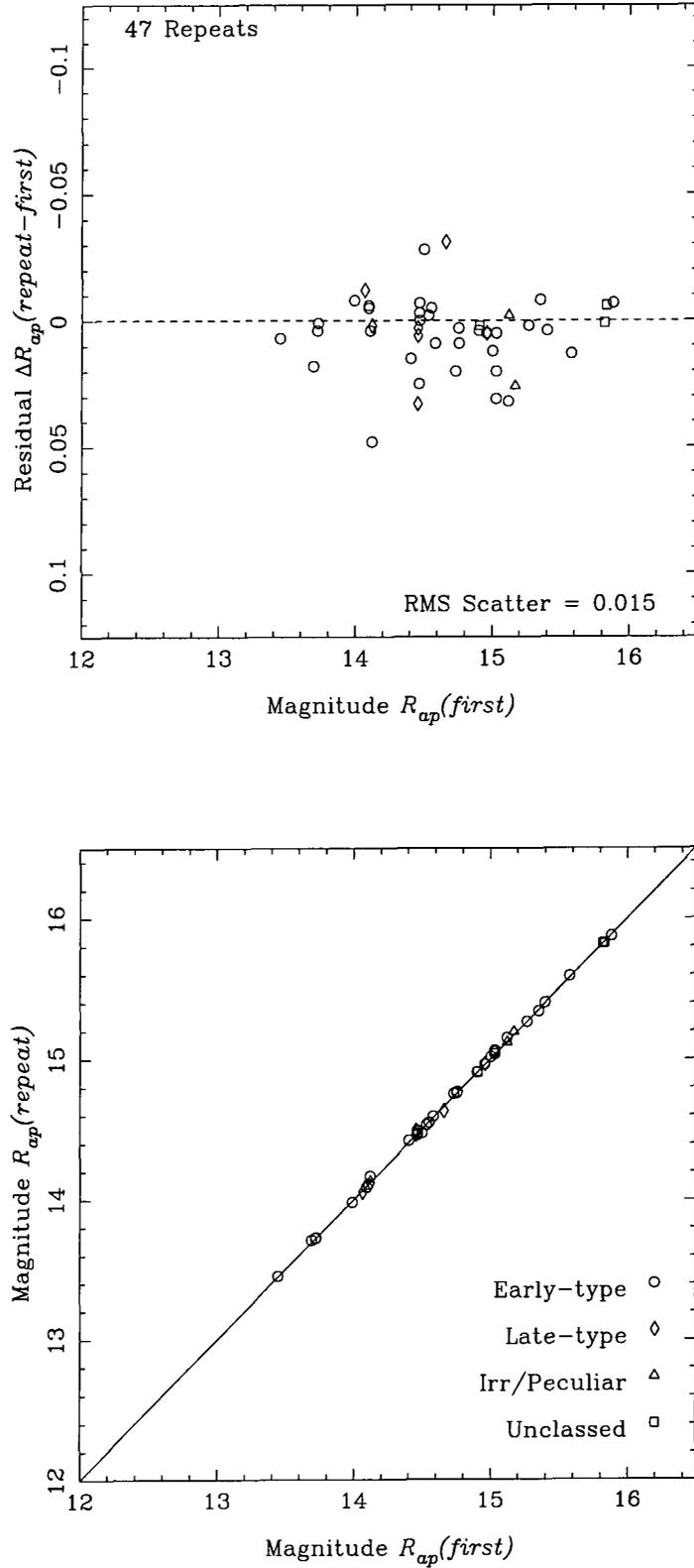
Figure 4.2: Internal comparison of circular aperture magnitudes (measured at diameter of 20″), comparing first against repeat observations. The upper plot shows the residual against magnitude. The lower plot shows the magnitude against magnitude.

quoted are derived from fitting a growth curve to elliptical aperture photometry. The model used for elliptical and S0 galaxies was a de Vaucouleurs $r^{\frac{1}{4}}$-law. There may a systematic difference between these model-dependent total magnitudes and the author's model-independent values, on top of the expected colour difference $r - R \sim 0.3$. The comparison is shown in Figure 4.4.

3. **Saglia, Bender & Dressler (1993)**. B-band CCD photometry of 61 central Coma galaxies taken from the Dressler (1987) sample. The magnitudes quoted are derived from fitting a generalised growth curve to both elliptical and circular aperture photometry. The elliptical photometry was chosen for the best comparison with the author's data. The expected colour difference is $B - R \sim 1.9$. The comparison is shown in Figure 4.5.

4. **Godwin, Metcalfe & Peach (1983)**. A catalogue of 6724 galaxies in an field 2.63 degrees^2 centred on Coma. The photometry is photographic (b-band) and isophotal magnitude $b_{26.5}$ (integrated magnitude within $b = 26.5$ isophote) measured for each galaxy. The catalogue has a magnitude-limit of $b_{26.5} = 21$. There will be a large difference due to the colour and the offset between isophotal and total magnitudes. The comparison is shown in Figure 4.6.

5. **Lobo et al. (1997)**. A catalogue of 7023 galaxies in an field 0.4 degrees^2 around the central cD galaxies in Coma. V-band CCD photometry, including isophotal magnitude $V_{26.5}$ (integrated magnitude within $V = 26.5$ isophote) are measured for each galaxy. The catalogue is complete to $V_{26.5} = 22.5$. There will be a large difference due to the colour and the offset between isophotal and total magnitudes. The comparison is shown in Figure 4.7.

6. **Doi et al. (1995)**. A catalogue of 450 galaxies in a field $9.8° \times 9.8°$ centred on Coma. The photometry is photographic (B-band) and a total magnitude is estimated for each galaxy (by fitting a de Vaucouleurs growth-curve to 3 isophotal magnitudes). The catalogue has a completeness limit of $B = 16.5$. There will be a large difference due to the colour ($B - R \sim 1.9$). The comparison is shown in Figure 4.8.

For each comparison, the mean offset and *RMS* scatter between the two systems are calculated. This measurement is repeated after rejecting any points which are more than
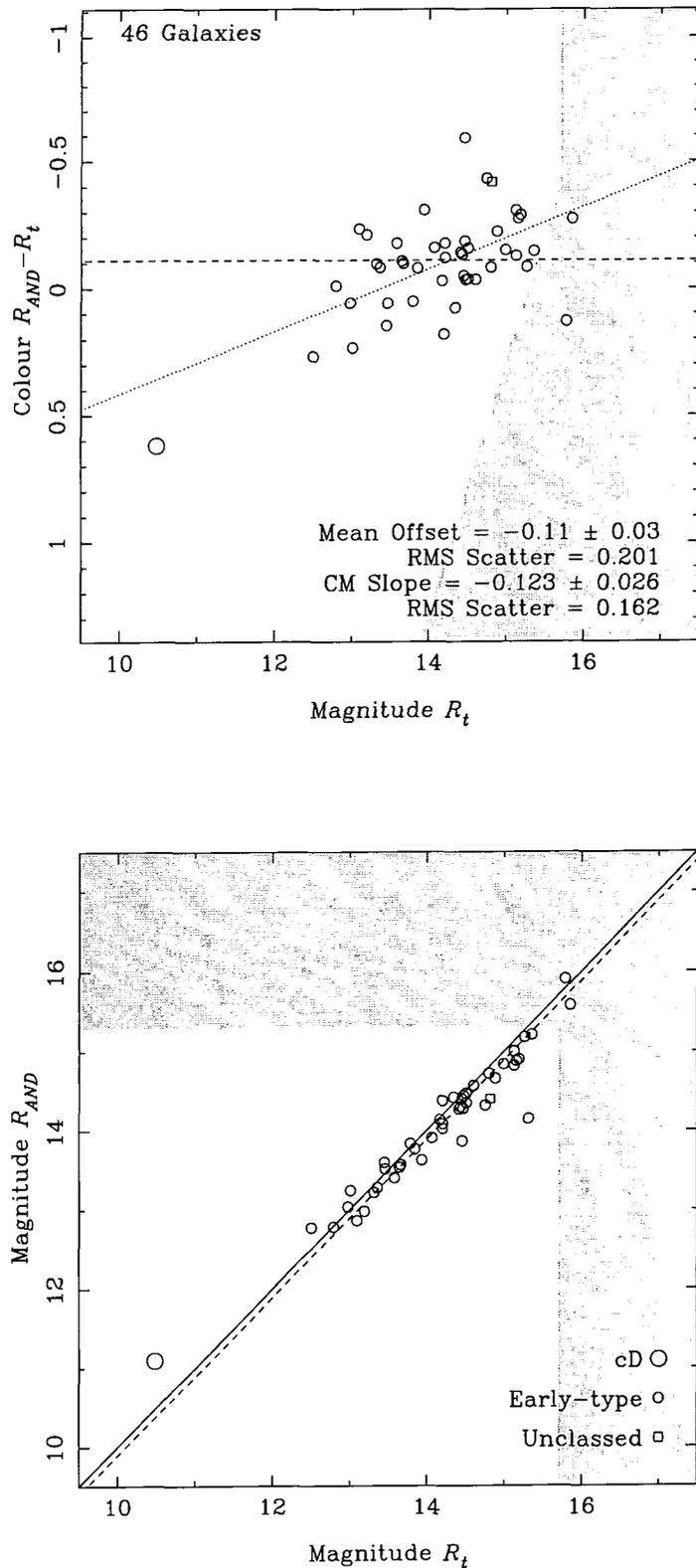
Figure 4.3: Comparison of total magnitudes of Steel with total R-band magnitudes of Andreon *et al.* (1996). The upper plot shows the residual (colour) against magnitude. The lower plot shows the magnitude against magnitude. The shaded area is beyond the magnitude-limit ($R\sim15.7$ for Steel, $R\sim15.3$ for Andreon *et al.*). In both plots, the dashed-line shows the mean offset, whilst the dotted-line shows the best-fitting colour-magnitude slope.
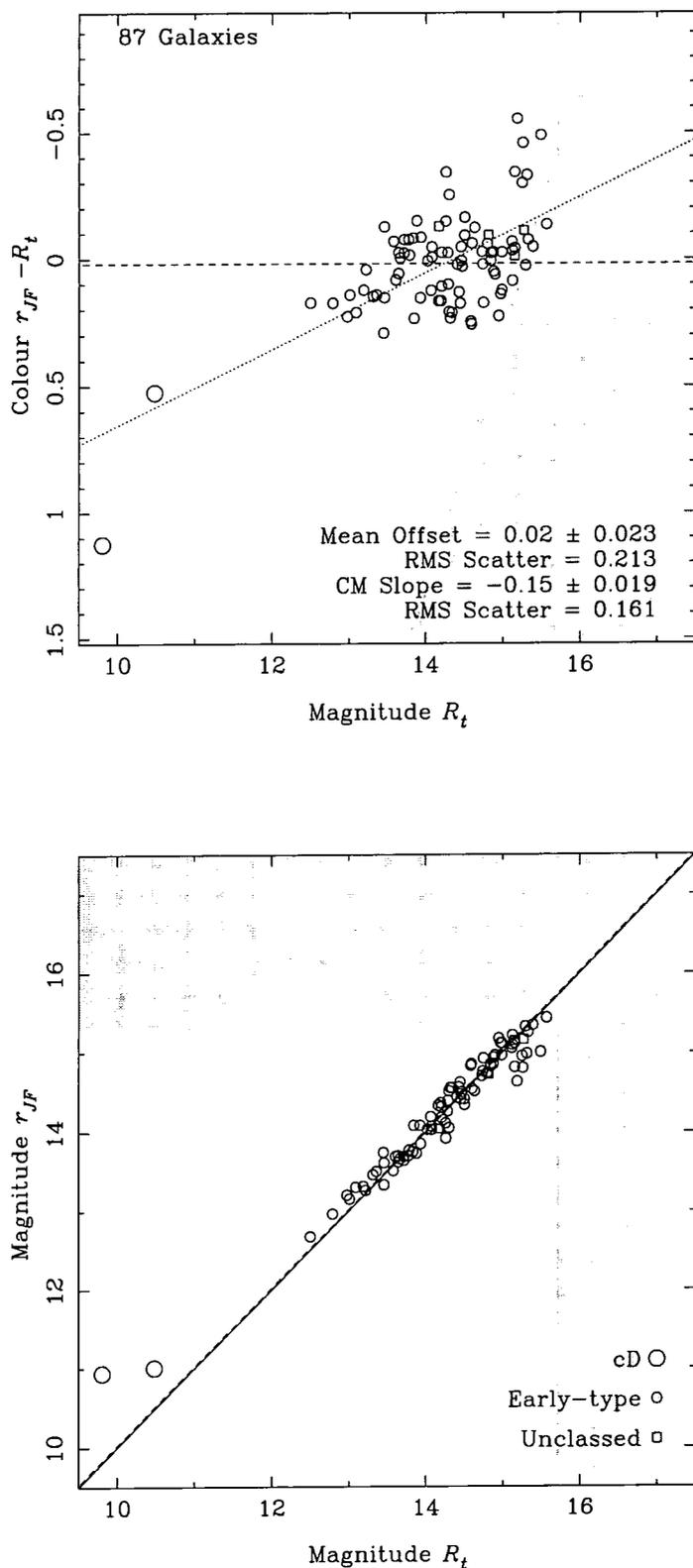
Figure 4.4: Comparison of total magnitudes of Steel with total Gunn-r magnitudes of Jorgensen & Franx (1994), derived from growth-curve model fitting. The upper plot shows the residual (colour) against magnitude. The lower plot shows the magnitude against magnitude. The shaded area is beyond the magnitude-limit ($R{\sim}15.7$ for Steel, $r{\sim}15.3$ for Jorgensen & Franx). Late-type galaxies are excluded from the comparison due to colour difference. In both plots, the dashed-line shows the mean offset, whilst the dotted-line shows the best-fitting colour-magnitude slope.
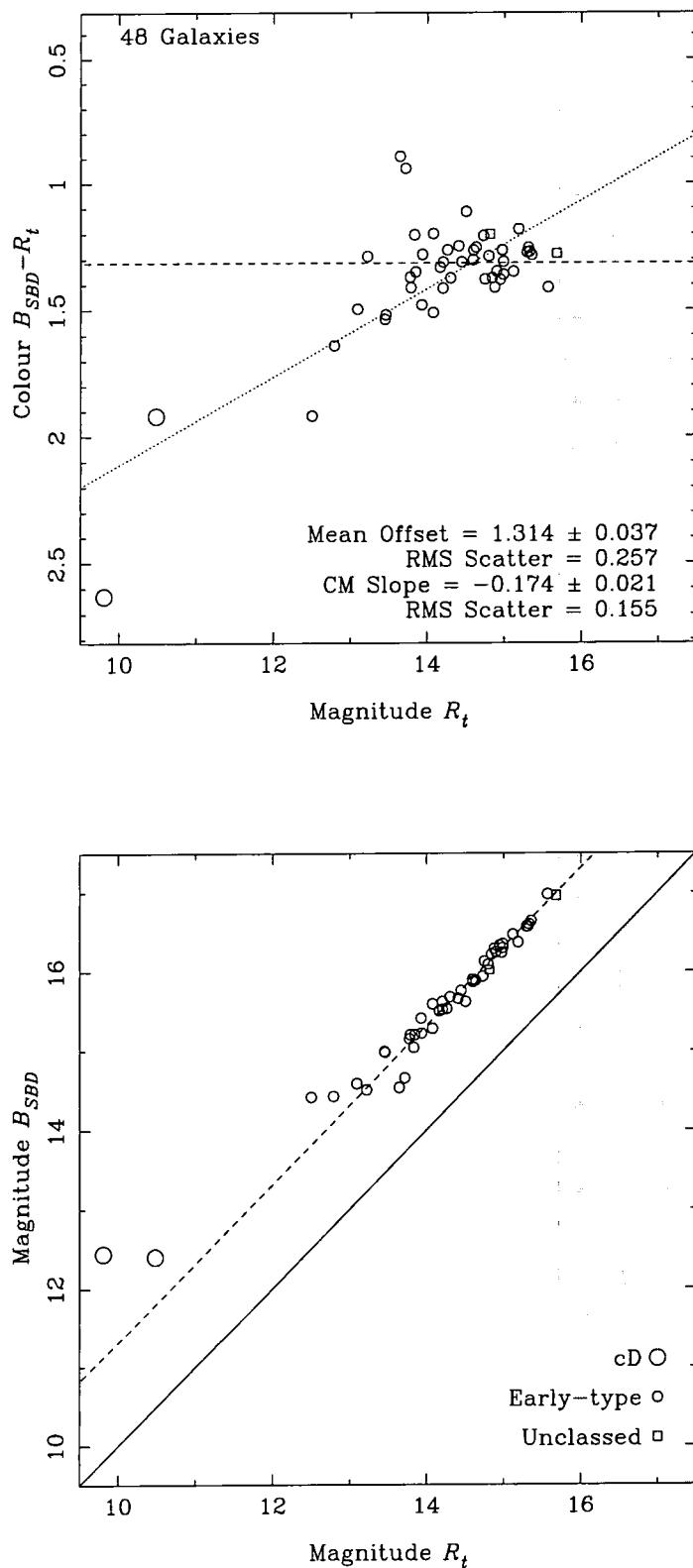
Figure 4.5:   Comparison of total magnitudes of Steel with total B-band magnitudes of Saglia *et al.* (1993), derived from growth-curve model fitting. The upper plot shows the residual (colour) against magnitude. The lower plot shows the magnitude against magnitude. The shaded area is beyond the magnitude-limit ($R \sim 15.7$ for Steel). Late-type galaxies are excluded from the comparison due to colour difference. In both plots, the dashed-line shows the mean colour, whilst the dotted-line shows the best-fitting colour-magnitude slope.
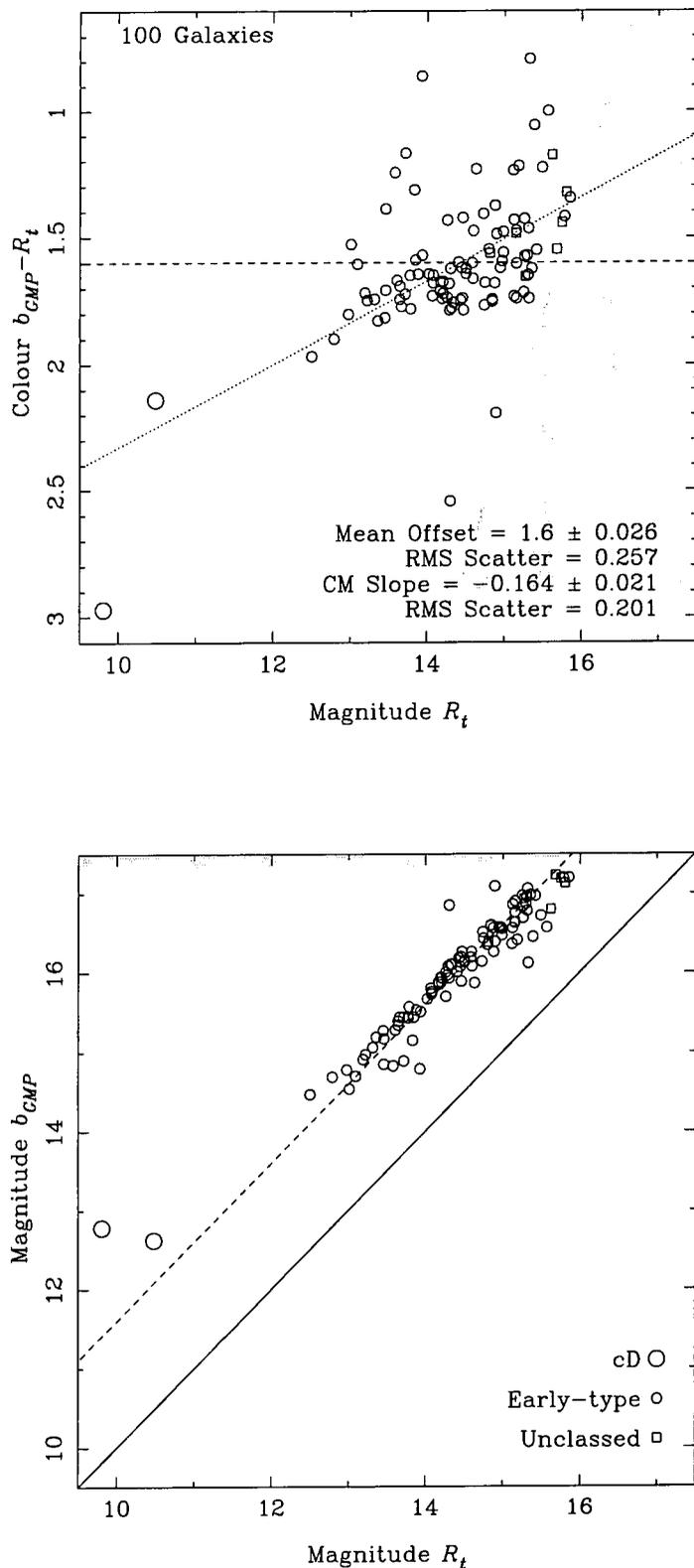
Figure 4.6: Comparison of total magnitudes of Steel with isophotal $b_{26.5}$ magnitudes of Godwin *et al.* (1983). The upper plot shows the residual (colour) against magnitude. The lower plot shows the magnitude against magnitude. The shaded area is beyond the magnitude-limit ($R \sim 15.7$ for Steel). Late-type galaxies are excluded from the comparison due to colour difference. In both plots, the dashed-line shows the mean colour, whilst the dotted-line shows the best-fitting colour-magnitude slope.
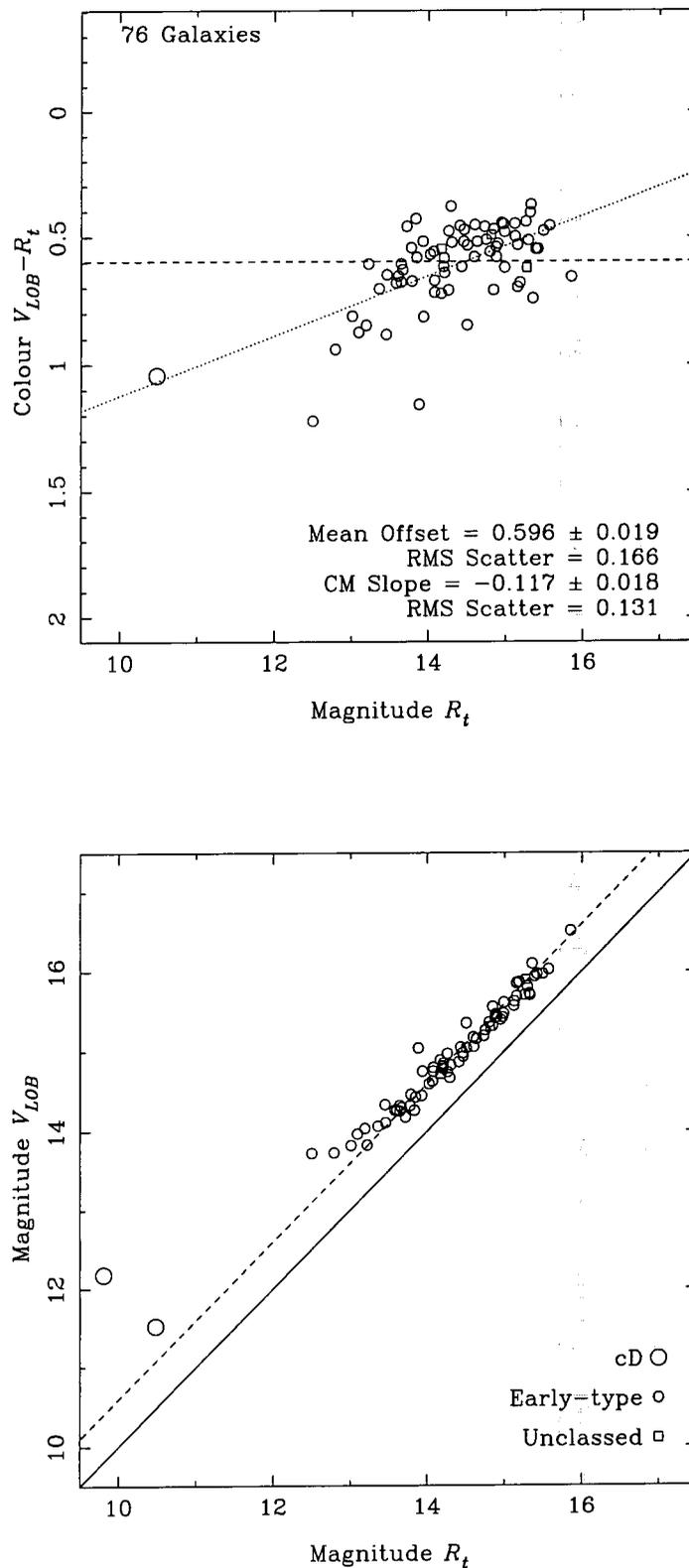
Figure 4.7: Comparison of total magnitudes of Steel with isophotal $V_{26.5}$ magnitudes of Lobo *et al.* (1997). The upper plot shows the residual (colour) against magnitude. The lower plot shows the magnitude against magnitude. The shaded area is beyond the magnitude-limit ($R\sim15.7$ for Steel). Late-type galaxies are excluded from the comparison due to colour difference. In both plots, the dashed-line shows the mean colour, whilst the dotted-line shows the best-fitting colour-magnitude slope.
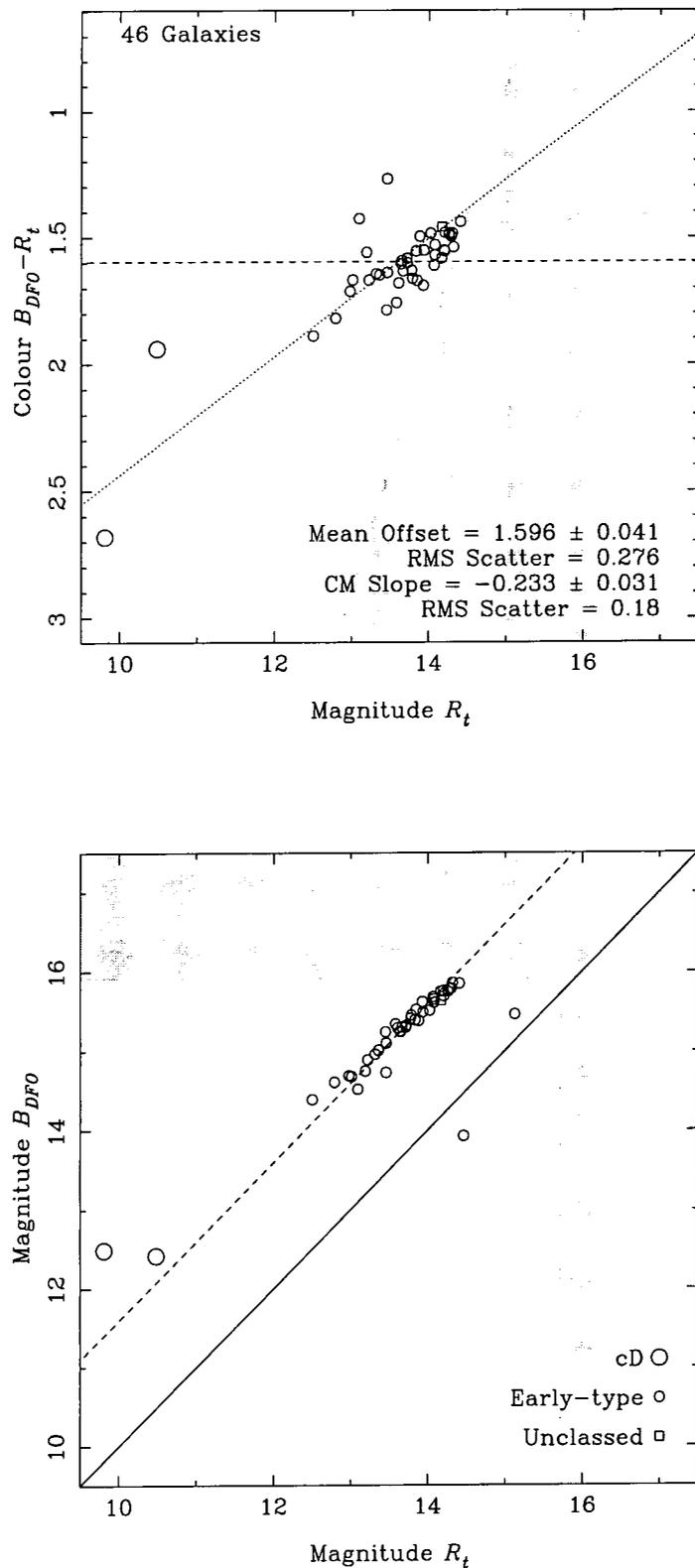
Figure 4.8: Comparison of total magnitudes of Steel with total B-band magnitudes of Doi *et al.* (1995), derived from growth-curve model fitting. The upper plot shows the residual (colour) against magnitude. The lower plot shows the magnitude against magnitude. The shaded area is beyond the magnitude-limit ($R{\sim}15.7$ for Steel, $B{\sim}15.9$ for Doi *et al.*). Late-type galaxies are excluded from the comparison due to colour difference. In both plots, the dashed-line shows the mean colour, whilst the dotted-line shows the best-fitting colour-magnitude slope.

Table 4.1: Comparison between the authors total magnitudes and other published data-sets. The parenthesised numbers after the offset and Colour-Magnitude-slope values are the standard errors on the last significant digit.

Data-set (authors)	Band	Type	N	Offset (mag)	RMS (mag)	CM-Slope (mag)	RMS (mag)
Andreon et al.	R	CCD,Total	46	-0.110(30)	0.201	-0.123(26)	0.162
Jorgensen & Franx	r	CCD,Total	87	0.020(23)	0.213	-0.150(19)	0.161
Saglia et al.	B	CCD,Total	48	1.314(37)	0.257	-0.174(21)	0.155
Godwin et al.	b	Phot,Isophotal	100	1.600(26)	0.257	-0.164(21)	0.201
Lobo et al.	V	CCD,Isophotal	76	0.596(19)	0.166	-0.117(18)	0.131
Doi et al.	B	Phot,Total	46	1.596(41)	0.276	-0.233(31)	0.180

$2 \times RMS$ from the offset. This is to ensure that rogue points do not bias the calculation. Additionally, to account for the colour-magnitude relation, the trend of residual against magnitude is fitted by a linear regression. Once again, rogue points are eliminated by clipping points which lay more than $3 \times RMS$ from the fit, and repeating the linear regression. The RMS scatter of points from the C-M fit shows a big improvement against the RMS from a simple offset. Table 4.1 shows the relative quality of the various comparisons.

For an extrapolated total magnitude, the comparisons are very good, with the typical RMS scatter between Steel and the other systems in the range 0.1-0.2 mag after the colour-magnitude term has been accounted for.

Although acceptable, the measurement errors on the total magnitudes are large due to the fact they involve an extrapolation. Circular aperture photometry, by comparison, is very simple to measure and results in smaller uncertainty. As a final check on the authors photometry, therefore, aperture magnitudes were measured for all galaxies (diameter equals $20''$). These are then compared with the V-band aperture photometry (same diameter) of Lucey et al. (1991). The comparison is shown in Figure 4.9. The RMS scatter is considerably lower than the previous comparisons at 0.016 mag. The mean colour index $V - R$ for this early-type sample is 0.56.
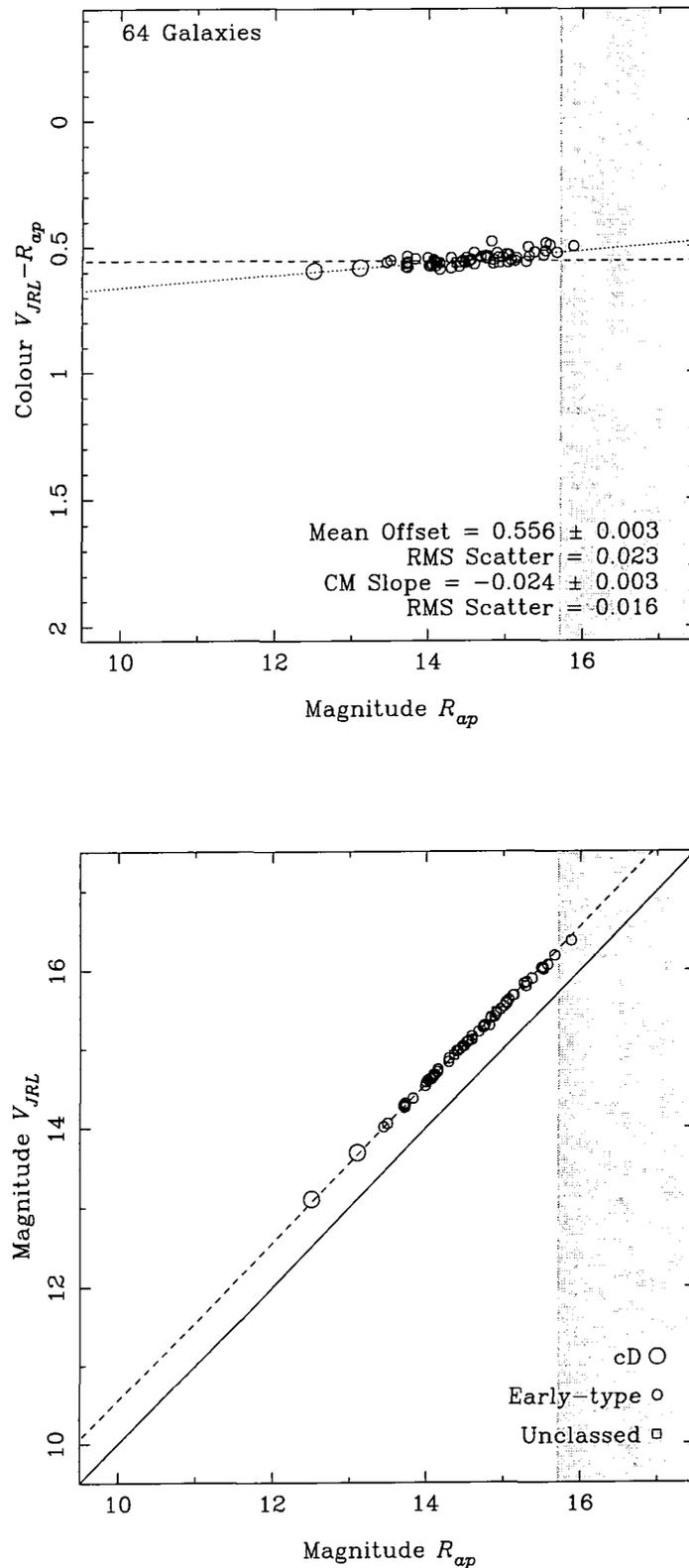
Figure 4.9: Comparison of apertures magnitudes of Steel with aperture magnitudes of Lucey *et al.* (1991). The upper plot shows the residual (colour) against magnitude. The lower plot shows the magnitude against magnitude. The shaded area is beyond the magnitude-limit ($R \sim 15.7$ for Steel). Late-type galaxies are excluded from the comparison due to colour difference. In both plots, the dashed-line shows the mean colour, whilst the dotted-line shows the best-fitting colour-magnitude slope.

4.7 Conclusion

This chapter has described the elliptical aperture photometry method used to calculate asymptotic magnitudes and half-light parameters. The quality of the photometry has been shown to be of a high standard, with an internal scatter on the total magnitude of 0.015 mag. The comparison with other published data is also good, with RMS scatters in the range $0.1 - 0.2$ mag after the colour-magnitude relation is accounted for. Reasonable offsets are also achieved in comparisons with the other data-sets, despite the different methodologies employed.

The next chapter will look at the surface photometry, and in particular, how to correct the surface brightness (and other) profiles for the effects of atmospheric seeing.

Chapter 5

Seeing Deconvolution

5.1   Introduction - Galaxy Profiles and Seeing

All ground-based astronomical observations suffer from atmospheric seeing. This is the blurring of an image caused by turbulent layers of air in the upper atmosphere. Without seeing, a 2.5 metre telescope would have a defraction-limited resolution of $\sim 0.05''$. However, the effect of seeing reduces this resolution to anything between $0.5''$ and $5''$, depending on the site and the weather conditions. A point source, such as a star, is convolved by seeing into a point spread function (PSF). If the telescope is in focus and optically perfect, the PSF should be circularly symmetric, and can be approximated by a functional form. The resolution which results from seeing is usually quantified as the full-width half-maximum (FWHM) of the PSF.

A problem occurs when we want to observe an extended source, such as a galaxy. Any structure on a scale of a few times the FWHM will be dampened, while structure finer than this may vanish altogether. At the distance of Coma, typical half-light radii of galaxies can be as small as $3''$, so clearly seeing will have a dramatic effect on ground-based observations. It is interesting to note that observing at the distance of Virgo (one-fifth the distance of Coma) reduces the effect of seeing on global properties of galaxies to well within tolerable levels. However, a large sample of galaxies at a common distance was required for this study, in addition to a rich-cluster environment (see Chapter 1) - in both these respects Coma is much more favourable than Virgo. Of central importance to this study is the photometric structure of early-type galaxies. The shape of the surface brightness profile, together with the ellipticity and higher order term profiles, can indicate the presence of photometric
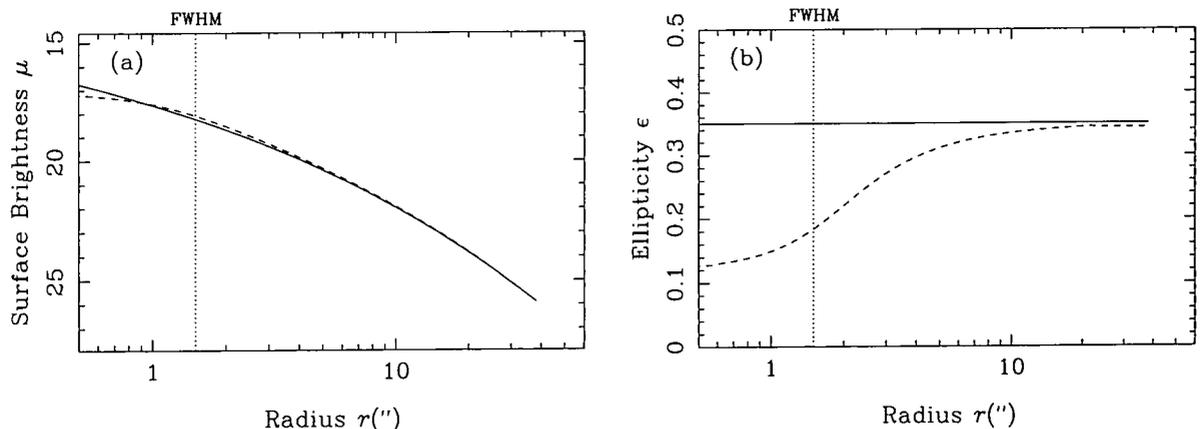
Figure 5.1: A demonstration of the effect of seeing upon an elliptical galaxy. (a) shows the surface brightness profiles. (b) shows the ellipticity profiles. The solid and dashed lines show the profiles before and after seeing convolution respectively. The profiles are produced by building an $r^{\frac{1}{4}}$-law model galaxy image ($r_e = 5''$, $\epsilon = 0.35$) and convolving with a seeing PSF ($FWHM = 1.5''$).

features such as disks, boxyness, rings, bars, and so on. A surface photometry algorithm, such as *GALPHOT* (Franx *et al.* 1989), will fit ellipses to a galaxy image and measure the surface brightness, ellipticity, position angle, centroid, and isophotal parameters for a galaxy, as a function of radius. Seeing has a dramatic effect on these profiles. Light from the sharply-peaked centre of the galaxy is redistributed further out, thus flattening the surface brightness profiles in the centre, but steepening them further out (up to a radius of 10 times the FWHM or more). If the galaxy is flattened (has a high ellipticity), the redistribution of light is anisotropic, with more light being scattered along the direction of the steeper light profiles, i.e. the minor axes. This means that the ellipticity (and high-order) profiles will be distorted, with the ellipticity very low (matching the PSF) at the centre, and increasing to the 'natural' value further out. The position angle and centroid profiles will also be affected to a lesser degree. An example of the effect of seeing upon surface brightness and ellipticity profiles is shown in figure 5.1.

In order to perform a complete morphological study of early-type galaxies using surface photometry (see Chapter 1), a great deal of attention must be payed to the problems of seeing, and how to correct surface photometry profiles for the effects of seeing. Section 5.2 will briefly describe the well-known image restoration algorithms and explain why they are unsuitable for the purposes of this study. Section 5.3 looks at the surface photometry packages used in this project. The remaining sections of this chapter describe the new

methodology which has been devised for this study to derive seeing-corrected profiles from ground-based data.

5.2   Image Restoration Methods

There are several methods which can be used to 'restore' an image which has been corrupted by PSF convolution. These techniques have been applied recently in dealing with the problems of spherically-aberrated images from the Hubble Space Telescope (now corrected since the servicing mission). The best known of these is probably the Lucy-Richardson Algorithm, which generates a restored image by an iterative method. The basic essence of the iteration is that an $(N + 1)^{th}$ estimate of the 'restored' image can be derived from the Nth estimate by multiplication with a 'correction' image:-

$$Image_{N+1} \ = \ Image_N . \left[\left(\frac{Original \ Data}{Image_N \star PSF} \right) \star reflect(PSF) \right] \qquad (5.1)$$

Where '$\star$' represents the convolution operator and '$reflect(PSF)$' is the reflection of the PSF, i.e. $reflect(PSF(x,y)) \ = \ PSF(-x, -y)$. The limitation of this method is the creation of artificial 'artifacts' by noise amplification (overfitting of noise). For a diffuse object, this occurs after a relatively low number of iterations - it is very difficult to decide the best stopping point for the iterations. As the FWHM for ground-based data is large (compared to the detail to be recovered), this is not a viable method for this study.

Alternative methods include Wiener filtering and Maximum Entropy. The Wiener method is an example of a Fourier non-iterative restoration. The main advantage over Lucy-Richardson is the shorter computation time required to reach a solution - the operations being made in the Fourier transform domain. Typically, Wiener filter restorations appear to be of lower quality than restorations from iterative methods. They require certain conditions of the data which, in the case of this study, would certainly not be met - such as signal-independent noise and a well-sampled PSF. Generally speaking, image restoration methods are a rather clumsy way of removing the effects of seeing from a CCD image, and the interpretation of results are not always unambiguous.

This study only requires the deconvolution of 1-D radial profiles of a galaxy. Therefore, a simpler method which retrieves this information and nothing else is needed. Firstly, an ellipse-fitting surface photometry algorithm is required to *measure* the raw radial profiles

in the first place. The routine which has been used here (based on *GALPHOT*), is outlined briefly in Section 5.3. Secondly, an iterative deconvolution method has been developed for this study and this data - this is outlined in Section 5.4.

5.3 Surface Photometry Measurement

In order to assess the effect of seeing on the surface photometry of a galaxy, it is first of all necessary to parametrise the surface brightness distribution. Given the symmetry of elliptical galaxies, the best way of doing this is to fit ellipses to the images. Provided the ellipses cover a large enough range in equivalent radius r ($= \sqrt{ab}$), then the $2D$ surface photometry of a galaxy is well described by the $1D$ profiles of ellipse parameters (ellipticity ϵ, position-angle Φ and centroid $[x_c, y_c]$) plus the photometry measured from the ellipses (mean intensity I and higher-order terms describing the deviation of I from the mean value around the ellipse).

Various ellipse-fitting algorithms have been used in the past to measure surface photometry of elliptical galaxies. The routine which has been used in this study is based on *GALPHOT*, created by Marjin Franx (see Franx *et al.* 1989). The advantage of *GALPHOT* over most other algorithms is that it uses the ellipse-fit to predict the intensity at *every* point in the image. Thus the final result is a unique, least-squares fit, $2D$ model for the galaxy image. The method normally used by other algorithms is to repeat iterations along various ellipses to minimize the residual intensity variations. At each iteration, the Fourier coefficients of the intensity residuals are determined. The 1st and 2nd order sine and cosine terms of the Fourier expansion (c_1, s_1, c_2, s_2) can be used to adjust the ellipse parameters to produce a better ellipse-fit (see, for example, Jedrzejewski 1987). This does not necessarily result in a least-squares fit to the whole $2D$ image, because a model intensity for every point is not defined from the ellipse-fits. *GALPHOT* works by first performing a regular ellipse-fit, then *correcting* it. This is done using an iterative process, whereby a $2D$ model image is reconstructed from the ellipse-fits and used to improve the ellipse-fits. Eventually, the reconstructed $2D$ model image matches the galaxy data, i.e. *GALPHOT* has self-corrected the inadequacies of the original ellipse-fit. Thus the algorithm is self-consistent - if *GALPHOT* is repeated on the *reconstructed model*, it will return the same ellipse-fit as it returned the first time. The image reconstruction
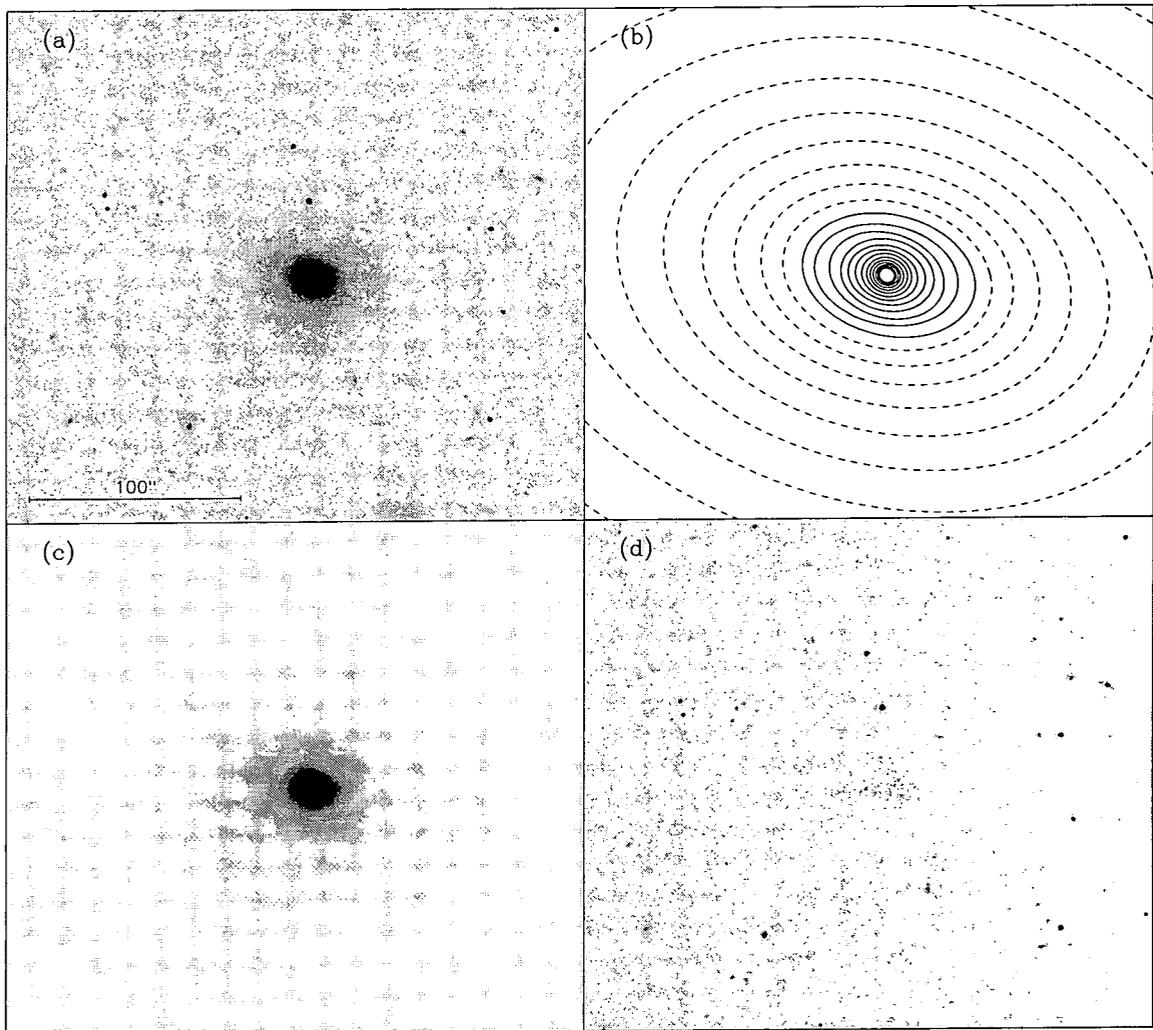
Figure 5.2: Using an ellipse-fitting algorithm (based on *GALPHOT*) to model the surface brightness distribution of a galaxy (*IC*4051 in Coma). (a) shows a grey-scale plot of the original CCD image. (b) shows the ellipses fitted to this image - only every second ellipse (with $r \geq 3.5''$) is shown for clarity. The ellipses are shown with a dashed-line beyond the radius where the ellipticity, PA and centroid are fixed. (c) shows the $2D$ model constructed by *GALPHOT* for this ellipse-fit. (d) shows how this model can be subtracted from the original image, leaving no residual.

is performed several times during the whole process, which is obviously time-consuming (taking a few minutes on a typical workstation).

At the heart of this algorithm is the calculation of intensity at a given point (x, y) on the image. If these coordinates are translated and rotated to $(\tilde{x}, \tilde{y})$, such that the origin is at the centre of a given ellipse l and the $\tilde{x}$-axis is parallel to the major-axis, then a function m_l for the particular ellipse can be defined:-

$$m_l{}^2 = \frac{\tilde{x}^2}{a_l{}^2} + \frac{\tilde{y}^2}{b_l{}^2} \tag{5.2}$$

Where m_l represents the position of the point (x, y) relative to the ellipse, e.g. $m_l{}^2 = 1$ if the point lies on the ellipse; $m_l{}^2 > 1$ if outside the ellipse; and $m_l{}^2 < 1$ if within the ellipse. To measure the intensity I at the point (x, y), the largest ellipse $l^\star$ is found which does not encompass the point. The value of $m_l{}^2(x, y)$ is calculated for this ellipse *and* its four nearest neighbours $(l^\star - 2 < l < l^\star + 2)$. As each ellipse has a measured mean intensity I, a function $I(m^2)$ is defined for the 5 points. This function is fitted by a 4th-order polynomial and solved for $m^2 = 1$, thus interpolating an 'imaginary' ellipse - of intensity I - passing through the point (x, y).

In the original *GALPHOT*, the count for a given pixel is simply calculated using the above method, with (x, y) at the *centre* of the pixel. However, whilst this does produce a self-consistent model, the returned ellipse information in the central few pixels is inaccurate. This is because the pixel size is significant compared with the ellipse radii. For this study, a correction was made to *GALPHOT*, whereby the model in the central region (within 20 pixels of the centre) is constructed by calculating the intensity at 121 points within each pixel (at the centres of 'sub-pixels' arranged in an 11×11 grid), using the method above. The pixel count is then the average of these values. The end result is more realistic profiles measured in the centre, with the same self-consistency (this was confirmed using made-up $r^{\frac{1}{4}}$-law galaxies, integrating the flux over the central pixels). This was necessary for this study, because the central profiles are crucial in the deconvolution. The cost of this is, of course, extra computational time.

The ellipses are fitted at equivalent radii separated by a factor 1.1. The range of the radii can be varied with *GALPHOT*, but for this study was fixed at $r = 0.3$ pixels for the innermost ellipse, whilst the outermost ellipse was the largest one *partially* within the image frame. The free-parameter fitting of the ellipse parameters $(\epsilon, \Phi, x_c, y_c)$ described

above is only performed out to a radius where the S/N is sufficient. *GALPHOT* uses the uncertainties on the Fourier coefficients to determine this radii. However, this radii seems to be somewhat unstable, often being too far out - beyond where the fitted ellipses start crossing. Crossing ellipses are undesirable because they produce defects in the reconstructed 2*D* model, which would cause problems in the deconvolution routine - see next section (5.4). Therefore a new cut-off radii has been devised, which has been found to be more stable - the cut-off radii is defined as that of the first ellipse whose intensity drops below 5% of the background count. Beyond this radii, the ellipse-parameters are fixed, and only the surface photometry is measured. The residuals from the mean intensity around the ellipse, parametrised in terms of Fourier coefficients (see section 1.5), are calculated only as far as 4th order, which is sufficient to distinguish a galaxy as disky or boxy. These coefficients are divided by $r.dI/dr$ so that they represent the relative radial deviation of the isophotes from ellipses. In theory, the sky background count can be extrapolated by fitting a model to the intensity profile, which includes the background. In reality, the raw CCD images (before chopping out of individual galaxies) are so large a more reliable method is to measure the sky interactively (prior to using *GALPHOT*). This is done using *AVIEW* - the sky can be measured by manually placing apertures at a sufficient distance from the galaxy (typically several arc-minutes). At the same time, a list of pixels are defined which are to be *excluded* from the ellipse-fitting - i.e. stars, companion galaxies, and cosmic rays. This is achieved using a version of *PISA*, which parametrises (as ellipses) sources of a given size which exceed the background by a certain count. These ellipses are displayed using *AVIEW*, and can be deleted or manipulated manually. Bad pixels which have not been enclosed by *PISA* ellipses can also be enclosed manually within circles. Finally, all enclosed 'bad' pixel coordinates are stored - to be used by the *GALPHOT*-based routine. The interactive data preparation procedures were described in detail in Chapter 3. The original *GALPHOT* routine operated in the *IRAF* environment on *IRAF* data-frames, and produced tables in *STSDAS* format. As it was required for this study to combine *GALPHOT* with other routines (see Section 5.4), a final alteration was made to the algorithm - the new version runs in a *UNIX* environment on *Starlink* data-frames, and produces tables in ordinary text files. Figure 5.2 gives an example of the operation of the ellipse-fitting routine, using an image of the Coma galaxy IC 4051. The original image, best-fitting ellipses, made-up 2*D* model, and the residual after model subtraction are all shown.

5.4 Profile Deconvolution

If an ellipse-fitting algorithm (such as *GALPHOT*) can produce profiles of surface brightness μ, ellipticity ϵ, position-angle Φ, centroid (x_c, y_c), and isophotal shapes (c_3, s_3, c_4, s_4) as a function of ellipse radius $r = \sqrt{ab}$ for a ground-based galaxy image, then can the same profiles be derived *minus* the effect of seeing? Of course, the unconvolved galaxy can never be perfectly re-constructed, as information about where each photon has come from has been lost by the seeing process. In fact, there will be a whole series of model galaxies, made using different profiles, which will fit the observed profiles when convolved with seeing. The best that can be hoped for is to derive a model which is well-behaved and reasonable. The method which has been devised achieves this objective, and the basic principles will now be outlined.

Before the deconvolution can proceed, there are a few variables which must be measured from the galaxy image interactively. These include the sky-background count (needed for the surface photometry), an estimate of the seeing FWHM (from fitting a model profile to a star), and a list of 'bad' pixels (i.e. stars, companion galaxies and cosmic-rays that are rejected from the fit). The PSF model used here to fit stars is the same as that used by Lucey *et al.* (1991), i.e. a Hankel transform of the combined modulation transfer function of the telescope and atmosphere (see Roddier 1981). This gives a much better fit to the observed stellar profiles than the often-used Gaussian PSF, which does not have enough power at large radii.

For the deconvolution itself, an iterative process is used to find a seeing-corrected surface photometry model. This iteration is based on the straightforward idea that when differences between the *convolution* of a model galaxy and the observed galaxy become small, the model galaxy is a close approximation to the observed galaxy *without* atmospheric seeing. The model galaxy is built using the profiles $\{\mu(r), \epsilon(r), \Phi(r), x_c(r), y_c(r)\}$ derived from ellipse-fitting, and it is these profiles which are altered to produce the final (seeing-corrected) model. The higher-order isophotal terms $\{c_3(r), s_3(r), c_4(r), s_4(r)\}$ are not included in this process because the measured profiles are too noisy. Therefore, these profiles are assumed to be zero. In essence, the criterion for a successful deconvolution can

be summarized as follows:-

$$If \left\{ \begin{array}{l} \mu_{model} \star (r) = \mu_{observed}(r) \\ \epsilon_{model} \star (r) = \epsilon_{observed}(r) \\ \Phi_{model} \star (r) = \Phi_{observed}(r) \\ x_{model} \star (r) = x_{observed}(r) \\ y_{model} \star (r) = y_{observed}(r) \end{array} \right\} \quad then \quad \left\{ \begin{array}{l} \mu_{correct}(r) = \mu_{model}(r) \\ \epsilon_{correct}(r) = \epsilon_{model}(r) \\ \Phi_{correct}(r) = \Phi_{model}(r) \\ x_{correct}(r) = x_{model}(r) \\ y_{correct}(r) = y_{model}(r) \end{array} \right\} \quad (5.3)$$

Where the '$\star$' symbol represents the convolution of the $1D$ profiles due to the $2D$ seeing convolution of the model galaxy. The form of these convolutions are complex and cannot be analytically determined in advance - they depend not only on the PSF and radius, but also on the shapes of *all* the profiles, including the profile being convolved. A useful way of expressing the effect of seeing on the profiles at a given radius is a *correction*, i.e.:-

$$If \left\{ \begin{array}{l} \mu_{model}(r) + \Delta\mu(r) = \mu_{observed}(r) \\ \epsilon_{model}(r) + \Delta\epsilon(r) = \epsilon_{observed}(r) \\ \Phi_{model}(r) + \Delta\Phi(r) = \Phi_{observed}(r) \\ x_{model}(r) + \Delta x(r) = x_{observed}(r) \\ y_{model}(r) + \Delta y(r) = y_{observed}(r) \end{array} \right\} \quad then \quad \left\{ \begin{array}{l} \mu_{correct}(r) = \mu_{model}(r) \\ \epsilon_{correct}(r) = \epsilon_{model}(r) \\ \Phi_{correct}(r) = \Phi_{model}(r) \\ x_{correct}(r) = x_{model}(r) \\ y_{correct}(r) = y_{model}(r) \end{array} \right\} \quad (5.4)$$

The whole problem now reduces to measuring the corrections ($\Delta\mu(r), \Delta\epsilon(r), etc.$), which will convert the observed profiles into the seeing-corrected profiles. Measuring the corrections is a simple task if the unconvolved profiles are known - an image can be built from the profiles, then convolved with seeing, and the convolved profiles measured from ellipse-fits to the new image. The correction is then just the difference between the convolved and unconvolved profiles. The problem here is to do this in reverse - calculate the unconvolved (i.e. corrected) profiles given the convolved (i.e. observed) profiles.

The iteration is begun by 'guessing' what the unconvolved profiles may look like. Firstly, the observed galaxy image is run through an ellipse-fitting program (i.e. *GALPHOT*), and the raw uncorrected profiles are recorded. The outer parts of the observed profiles are noisy due to low signal-to-noise ratio (or bad flat-fielding). Since such noise would be 'over-fit' in the iteration, these parts of the observed profiles are smoothed using a cubic-spline approximation. Secondly, the $\mu(r)$ profile is replaced within the seeing affected area by an $r^{\frac{1}{4}}$-law (fitted between $5''$ and $15''$). To ensure a continuous $\mu(r)$ profile, radius-dependent weighting has been used to merge this into the outer profile. An $r^{\frac{1}{4}}$-law was chosen because

a central profile more 'peaky' than the raw profile was required, and not out of any bias for what the final central profile might look like. Finally, the position angle, centroid, and ellipticity profiles are truncated in the centre as a first attempt to remove the effects of seeing.

Given an estimate for the unconvolved (or seeing-corrected) profiles, it is possible to derive an estimate for the seeing-corrections using the method outlined above, i.e.:-

$$\left\{ \begin{array}{l} \Delta\mu^1(r) = \mu^1{}_{model} \star (r) - \mu^1{}_{model}(r) \\[2mm] \Delta\epsilon^1(r) = \epsilon^1{}_{model} \star (r) - \epsilon^1{}_{model}(r) \\[2mm] \Delta\Phi^1(r) = \Phi^1{}_{model} \star (r) - \Phi^1{}_{model}(r) \\[2mm] \Delta x^1(r) = x^1{}_{model} \star (r) - x^1{}_{model}(r) \\[2mm] \Delta y^1(r) = y^1{}_{model} \star (r) - y^1{}_{model}(r) \end{array} \right\} \tag{5.5}$$

Where (^{1}) denotes the *first* estimate of the seeing-corrected profiles and the resulting corrections. By subtracting these corrections from the observed profiles, a much better estimate for the seeing-corrected profiles can be derived:-

$$\left\{ \begin{array}{l} \mu^2{}_{model}(r) = \mu_{observed}(r) - \Delta\mu^1(r) \\[2mm] \epsilon^2{}_{model}(r) = \epsilon_{observed}(r) - \Delta\epsilon^1(r) \\[2mm] \Phi^2{}_{model}(r) = \Phi_{observed}(r) - \Delta\Phi^1(r) \\[2mm] x^2{}_{model}(r) = x_{observed}(r) - \Delta x^1(r) \\[2mm] y^2{}_{model}(r) = y_{observed}(r) - \Delta y^1(r) \end{array} \right\} \tag{5.6}$$

With these new estimates for the seeing-corrected profiles, the loop is repeated, i.e. new corrections are derived, which are then applied to the observed profiles to produce even better estimates for the seeing-corrected profiles. The 'convolution' of the 1D model profiles is performed by building a 2D model galaxy using *GALPHOT*, convolving the image with the *PSF* (using a fast Fourier transform), and re-fitting the resultant image with *GALPHOT* to obtain the convolved 1D profiles. Eventually, the iteration must converge - the seeing-corrected profiles, when 'convolved' with seeing, become close to the observed profiles. This is tested by measuring the *RMS* difference between the observed and convolved $\mu(r)$ profiles. The iterations are terminated if the *RMS* drops below 0.03 mag and has not changed by more than 10% from the previous iteration. The conditions for termination are thus (where n = number of iterations):-

$$RMS_n = \sqrt{\frac{1}{m}\sum_{i=1}^{m}\left[\mu_{observed}(r_i) - \mu^n{}_{model} \star (r_i)\right]^2} \leq 0.03 \tag{5.7}$$

$$and \qquad \frac{|RMS_n - RMS_{n-1}|}{RMS_{n-1}} < 0.1 \qquad \qquad (5.8)$$

One potential barrier to a successful convergence has already been mentioned - changing the shape of one profile (e.g. $\epsilon(r)$) effects the form of the seeing-correction of *another* profile (e.g. $\mu(r)$). The seeing-corrections are applied to all the observed profiles simultaneously to derive new estimates for the seeing-corrected profiles. If one seeing-corrected profile has changed significantly since the last iteration, it could make the seeing-corrections for the other profiles invalid. This would have the effect of the algorithm trying to correct one profile, but perturbing all the others at the same time, making it hard to reach a convergence. In practise, this appears to be a second-order effect. The change in the seeing-correction for a given profile between iterations is too small to effect the other seeing-corrections, especially as the initial estimates for the corrected profiles are quite good. For a typical Coma galaxy, the convergence is reached after only 3 or 4 iterations. If a convergence, as determined by the conditions above, has not been reached by the 9th iteration, then the iterations are automatically terminated (it is assumed that a good convergence *has* been reached, but fine structure in the observed $\mu(r)$ is preventing a perfect match).

The 'mapping' of the corrections in the scheme outlined above can be improved by mapping the seeing-corrected profiles at radius r to the convolved profiles at $r + \Delta r$. This is because 'features' in the profiles are moved to slightly higher radii because of seeing convolution. This is demonstrated in figure 5.3(a) and (d), where the 'bump' in the $\epsilon(r)$ profile (solid line) is moved outwards when convolved with seeing (dashed line). To produce these graphs, an image was built from a perfect $r^{\frac{1}{4}}$-law $\mu(r)$ profile ($r_e = 5''$) and a flat $\epsilon(r)$ *plus* a 'bump'. This image was convolved with seeing ($FWHM = 1.5''$), and the 'convolved' $\epsilon(r)$ profile measured from the resulting image. The 'bump' in the $\epsilon(r)$ profile here represents the inevitable point during the iterations where the seeing-corrected estimate is different from the 'true' value (say a flat $\epsilon(r)$ profile) by a small perturbation. The outward shift Δr is roughly dependent on $FWHM$ and is found to be about $0.6 \times FWHM$ for $\mu(r)$, and $0.3 \times FWHM$ for the other profiles. In (a), the corrections are mapped the normal way, by comparing the seeing-corrected and convolved profiles at the same radius - the 'point-pairs' from which the correction is measured are linked by dotted lines. In (d), however, the
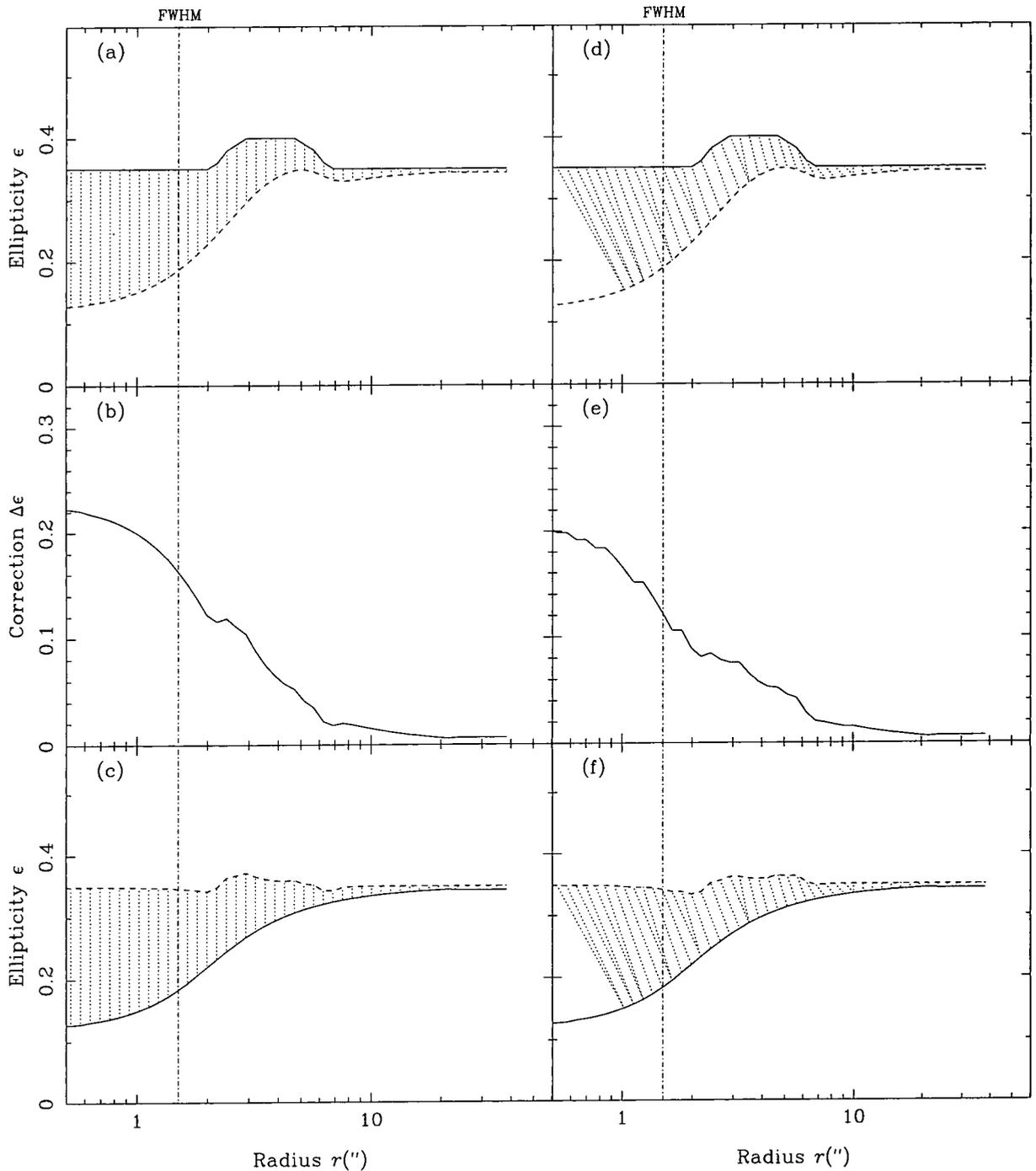
Figure 5.3: A demonstration of how estimates of seeing-corrected profiles can be improved (using model galaxies). In (a) and (d), an estimated seeing-corrected $\epsilon(r)$ profile (solid line) is convolved with seeing ($FWHM = 1.5''$) to produce the dashed lines. In (a), the seeing-correction is measured between points of the same radii (dotted lines), whilst a radius increment is used in (d). See the text for full details of these different methods. The magnitudes of the seeing-corrections measured in (a) and (d) are shown in (b) and (e) respectively. If the 'true' seeing-corrected profile is flat, we can convolve this with seeing to simulate the 'observed' $\epsilon(r)$ profile - this is shown as the solid line is (c) and (f). The corrections can then be added to these profiles (dotted lines) to produce better estimates of the seeing-corrected profiles (dashed lines) - for each method, the corrected profiles are flatter.

corrections have been calculated as follows:-

$$\Delta \epsilon^n(r) = \epsilon^n_{model} \star (r + \Delta r) - \epsilon^n_{model}(r) \qquad (5.9)$$

Of course, the profiles are built and measured at discrete radii, so $r + \Delta r$ is rounded to the nearest valid r, where $\Delta r = 0.3 \times FWHM$ for the ellipticity profile. The 'magnitude' of the correction profile $\Delta \epsilon(r)$ is shown in (b) and (e). Figures (c) and (f) show how *new* seeing-corrected estimate profiles (dashed lines) are built by adding the corrections to the 'true' convolved profile (solid line - produced by convolving a model image made with a *flat* $\epsilon(r)$ profile). Again, the point-to-point mapping for adding the corrections is shown by the dotted lines. It can be quickly seen that for the basic method of correcting (figures $a \rightarrow b \rightarrow c$), the size of the 'bump' is reduced in only 1 iteration. However, when a radius increment is used (figures $d \rightarrow e \rightarrow f$), the size of the perturbation is reduced still further, because the outward shift during convolution is partly accounted for. This means a solution will be found quicker and more cleanly. Another major advantage of this method is that the 'inner' regions ($\sim 0.5''$) of the convolved profiles are excluded from the fit. It can be hard to fit the inner region using the basic method because the convolved profiles here are extremely insensitive to changed in the unconvolved profiles *at the same radius*. Also, the low pixel resolution at these radii make measuring the convolved profiles difficult, producing 'artifacts' in the ellipse-fits - thus using these profiles for seeing-correction is not desirable.

The final set of equations for measuring the seeing-corrections from the estimated seeing-corrected profiles and their convolution is thus:-

$$\left\{ \begin{array}{l} \Delta \mu^n(r) = \mu^n_{model} \star (r + \Delta r) - \mu^n_{model}(r) \\ \Delta \epsilon^n(r) = \epsilon^n_{model} \star (r + \Delta r) - \epsilon^n_{model}(r) \\ \Delta \Phi^n(r) = \Phi^n_{model} \star (r + \Delta r) - \Phi^n_{model}(r) \\ \Delta x^n(r) = x^n_{model} \star (r + \Delta r) - x^n_{model}(r) \\ \Delta y^n(r) = y^n_{model} \star (r + \Delta r) - y^n_{model}(r) \end{array} \right\} \qquad (5.10)$$

(where $\Delta r = 0.6 \times FWHM$ for $\mu(r)$ and $0.3 \times FWHM$ for other profiles)

Using these corrections, a better estimate for the seeing-corrected profiles is calculated by:-

$$\left\{ \begin{array}{l} \mu^{n+1}{}_{model}(r) = \mu_{observed}(r + \Delta r) - \Delta\mu^n(r) \\ \epsilon^{n+1}{}_{model}(r) = \epsilon_{observed}(r + \Delta r) - \Delta\epsilon^n(r) \\ \Phi^{n+1}{}_{model}(r) = \Phi_{observed}(r + \Delta r) - \Delta\Phi^n(r) \\ x^{n+1}{}_{model}(r) = x_{observed}(r + \Delta r) - \Delta x^n(r) \\ y^{n+1}{}_{model}(r) = y_{observed}(r + \Delta r) - \Delta y^n(r) \end{array} \right\} \qquad (5.11)$$

A final adjustment must be performed on the estimated seeing-corrected profiles, in order to ensure a convergence. If there are small amplitude fluctuations in the profiles (with a scale of less than a few times $FWHM$), they will be smoothed out by the convolution. Thus, the correction functions calculated for these seeing-corrected profiles will also have fine structure. As the iterations progress, this fine structure will build-up into more or less random noise. Eventually, it will reach an equilibrium when it cancels itself out through the correction process, and stops growing. It is obviously not desirable to end up with final corrected profiles which contain unnecessary noise (note that this may still be a *valid* solution provided the noise is smoothed out in the convolved profiles, which must match the observed profiles). The solution is to 'smooth' fluctuations in the seeing-corrected profiles as they are produced. This is done simply by averaging each point in each profile by their nearest neighbour. Noting that the points in each profile are separated by a radius factor of 1.1, the smoothing is mathematically described as follows:-

$$\left\{ \begin{array}{l} \epsilon^n(r) = \frac{1}{3}\left[\epsilon^n(1.1r) + \epsilon^n(r) + \epsilon^n(1.1^{-1}r)\right] \\ \Phi^n(r) = \frac{1}{3}\left[\Phi^n(1.1r) + \Phi^n(r) + \Phi^n(1.1^{-1}r)\right] \\ x^n(r) = \frac{1}{3}\left[x^n(1.1r) + x^n(r) + x^n(1.1^{-1}r)\right] \\ y^n(r) = \frac{1}{3}\left[y^n(1.1r) + y^n(r) + y^n(1.1^{-1}r)\right] \\ \mu^n(r) = \frac{1}{3}\left[\mu^n(1.1r) + \mu^n(r) + \mu^n(1.1^{-1}r)\right] \quad (r < 20'') \end{array} \right\} \qquad (5.12)$$

There was no need to smooth the surface brightness profile farther out than $r = 20''$, because it was more robust than the other profiles. On the other hand, it was necessary to repeat the smoothing for $\epsilon(r)$ $(r < 1.5 \times FWHM)$ and $\Phi(r)$ $(r < FWHM)$, as these profiles are particularly unstable in the centre. In fact, the central region, where the profile information is based only upon a few pixels, is a particular problem. In this region, the ellipse parameters (ϵ, Φ, x, y) can occupy whole ranges of values with little or no effect on the seeing-convolved profiles. The only reasonable guess that can be made about these

CCD frame containing galaxy image is reduced, i.e. de-biased and flat-fielded, and the galaxy is 'chopped' out of the frame.

Sky count is measured manually from circular apertures at large r from the galaxy. The seeing FWHM is measured by fitting a theoretical PSF (Hankel Transform) to nearby stars. Bad pixels (i.e. cosmic-rays, stars) are flagged manually or by using a program that locates and parametrises sources.

Profiles of observed galaxy measured using an ellipse-fitting program, as a function of equivalent radius $r = \sqrt{ab}$.

The observed profiles are adjusted - $\mu(r)$ is replaced at large r by an extrapolation. Other profiles are smoothed at large r using a cubic spline approximation. This is to prevent fluctuations at large radii (due to low S/N or bad flat-fielding) feeding into the iteration. Also, crossing ellipses are removed by interpolating ellipse parameters between the nearest 'good' or non-crossing ellipses.

A first estimate of the seeing-corrected profiles are required to start the iteration. These are derived by extrapolating an $r^{\frac{1}{4}}$-law fit into the centre of the $\mu(r)$ profile. The other profiles are guessed by truncating (flattening) in the centre.

As we now have a first estimate for the corrected model profiles, we can move on to the iterative part of the algorithm - see flow chart overleaf ...

Figure 5.4: Flow Chart of Profile Deconvolution (Initial Stage)

... continued from previous flowchart

Seeing-corrected profile estimates are cleaned up -
crossing ellipses are replaced by interpolation.

Using seeing-corrected model profiles, build an
image and FFT-convolve with a PSF (Hankel transform,
with measured FWHM). Convolution is performed with
twice the pixel resolution to sample the PSF better.

Using an ellipse-fitting routine, measure profiles
from this convolved image (replace crossing and
missing ellipses by interpolation, as before).

Calculate 'seeing-correction' profiles using the
seeing-corrected profiles estimates and the convolved
profiles measured above (see equations 5.10 in text).

The corrections are applied to the observed profiles
to produce a set of seeing-corrected profile estimates,
which should be better than the previous estimates
(see equations 5.11 in text).

Smoothing and damping of the seeing-corrected profiles
is required to ensure noise or detail which is too
fine to be fitted is not fed back into the iteration
loop (see equations 5.12 and 5.13 in text).

To test whether the iterations are converging, the
RMS difference between the observed and convolved $\mu(r)$
profiles is calculated (for the conditions to decide whether
RMS difference is acceptable, see eqns 5.7 & 5.8 in text).

Is
RMS difference
Acceptable? (see above)
OR have there been 9
iterations?

NO

YES

Last seeing-corrected profiles are accepted as the final
solution (any crossing ellipses are cleaned up by
interpolation). Various fitting laws are fitted to the
seeing-corrected $\mu(r)$ profile, and global parameters
$(r_e, \langle\mu\rangle_e)$ are calculated. Errors are calculated on all
profiles. Graphs are produced to show the corrected
profiles and errors. An image is produced from the
corrected profiles, convolved, and ellipse-fitted to
produce graphs showing the quality of the final correction.

END

Figure 5.5: Flow Chart of Profile Deconvolution (Iteration Loop)

profiles is that they are approximately constant. Thus to prevent instability, it is thus necessary to 'damp' the ellipse parameter profiles within $r = FWHM$. This can be done by averaging each parameter with its own value *at FWHM*, i.e.:-

$$\left\{ \begin{array}{l} \epsilon^n(r) = \frac{1}{2}\left[\epsilon^n(r) + \epsilon^n(fwhm)\right] \\ \Phi^n(r) = \frac{1}{3}\left[2\Phi^n(r) + \Phi^n(fwhm)\right] \\ x^n(r) = \frac{1}{3}\left[2x^n(r) + x^n(fhwm)\right] \\ y^n(r) = \frac{1}{3}\left[2y^n(r) + y^n(fwhm)\right] \end{array} \right\} \tag{5.13}$$

This is the method employed by this study to obtain seeing-corrected ellipse-fit profiles from a CCD galaxy image. The important equations in the process are thus 5.10, 5.11, 5.12 and 5.13. A flow-chart summarizing the whole algorithm is given in figures 5.4 and 5.5. Section 5.5 presents illustrations of the success of the process, using synthetic (i.e. made-up) model galaxy images.

5.5 Examples using Synthetic Galaxy Models

In order to verify the correct operation of the deconvolution process, several different galaxy 'model' images have been constructed, and reduced in the standard way. The synthetic images are built with perfect $r^{\frac{1}{4}}$-law intensity profiles (different profile laws are also considered later on). The scaling-parameters $(r_e, \langle\mu\rangle_e)$, ellipticity and background-level are chosen to be representative of galaxies observed in the Coma data-set. Using the same pixel scale $(0.55''/pixel)$ and zero-point as the real data, the models simulate observations with a $60s$ exposure time (the shorter of the two exposure times used for the data). Finally, the images are convolved with a representative seeing PSF $(FWHM \simeq 1.1'' \rightarrow 2.6'')$, and photon noise is added to the pixels.

The first example has $r^{\frac{1}{4}}$-law parameters of $r_e = 8.5''$ and $\langle\mu\rangle_e = 19.3$ making a bright 'Coma' galaxy of magnitude $R = 12.66$. The ellipticity profile is a constant at 0.29 and, likewise, the position-angle and ellipse-centroid are fixed with radius. All the higher order terms are zero - so the ellipses are regular and concentric. Figures 5.6(a-e) show, for the $\mu(r)$ profile, how well the fit is proceeding at 1, 2, 3, 6 iterations, and *after* the final (9th) iteration. Each graph shows the residual between the corrected profiles (raw and convolved) and the observed $\mu(r)$ profile. The convolved residual eventually drops to zero as the iterations progress, as expected - the convolved profile should match the observed

profile if a solution is to be found for the corrected profile. As expected, the residual between the (unconvolved) corrected profile and the observed profile is very large for small r (in fact, this residual was divided by 10 to fit it on the plots). If the corrected $\mu(r)$ profile matches, within error, the original model (pre-convolution) profile, then this is a solid verification that the program has worked. This is indeed the case - figure 5.6(f) shows the residual between the final corrected $\mu(r)$ profile and a best fit $r^{\frac{1}{4}}$-law, plus the seeing correction which has been made to each point. Also shown is the error envelope on the deconvolved $\mu(r)$ profile - the errors are calculated by adding in quadrature the error due to the background uncertainty with $\frac{1}{5}$ times the local seeing-correction. Ignore the apparent seeing-correction at large radii ($r > 40''$) - this is due to edge-effects in the FFT seeing convolution. Given that we have an estimate of the errors on the corrected $\mu(r)$ profile, we can minimize χ^2 to get our best-fit $r^{\frac{1}{4}}$-law. The range in r over which the $r^{\frac{1}{4}}$-law is fitted is defined by $2 \times FWHM < r < r(Count \simeq 1.5 \times \Delta Sky)$. The scale-parameters returned from the fit match perfectly the input parameters used to make the model (see table 5.1). For comparison, a best-fitting $r^{\frac{1}{3}}$-law and $r^{\frac{1}{5}}$-law are calculated in the same way, and are shown on the residual plots. Despite the photometric similarity of galaxies with these profiles to an $r^{\frac{1}{4}}$-law galaxy when convolved with seeing, the deconvolution very clearly distinguishes that this galaxy has an $r^{\frac{1}{4}}$-law profile.

Of course, the intensity profile is not the only profile to be effected by seeing - the ellipticity profile $\epsilon(r)$ is strongly perturbed within about $4 \times FWHM$. Figure 5.7 shows the fitting process for the $\epsilon(r)$ profile, just as figure 5.6 did for the $\mu(r)$ profile. Instead of showing a residual, figures 5.7(a-e) show the absolute ellipticities at different iterations - the graphs show both the corrected $\epsilon(r)$ and its 'convolution', in addition to the observed profile, which includes some smoothing at high-r using a cubic-spline approximation (this removes the noise at high-r, and is used as the 'observed' profile in the fitting - see section 5.4). As expected, the corrected profile ends up flat, while the convolved profile matches the observed profile. In fact, the match is extremely good for the *first* estimate of the corrected profile, and gets worse before it improves. This is because the first guess - replacing $\epsilon(r)$ with a constant at low radii - is close to the *true* profile (which is, of course, a constant at *all* radii). The fitting of the *other* profiles drives the match away slightly in subsequent iterations, but eventually a convergence is reach when *all* the corrected profiles are close to their *true* profiles. Note the strange behaviour of the observed/convolved $\epsilon(r)$ profile within about 2

Model #	Fig #	$FWHM$ ($''$)	Prof $r^{\frac{1}{n}}$	c_4	Input $\log r_e$	Input $\langle\mu\rangle_e$	Input ϵ	Output $\log r_e$	Output $\langle\mu\rangle_e$	Output $\epsilon(r_e)$
1	5.6	1.1	4	0.00	0.929	19.3	0.29	0.930(4)	19.30(1)	0.290(3)
2	5.8	1.6	4	0.00	0.929	19.3	0.29	0.929(5)	19.30(2)	0.290(3)
3	5.9	2.6	4	0.00	0.929	19.3	0.29	0.934(7)	19.32(3)	0.291(6)
4	5.10	1.3/1.2	4	0.00	0.929	19.3	0.29	0.922(4)	19.26(1)	0.284(3)
5	5.11	1.3/1.4	4	0.00	0.929	19.3	0.29	0.927(4)	19.30(2)	0.287(3)
6	5.12	1.1	4	0.05	0.929	19.3	0.29	0.937(4)	19.33(1)	0.293(6)
7	5.13	1.1	4	0.00	0.929	19.3	0.05-0.5	0.931(4)	19.31(1)	—
8	5.14	1.1	4	0.05	0.929	19.3	0.05-0.5	0.927(4)	19.29(1)	—
9	5.15	1.1	4	0.00	0.929	19.3	0.5-0.05	0.931(4)	19.31(1)	—
10	5.16	1.1/1.2	4	0.00	0.929	19.3	0.05-0.5	0.934(4)	19.33(1)	—
11	5.17	1.1	4	0.00	0.653	18.7	0.29	0.650(4)	18.69(2)	0.293(4)
12	5.18	1.1	4	0.00	1.033	20.1	0.29	1.036(4)	20.11(1)	0.293(4)
13	5.19	1.1	3	0.00	0.929	19.3	0.29	—	—	0.289(3)
14	5.20	1.1	5	0.00	0.929	19.3	0.29	—	—	0.295(3)
15	5.21	1.1	3	0.05	0.929	19.3	0.05-0.5	—	—	—

Table 5.1: Comparison of scale-parameters and ellipticity of model galaxies which have been deconvolved, to the same parameters of the original (undegraded) models. The first two columns give the number and figure reference of the model galaxy. The next three columns give details of how the models were made, the $FWHM$ of the PSF, the shape of the profile ($r^{\frac{1}{n}}$) and the 'diskyness' of the isophote (c_4 - the Fourier coefficient is divided by $r.dI/dr$ to represent the relative radial distortion from an elliptical isophote). Where there are two figures for the $FWHM$, the first signifies the PSF with which the original model was degraded with and the second is the PSF used for the deconvolution (thus representing a error in the seeing measurement). The next three columns give the scale-parameters (appropriate to the profile) and ellipticity of the made-up model, before convolution. Where a range is given for the ellipticity, the ellipticity was modelled with a linear function in $\log r$ between the two values, rather than a constant. The final three columns (on the right) give the output parameters from the deconvolution routine - the scale-parameters from an $r^{\frac{1}{4}}$-law fit and the ellipticity interpolated at the half-light radius. The numbers in brackets are the calculated error on the last significant digit. The parameters are not shown where they are meaningless (i.e. for non-$r^{\frac{1}{4}}$-law profiles and varying ellipticities).
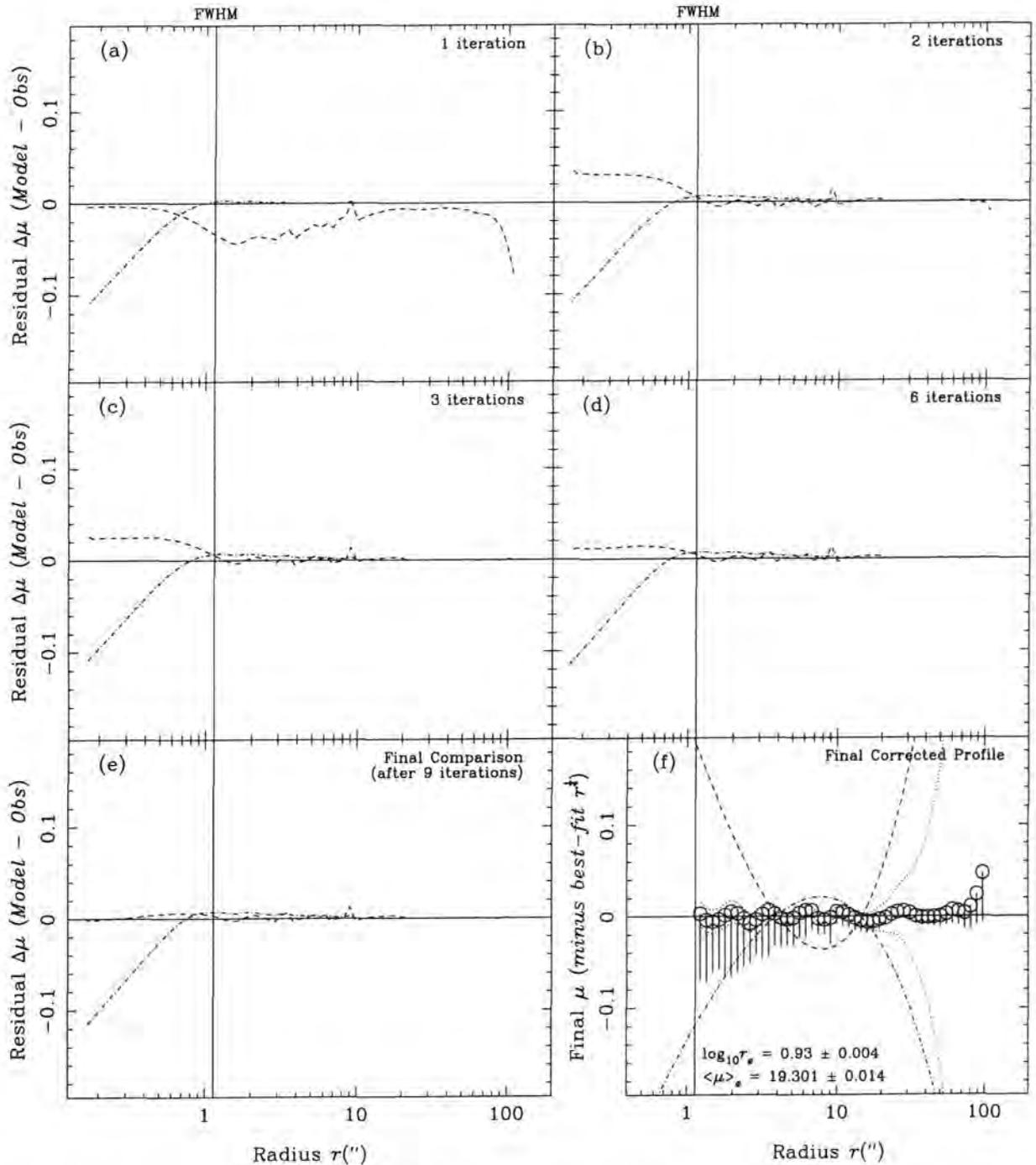
Figure 5.6: Fitting the surface brightness of a perfect $r^{\frac{1}{4}}$-law model galaxy ($\log r_e = 0.929$, $\langle \mu \rangle_e = 19.3$, $\epsilon = 0.29$) 'observed' in *good* seeing ($FWHM = 1.1''$). These plots show the comparison between the corrected $\mu(r)$ profile (convolved with seeing) and the 'observed' $\mu(r)$ profile, at various stages in the routine - at iteration 1: plot (a); at iteration 2: plot (b); at iteration 3: plot (c); at iteration 6: plot (d); *after* the final (9th) iteration: plot (e). The dashed line shows the *difference* between the corrected profile (convolved with seeing) and the observed profile. Note that this residual drops to nearly zero as the iterations progress, as expected. The residual between the *true* (i.e. unconvolved) corrected profile and the observed (i.e. degraded) profile is shown by the dot-dashed line, which was divided by 10 to fit onto the plots. The final plot (f) shows the residual (circles) between the final corrected $\mu(r)$ profile and a best-fit $r^{\frac{1}{4}}$-law (scale-parameters are shown, see figure 5.8 for more detail). The 'tails' represent the seeing correction and the dotted lines are the error-envelopes, whilst the dashed and dot-dashed lines are the best-fit $r^{\frac{1}{3}}$-law and $r^{\frac{1}{5}}$-law profiles respectively (with the $r^{\frac{1}{4}}$-law subtracted off).
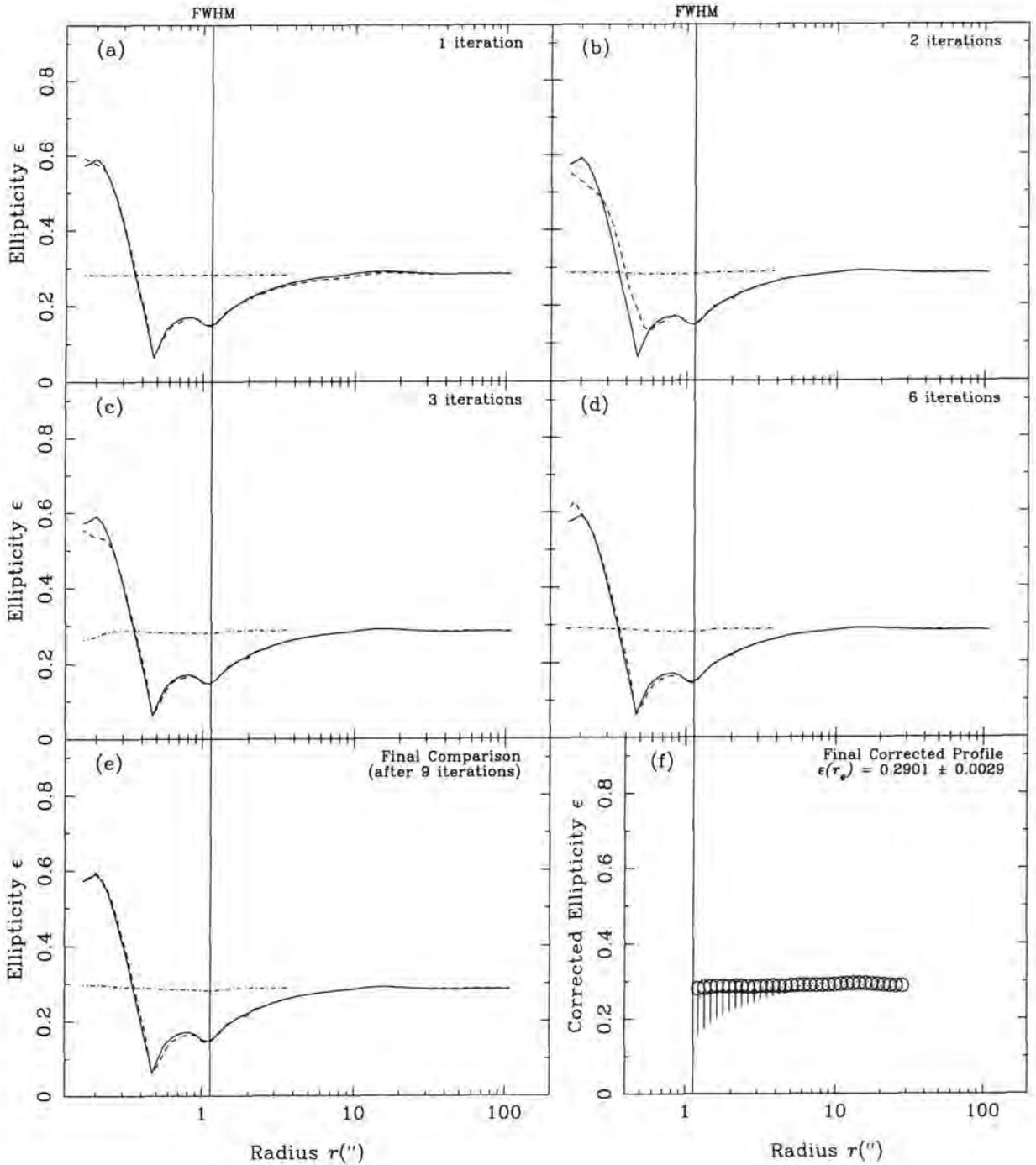
Figure 5.7: Fitting the ellipticity of a perfect $r^{\frac{1}{4}}$-law model galaxy ($\log r_e = 0.929$, $\langle\mu\rangle_e = 19.3$, $\epsilon = 0.29$) 'observed' in *good* seeing ($FWHM = 1.1''$) - the same model as in figure 5.6. These plots show the comparison between the corrected $\epsilon(r)$ profile (convolved with seeing) and the 'observed' $\epsilon(r)$ profile, at various stages in the routine - at iteration 1: plot (a); at iteration 2: plot (b); at iteration 3: plot (c); at iteration 6: plot (d); *after* the final (9th) iteration: plot (e). The corrected profile (after seeing convolution), shown by a dashed line, starts close to the observed profile, which is encouraging (this is because the original $\epsilon(r)$ profile was just a simple constant). The match is knocked off slightly in iteration 2 (due to the fitting of other profiles), but quickly returns to the previous good fit. The *true* (i.e. unconvolved) corrected profile is shown by the dot-dashed line, and as expected remains nearly flat throughout the iterations. The final plot (f) shows the final corrected $\epsilon(r)$ profile (circles) and seeing-correction ('tails'). The interpolated ellipticity at the half-light radius r_e is also printed.

pixels. This is merely an artifact introduced by the ellipse-fitting and low pixel sampling - if the centroid is near the boundary of 2 pixels, these inner radii will be fitted with a highly elliptical isophote, regardless of the true ellipticity! It can be seen, however, that the deconvolved profile does end up flat in the centre, and the convolved profile fits the observed perfectly. If a *real* galaxy does have an ellipticity gradient within its central few pixels, this will *not*, of course, be resolved. The final corrected output $\epsilon(r)$ profile is shown is figure 5.7(f) - with seeing-correction and errors shown. The ellipticity at r_e from this line is almost exactly that of the constant ellipticity originally fed-in (see table 5.1).

The next series of models are based on the first model, with the same $r^{\frac{1}{4}}$-law parameters, but are perturbed in various ways which *should* made them harder to deconvolve. This is a test of the limitations of the routine. For the first two models, the seeing FWHM is increased to 1.6″ and 2.6″, to simulate poor observing conditions. The final corrected profiles fitted to these models are shown as figures 5.8 and 5.9 respectively (the position angle and centroid are included as well as intensity and ellipticity). The key in both these figures are the same as for figure 5.6(f) for the $r^{\frac{1}{4}}$ residual plots, with the circles representing the residual, and figure 5.7(f) for the other plots, with the circles representing the final corrected profiles - see the captions for a detailed key. Seeing-corrections are shown as tails. As the figures show, the ripples in the $\mu(r) - r^{\frac{1}{4}}$ residual plot increase with seeing, as the seeing-correction increases. However, even at 2.6″ seeing (about the worst in the Coma data-set), the routine still produces a good fit to the original model, with flat $\epsilon(r)$, $\Phi(r)$, and centroid profiles. The best-fit $r^{\frac{1}{4}}$-law parameters have changed slightly, but are still correct within error.

The next problem we may encounter with real data is an error on the measurement of the seeing $FWHM$. In fact, as the theoretical seeing PSF's used for the deconvolution are in steps of 0.1″ (of $FWHM$), there will always be a small error (∼0.025″) in this respect. To test this problem, a model was constructed (same parameters as before) with $FWHM = 1.3″$. This model was then deconvolved twice - once using 1.2″ as my 'measured' seeing, and again using 1.4″, thus simulating a seeing measurement error of $\Delta FWHM = \pm0.1$. The results are shown in figures 5.10 and 5.11 respectively. Again, it is seen that a good fit is made to the model in both cases. The $r^{\frac{1}{4}}$-law parameters *are* perturbed by about 2σ from their correct values, but this is not hugely significant and the shape of the corrected $\mu(r)$ profile is still clearly $r^{\frac{1}{4}}$.

What if the galaxy to be deconvolved is not a 'perfect' elliptical, but has disky isophotes,
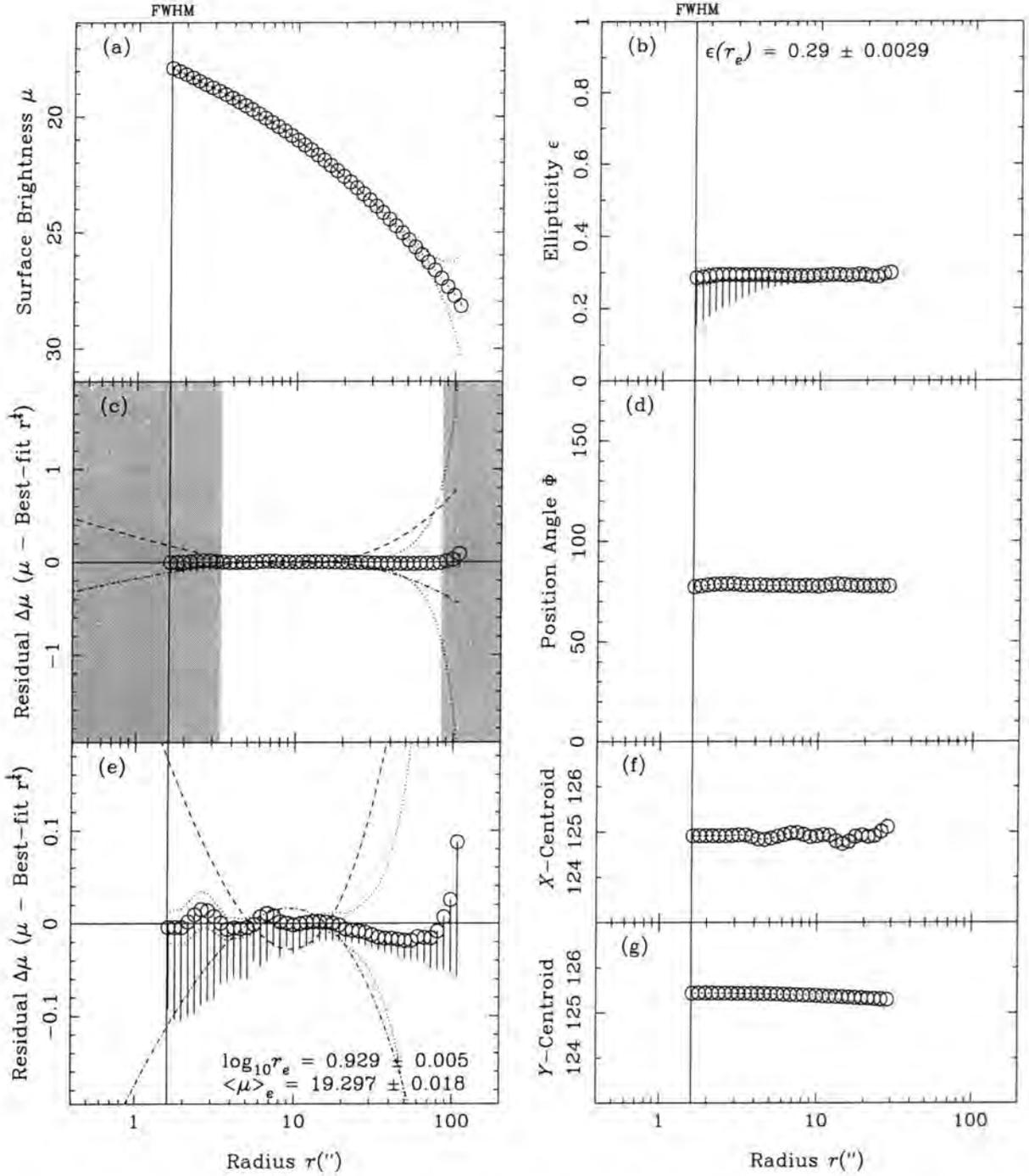
Figure 5.8: Deconvolution of a perfect $r^{\frac{1}{4}}$-law model galaxy ($\log r_e = 0.929$, $\langle\mu\rangle_e = 19.3$, $\epsilon = 0.29$) 'observed' in *moderate* seeing ($FWHM = 1.6''$). These plots show the final corrected profiles (circles), with the seeing-correction ('tails' or solid lines) and error-envelope of the corrected profiles (dotted lines). (a) shows the surface brightness (μ) profile, (b) shows the ellipticity (ϵ) profile, (d) shows the position-angle (Φ) profile, while (f) and (g) show the ellipse-centroid (x, y) profiles. The plot (c) shows the residual between the final corrected surface brightness profiles and the best-fitting $r^{\frac{1}{4}}$-law. This $r^{\frac{1}{4}}$-law was fitted over the *unshaded* area - defined by $2 \times FWHM < r < r(Count \simeq 1.5 \times \Delta Sky)$ - using the calculated errors to weight the least-squares fit. (e) shows the same residual plot as (c), but with the y-axis scale increased by a factor of 10 to show more detail. In both (c) and (e), the best-fitted $r^{\frac{1}{3}}$ and $r^{\frac{1}{5}}$-law profiles are shown for comparison - these are the dashed and dot-dashed lines respectively. The values of the best-fit $r^{\frac{1}{4}}$-law scale parameters are printed in plot (e), while the interpolated value for the corrected ellipticity at r_e is displayed in plot (b).

Figure 5.9: Deconvolution of a perfect $r^{\frac{1}{4}}$-law model galaxy ($\log r_e = 0.929$, $\langle \mu \rangle_e = 19.3$, $\epsilon = 0.29$) 'observed' in *poor* seeing ($FWHM = 2.6''$). These plots show the final corrected profiles (circles), with the seeing-correction ('tails' or solid lines) and error-envelope of the corrected profiles (dotted lines). (a) shows the surface brightness (μ) profile, (b) shows the ellipticity (ϵ) profile, (d) shows the position-angle (Φ) profile, while (f) and (g) show the ellipse-centroid (x, y) profiles. The plot (c) shows the residual between the final corrected surface brightness profiles and the best-fitting $r^{\frac{1}{4}}$-law. This $r^{\frac{1}{4}}$-law was fitted over the *unshaded* area - defined by $2 \times FWHM < r < r(Count \simeq 1.5 \times \Delta Sky)$ - using the calculated errors to weight the least-squares fit. (e) shows the same residual plot as (c), but with the y-axis scale increased by a factor of 10 to show more detail. In both (c) and (e), the best-fitted $r^{\frac{1}{3}}$ and $r^{\frac{1}{5}}$-law profiles are shown for comparison - these are the dashed and dot-dashed lines respectively. The values of the best-fit $r^{\frac{1}{4}}$-law scale parameters are printed in plot (e), while the interpolated value for the corrected ellipticity at r_e is displayed in plot (b).
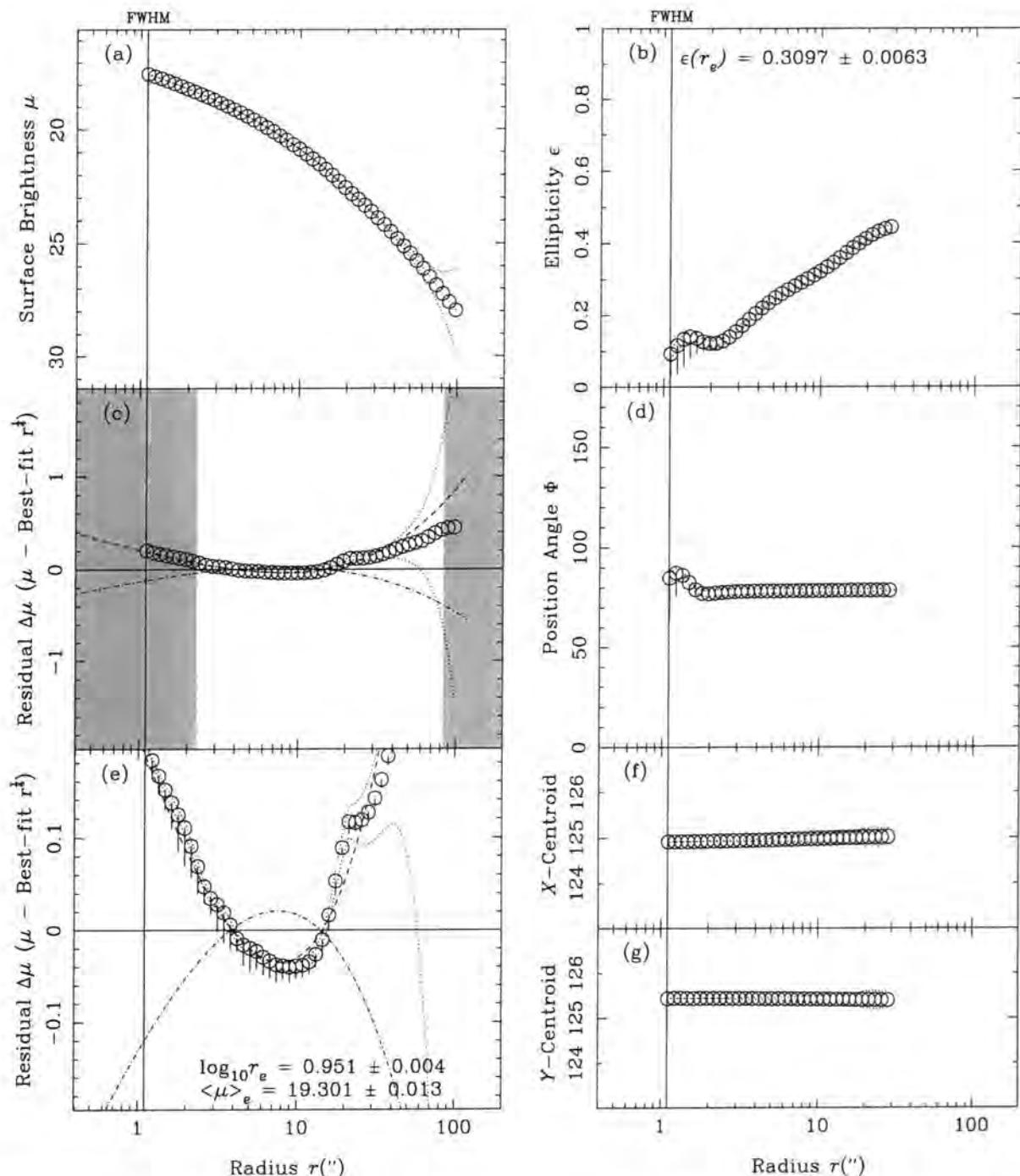
Figure 5.10: Deconvolution of a perfect $r^{\frac{1}{4}}$-law model galaxy ($\log r_e = 0.929$, $\langle\mu\rangle_e = 19.3$, $\epsilon = 0.29$). The image was degraded using a seeing PSF with $FWHM = 1.3''$, but deconvolved using $FWHM = 1.2''$ - this represents a seeing $FWHM$ measurement error of $0.1''$. These plots show the final corrected profiles (circles), with the seeing-correction ('tails' or solid lines) and error-envelope of the corrected profiles (dotted lines). (a) shows the surface brightness (μ) profile, (b) shows the ellipticity (ϵ) profile, (d) shows the position-angle (Φ) profile, while (f) and (g) show the ellipse-centroid (x, y) profiles. The plot (c) shows the residual between the final corrected surface brightness profiles and the best-fitting $r^{\frac{1}{4}}$-law. This $r^{\frac{1}{4}}$-law was fitted over the *unshaded* area - defined by $2 \times FWHM < r < r(Count \simeq 1.5 \times \Delta Sky)$ - using the calculated errors to weight the least-squares fit. (e) shows the same residual plot as (c), but with the y-axis scale increased by a factor of 10 to show more detail. In both (c) and (e), the best-fitted $r^{\frac{1}{3}}$ and $r^{\frac{1}{5}}$-law profiles are shown for comparison - these are the dashed and dot-dashed lines respectively. The values of the best-fit $r^{\frac{1}{4}}$-law scale parameters are printed in plot (e), while the interpolated value for the corrected ellipticity at r_e is displayed in plot (b).

Figure 5.11: Deconvolution of a perfect $r^{\frac{1}{4}}$-law model galaxy ($\log r_e = 0.929$, $\langle\mu\rangle_e = 19.3$, $\epsilon = 0.29$). The image was degraded using a seeing PSF with $FWHM = 1.3''$, but deconvolved using $FWHM = 1.4''$ - this represents a seeing $FWHM$ measurement error of $0.1''$ (in the opposite sense to figure 5.10). These plots show the final corrected profiles (circles), with the seeing-correction ('tails' or solid lines) and error-envelope of the corrected profiles (dotted lines). (a) shows the surface brightness (μ) profile, (b) shows the ellipticity (ϵ) profile, (d) shows the position-angle (Φ) profile, while (f) and (g) show the ellipse-centroid (x, y) profiles. The plot (c) shows the residual between the final corrected surface brightness profiles and the best-fitting $r^{\frac{1}{4}}$-law. This $r^{\frac{1}{4}}$-law was fitted over the *unshaded* area - defined by $2 \times FWHM < r < r(Count \simeq 1.5 \times \Delta Sky)$ - using the calculated errors to weight the least-squares fit. (e) shows the same residual plot as (c), but with the y-axis scale increased by a factor of 10 to show more detail. In both (c) and (e), the best-fitted $r^{\frac{1}{3}}$ and $r^{\frac{1}{5}}$-law profiles are shown for comparison - these are the dashed and dot-dashed lines respectively. The values of the best-fit $r^{\frac{1}{4}}$-law scale parameters are printed in plot (e), while the interpolated value for the corrected ellipticity at r_e is displayed in plot (b).

or an ellipticity gradient, or both? Figure 5.12 shows the corrected profiles for a model built with a positive c_4 term of 0.05, representing strong disky isophotes. Figure 5.13 shows the same for a model built with a $\epsilon(r)$ profile increasing from 0.05 to 0.5 (linearly in $\log r$). A typical S0 galaxy might well have both an increasing ellipticity and disky isophotes, so a model was built combining the features of the two previous models - the corrected profiles are shown in figure 5.14. Occasionally, the ellipticity of a galaxy might actually *decrease* with radius (such as a face-on SB0) - the fit to this model is shown in figure 5.15. Finally, figure 5.16 shows the corrected profiles for the same model as figure 5.13 (i.e. no c_4, but increasing $\epsilon(r)$), but with a different seeing (1.2″) used for the deconvolution from that used to convolve the model (1.1″). For all these models, it can be immediately seen from the residuals of the corrected $\mu(r)$ from a best-fit $r^{\frac{1}{4}}$ that all the models were constructed with $r^{\frac{1}{4}}$-laws, rather than any other function of $\mu(r)$. The scale-parameters of the best-fit $r^{\frac{1}{4}}$ in each case recover the parameters of the input $r^{\frac{1}{4}}$ to an acceptable accuracy (see table 5.1). The ellipticity profile is also well recovered in each example - whether constant, increasing linearly, or decreasing linearly.

All the model galaxies in the examples above were built with an $r^{\frac{1}{4}}$-law profile, using identical scale-parameters ($\log r_e = 0.929$, $\langle \mu \rangle_e = 19.3$). The next two figures (5.17 and 5.18) show the corrected profiles for $r^{\frac{1}{4}}$-law models, made with different scale-parameters - $\log r_e = 0.653$ & $\langle \mu \rangle_e = 18.7$ representing a more compact galaxy, and $\log r_e = 1.033$ & $\langle \mu \rangle_e = 20.1$ representing a more extended galaxy. The fits to both of these models shows once again how remarkably well the original profiles are recovered. Of course, many real galaxies do not follow $r^{\frac{1}{4}}$ laws. Figures 5.19 and 5.20 shows the corrected profiles for models made up with $r^{\frac{1}{3}}$-law and $r^{\frac{1}{5}}$-law profiles respectively. In the residual plots (c) and (e), the best-fit $r^{\frac{1}{3}}$ and $r^{\frac{1}{5}}$ profiles are shown as dashed and dot-dashed lines respectively (they resemble parabola when the $r^{\frac{1}{4}}$ is subtracted). As expected, the seeing-corrected $\mu(r)$ profiles follow these very precisely. The scale-parameters are wrong by a large margin, but this is expected as they describe the best-fitting $r^{\frac{1}{4}}$-law. If the deconvolution routine can distinguish between $r^{\frac{1}{3}}$, $r^{\frac{1}{4}}$ and $r^{\frac{1}{5}}$ profiles, which are photometrically very similar, it will easily pick-up exponential-disks hidden in ellipticals, and other features of interest. The final example model to be deconvolved has an $r^{\frac{1}{3}}$-law $\mu(r)$ profile, a positive c_4 parameter (0.05), and an increasing ellipticity profile (identical to the model in 5.13). Figure 5.21 shows the corrected profile fits, demonstrating again how successful this routine is. Note the slight
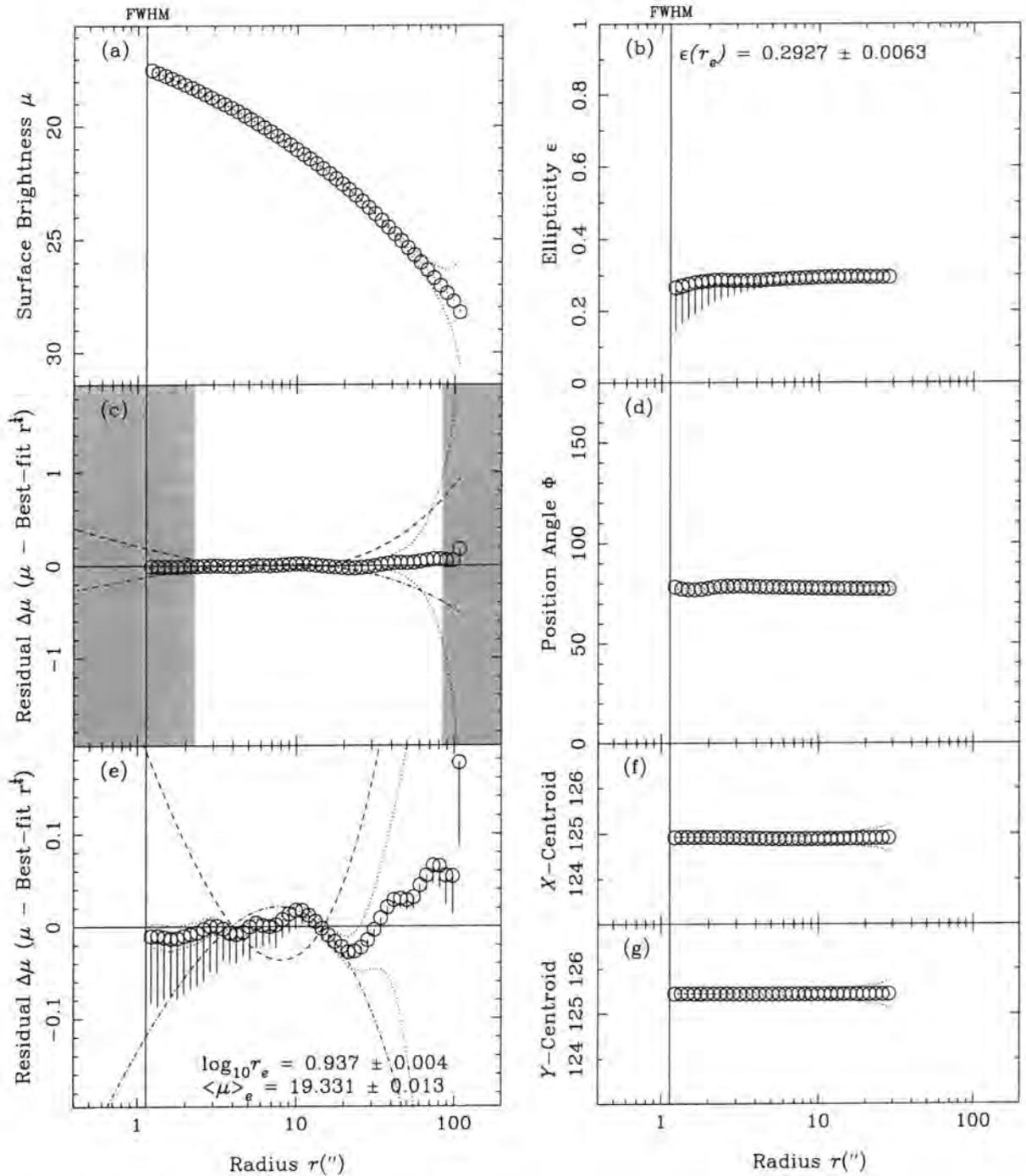
Figure 5.12: Deconvolution of a *disky* $r^{\frac{1}{4}}$-law model galaxy ($\log r_e = 0.929$, $\langle\mu\rangle_e = 19.3$, $\epsilon = 0.29$, $c_4 = 0.05$) 'observed' in *good* seeing ($FWHM = 1.1''$). These plots show the final corrected profiles (circles), with the seeing-correction ('tails' or solid lines) and error-envelope of the corrected profiles (dotted lines). (a) shows the surface brightness (μ) profile, (b) shows the ellipticity (ϵ) profile, (d) shows the position-angle (Φ) profile, while (f) and (g) show the ellipse-centroid (x, y) profiles. The plot (c) shows the residual between the final corrected surface brightness profiles and the best-fitting $r^{\frac{1}{4}}$-law. This $r^{\frac{1}{4}}$-law was fitted over the *unshaded* area - defined by $2 \times FWHM < r < r(Count \simeq 1.5 \times \Delta Sky)$ - using the calculated errors to weight the least-squares fit. (e) shows the same residual plot as (c), but with the y-axis scale increased by a factor of 10 to show more detail. In both (c) and (e), the best-fitted $r^{\frac{1}{3}}$ and $r^{\frac{1}{5}}$-law profiles are shown for comparison - these are the dashed and dot-dashed lines respectively. The values of the best-fit $r^{\frac{1}{4}}$-law scale parameters are printed in plot (e), while the interpolated value for the corrected ellipticity at r_e is displayed in plot (b).

Figure 5.13: Deconvolution of an $r^{\frac{1}{4}}$-law model galaxy ($\log r_e = 0.929$, $\langle\mu\rangle_e = 19.3$) 'observed' in *good* seeing ($FWHM = 1.1''$). The ellipticity of the 'manufactured' model was made to vary linearly (in $\log r$) between $\epsilon = 0.05$ (at $r = 1.0''$) and $\epsilon = 0.5$ (at $r = 45.7''$). This was done in order to test the recovery of the ellipticity profile. These plots show the final corrected profiles (circles), with the seeing-correction ('tails' or solid lines) and error-envelope of the corrected profiles (dotted lines). (a) shows the surface brightness (μ) profile, (b) shows the ellipticity (ϵ) profile, (d) shows the position-angle (Φ) profile, while (f) and (g) show the ellipse-centroid (x, y) profiles. The plot (c) shows the residual between the final corrected surface brightness profiles and the best-fitting $r^{\frac{1}{4}}$-law. This $r^{\frac{1}{4}}$-law was fitted over the *unshaded* area - defined by $2\times FWHM < r < r(Count \simeq 1.5 \times \Delta Sky)$ - using the calculated errors to weight the least-squares fit. (e) shows the same residual plot as (c), but with the y-axis scale increased by a factor of 10 to show more detail. In both (c) and (e), the best-fitted $r^{\frac{1}{3}}$ and $r^{\frac{1}{5}}$-law profiles are shown for comparison - these are the dashed and dot-dashed lines respectively. The values of the best-fit $r^{\frac{1}{4}}$-law scale parameters are printed in plot (e), while the interpolated value for the corrected ellipticity at r_e is displayed in plot (b).

Figure 5.14: Deconvolution of a *disky* $r^{\frac{1}{4}}$-law model galaxy ($\log r_e = 0.929$, $\langle\mu\rangle_e = 19.3$, $c_4 = 0.05$) 'observed' in *good* seeing ($FWHM = 1.1''$). The ellipticity of the 'manufactured' model was made to vary linearly (in $\log r$) between $\epsilon = 0.05$ (at $r = 1.0''$) and $\epsilon = 0.5$ (at $r = 45.7''$). This might represent, for instance, a disky elliptical or S0 galaxy. These plots show the final corrected profiles (circles), with the seeing-correction ('tails' or solid lines) and error-envelope of the corrected profiles (dotted lines). (a) shows the surface brightness (μ) profile, (b) shows the ellipticity (ϵ) profile, (d) shows the position-angle (Φ) profile, while (f) and (g) show the ellipse-centroid (x, y) profiles. The plot (c) shows the residual between the final corrected surface brightness profiles and the best-fitting $r^{\frac{1}{4}}$-law. This $r^{\frac{1}{4}}$-law was fitted over the *unshaded* area - defined by $2 \times FWHM < r < r(Count \simeq 1.5 \times \Delta Sky)$ - using the calculated errors to weight the least-squares fit. (e) shows the same residual plot as (c), but with the y-axis scale increased by a factor of 10 to show more detail. In both (c) and (e), the best-fitted $r^{\frac{1}{3}}$ and $r^{\frac{1}{5}}$-law profiles are shown for comparison - these are the dashed and dot-dashed lines respectively. The values of the best-fit $r^{\frac{1}{4}}$-law scale parameters are printed in plot (e), while the interpolated value for the corrected ellipticity at r_e is displayed in plot (b).

Figure 5.15: Deconvolution of an $r^{\frac{1}{4}}$-law model galaxy ($\log r_e = 0.929$, $\langle\mu\rangle_e = 19.3$) 'observed' in *good* seeing ($FWHM = 1.1''$). The ellipticity of the 'manufactured' model was made to decrease linearly (in $\log r$) between $\epsilon = 0.5$ (at $r = 1.2''$) and $\epsilon = 0.05$ (at $r = 55.2''$). This might represent, for instance, a face-on barred S0 galaxy. These plots show the final corrected profiles (circles), with the seeing-correction ('tails' or solid lines) and error-envelope of the corrected profiles (dotted lines). (a) shows the surface brightness (μ) profile, (b) shows the ellipticity (ϵ) profile, (d) shows the position-angle (Φ) profile, while (f) and (g) show the ellipse-centroid (x, y) profiles. The plot (c) shows the residual between the final corrected surface brightness profiles and the best-fitting $r^{\frac{1}{4}}$-law. This $r^{\frac{1}{4}}$-law was fitted over the *unshaded* area - defined by $2 \times FWHM < r < r(Count \simeq 1.5 \times \Delta Sky)$ - using the calculated errors to weight the least-squares fit. (e) shows the same residual plot as (c), but with the y-axis scale increased by a factor of 10 to show more detail. In both (c) and (e), the best-fitted $r^{\frac{1}{3}}$ and $r^{\frac{1}{5}}$-law profiles are shown for comparison - these are the dashed and dot-dashed lines respectively. The values of the best-fit $r^{\frac{1}{4}}$-law scale parameters are printed in plot (e), while the interpolated value for the corrected ellipticity at r_e is displayed in plot (b).

Figure 5.16: Deconvolution of an $r^{\frac{1}{4}}$-law model galaxy ($\log r_e = 0.929$, $\langle\mu\rangle_e = 19.3$). The image was degraded using a seeing PSF with $FWHM = 1.1''$, but deconvolved using $FWHM = 1.2''$ - this represents a seeing $FWHM$ measurement error of $0.1''$. As in figure 5.13, the ellipticity of the 'manufactured' model was made to vary linearly (in $\log r$) between $\epsilon = 0.05$ (at $r = 1.0''$) and $\epsilon = 0.5$ (at $r = 45.7''$). These plots show the final corrected profiles (circles), with the seeing-correction ('tails' or solid lines) and error-envelope of the corrected profiles (dotted lines). (a) shows the surface brightness (μ) profile, (b) shows the ellipticity (ϵ) profile, (d) shows the position-angle (Φ) profile, while (f) and (g) show the ellipse-centroid (x, y) profiles. The plot (c) shows the residual between the final corrected surface brightness profiles and the best-fitting $r^{\frac{1}{4}}$-law. This $r^{\frac{1}{4}}$-law was fitted over the *unshaded* area - defined by $2 \times FWHM < r < r(Count \simeq 1.5 \times \Delta Sky)$ - using the calculated errors to weight the least-squares fit. (e) shows the same residual plot as (c), but with the y-axis scale increased by a factor of 10 to show more detail. In both (c) and (e), the best-fitted $r^{\frac{1}{3}}$ and $r^{\frac{1}{5}}$-law profiles are shown for comparison - these are the dashed and dot-dashed lines respectively. The values of the best-fit $r^{\frac{1}{4}}$-law scale parameters are printed in plot (e), while the interpolated value for the corrected ellipticity at r_e is displayed in plot (b).

Figure 5.17: Deconvolution of a perfect $r^{\frac{1}{4}}$-law model galaxy ($\epsilon = 0.29$) 'observed' in *good* seeing ($FWHM = 1.1''$). Different scale-parameters ($\log r_e = 0.653$, $\langle\mu\rangle_e = 18.7$) are used from the previous models, representing a more compact elliptical. These plots show the final corrected profiles (circles), with the seeing-correction ('tails' or solid lines) and error-envelope of the corrected profiles (dotted lines). (a) shows the surface brightness (μ) profile, (b) shows the ellipticity (ϵ) profile, (d) shows the position-angle (Φ) profile, while (f) and (g) show the ellipse-centroid (x, y) profiles. The plot (c) shows the residual between the final corrected surface brightness profiles and the best-fitting $r^{\frac{1}{4}}$-law. This $r^{\frac{1}{4}}$-law was fitted over the *unshaded* area - defined by $2\times FWHM < r < r(Count \simeq 1.5 \times \Delta Sky)$ - using the calculated errors to weight the least-squares fit. (e) shows the same residual plot as (c), but with the y-axis scale increased by a factor of 10 to show more detail. In both (c) and (e), the best-fitted $r^{\frac{1}{3}}$ and $r^{\frac{1}{5}}$-law profiles are shown for comparison - these are the dashed and dot-dashed lines respectively. The values of the best-fit $r^{\frac{1}{4}}$-law scale parameters are printed in plot (e), while the interpolated value for the corrected ellipticity at r_e is displayed in plot (b).

Figure 5.18: Deconvolution of a perfect $r^{\frac{1}{4}}$-law model galaxy ($\epsilon = 0.29$) 'observed' in *good* seeing ($FWHM = 1.1''$). Again, different scale-parameters ($\log r_e = 1.033$, $\langle\mu\rangle_e = 20.1$) are used from the previous models, representing a more extended elliptical. These plots show the final corrected profiles (circles), with the seeing-correction ('tails' or solid lines) and error-envelope of the corrected profiles (dotted lines). (a) shows the surface brightness (μ) profile, (b) shows the ellipticity (ϵ) profile, (d) shows the position-angle (Φ) profile, while (f) and (g) show the ellipse-centroid (x, y) profiles. The plot (c) shows the residual between the final corrected surface brightness profiles and the best-fitting $r^{\frac{1}{4}}$-law. This $r^{\frac{1}{4}}$-law was fitted over the *unshaded* area - defined by $2\times FWHM < r < r(Count \simeq 1.5 \times \Delta Sky)$ - using the calculated errors to weight the least-squares fit. (e) shows the same residual plot as (c), but with the y-axis scale increased by a factor of 10 to show more detail. In both (c) and (e), the best-fitted $r^{\frac{1}{3}}$ and $r^{\frac{1}{8}}$-law profiles are shown for comparison - these are the dashed and dot-dashed lines respectively. The values of the best-fit $r^{\frac{1}{4}}$-law scale parameters are printed in plot (e), while the interpolated value for the corrected ellipticity at r_e is displayed in plot (b).

Figure 5.19: Deconvolution of a 'perfect' model galaxy. To test how well the deconvolution routine recovers non-$r^{\frac{1}{4}}$ surface brightness profiles, an $r^{\frac{1}{3}}$-law profile was used to construct the model ($\log r_e = 0.929$, $\langle\mu\rangle_e = 19.3$, $\epsilon = 0.29$). The model was 'observed' in *good* seeing ($FWHM = 1.1''$). These plots show the final corrected profiles (circles), with the seeing-correction ('tails' or solid lines) and error-envelope of the corrected profiles (dotted lines). (a) shows the surface brightness (μ) profile, (b) shows the ellipticity (ϵ) profile, (d) shows the position-angle (Φ) profile, while (f) and (g) show the ellipse-centroid (x, y) profiles. The plot (c) shows the residual between the final corrected surface brightness profiles and the best-fitting $r^{\frac{1}{4}}$-law. This $r^{\frac{1}{4}}$-law was fitted over the *unshaded* area - defined by $2 \times FWHM < r < r(Count \simeq 1.5 \times \Delta Sky)$ - using the calculated errors to weight the least-squares fit. (e) shows the same residual plot as (c), but with the y-axis scale increased by a factor of 10 to show more detail. In both (c) and (e), the best-fitted $r^{\frac{1}{3}}$ and $r^{\frac{1}{5}}$-law profiles are shown for comparison - these are the dashed and dot-dashed lines respectively. The interpolated value for the corrected ellipticity at r_e (from the $r^{\frac{1}{4}}$-law fit) is displayed in plot (b).

$\epsilon(r_e) = 0.2954 \pm 0.0028$

$\log_{10} r_e = 0.908 \pm 0.004$
$\langle\mu\rangle_e = 19.294 \pm 0.014$

Radius $r('')$

Radius $r('')$

Figure 5.20: Deconvolution of a 'perfect' model galaxy. To test how well the deconvolution routine recovers non-$r^{\frac{1}{4}}$ surface brightness profiles, an $r^{\frac{1}{5}}$-law profile was used to construct the model ($\log r_e = 0.929, \langle\mu\rangle_e = 19.3, \epsilon = 0.29$). The model was 'observed' in *good* seeing ($FWHM = 1.1''$). These plots show the final corrected profiles (circles), with the seeing-correction ('tails' or solid lines) and error-envelope of the corrected profiles (dotted lines). (a) shows the surface brightness (μ) profile, (b) shows the ellipticity (ϵ) profile, (d) shows the position-angle (Φ) profile, while (f) and (g) show the ellipse-centroid (x, y) profiles. The plot (c) shows the residual between the final corrected surface brightness profiles and the best-fitting $r^{\frac{1}{4}}$-law. This $r^{\frac{1}{4}}$-law was fitted over the *unshaded* area - defined by $2 \times FWHM < r < r(Count \simeq 1.5 \times \Delta Sky)$ - using the calculated errors to weight the least-squares fit. (e) shows the same residual plot as (c), but with the y-axis scale increased by a factor of 10 to show more detail. In both (c) and (e), the best-fitted $r^{\frac{1}{3}}$ and $r^{\frac{1}{5}}$-law profiles are shown for comparison - these are the dashed and dot-dashed lines respectively. The interpolated value for the corrected ellipticity at r_e (from the $r^{\frac{1}{4}}$-law fit) is displayed in plot (b).

Figure 5.21: Deconvolution of a *disky* $r^{\frac{1}{3}}$-law model galaxy ($\log r_e = 0.929$, $\langle \mu \rangle_e = 19.3$, $c_4 = 0.05$) 'observed' in *good* seeing ($FWHM = 1.1''$). The ellipticity of the 'manufactured' model was made to vary linearly (in $\log r$) between $\epsilon = 0.05$ (at $r = 1.0''$) and $\epsilon = 0.5$ (at $r = 45.7''$). As an $r^{\frac{1}{4}}$-law galaxy contaminated with an exponential disk may sometimes have an $r^{\frac{1}{3}}$-like profile, this galaxy could represent, for instance, an S0 galaxy. These plots show the final corrected profiles (circles), with the seeing-correction ('tails' or solid lines) and error-envelope of the corrected profiles (dotted lines). (a) shows the surface brightness (μ) profile, (b) shows the ellipticity (ϵ) profile, (d) shows the position-angle (Φ) profile, while (f) and (g) show the ellipse-centroid (x, y) profiles. The plot (c) shows the residual between the final corrected surface brightness profiles and the best-fitting $r^{\frac{1}{4}}$-law. This $r^{\frac{1}{4}}$-law was fitted over the *unshaded* area - defined by $2 \times FWHM < r < r(Count \simeq 1.5 \times \Delta Sky)$ - using the calculated errors to weight the least-squares fit. (e) shows the same residual plot as (c), but with the y-axis scale increased by a factor of 10 to show more detail. In both (c) and (e), the best-fitted $r^{\frac{1}{3}}$ and $r^{\frac{1}{5}}$-law profiles are shown for comparison - these are the dashed and dot-dashed lines respectively. The interpolated value for the corrected ellipticity at r_e (from the $r^{\frac{1}{4}}$-law fit) is displayed in plot (b).

Diameter $D('')$	$M(< D)$ (degraded)	$M(< D)$ (corrected)	ΔM (Steel)	ΔM (Lucey)
6.0	13.999	13.935	0.064	0.067
8.0	13.752	13.714	0.038	0.041
10.0	13.580	13.555	0.025	0.027
13.0	13.399	13.384	0.015	0.016
16.0	13.269	13.259	0.010	0.010
20.0	13.146	13.140	0.006	0.006
25.0	13.039	13.037	0.002	0.004
32.0	12.935	12.935	0.000	0.002
40.0	12.856	12.856	0.000	0.001
50.0	12.791	12.791	0.000	0.001

Table 5.2: Comparison of aperture-photometry seeing-corrections derived from a degraded model corrected with the deconvolution routine, with the seeing-corrections of Lucey *et al.* (1991) and Bower *et al.* (1992). The model was circular, with a half-light radius of 7.0″.

'kink' in the $\mu(r)$ profile at $r = 20''$. This is caused by the replacement of the observed $\mu(r)$ profile in its noisy outer regions by a profile fitted further in (to avoid noise-propagation - see section 5.4). This profile is chosen from an $r^{\frac{1}{4}}$, $r^{\frac{1}{2}}$ or exponential, depending which gives the lowest χ^2 - in this case an $r^{\frac{1}{4}}$ was chosen, producing a kink where it joins the $r^{\frac{1}{3}}$.

5.6 Seeing Corrections and Aperture Photometry

As a further validation of the surface photometry deconvolution method outlined in section 5.4, a model image was constructed ($r^{\frac{1}{4}}$-law, $r_e = 7.0''$, $\langle \mu \rangle_e = 18.8$, $\epsilon = 0.0$) and convolved with a PSF ($FWHM = 1.4''$). This image was processed with the deconvolution routine, and a 'seeing-corrected' image was built from the final corrected profiles. Aperture magnitudes (i.e. total flux *within* a circular aperture) were measured for both the degraded and corrected images. This was done using the same software ($AVIEW$) and standard aperture diameters as Lucey *et al.* (1991) and Bower *et al.* (1992). It is then a simple matter to subtract the aperture magnitudes to calculate a seeing-correction for each diameter. $AVIEW$ contains a catalogue of seeing-corrections at the standard diam-

Diameter $D('')$	$M(< D)$ (degraded)	$M(< D)$ (corrected)	ΔM (Steel)	ΔM (Lucey)
6.0	14.012	13.945	0.067	0.067
8.0	13.765	13.723	0.042	0.041
10.0	13.592	13.564	0.028	0.027
13.0	13.411	13.394	0.017	0.016
16.0	13.280	13.269	0.011	0.010
20.0	13.156	13.149	0.007	0.006
25.0	13.048	13.044	0.004	0.004
32.0	12.944	12.941	0.003	0.002
40.0	12.864	12.863	0.001	0.001
50.0	12.798	12.797	0.001	0.001

Table 5.3: The same as table 5.2, but using a flattened model galaxy to calculate the seeing-corrections ($\epsilon = 0.35$).

eters for a range of $FWHM$ and r_e (those at $r_e = 5.0''$ and $r_e = 30.0''$ are tabulated in Bower *et al.* 1992 - note that the dependence on r_e is weak). These corrections were determined by convolving a model galaxy image with the given PSF, then measuring aperture magnitudes for the image before and after convolution - the offset is thus the correction. Since the PSF used in this study is identical to that used in Lucey *et al.* (1991) (a Hankel transform), the seeing-corrections derived from the deconvolution routine can be compared directly to the catalogued values - the results of this are shown in table 5.2. The RMS difference between the two sets of corrections is tiny (0.0018 mag), demonstrating that the deconvolution routine accurately reproduces the aperture photometry characteristics of the original, unconvolved image. This exercise is repeated for the same model galaxy, but with $\epsilon = 0.35$, representing a highly flattened elliptical galaxy. The result (shown in table 5.3) proves that the dependence of aperture photometry seeing-corrections on the ellipticity is negligible.

5.7   Conclusions

This chapter has outlined the problems involved in correcting surface photometry for the effects of atmospheric seeing. An iterative deconvolution routine has been developed to correct 1D profiles from an ellipse-fitting algorithm. Using made-up model galaxies, it has been shown that iterative routine can accurately reproduce the surface brightness, ellipticity and position-angle profiles to well within the $FWHM$. The robustness was tested by deconvolving with a different $FWHM$ from that which was used to convolve the model $(\Delta FWHM = 0.1'')$, and the result was the same. Models with pointy isophotes, poor seeing and varying ellipticity were also tested, and the results were the same. Of course, with real images it is not likely to be quite so impressive - asymmetry, dust-lanes (and other structures), pixel defects and focussing problems will all contribute to degenerating the final solution. Nonetheless, it is reasonable to expect that the resultant deconvolved profiles are unaffected by seeing distortions to within perhaps $2\times FWHM$, compared to $5 - 10\times FWHM$ for uncorrected data, thus making the exercise worthwhile. Appendix C shows the deconvolved profiles (including seeing corrections) for the whole sample of 153 galaxies (208 separate images) from the INT March 1994 data-set.

The next chapter will look at the shapes of the surface brightness profiles. The fitting of several different models to the deconvolved light profiles is described, which will hopefully provide important information about the structure of early-type galaxies.

Chapter 6

Parametrising the Surface Brightness Profile

6.1 Introduction

The shapes of the surface brightness profiles of early-type galaxies are important in determining their morphology (see Chapter 1). For instance, a deviation of the $\mu(r)$ profile from a pure power-law (such as an $r^{\frac{1}{4}}$-law) can be indicative of a second photometric component, such as a disk.

In the previous chapter, a non-parametric method was described to remove the effects of atmospheric seeing from the surface brightness profile. The next step is to parametrise the profiles in order that morphological information can be obtained from the data. Each galaxy in the sample was fitted by 4 different profiles, and the best-fitting parameters retrieved, along with measurements of χ^2 and RMS to indicate the comparative goodness-of-fit of the different models. Three of the models were single power-laws ($r^{\frac{1}{3}}$-, $r^{\frac{1}{4}}$- and $r^{\frac{1}{5}}$-laws), which required only linear regression to fit to the data. The fitting of single power-laws is described in Section 6.2. The fourth profile was a sum of two power-laws (an $r^{\frac{1}{4}}$ plus an exponential), representing a two-component galaxy (i.e. an S0 or disky E). This requires a more complex χ^2 minimisation procedure, which is covered in Section 6.3. Finally, in Section 6.4, made-up 1D surface brightness profiles are used to verify the fitting techniques which are being employed.

Profile $r^{\frac{1}{m}}$	α_m	β_m
$m = 3$	1.24509	6.15678
$m = 4$	1.39295	8.32678
$m = 5$	1.50925	10.4968

Table 6.1: The constants used in the power-law equation (6.1) to define the scaling parameters (effective radius and effective surface brightness) for $m = 3, 4, 5$.

6.2 Fitting Single Power-law Profiles

Fitting a single-power law to a surface brightness profile $\mu(r)$ is a straightforward linear-regression problem. The generalised $r^{\frac{1}{m}}$-law profile (Sersic 1968) is given in Equation 6.1.

$$\mu_m(r) = \langle\mu\rangle_e + \alpha_m + \beta_m \left[\left(\frac{r}{r_e}\right)^{\frac{1}{m}} - 1\right] \tag{6.1}$$

If the constants α_m and β_m are chosen correctly, then the parameters r_e and $\langle\mu\rangle_e$ take on the physical meanings of effective (i.e. half-light) radius and effective surface brightness (i.e. mean SB within r_e). For an $r^{\frac{1}{4}}$-law, the constants can calculated analytically by integrating the power-law over all radii (a fuller mathematical description of SB laws is given in Section 1.5). For other power-laws ($m \neq 4$), the integral is more complex and numerical solutions are required. According to Caon et al. (1993), who calculated numerical solutions for a wide range of m, the constants are well approximated by the following relations:-

$$\alpha_m = 0.075(\log m)^2 + 1.1025 \log m + 0.70199 \tag{6.2}$$

$$\beta_m = 2.170m - 0.35322 \tag{6.3}$$

These are basically the Equations 5, 6 & 7 in Caon et al. (1993) rewritten in the convention used here. The constants have been changed very slightly such that the α_m and β_m calculated for an $r^{\frac{1}{4}}$-law match those calculated analytically. The above relations can now be used to find α_m and β_m for the $r^{\frac{1}{3}}$- and $r^{\frac{1}{5}}$-law profiles (see Table 6.1).

Now that the formulae have been defined for the 3 different power-laws, it is straightforward to perform a weighted linear-regression on the data:-

$$\mu_m(r) = I + Sr^{\frac{1}{m}} \tag{6.4}$$

This relation is fitted for each power-law, measuring the intercept I and slope S. Combining Equations 6.1 and 6.4, the scaling parameters can be calculated by:-

$$r_e = \left(\frac{\beta_m}{S}\right)^m, \quad \langle\mu\rangle_e = I + \beta_m - \alpha_m \tag{6.5}$$

The choice of radial range to fit the power-law is significant, and can diminish the quality of the results if chosen badly. The inner radius limit is chosen to be equal to the *FWHM* of the seeing PSF - this is about the lowest radius where the seeing-correction made to the $\mu(r)$ profile can be regarded as reliable (typically 2 or 3 pixels in this data). In certain circumstances (see Section 6.3), this inner radius limit is increased to $2 \times FWHM$. The outer limit is set to the radius where the surface brightness drops below the standard error on the sky measurement. These limits define a set of n measurements of μ and associated error σ at discrete radii r_i. These are the values used in the weighted linear regression. The goodness-of-fit for each power-law is expressed by χ^2 and RMS, determined as follows:-

$$\chi^2 = \frac{1}{n-2}\sum_{i=1}^{n}\frac{[\mu(r_i) - \mu_m(r_i)]^2}{\sigma(r_i)^2} \tag{6.6}$$

$$RMS = \sqrt{\frac{1}{n}\sum_{i=1}^{n}[\mu(r_i) - \mu_m(r_i)]^2} \tag{6.7}$$

The errors on the data-points $\sigma(r_i)$ are the original measurement errors from the ellipse-fitting program (plus a term at small r for the seeing correction). As the profiles have been smoothed by the deconvolution process, the value of χ^2 defined above does *not* have its usual statistical meaning (see Section 6.3). For the given galaxy, however, the χ^2 values for the different power-laws and the two-component model *can* be directly compared as an indication of which gives the better fit (as can the RMS values).

As with the two-component model (Section 6.3), the dominant error on the fitting procedure is not the random isophote measurement error, but the systematic sky measurement error. The errors on the r_e and $\langle\mu\rangle_e$ parameters for a given power-law can be calculated by making two further linear regressions - one with sky error added to $\mu(r)$, the other with the sky error subtracted. The error on the scaling parameters is then estimated as the RMS difference between the values measured with $\mu(r)$ perturbed by the sky error, and the measurement without any sky error (see Equation 6.14, next section).

In addition to the scaling parameters, the total magnitudes of the model are calculated for each power-law fit. Given that the total luminosity equals $2\pi\langle I\rangle_e r_e{}^2$ (where $\langle I\rangle_e$ is $\langle\mu\rangle_e$

expressed in counts), then it can easily be seen that the total magnitude can be calculated as:-

$$M_{tot} = \langle \mu \rangle_e - 5 \log r_e - 2.5 \log (2\pi) \qquad (6.8)$$

The errors on M_{tot} are calculated in the same way as the scaling parameters. In general, the better the power-law fit, the smaller the difference between the model magnitude calculated above and the non-parametric asymptotic magnitude (calculated from the aperture photometry, see Chapter 4).

6.3   Fitting a Two-component Profile

Fitting a two-component model to $\mu(r)$ is a more complicated procedure than the previous case. The problem is that the shapes of the bulge and disk profiles, usually modelled as an $r^{\frac{1}{4}}$-law and an exponential, are photometrically rather similar. Often, different models for the bulge and disk, with a range of parameter values, can combine to produce almost identical profiles. Thus, any attempt to deconvolve the two is fraught with difficulty. Many different methods have been developed in the past to overcome this - they can be grouped roughly into three general approaches:-

- **Iterative Methods (1D)**

  Kormendy (1977) used an iterative process whereby the 1D $\mu(r)$ profile was divided into two ranges - one where the bulge dominates, and the other dominated by the disk. The two ranges were identified by eye, and separated by a gap where neither component dominates. The disk range was fitted by a exponential law, which was then extrapolated to the bulge range and subtracted. An $r^{\frac{1}{4}}$-law was then fitted to the residual. This was, in turn, subtracted from the profile in the disk range, and a new exponential fitted to *this* residual. The whole process is repeated until some convergence criterion is satisfied. This method is not particularly subjective, and only works well where the disk is bright ($B/D\ ratio \lesssim 1$), as with spirals. It is less successful with the fainter disks of S0's and disky ellipticals. Related methods have been used by Burstein (1979) and Boroson (1981).

- **Simultaneous Fitting (1D)**

  An alternative to the iterative method is to solve for all the bulge and disk parame-

ters simultaneously, applying some non-linear least-squares fit algorithm to the whole radial range, between suitable limits (see, e.g. Kormendy 1977, Schombert & Bothun 1987, Baggley 1996). Schombert & Bothun (1987) use a grid search method to minimise χ^2 and retrieve the best-fitting scale-parameters for the $r^{\frac{1}{4}}$ and exponential components. They test their method on both model and real profiles, and conclude that the simple two-component model is inappropriate for most of their profiles, because the χ^2 returned is too high (even when the fit appears reasonable to the eye). This is to be expected, however, as most of their objects are spirals, which generally *are* more complex in their structure than S0's, and probably require additional photometric components. The other main problem with this type of fitting is the systematic effect due to representing a 2D system by a 1D profile. As the inclination angle increases, so does the difference between the projected ellipticities of the two components (the disk is intrinsically much flatter than the bulge). It is not clear in this case where the 1D $\mu(r)$ profile should be measured from. Schombert & Bothun (1987) used major-axis profiles, while the EFAR collaboration (Saglia *et al.* 1997, see also Baggley 1996) measure profiles from surface photometry of circular annuli. For the former method, the different ellipticities result in different 'equivalent' radii being sampled at any point along the major-axis. Similarly, with circular annuli, a range of equivalent radii will be probed in *both* components. The best method is to fit ellipses and calculate surface brightness from these ellipses, and express as a function of equivalent radii. This means that the ellipse from which the surface photometry is calculated is, at least, intermediate between the projected ellipticities of the two components. A range of radii will still be sampled, but the distortion from a perfect $r^{\frac{1}{4}}$ plus exponential law is reduced and restricted to the region where the two components are of similar brightness. This is the method used in this study, and a detailed investigation of the systematics caused by this inclination effect is given in Section 6.4.

- **2-dimensional Fitting**

A third class of fitting procedures are those which use information about the 2D distribution of light in a galaxy image to decouple the bulge and disk components. At the simplest level, differences between the major and minor axis profiles, coupled

with an assumption of the projected ellipticities of the two components, can allow a separation of the two profiles (e.g. Kent 1986). More complex methods use deviations from perfectly elliptical isophotes to detect and remove a disk component (e.g. Simien & Michard 1990, Scorza & Bender 1990). Jorgensen & Franx (1994) use an averaged Fourier coefficient c_4 coupled with an ellipticity measurement to statistically investigate bulge-disk contributions. Another approach is fit the entire 2D light distribution with a mixed bulge and disk model - solving for all the parameters required to construct such a model (e.g. Shaw & Gilmore 1990). Typically, this requires a minimum of 6 parameters - 2 scale-parameters for each component, plus a parameter defining the isophote shape (i.e. ellipticity, scale-height) of each component. Generally, fitting such a rigid model with a large number of parameters will not produce a meaningful result. Rigidity is a general problem with this class of procedures - as well as making assumptions about the $\mu(r)$ profiles, it is necessary to make assumptions about the 2D shapes of the components, which may prove to be unrealistic.

The method used here is somewhat similar to that of Schombert and Bothun (1987). The $\mu(r)$ profile is fitted simultaneously by an $r^{\frac{1}{4}}$-law plus an exponential disk. The fitting is initially performed on the deconvolved $\mu(r)$ profile with the nominal (measured) sky count I_{sky} subtracted from the counts. The range of the fit is the same as for the single power-law fits - from $r = FWHM$ to $\mu(r) = SB(\Delta Sky)$. The fitting function itself is described as follows:-

$$\mu_{model}(r) = -2.5 \log\left(10^{-0.4\mu_b(r)} + 10^{-0.4\mu_d(r)}\right) \tag{6.9}$$

$$where \quad \mu_b(r) = \langle \mu^b \rangle_e + \alpha_b + \beta_b \left[\left(\frac{r}{r^b_e}\right)^{\frac{1}{4}} - 1\right] \tag{6.10}$$

$$and \quad \mu_d(r) = \langle \mu^d \rangle_e + \alpha_d + \beta_d \left(\frac{r}{r^d_e}\right) \tag{6.11}$$

Where the constants are set as $\alpha_b = 1.39295$, $\beta_b = 8.32678$, $\alpha_d = -1.12441$ and $\beta_d = 1.82224$. With the constants defined as such, the parameters r^b_e and r^d_e represent the effective radii of the bulge and disk respectively, while $\langle \mu^b \rangle_e$ and $\langle \mu^d \rangle_e$ represent the effective surface brightnesses of the bulge and disk models respectively (the values of these constants can be calculated by integrating the profile-laws from $r = 0$ to $r = \infty$ and from $r = 0$ to $r = r_e$, where the integrated luminosity to r_e is half that to $r = \infty$). Note that these disk parameters are *not* the same as the standard parameters μ_0 and λ_D, the central surface

brightness and scale-length respectively. The half-light parameters were chosen to allow direct comparison with the bulge and single power-law parameters.

A least-squares fit is performed on the observed $\mu(r)$ profile by finding the values of the 4 model parameters which minimise χ^2. The profile consists of n data points at radii r_i (where $i = 1, ..., n$), and the random error on each data point $\mu(r_i)$ is $\sigma(r_i)$. The normalised or reduced χ^2 is then defined as:-

$$\chi^2 = \frac{1}{n-4} \sum_{i=1}^{n} \frac{[\mu(r_i) - \mu_{model}(r_i)]^2}{\sigma(r_i)^2} \tag{6.12}$$

As with the single power-law fitting, the errors on the data-points $\sigma(r_i)$ are random errors associated with the photometry (from the ellipse-fitting routine), and not systematic errors (i.e. zero-point error, sky background error). The seeing-correction error (estimated as one-fifth the seeing-correction) on the deconvolved profiles *has* been included in $\sigma(r_i)$, by adding in quadrature. Technically, this is a systemic error, but it effects only the central few points and allows a greater flexibility of fitting in this area. Also, the profile itself has been smoothed by the deconvolution process. This all means that the χ^2 value does not quite represent a normalised χ^2 - in fact it will typically be underestimated by some factor. The χ^2 is still, however, a valid estimator of goodness-of-fit and can be used to find a reasonable least-squares fit to the data. The minimum χ^2 is also directly comparable to those calculated from fitting single power-laws to the data.

The χ^2 is minimised by searching a grid of the 4 parameters. Although time-consuming, this is more robust than most minimisation algorithms (such as Newton-type methods) which can fall down the wrong minima. As mentioned above, the $r^{\frac{1}{4}}$ and exponential functions are such that different sets of parameter values can combine to produce models which are near-identical. In other words, there are many *local* χ^2 minima, which must be rejected in order to find the *global* minimum. The initial grid search covers a large volume of parameter-space, including all reasonable models, but at a large step size between neighbouring parameter values. The limits and step sizes for each parameter are given below:-

$$A - 2 < \log r^b_e < A + 2 \quad (step\ 0.2)$$
$$B - 2 < \langle \mu^b \rangle_e < B + 2 \quad (step\ 0.2)$$
$$C - 2 < \log r^d_e < C + 2 \quad (step\ 0.2) \tag{6.13}$$
$$D - 4 < \langle \mu^d \rangle_e < D + 4 \quad (step\ 0.4)$$

The grid centre-points for the bulge parameters - A and B - were found by fitting a $r^{\frac{1}{4}}$-law profile from the seeing radius to the half-light radius (as measured from the whole-profile $r^{\frac{1}{4}}$-law fit). The maximum allowed centre-point for the bulge effective radius is $20''$. If the value of the centre-point is greater than this, the $r^{\frac{1}{4}}$ fit is probably suspect and the centre-point is reset to $20''$ (the bulge surface brightness centre-point is also adjusted to conserve the magnitude). The disk effective radius centre-point C is always fixed at $\log 20''$ - giving a search range between $0.2''$ and $2000''$. The disk surface brightness is often fainter than the bulge, so the grid centre-point D was set to equal $B + 1$ rounded to the nearest unit (the search area was also widened to cover 8 magnitudes). In total, 194481 different parameter combinations are selected in the first grid search. If this initial search has produced a high value for minimum χ^2 (> 100) or low disk effective radius ($< 1''$), it is likely that the grid was too coarse, and the region of the global minimum has been skipped over. In this event, the grid search is repeated, with the same number of parameter combinations, but reducing the range and step sizes by a half. The centre-points are moved from the initial centre-points by half a step size to ensure that the parameter combinations are all independent. Note that a very low *bulge* effective radius ($< 0.05''$) is disallowed in *all* grid-searches - such values can sometimes produce a local minimum (especially for disky systems), but cannot be physically genuine. If a grid-search includes these values, they are ignored in the search for a minimum χ^2.

When the minimum χ^2 is found from the above grid search, a series of more detailed searches are undertaken in progressively smaller regions of parameter-space for an even better fit. These are summarised in Table 6.2. At each level, the centre-points of the grid are set to the minimum χ^2 values from the previous search. Note the search range for each parameter overlaps by some margin the nearest sampled points from the previous grid-search, in case the minimum reached was not a global one. If, on any grid search, the minimum χ^2 occurs at (or near) the boundary of one of the parameter ranges, this may imply that the previous minimum was local, and the actual minimum is outwith the area of the grid search. The minimum allowed distance from the range boundary is one step size for grid volumes 3 and 6, two step sizes for volume 5 and three step sizes for volume 4 (see Table 6.2). In this case, the grid search is repeated with the same volume of parameter-space, but with the centre-points moved to new values. The new value for each parameter centre-point is calculated as the minimum χ^2 value plus or minus the maximum

Grid #	Range W	Step-Size ΔW	# of Points n	Max # of Steps W_{max}	*Origin of Centre-Point Values*
1	± 2	0.2	194481	W	Initial guess (see text)
(2)	± 1	0.1	194481	W	(As 1, but moved by $\frac{1}{2}\Delta W$)
3(a)	± 0.24	0.02	390625	$W - \Delta W$	From minimum, grid 1 (or 2)*
3(b)	± 0.16	0.02	83521	$W - \Delta W$	(from zero sky-error solution)*
4	± 0.048	0.008	28561	$W - 3\Delta W$	From minimum, grid 3(a) or (b)*
5	± 0.0096	0.0016	28561	$W - 2\Delta W$	From minimum, grid 4*
6	± 0.00512	0.00064	83521	$W - \Delta W$	From minimum, grid 5*

Table 6.2: Table showing the different 'levels' in the grid-search minimisation algorithm. The first column gives the level number. Grid 2 is only searched if grid 1 has not found a satisfactory minimum (see text). Grid 3(a) is executed in the principal (zero sky-error) minimisation, whilst grid 3(b) is the starting point for the two minimisations (with $\pm$ sky-error) used to calculate the errors on the profile fits. Grid-levels 4, 5 and 6 are executed in all three minimisations. The second column gives the range searched for each parameter from the chosen 'centre-point' - the units of W are equal to $\log r^b{}_e$, $\langle \mu^b \rangle_e$ and $\log r^d{}_e$, but the range of $\langle \mu^d \rangle_e$ is $\pm 2W$. The spaces between the sampled parameter values are given in the third column. Given that there are 4 parameters, the number of parameter combinations sampled is given by $n = (1 + 2W/\Delta W)^4$ - this is displayed in the fourth column. The next column shows W_{max} - the maximum number of steps which the solution is allowed to be displaced from the centre-point (for each parameter). If the minimised value of any parameter exceeds W_{max} (which can't happen for grids 1 and 2) then the search is repeated at that grid-level (*see text for explanation of how the centre-points are chosen in this case*). The final column explains how the centre-points are chosen for each *new* grid-level.

allowed distance from the centre-point. Thus the old minimum remains within the volume of the new grid search. This shift in parameter-space is allowed up to a maximum of 13 times per level - the routine is then forced to set a smaller grid volume, unless it is already on the smallest grid volume, in which case the minimum found is accepted.

If the grid search has succeeded in finding the global minimum, then given the step size of the final search volume, the minimizing parameters are determined to an accuracy of ± 0.0003 mag in $\langle \mu^b \rangle_e$, ± 0.0006 mag in $\langle \mu^d \rangle_e$, and less than $\pm 0.1\%$ in r^b_e and r^d_e. This is, of course, considerably finer than the standard errors on the fitted parameters (see below). However, there is a small possibly that despite the rigorous grid search, the true minimum has not been descended upon. As an insurance, therefore, a quasi-Newton algorithm is used to minimise χ^2. The search bounds for this algorithm are set to ± 0.4 for $\log r^b_e$, $\langle \mu^b \rangle_e$ and $\log r^d_e$, and ± 0.8 for $\langle \mu^d \rangle_e$ - using the grid-search minima as the centre-point of the volume defined by the bounds. The starting-point for the algorithm is set to the grid-search minima *plus* a random displacement (the maximum magnitude of which is ± 0.1 for $\log r^b_e$, $\langle \mu^b \rangle_e$ and $\log r^d_e$, and ± 0.2 for $\langle \mu^d \rangle_e$). This algorithm is taken from the NAG Fortran library (routine number $E04JAF$). The algorithm will find a minimum χ^2 at some point in the parameter-space. If the value of this χ^2 is less than the grid-search minimum χ^2, then these minimised parameters will be chosen as final parameter solution rather than those found from the grid-search. In practise, this rarely happens, which indicates the strength of the grid-search method. When the final parameter solution has been decided, the RMS difference between data and model (Equation 6.7) is also calculated, in addition to minimum χ^2, for comparison purposes.

If the value of the disk effective radius r^d_e resulting from this initial minimisation process appears to be small relative to the bulge and the seeing $FWHM$, this may indicate a larger systematic error at low radius (from the seeing deconvolution) than has been accounted for by the errors $\sigma(r_i)$ on the data-points $\mu(r_i)$. Alternatively, a small exponential disk may well be a physically genuine feature of the galaxy core. As an attempt to discriminate, the initial minimisation is repeated using $r = 2 \times FWHM$ as the inner radius cutoff, thus masking the area most likely to be affected by systematic errors. The disk effective radius is regarded as too small if r^d_e is smaller than either 0.5 times the bulge effective radius r^b_e or the $FWHM$ of the seeing PSF. Additionally, if r^d_e is smaller than *both* $2 \times FWHM$ *and* $1.5 \times r^b_e$, then the disk radius is also flagged as small. These limits are sufficiently

liberal enough to ensure that all ambiguous two-component fits are double-checked. If the new fit produces either an extended disk ($r^d_e > 1.5r_{be}$) or a 'null' disk ($r^d_e < 0.5''$ or disk luminosity less than 5% of total, see below), then the original fit is replaced by the new fit. Otherwise, it is deemed that the fit has not substantially changed, and therefore the original fit is acceptable.

Of course, it is very important to get an estimate for the errors on the minimised parameters. If the individual data-points were only affected by random (Gaussian) errors, and χ^2 was normalised, then the errors could be determined from the shape of the χ^2 minimum. However, this is not the case, as mentioned above. The data-points are affected by systematic errors - in particular the zero-point error and sky measurement error. The zero-point error (i.e. the total uncertainty when converting counts into magnitudes) will perturb all the points by an equal amount, and will thus not affect the fit - only changing the two surface brightness parameters by the same (very small) increment. However, the sky measurement error changes the shape of the $\mu(r)$ profile significantly, thus perturbing all 4 fitted parameters by various amounts - especially the disk parameters. It can safely be assumed that this is the dominant error in fitting a two-component law to a $\mu(r)$ profile, and *not* the random errors. In order to estimate the size of these errors on the fitted parameters, the whole fitting process is repeated twice again - first with the sky measurement 1σ error added to the sky background, and then with it subtracted. In these two minimisations, the starting points are taken from the first minimisation (i.e. *without* sky error), the first two grid-searches (covering a huge volume of parameter-space) are omitted, and the third grid-search is reduced in volume (see volume number 3(b) in Table 6.2). Note that the inner radius-limit is same as that for the accepted first minimisation (i.e. $FWHM$ or $2FWHM$). If a given parameter P is measured as P^0 with no sky error, P^+ with sky error added, and P^- with sky error subtracted, then the error ΔP on P is estimated as:-

$$\Delta P = \sqrt{\frac{(P^+ - P^0)^2 + (P^- - P^0)^2}{2}} \qquad (6.14)$$

From the best-fitting parameters, it is possible to calculate the total magnitude of each component individually (using Equation 6.8), in addition to the whole object. The errors on these magnitudes are estimated using the same method as for the scale-parameters above.

It is common to find the term *Bulge-to-Disk Ratio* used to describe the relative importance of the two photometric components in spiral galaxies. For early-type galaxies, where

the disk component can be faint or non-existent, we normally use the inverse (Disk-to-Bulge Ratio) to avoid large numbers. This is easily estimated from the magnitudes of the two fitted components:-

$$\frac{D}{B} = 10^{-0.4(M_{disk} - M_{bulge})} \tag{6.15}$$

Additionally, it is sometimes useful to express the bulge or disk luminosity as a fraction of the total light. This has the advantage of giving us a number in the range 0 to 1. The bulge and disk fractions are defined in this work as follows:-

$$\frac{B}{T} = 10^{-0.4(M_{bulge} - M_{B+D})}, \quad \frac{D}{T} = 10^{-0.4(M_{disk} - M_{B+D})} \tag{6.16}$$

Typically B/T is in the range 0.5 to 1.0 for early-type galaxies ($D/T \sim 0.0 - 0.5$). The total model magnitude M_{B+D} is calculated by adding the luminosities of the fitted bulge and disk components - note that this may be slightly different from the non-parametric asymptotic magnitude M_{tot} (calculated from the aperture photometry, see Chapter 4), depending on the quality of the fit. By calculating the magnitudes and luminosity fractions with the sky set to *sky plus error* and *sky minus error*, it is possible to use Equation 6.14 to estimate the standard errors on the bulge and disk magnitudes, and therefore, the luminosity fractions.

The end product of the two-component profile fit must be consistent with the sensitivity of the deconvolution and be a physically reasonable model. In order to ensure this, limits are adopted on the detection of each component. For the disk component, these limits are outlined below:-

- **D/B < 0.0526.** Equivalent to D/T less than 5%. All disks measured in this range are too faint to be regarded as a reliable detection and are thus rejected.

- **0.0526 < D/B < 0.15.** These disks are still faint, but acceptable if the detection is greater than 1.5σ (i.e. $D/B > 1.5\Delta D/B$), and the disks are of a reasonable size. The size criterion is that r^d_e is greater than both $0.5''$ (due to pixel resolution) and $r^b_e/3$ (to ensure detection above the central bulge component). This is not to say that disks this small do not physically exist, only that they are outside the range of sensitivity of the method used here.

- **0.15 < D/B < 0.5.** The disks are accepted if they meet only the radius criterion above, regardless of the error on D/B.

- **D/B > 0.5**. Disks this bright are accepted regardless of their radius or any other property.

If the disk component is rejected, then the bulge parameters are replaced by the single power-law $r^{\frac{1}{4}}$ parameters and no disk parameters are returned. The disk-bulge ratio D/B is set to 0 ($D/T = 0$, $B/T = 1$) - the error on D/B now becomes an upper limit and is taken as the measured value of D/B with no sky error (see Table A.2 in Appendix A). Fortunately, very few galaxies in the Coma/Abell 1367 data-set are actually affected by the disk-detection limit - only 13 out of 153 have no detectable disk. As late-type galaxies are also included in the sample, it is also necessary to place limits on the detection of the $r^{\frac{1}{4}}$ or bulge component. These limits are listed below:-

- **D/B > 19.0**. Equivalent to B/T less than 5%. All bulges measured in this range are too faint to be regarded as a reliable detection and are thus rejected.

- **19.0 > D/B > 6.666**. These bulges are still faint, but acceptable if the detection is greater than 1.5σ (i.e. $B/D > 1.5\Delta B/D$), and the bulge are of a reasonable size ($r^b_e > 0.5''$ due to pixel resolution) and surface brightness ($\langle\mu\rangle^b_e < 25\,\text{mag}$ to ensure detection above the disk component).

- **D/B < 6.666**. Bulges this bright are accepted, provided they meet the radius and surface brightness criteria defined above.

If the bulge component is rejected, then the disk parameters are replaced by the single power-law (exponential) parameters and no bulge parameters are returned. The disk-bulge ratio D/B is set to ∞ ($D/T = 1$, $B/T = 0$). Once again, a glance at Table A.2 in Appendix A confirms that very few galaxies in the Coma/Abell 1367 data-set are actually affected by the bulge-detection limit - only 10 out of 153 have no detectable bulge (of which 8 are late-type galaxies and 2 are unclassified).

6.4 Testing the Profile Fitting

In order to demonstrate the reliability of the above methods, it is necessary to experiment with made-up models and profiles, whose parametric forms are precisely known. In the first set of examples, six 1D $\mu(r)$ profiles are made-up, using the four different parametric forms

described above. Three of the profiles are calculated from single power-laws (one each from $r^{\frac{1}{3}}$, $r^{\frac{1}{4}}$ and $r^{\frac{1}{5}}$), with scale-parameters typical of Coma E galaxies (in fact, $\langle\mu\rangle_e$ and r_e are approximately set to the non-parametric values measured for NGC 4908). The remaining three profiles are combined $r^{\frac{1}{4}}$ bulge and exponential disk models, with parameters chosen to give a range in bulge-to-disk ratio - the disk fractions are 8% ($\sim$ disky E), 30% ($\sim$ S0) and 65% ($\sim$ S0/a). All six profiles have Gaussian errors added to the individual data-points which are typical in magnitude to those of real measured profiles (although the errors on the *real* profiles are actually smaller, because of the smoothing from the deconvolution algorithm).

The six model profiles are put through the same procedure as the real galaxies - the results are shown in Figures 6.1 to 6.6. Plot (a) in each figure shows the best-fitting $r^{\frac{1}{4}}$ *plus* exponential law, plotted over the 'data'. The individual components are plotted as dashed lines, while the sum is a solid line. Note that the abscissa is $r^{\frac{1}{4}}$ - so a pure-$r^{\frac{1}{4}}$ surface brightness profile is represented by a straight line, while an exponential is a convex curve. If the fitting procedure returns a disk with an effective radius of less than 0.5″, or with a total luminosity less than 1% of the whole galaxy, it is assumed that no disk has been detected. In this event, the bulge parameters are set equal to those returned by a pure $r^{\frac{1}{4}}$-law fit, and no disk parameters are returned (Figure 6.1 shows an example of this). These are less stringent conditions for non-detection of disks than outlined in Section 6.3, but it was deemed important to observe exactly what was fitted for each of the model profiles. The limits of the fit - defined by $r = FWHM$ and $\mu = SB(\Delta Sky)$ - are shown by dotted lines. The random errors on the data are shown by error bars (within $SB(\Delta Sky)$), whilst the systemic shift caused by a 1σ sky-error is shown by the crosses. Plot (b) uses the same key, but displays the residual between the 'data' and the best-fit combined law. Plot (c) shows the best-fit pure $r^{\frac{1}{4}}$-law (*straight* solid line) overlying the 'data', with the best fitting $r^{\frac{1}{3}}$ (dot-dashed line) and $r^{\frac{1}{5}}$ (dotted line) curves also plotted. Plot (d) shows the residual between the 'data' and $r^{\frac{1}{4}}$-law - and is thus directly comparable with plot (b) above. The difference between the best-fitting $r^{\frac{1}{3}}$ & $r^{\frac{1}{5}}$ curves and the best-fit $r^{\frac{1}{4}}$ are also shown, using the same key as plot (c). The table beneath the plots shows the best-fitting parameters for each profile, plus sky subtraction errors, total magnitudes, RMS and χ^2.

The results for the first three models show clearly how well this procedure identifies the best power-law profile. For each model, the appropriate profile is fitted to a χ^2 of
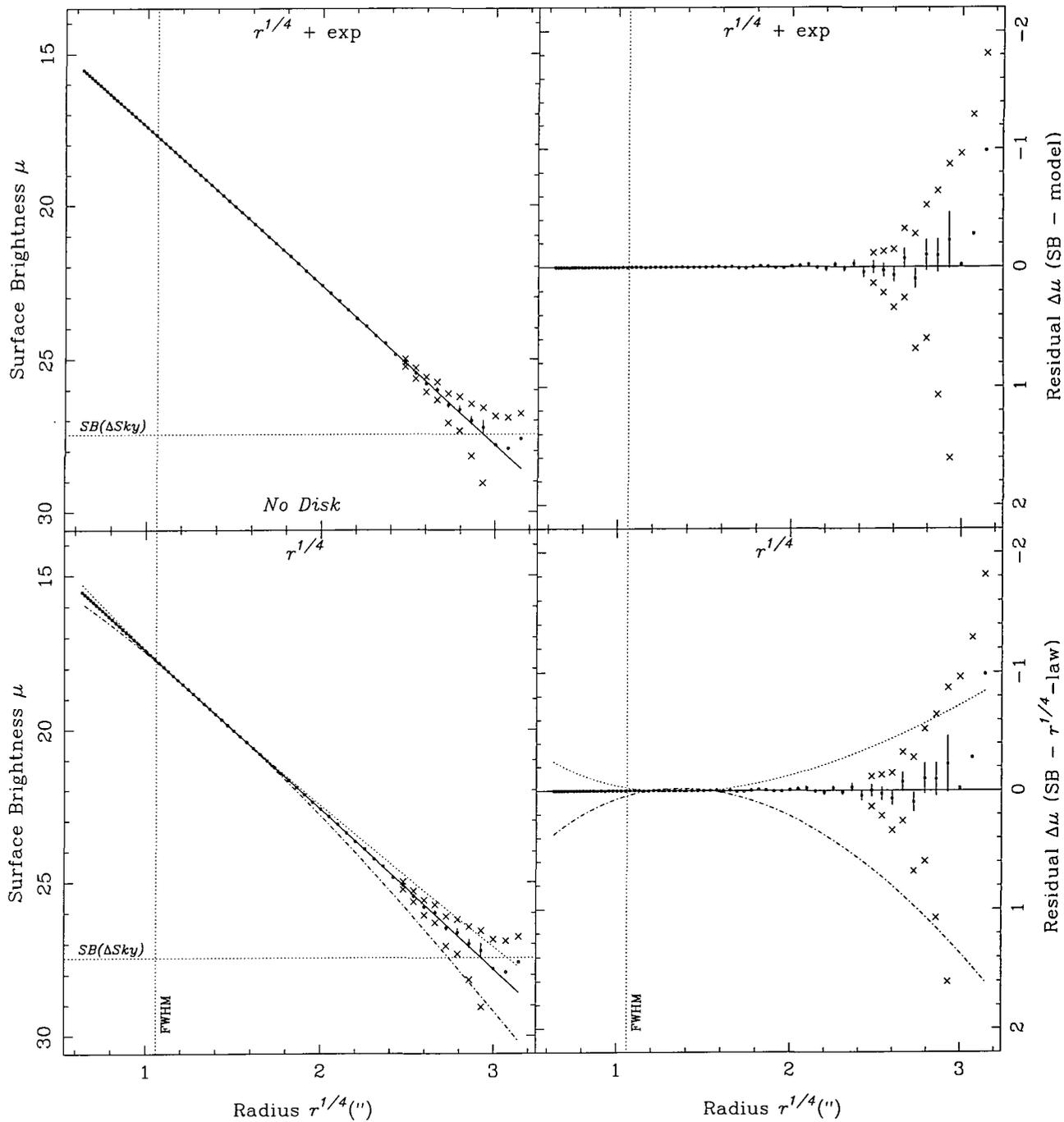
Fitting Law	r_e	Δr_e	$<\mu>_e$	$\Delta<\mu>_e$	M_{tot}	ΔM_{tot}	RMS	χ^2
$r^{1/4}$ + exp	– – – –	– – – –	– – – –	– – – –	13.067	0.004	0.047	1.073
(bulge)	6.532	0.041	19.138	0.01	13.067	0.004	– – – –	– – – –
(disk)	N	O	– – –	D	I	S	K	– – –
$r^{1/3}$	5.346	0.047	18.874	0.013	13.238	0.006	0.477	256.91
$r^{1/4}$	6.532	0.041	19.138	0.01	13.067	0.004	0.047	1.073
$r^{1/5}$	8.075	0.037	19.446	0.007	12.915	0.003	0.235	84.485

Fitting Range:– 1.34" to 73.56"   Bulge Fraction = 1 ± 0

Figure 6.1: Parametric fits to a perfect $r^{\frac{1}{4}}$-law 1D $\mu(r)$ profile. See Page 113 for key.
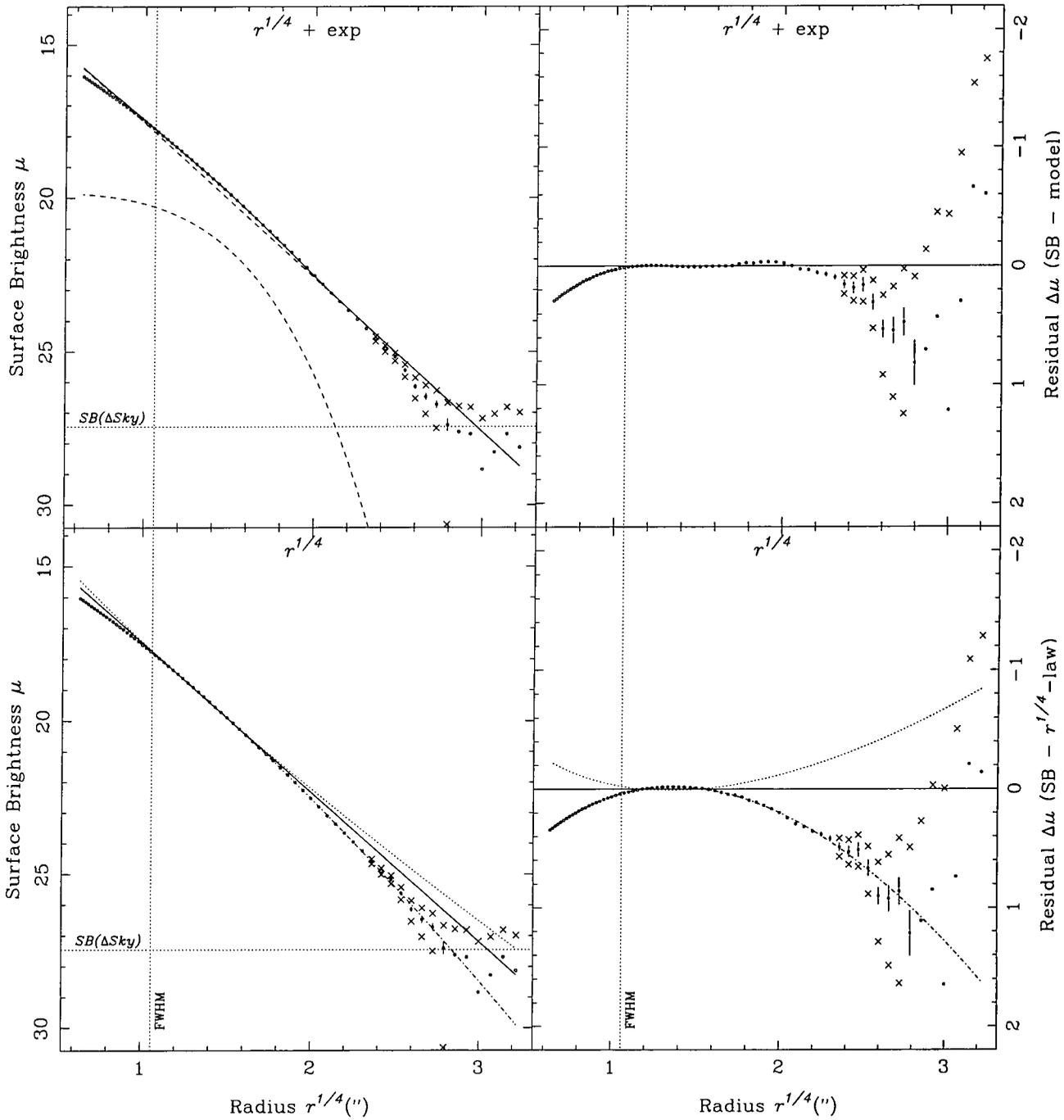
Fitting Law	r_e	Δr_e	$<\mu>_e$	$\Delta<\mu>_e$	M_{tot}	ΔM_{tot}	RMS	χ^2
$r^{1/4}$ + exp	----	----	----	----	12.997	0.011	0.202	16.152
(bulge)	7.569	0.157	19.501	0.025	13.11	0.019	----	----
(disk)	4.894	0.121	20.946	0.013	15.502	0.066	----	----
$r^{1/3}$	6.537	0.031	19.14	0.007	13.068	0.004	0.049	1.043
$r^{1/4}$	8.543	0.022	19.519	0.004	12.865	0.002	0.38	235.736
$r^{1/5}$	11.284	0.008	19.939	0.001	12.681	0.001	0.577	585.853

Fitting Range:– 1.34" to 60.79"   Bulge Fraction = 0.901 ± 0.018

Figure 6.2: Parametric fits to a perfect $r^{\frac{1}{3}}$-law 1D $\mu(r)$ profile. See Page 113 for key.
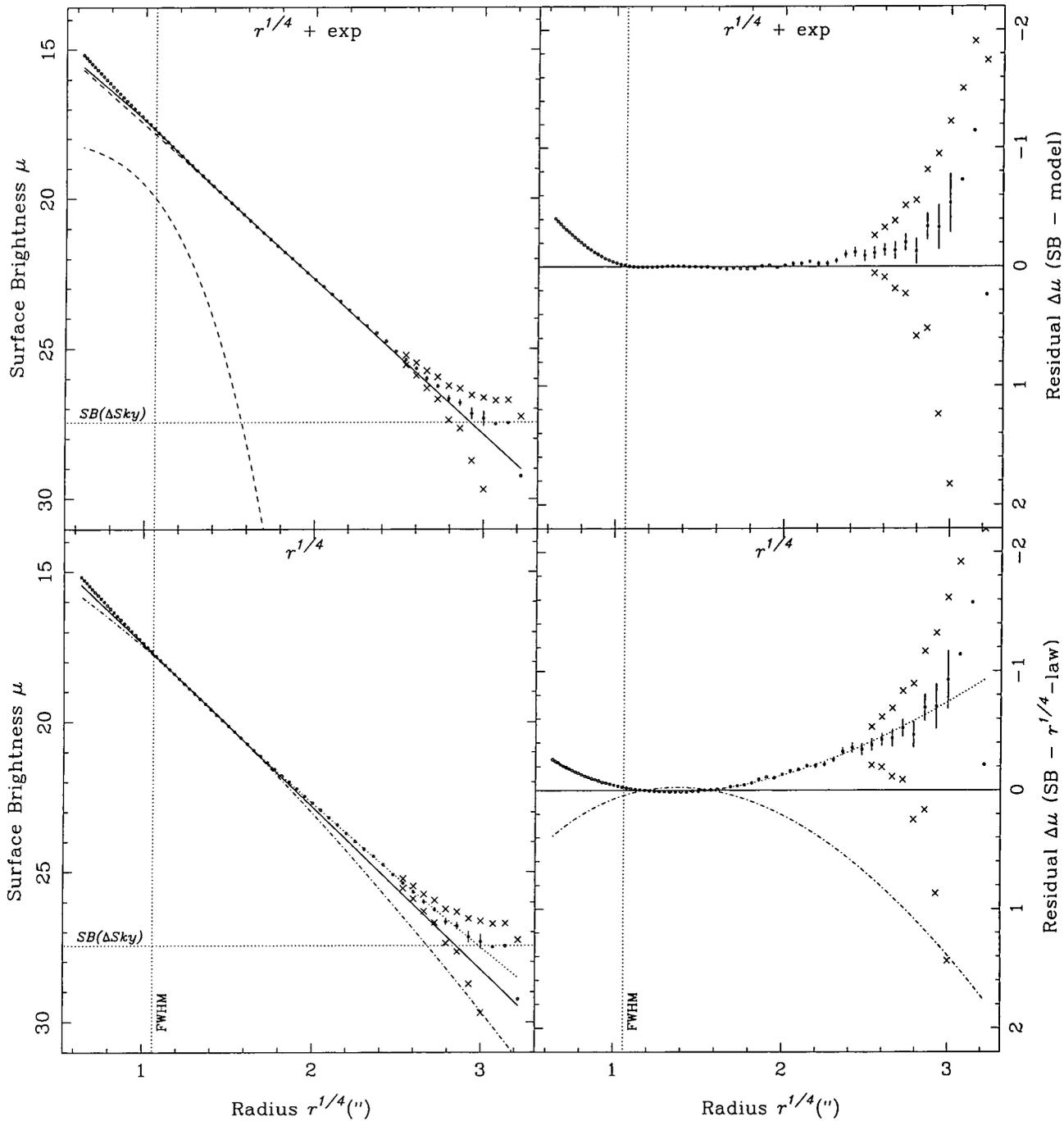
Fitting Law	r_e	Δr_e	$<\mu>_e$	$\Delta<\mu>_e$	M_{tot}	ΔM_{tot}	RMS	χ^2
$r^{1/4}$ + exp	----	----	----	----	13.133	0.015	0.123	6.098
(bulge)	6.794	0.313	19.327	0.09	13.171	0.008	----	----
(disk)	1.172	0.06	19.148	0.076	16.808	0.186	----	----
$r^{1/3}$	4.77	0.063	18.736	0.021	13.348	0.007	0.783	612.768
$r^{1/4}$	5.551	0.059	18.917	0.017	13.2	0.006	0.283	84.247
$r^{1/5}$	6.543	0.057	19.142	0.014	13.068	0.005	0.037	0.736

Fitting Range:– 1.34" to 80.91"   Bulge Fraction = 0.966 ± 0.015

Figure 6.3: Parametric fits to a perfect $r^{\frac{1}{5}}$-law 1D $\mu(r)$ profile. See Page 113 for key.

approximately unity, whilst χ^2 for the other profiles is of the order of 100 or greater. For the first model (Figure 6.1) the input profile is a pure $r^{\frac{1}{4}}$. As expected, the combined $r^{\frac{1}{4}}$ and exponential profile fitting fails to find a significant disk. The next two models (Figures 6.2 and 6.3) are constructed using pure $r^{\frac{1}{3}}$ and $r^{\frac{1}{5}}$ profiles respectively. In these cases, the two-component fit *does* attempt to fit an exponential disk to the deviations from the $r^{\frac{1}{4}}$-law. The disk luminosities are 10% and 3% of the total luminosities for the $r^{\frac{1}{3}}$ and $r^{\frac{1}{5}}$ models respectively (note that a disk fraction of 3% would be below the detection limit for disks using the criterion applied to the real data). The χ^2 values for these fits, however, are considerably greater than those for a pure power-law fit - although it is important to consider that such distinctions may not be so significant in real data, especially if the bulge and disk profiles diverge significantly from the empirical $r^{\frac{1}{4}}$ and exponential laws.

The next three model profiles are built by adding a 1D $r^{\frac{1}{4}}$-law profile with an exponential law. The $r^{\frac{1}{4}}$ parameter values are typical of those found for Coma galaxies. To these profiles are added three disks of very different luminosities. The results of the profile-fitting is shown in Figures 6.4, 6.5 and 6.6. It can instantly be seen by glancing at residual plots (b) and (d), that the two-component fit is considerably better than the single power-law fits, and this is borne out by the χ^2 values. The obvious test of whether the two-component fit has found the correct minimum is to compare the input and output values. This is shown in Table 6.3, which also compares the input and output parameters for the three single power-law models.

It can readily be observed from Table 6.3 that the measured parameters match very closely the parameters used to construct the 1D profiles. In fact, the differences between the input and output parameters, which are due to random errors and inadequacies in the profile fitting, are much smaller than the quoted sky subtraction errors. This justifies the earlier statement that sky uncertainty is dominant source of error in the fitting of functions to surface brightness profiles. Although a typical sky error ($\sim$ 0.2%) was used in the calculations here, none was added to actual background - hence the close match between input and output parameters.
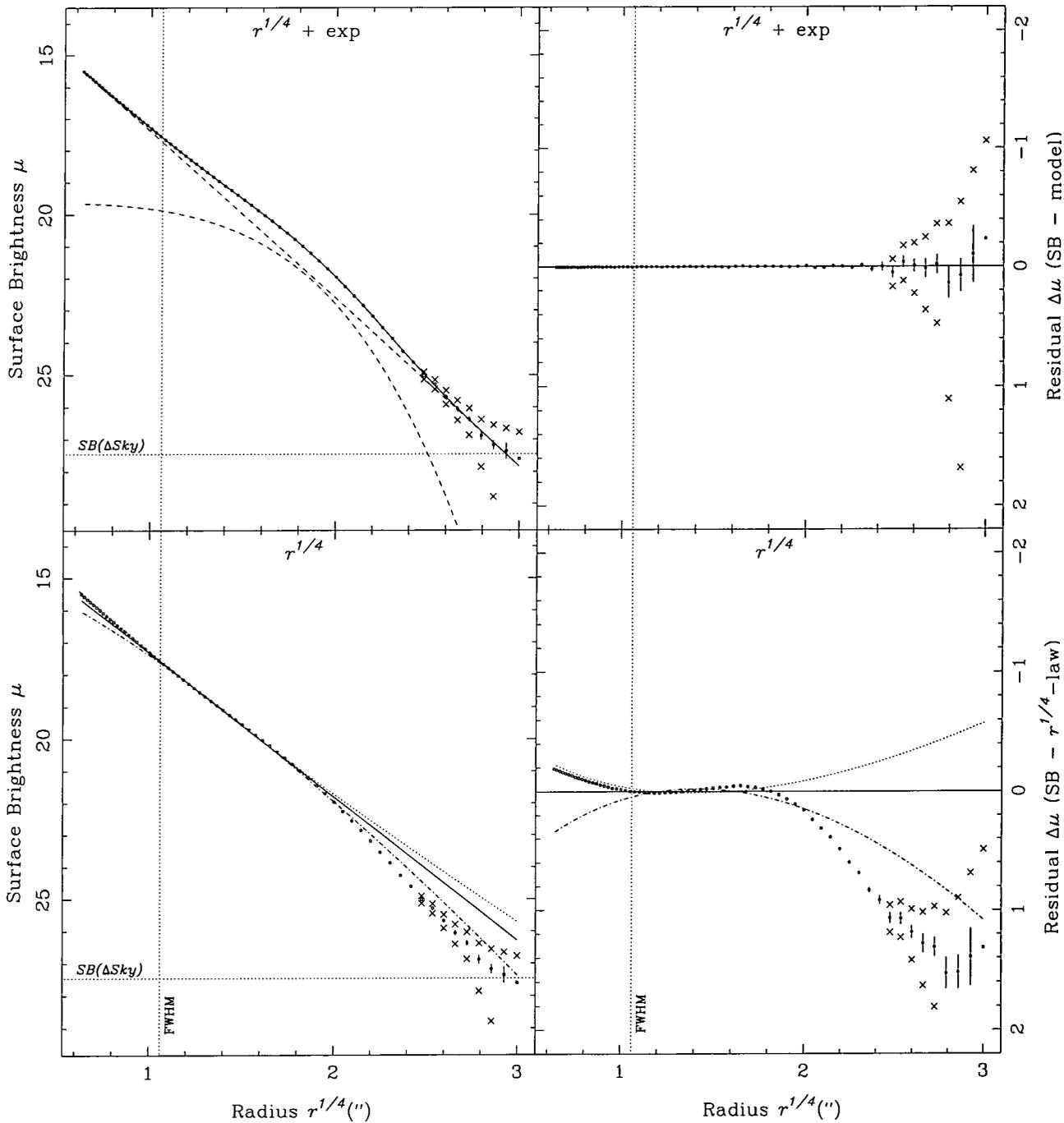
Fitting Law	r_e	Δr_e	$<\mu>_e$	$\Delta<\mu>_e$	M_{tot}	ΔM_{tot}	RMS	χ^2
$r^{1/4} + exp$	————	————	————	————	12.672	0.02	0.031	0.862
(bulge)	6.51	0.549	19.134	0.101	13.071	0.074	————	————
(disk)	9.12	0.075	20.749	0.099	13.954	0.113	————	————
$r^{1/3}$	8.648	0.027	19.304	0.004	12.624	0.003	0.276	255.22
$r^{1/4}$	11.885	0.015	19.768	0.002	12.398	0.001	0.621	481.944
$r^{1/5}$	16.506	0.058	20.271	0.006	12.187	0.002	0.813	914.939

Fitting Range:– 1.34" to 73.56"   Bulge Fraction = 0.692 ± 0.049

Figure 6.4: Parametric fits to a perfect two-component $r^{\frac{1}{4}} + exp$ 1D $\mu(r)$ profile, representing a "typical" S0 with a medium brightness disk (30% of total). See Page 113 for key.
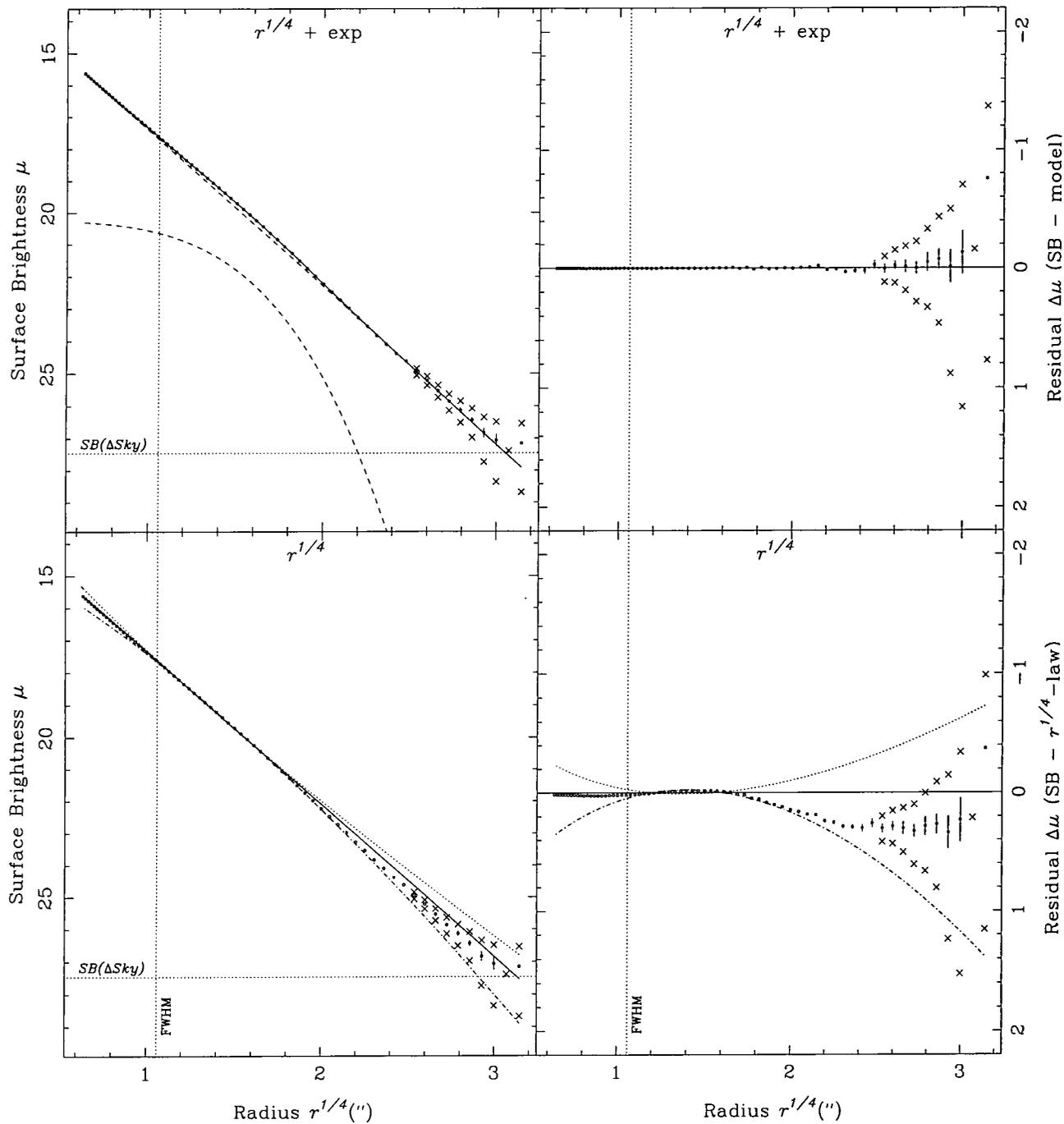
Fitting Law	r_e	Δr_e	$<\mu>_e$	$\Delta<\mu>_e$	M_{tot}	ΔM_{tot}	RMS	χ^2
$r^{1/4}$ + exp	– – – –	– – – –	– – – –	– – – –	12.749	0.016	0.026	0.992
(bulge)	8.388	0.256	19.452	0.036	12.838	0.03	– – – –	– – – –
(disk)	5.964	0.275	21.373	0.042	15.5	0.142	– – – –	– – – –
$r^{1/3}$	7.208	0.054	19.129	0.011	12.844	0.005	0.27	58.107
$r^{1/4}$	9.43	0.033	19.513	0.005	12.645	0.003	0.171	153.206
$r^{1/5}$	12.487	0.013	19.939	0.001	12.461	0.001	0.395	516.551

Fitting Range:– 1.34" to 80.91"   Bulge Fraction = 0.921 ± 0.029

Figure 6.5: Parametric fits to a perfect two-component $r^{\frac{1}{4}} + exp$ 1D $\mu(r)$ profile, representing a "typical" disky E with a faint disk (8% of total). See Page 113 for key.
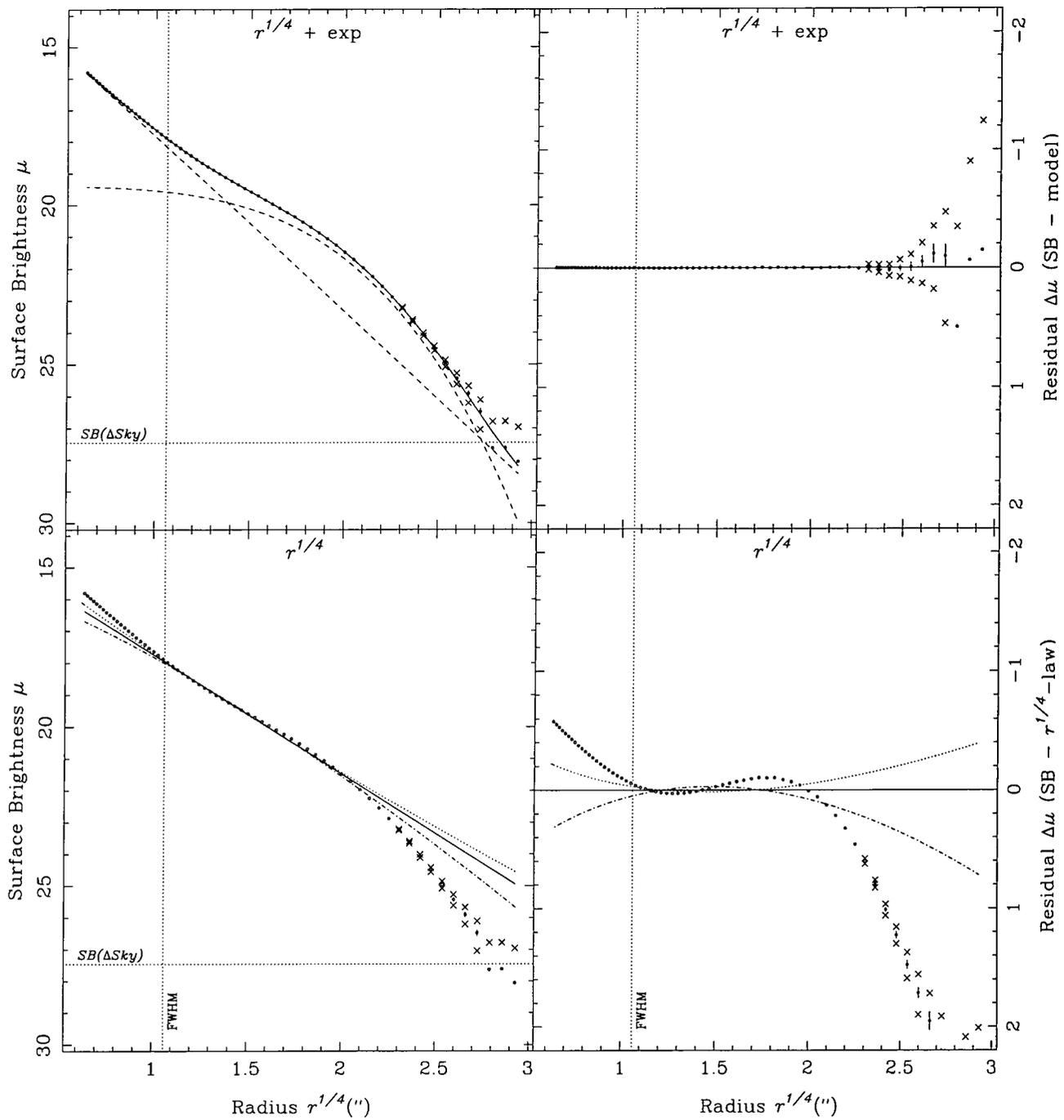
Fitting Law	r_e	Δr_e	$<\mu>_e$	$\Delta<\mu>_e$	M_{tot}	ΔM_{tot}	RMS	χ^2
$r^{1/4} + exp$	----	----	----	----	12.539	0.009	0.026	0.839
(bulge)	5.254	0.232	19.272	0.058	13.674	0.036	----	----
(disk)	12.705	0.127	20.524	0.028	13.009	0.006	----	----
$r^{1/3}$	15.582	0.033	20.255	0.002	12.296	0.003	0.499	1175.911
$r^{1/4}$	24.51	0.034	20.925	0.001	11.983	0.002	0.674	1125.692
$r^{1/5}$	39.061	0.032	21.632	0.001	11.678	0.001	0.774	1439.574

Fitting Range:– 1.34" to 55.26"   Bulge Fraction = 0.352 ± 0.012

Figure 6.6: Parametric fits to a perfect two-component $r^{\frac{1}{4}} + exp$ 1D $\mu(r)$ profile, representing a "typical" S0/a or Sa with a bright disk (65% of total). See Page 113 for key.

Mod #	Law	In r_e	Out r_e	Error Δr_e	In $\langle\mu\rangle_e$	Out $\langle\mu\rangle_e$	Error $\Delta\langle\mu\rangle_e$	In $\frac{B}{T}$	Out $\frac{B}{T}$	Error $\Delta\frac{B}{T}$
1	$r^{\frac{1}{4}}$	6.541	6.532	0.041	19.141	19.138	0.010	1.000	1.000	0.000
2	$r^{\frac{1}{3}}$	6.541	6.537	0.031	19.141	19.140	0.007	—	0.901	0.018
3	$r^{\frac{1}{5}}$	6.541	6.543	0.057	19.141	19.142	0.014	—	0.966	0.015
4	$r^{\frac{1}{4}}$	6.541	6.510	0.549	19.141	19.134	0.101	0.695	0.692	0.049
	exp	9.100	9.120	0.075	20.750	20.749	0.099			
5	$r^{\frac{1}{4}}$	8.362	8.388	0.256	19.450	19.452	0.036	0.919	0.921	0.029
	exp	5.950	5.964	0.275	21.350	21.373	0.042			
6	$r^{\frac{1}{4}}$	5.210	5.254	0.232	19.260	19.272	0.058	0.350	0.352	0.012
	exp	12.700	12.705	0.127	20.520	20.524	0.028			

Table 6.3: Comparison of the input and output parameters for the six experimental models. For the single power-law models (1 to 3), the input parameters are compared only with the output parameters of the *appropriate* power-law fit. Effective radii are expressed in arc-sec. $\frac{B}{T}$ is the bulge-to-total luminosity ratio.

6.5 Inclination Effects

A further experiment was conducted to test the effect of inclination on the 1D profile of a combined $r^{\frac{1}{4}}$ bulge and exponential disk galaxy. As was mentioned in Section 6.3, the shape of the 1D $\mu(r)$ profile, as measured from ellipse-fitting, departs from a perfect two-component model (Equations 6.9, 6.10 and 6.11) as inclination increases. This is because, as the galaxy becomes more edge-on, the projected ellipticity of the flattened disk becomes much greater than that of the intrinsically much less flattened bulge component. For an oblate ellipsoid, the relationship between projected ellipticity ϵ_i, intrinsic ellipticity ϵ_0 and inclination angle i is given by:-

$$\epsilon_i = 1 - \sqrt{\cos^2 i + (1 - \epsilon_0)^2 \sin^2 i} \qquad (6.17)$$

Thus the ellipticity of given fitted ellipse will be intermediate between the different projected ellipticities of the two components. The pixel flux along this ellipse will thus arise from a *range* of equivalent radii in both components. This will, of course, mainly affect the region where the surface brightnesses of the two components are comparable.
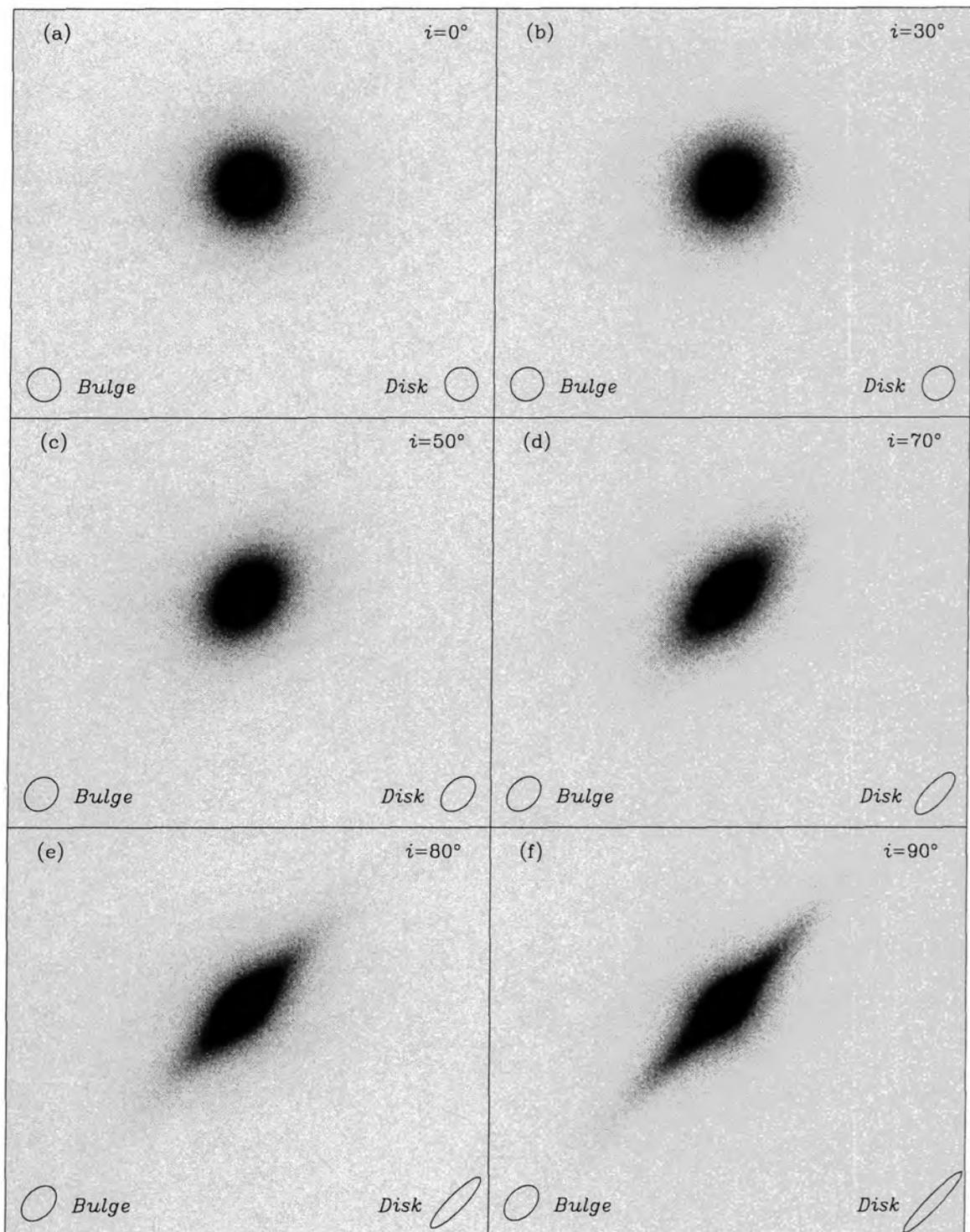
Figure 6.7: The six 2D images used to investigate the inclination-effect on fitted parameters. The sequence (a) to (f) is one of increasing inclination angle, from face-on to edge-on. The ellipses at the bottom corners of each image show the projected ellipticities of the separate components. Note how the difference between the bulge and disk projected ellipticity becomes more apparent as the inclination angle increases. The intrinsic (edge-on) ellipticities of the bulge and disk components are modelled as 0.35 and 0.85 respectively.

It is important to test the significance of this effect on the fitted parameters. Six 2D model images were constructed using the same parameters as model 4 above (a "typical" S0 with a 30% disk). The inclination of the models were changed from face-on ($0°$) to edge-on ($90°$) by varying the projected ellipticity of the two components according to Equation 6.17. The intrinsic ellipticities of bulge and disk are set to 0.35 and 0.85 respectively, and the position angles are equal . The six images are shown in Figure 6.7. Each image is analysed with the $GALPHOT$-based ellipse-fitting program to produce the 1D surface brightness profiles. The images had Poisson noise added, but were not convolved by a seeing PSF, so the $\mu(r)$ profiles are equivalent to those of real galaxies which have been deconvolved by the algorithm described in Chapter 5.

Each of the six $\mu(r)$ profiles were fitted by the same set of functions as in the previous experiment. The results for the two extreme cases (face-on and edge-on) are shown in Figures 6.8 and 6.9 respectively. Ignore the discrepant $\mu(r)$ profiles within $r = FWHM$ - these are a result of the inability of the ellipse-fitting routine to handle steep $\mu(r)$ gradients within the central few pixels (this is not a problem for real galaxies, whose $\mu(r)$ profiles are flattened by seeing in the central region). Of particular interest is the two-component fit. It can instantly be seen that the edge-on model is fitted just as adequately as the face-on model (the χ^2 values are greater than 1 in both cases - this is a result of the problem mentioned above). The best-fitting parameters for the two-component model have changed somewhat, however. Both components are slightly more extended, but with lower surface brightness. The disk component is affected more, with the bulge-to-total luminosity fraction increasing from ~ 0.7 to ~ 0.8. This is due to an increased amount of bulge light at equivalent radii where the disk light is normally significant. The total luminosity is, of course, conserved. Figure 6.10 shows how the fitted two-component parameters (and bulge fraction) vary with inclination. Is is apparent that about one-tenth of disky galaxies (those with $i \gtrsim 80°$) will display systematic errors in their fitted parameters of the order 5-20%. However, these errors will be matched by those which result from deviations in real galaxies from a clean $r^{\frac{1}{4}}$ plus exponential profile - which is independent of inclination.
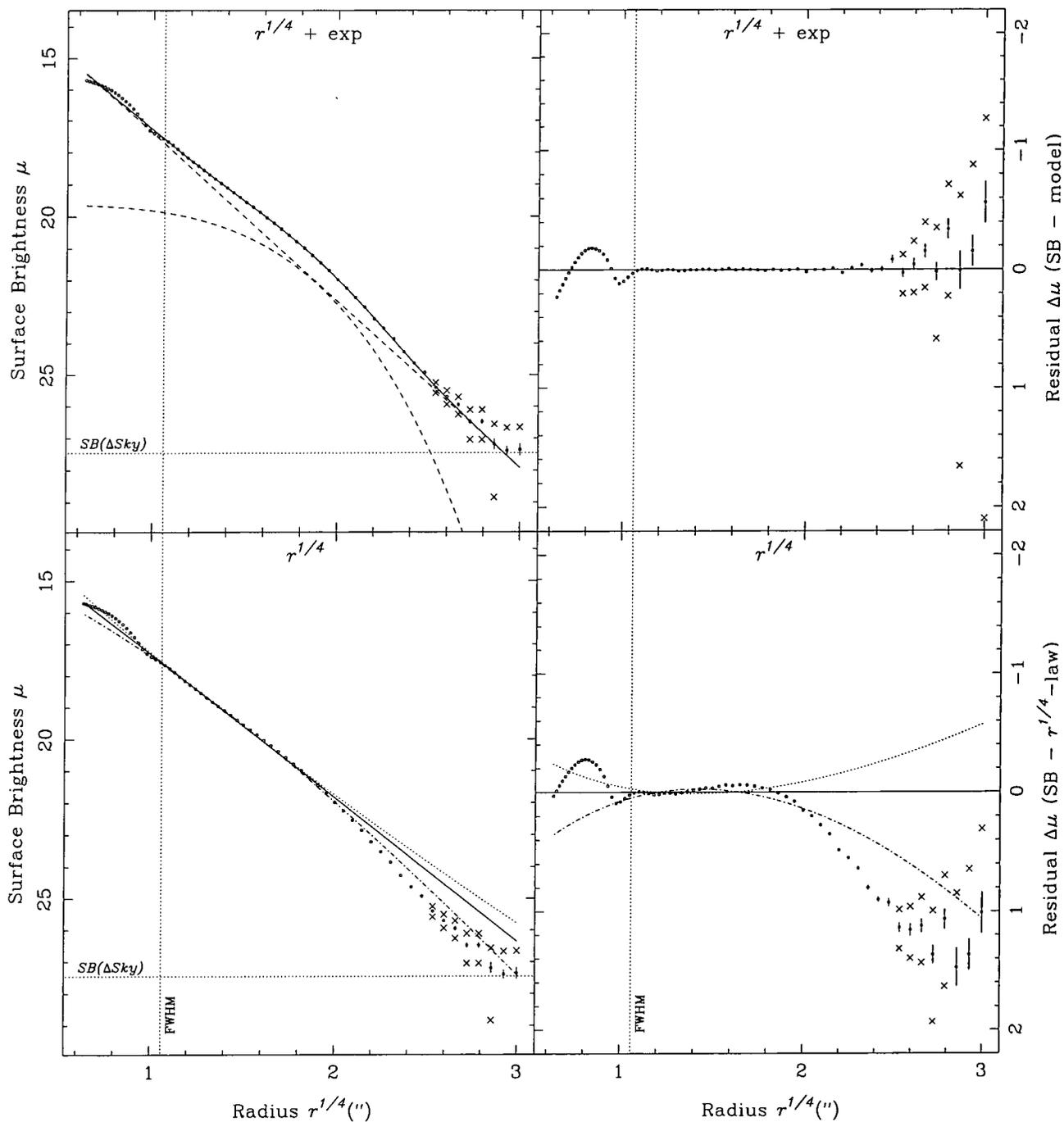
Fitting Law	r_e	Δr_e	$<\mu>_e$	$\Delta<\mu>_e$	M_{tot}	ΔM_{tot}	RMS	χ^2
$r^{1/4}$ + exp	————	————	————	————	12.676	0.016	0.106	12.754
(bulge)	6.274	0.427	19.077	0.084	13.094	0.06	————	————
(disk)	9.252	0.034	20.741	0.081	13.914	0.083	————	————
$r^{1/3}$	8.521	0.028	19.283	0.004	12.635	0.003	0.245	327.454
$r^{1/4}$	11.514	0.008	19.723	0.001	12.421	0.001	0.594	598.373
$r^{1/5}$	15.752	0.018	20.203	0.002	12.221	0	0.797	1082.268
Non—parametric	7.261	0.067	19.006	0.034	12.705	0.02	————	————

Fitting Range:— 1.34" to 80.91"   Bulge Fraction = 0.699 ± 0.041

Figure 6.8: Parametric fits to a $\mu(r)$ profile measured from a made-up 2D $r^{\frac{1}{4}} + exp$ galaxy. This galaxy is *face-on* (see Figure 6.7a) and has a bulge fraction of 0.695. See Page 113 for key.
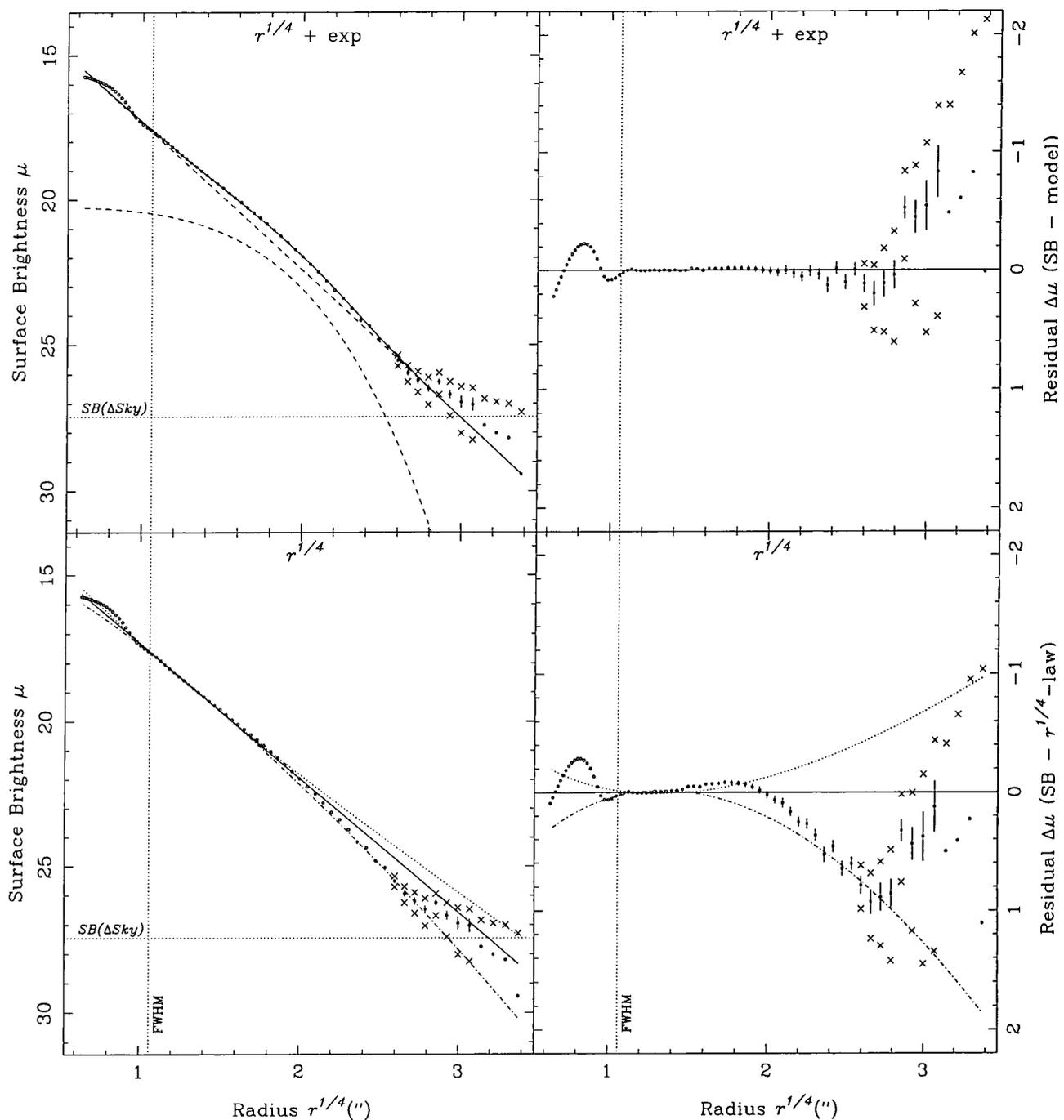
Fitting Law	r_e	Δr_e	$<\mu>_e$	$\Delta<\mu>_e$	M_{tot}	ΔM_{tot}	RMS	χ^2
$r^{1/4}$ + exp	————	————	————	————	12.66	0.039	0.187	5.651
(bulge)	7.291	1.034	19.234	0.158	12.925	0.134	————	————
(disk)	10.265	0.137	21.373	0.391	14.321	0.399	————	————
$r^{1/3}$	7.475	0.134	19.137	0.023	12.773	0.016	0.295	55.55
$r^{1/4}$	10.475	0.05	19.627	0.006	12.531	0.004	0.337	32.916
$r^{1/5}$	14.941	0.092	20.167	0.009	12.3	0.004	0.587	71.7
Non—parametric	7.621	0.028	19.112	0.016	12.706	0.01	————	————

Fitting Range:— 1.34" to 89"   Bulge Fraction = 0.817 ± 0.101

Figure 6.9: Parametric fits to a $\mu(r)$ profile measured from a made-up 2D $r^{\frac{1}{4}} + exp$ galaxy (*edge-on*, see Figure 6.7f). Compare with the fits to an identical, but *face-on* galaxy (Figure 6.8). See Page 113 for key.
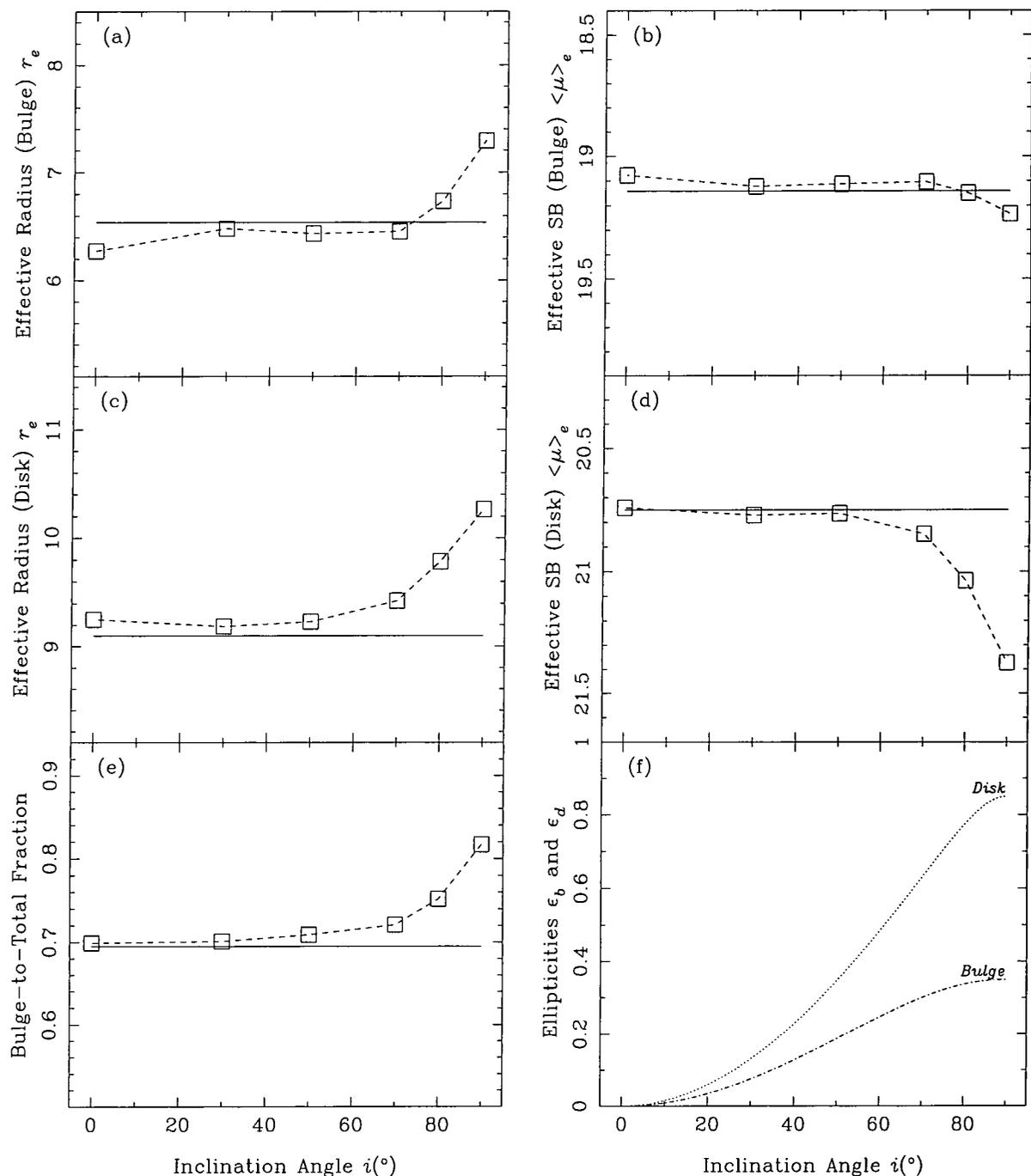
Figure 6.10: Graphs showing the variation of fitted two-component parameters with changing inclination (the galaxy model used here is described on Page 123). The plots (a) to (d) show the four measured disk and bulge parameters against inclination angle, with the solid-line giving the value of the 'true' parameter. Note how the fit diverges at angles greater than 70°. The same plot for Bulge-to-Total luminosity fraction is shown in (e). The final plot (f) shows the continuous functions (Equation 6.17) of projected ellipticities used to build the six different models.

6.6 Fitting a Seeing-Convolved Model

The experiments above have demonstrated that it is possible to decide whether a galaxy is likely to have a disk, by determining whether the $\mu(r)$ profile is best fit by a single power-law or two-component model. Using model profiles, the reproduction of the input parameters by the fitting routine is remarkably good. Of course, with the deconvolution of real galaxy profiles, the fitting is likely to be affected by errors which have not been explored here. One complication, the inclination of galaxies, has been looked at. It was found that the inclination does not seriously affect the fitted parameters, except for the most edge-on galaxies - not more than 10% of the total. However, it is likely that systematic errors arising from the deconvolution algorithm will be more serious.

As a final, more realistic, test of the profile-fitting routine, a model 2D image is convolved with a seeing PSF, Poisson-noise added, and then reduced in precisely the same way as a real galaxy image. The image is put through the deconvolution routines and the corrected $\mu(r)$ profile is analysed with the profile fitting routines described above. The model used has the same parameters as used in the previous experiment (see model 4 in Table 6.3), with an inclination of 50°, and a seeing $FWHM$ of 1.27″. The results of the profile fitting is shown in Figure 6.11. Note how the deconvolution has smoothed the profile in the outer part. The two-component parameters match the input well within the sky uncertainty. This demonstrates that the profile of a *real* seeing degraded galaxy image can be adequately recovered after deconvolution.

6.7 Conclusions

In this chapter, a method has been developed for fitting and parametrising the surface brightness profiles of early-type galaxies. This method thus operates in tandem with the technique developed in Chapter 5 to correct the SB (and other) profiles for the effects of seeing. It has been demonstrated, using simulated data, that the method is both effective and robust. Using a relatively straightforward method, the 'useful' surface brightness data for a ground-observed elliptical galaxy (at Coma/Abell 1367 distance) has been extended inwards to one or two times the seeing $FWHM$ from the core. Using the improved profiles, it is now possible to gleam a great deal more information about the structure of early-type
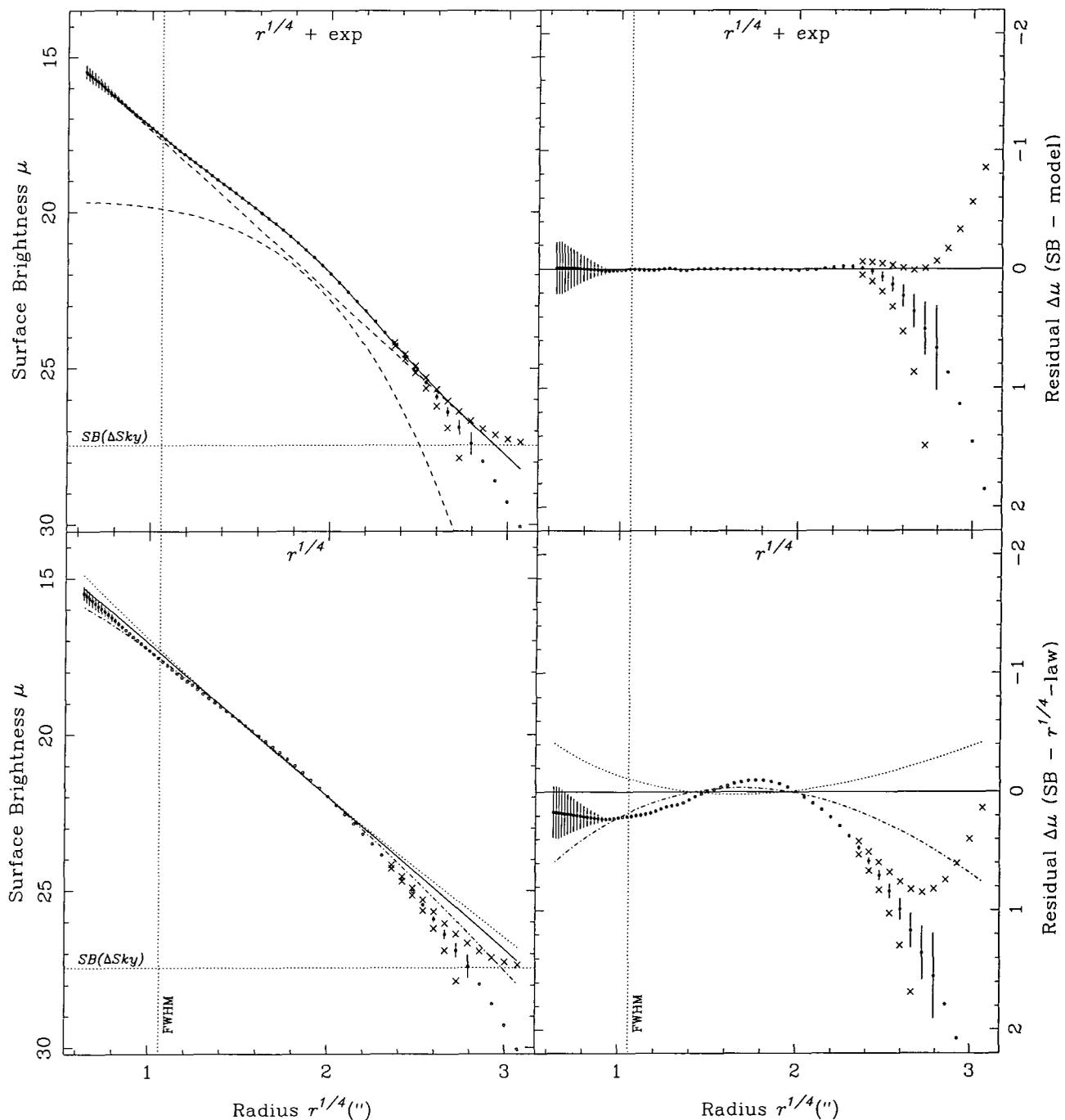
Fitting Law	r_e	Δr_e	$<\mu>_e$	$\Delta<\mu>_e$	M_{tot}	ΔM_{tot}	RMS	χ^2
$r^{1/4}$ + exp	----	----	----	----	12.673	0.013	0.147	1.39
(bulge)	6.469	0.456	19.114	0.101	13.064	0.049	----	----
(disk)	9.159	0.15	20.775	0.04	13.97	0.072	----	----
$r^{1/3}$	7.948	0.069	19.127	0.015	12.63	0.004	0.314	81.065
$r^{1/4}$	8.341	0.056	19.114	0.011	12.512	0.004	0.469	208.368
$r^{1/5}$	8.852	0.045	19.142	0.008	12.411	0.003	0.559	319.81
Non−parametric	7.261	0.074	19.012	0.036	12.709	0.02	----	----

Fitting Range:− 1.34" to 60.79"   Bulge Fraction = 0.721 ± 0.035

Figure 6.11: Parametric fits to a $\mu(r)$ profile from a made-up 2D seeing-convolved $r^{\frac{1}{4}} + exp$ galaxy - corrected using the deconvolution algorithm. The inclination angle is 50°. See Page 113 for key.

galaxies from their photometry. The bulge-disk fitting technique, for instance, provides an inclination independent method of checking for the presence of a disk component (unlike using higher-order terms).

The next step is to use the profile-fitting procedure on all 153 galaxies of the Coma/Abell 1367 sample. The results for each individual galaxy are displayed in in Appendix D. The statistical results of the profile-fitting for the whole sample are presented and discussed in Chapter 7. Note that where repeat images exist for a given galaxy, the deconvolved profiles from each image are binned (using a weighted mean) to produce a single set of deconvolved profiles with higher signal-to-noise ratio. Of the 153 galaxies in the sample, only 23 were not fitted by a two-component model. This adequately demonstrates the range of validity of the fitting technique - this range includes all galaxies with a disk component contributing more than around 8% of the total light.

Chapter 7

Results and Discussion

7.1 Introduction

In this chapter, the deconvolution and profile-fitting methods developed in the last two chapters are applied to the sample of 153 galaxies in Coma and Abell 1367. In Section 7.2, the bulge-disk deconvolution is compared with the results of two other studies - Dressler (1980a) and Saglia *et al.* (1997). In Section 7.3, the problems of morphological classification are examined, using the distribution of ellipticities of the different types. Using the inclination-independent disk luminosity fraction D/T, calculated from the profile fitting, it is possible to identify many of the 'missing' low-inclination S0's which have normally been classified as ellipticals. In Section 7.4, the relative merits of the one-component and two-component profile models are discussed, along with a demonstration of the correlation between profile shape and galaxy size. In Section 7.5, we present the results of an isophotal shape analysis for the 153 galaxies, and use these results to strengthen the conclusions of the profile fitting. Finally, Chapter 8 sums up the various conclusions about early-type galaxy morphology and puts them in the context of galaxy evolution in rich clusters.

7.2 Two-Component Fitting - Comparisons

Bulge-to-Total luminosity fraction's have been measured from the surface-brightness profiles for the whole sample of 153 Coma and Abell 1367 galaxies, following the methodology outlined in Chapter 6. The results of the bulge-disk decomposition for individual galaxies are displayed as figures in Appendix D, which also includes tables giving the best-fit pa-
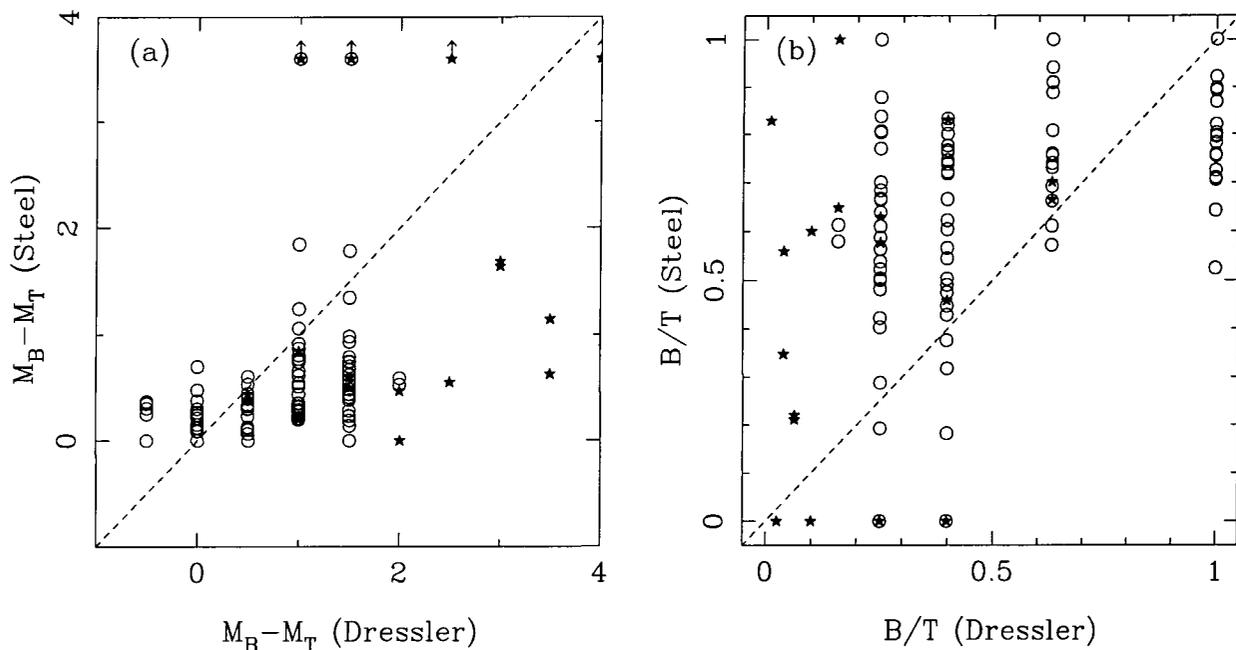
Figure 7.1: A comparison of the bulge-total luminosity fraction's calculated in this study with those calculated from the bulge and total magnitudes of Dressler (1980b) for the 111 galaxies in common. The comparison is made in two different ways. In plot (a), the bulge-total magnitude difference $(M_B - M_T)$ is compared (note the quantization of Dressler's data into half-magnitude bins). Plot (b) compares the bulge-total luminosity fraction's (B/T). It can be seen in plot (a) that for a few objects Dressler assigns bulges with luminosity greater that the total - these are assumed to have B/T equal to unity in plot (b). The open circles represent early-type galaxies, whilst the stars represent spirals and irregulars. The dotted line is the line of equivalence between the two axes in both plots.

rameters of models fitted. It is apparent that while an idealized $r^{\frac{1}{4}}$ plus exponential profile fit is very appropriate for some early-type galaxies (e.g. NGC 4906), it does not accurately portray the shapes of many others (e.g. NGC 4919).

The results of Dressler (1980a), which show an environmental trend in bulge luminosity, were based on 'eyeball' bulge-disk decompositions from photographic plates - both the total and bulge magnitudes were estimated by comparison with a 'fly-spanker' (a photographic strip with a sequence of exposures of standard galaxies). This is necessarily crude - the size of the magnitude bins alone being 0.5 and 1.0 for bulge and total magnitudes respectively. Nonetheless, the dearth of extensive bulge-disk deconvolution data in the literature makes it interesting to compare Dressler's values for bulge-total magnitude difference with those calculated here from a CCD-based bulge-disk decomposition (the comparison is shown in Figure 7.1).

The large errors involved in measuring bulge luminosities are apparent in Figure 7.1. In

particular, the scatter in these plots is likely to arise from measurement errors in both data-sets, and the heavy quantization of Dressler's magnitudes. The RMS measurement error in the author's $M_B - M_T$ values is ~ 0.094 mag, which is too small to explain the scatter here. Also present is a systematical trend in the sense that Dressler's bulge magnitudes tend to underestimate the bulge contribution with respect to the author's measurements - this is particularly true for late-type galaxies. Table 7.1 below gives the mean bulge-total luminosity fraction (B/T) for both data-sets, sorted by morphological type.

The morphological classes used in Table 7.1 are those outlined in Chapter 2 (i.e. E,S,I and U). However, the early-type class (E) has divided into two *visual* classes - *Ellipticals* being those classed E, E/S0 by Dressler (1980b), while *Lenticulars* are those which Dressler classed S0, S0/E, S0/a, SB0 or later (the 2 Coma cD Galaxies are not included). Table 7.1 shows good agreement on the average 'bulge' fraction of ellipticals, which both data-sets give as around 76±3%. However, for the 51 lenticulars in common, there is a significant difference in average bulge fraction - 67% here, but 44% using Dresslers data. In fact, there is not a large difference between mean B/T for ellipticals and the mean B/T for S0's according to the authors data. This is important because the presence (or absence) of a disk component is the main morphological distinction between Hubble's E and S0 classes. This result, therefore, suggests that the traditional separation of early-type galaxies into ellipticals and S0's is an artificial one - based primarily on difference in viewing angles rather than any real physical difference between the objects (this possibility will be analysed further in Section 7.3). Of course, early-type galaxies with more prominent disks will display an 'S0' morphology over a greater range of viewing-angle, which may explain why the mean B/T is nonetheless slightly smaller for those objects classed S0 by Dressler.

A much more recent photometric study of over 700 mainly early-type galaxies in 84 clusters has been undertaken by the EFAR collaboration (Saglia *et al.* 1997). This includes detailed measurements of photometric parameters from CCD data, including disk-bulge luminosity ratio. Unfortunately, the number of Coma galaxies observed by EFAR is not large. Of the 32 Dressler galaxies in Coma observed by EFAR, only 21 galaxies were given the two-component (bulge and disk) fit. Of these 21 galaxies, only 16 objects are also included in the Steel sample. Despite the small number of common objects, a comparison between the two data-sets is still worthwhile.

The photometric fitting procedure adopted by EFAR differs somewhat from that which

Table 7.1: Table of mean B/T luminosity fraction's calculated from this study and from the magnitudes of Dressler (1980b), sorted by morphology.

Morphology	Number of Objects	$\langle B/T \rangle$ (Steel)	Error $\Delta\langle B/T \rangle$	$\langle B/T \rangle$ (Dressler)	Error $\Delta\langle B/T \rangle$
Elliptical	35	0.79	0.02	0.73	0.05
Lenticular	51	0.67	0.03	0.44	0.03
Early-Type	86	0.72	0.02	0.56	0.03
Spiral	15	0.44	0.07	0.22	0.05
Irregular	4	0.41	0.21	0.21	0.10
Late-Type	19	0.44	0.07	0.21	0.04
Unclassed	6	0.33	0.12	0.35	0.03
All Types	111	0.65	0.02	0.49	0.03

is used here and hence it is certain to produce some systematic differences between the two data-sets. Both methods involve the minimisation of a goodness-of-fit (χ^2) function in order to find the best-fitting parameters. However, EFAR uses circularly averaged surface-brightness profiles, whereas elliptically averaged profiles (taken from fitted ellipses) have been used in this study. This removes one possible source of systematic error from this study - circularly averaged photometry of a flattened galaxy is actually an integration of light from a range of elliptical isophotes. This means that at a given radius, the measured surface brightness will be a function of both the surface brightness along an ellipse of identical equivalent radius AND the form of the surface brightness profile in the neighbourhood. Of course, the effect is reduced for low-ellipticity galaxies, and 96% of EFAR's galaxies have ellipticity less than 0.4 (compared with only about 60% of the early-type galaxies in this study).

Another difference is the treatment of sky brightness level and seeing $FWHM$. These are treated as free parameters by EFAR, to be minimised along with the other profile parameters, whereas they are measured and fixed in this study (see Chapter 6). This has the effect of reducing the volume and complexity of the parameter-space to be searched. In many cases, it is possible to engineer a better fit by arbitrarily shifting the sky level

or *FWHM* and changing the profile. For instance, a galaxy which appears to follow an $r^{\frac{1}{4}}$ law with the measured sky level will often fit an $r^{\frac{1}{4}}$ plus exponential law even better (i.e. with lower χ^2) if the sky level is reduced. Of course, the measurement of the sky background will always have a error - this is accounted for in this study by performing the minimisation three times (using the measured sky level, sky *plus* estimated error and sky *minus* error). The errors on the individual minimised parameters were then calculated from the differences between the three minimisations. The large field size of the CCD data used in this survey ($11.4'' \times 10.5''$) makes the accurate measurement of sky level and seeing *FWHM* straightforward. This is perhaps not the case with EFAR as some of their data was observed with CCD fields of only $2.9'' \times 1.9''$.

The comparison of bulge-disk parameters between EFAR and Steel is shown in Figure 7.2. The 2 cD galaxies have not been included because the sky subtraction errors for these objects make a comparison meaningless, leaving a common sample of 14 objects. Figure 7.2(a) shows the comparison between disk-to-bulge luminosity ratio (D/B) for the two samples, while Figure (b) shows the residual of D/B plotted against isophotal ellipticity $\epsilon_{21.5}$. Figures (c) to (f) show the comparison for the individual bulge and disk parameters - EFAR use different parameters to describe the disk component (scale-length and central surface brightness), but these are easily converted to the parameters used by Steel (effective radius and effective surface brightness). Note that two of the 14 galaxies (IC 4051 and NGC 4860) were deemed not to have a significant exponential component by Steel, and therefore are not included in the disk parameter comparisons. No attempt is made by EFAR to assign uncertainties in the bulge/disk parameters for the individual galaxies, hence Figure 7.2 only shows error bars for the authors data. One can assume, however, that the measurement errors on the EFAR data are of similar order to those of Steel.

The considerable scatter (RMS of 33.7%) in the comparison with the EFAR D/B ratios does not appear encouraging at first glance. However, it must be remembered that the range in D/B is not large for the EFAR sample (typically $D/B < 0.5$ or $D/T < 0.3$), whereas all galaxies are included in the Steel sample, regardless of morphology. Measurement error must account for much of the scatter (note the error bars in Figure 7.2(a) only show the authors measurement errors). Given the different methodology of the two studies (circular photometry versus elliptical photometry), there must also be some systematic error present. However, Figure 7.2(b), which shows D/B residual versus ellipticity does not display any

convincing trends - the number of common galaxies is too small and the measurement errors too large. Curiously, the galaxy with the greatest disparity between Steel and EFAR (NGC 4886) is also the most face-on. The difference in this case is very probably due to the background subtraction, as NGC 4886 lies embedded within the halo of cD galaxy NGC 4889. The treatment of such objects in this study was to mask out the galaxy in question, and then fit the varying background light. If the varying background was due to a larger galaxy (as in this case), then *GALPHOT* can be used to fit and model the unwanted galaxy light - otherwise, a spline-fit will suffice. This surface can then be subtracted from the original image and a constant added (to avoid negative pixels). The resulting frame has a flat background and the target galaxy can be processed as normal (see Chapter 3).

A much better comparison between Steel and EFAR is seen in the individual scale parameters of the two components, which are matched remarkably well, see Figure 7.2(c)-(f). The RMS scatters for the four parameters are as follows: 0.180 ($\log r_e^b$); 0.908 ($\langle \mu^b \rangle_e$); 0.099 ($\log r_e^d$); 0.585 ($\langle \mu^b \rangle_e$). Perhaps contrary to expectations, the exponential component seems to be recoverable with smaller error than the $r^{\frac{1}{4}}$ component. A reasonable explanation is that the $r^{\frac{1}{4}}$ component, being more centrally concentrated, is more affected by errors in the seeing correction than the extended exponential component. Of course, the exponential component fitting is similarly affected by sky subtraction, but this would appear to be less significant. In any case, there is a clear and unequivocal correlation between the photometric parameters calculated by Steel and EFAR.

The conclusion, therefore, is that the deconvolution of an early-type galaxy surface brightness profile into an $r^{\frac{1}{4}}$ component and an exponential component represents a repeatable measurement. What remains to be seen is the physical usefulness of such an approach in determining the characteristics of early-type galaxies.

7.3 The Missing S0 Problem

There has been much speculation over the past few years concerning the nature of S0 galaxies, and particularly their relationship to elliptical galaxies. The use of the c_4 coefficient to identify *pointy* or *disky* elliptical galaxies has led to suggestions that disky ellipticals and S0's together form a single class of galaxies (distinct from boxy ellipticals) with a continuous distribution of bulge-to-disk ratio - the S0's naturally being the more disk-dominated
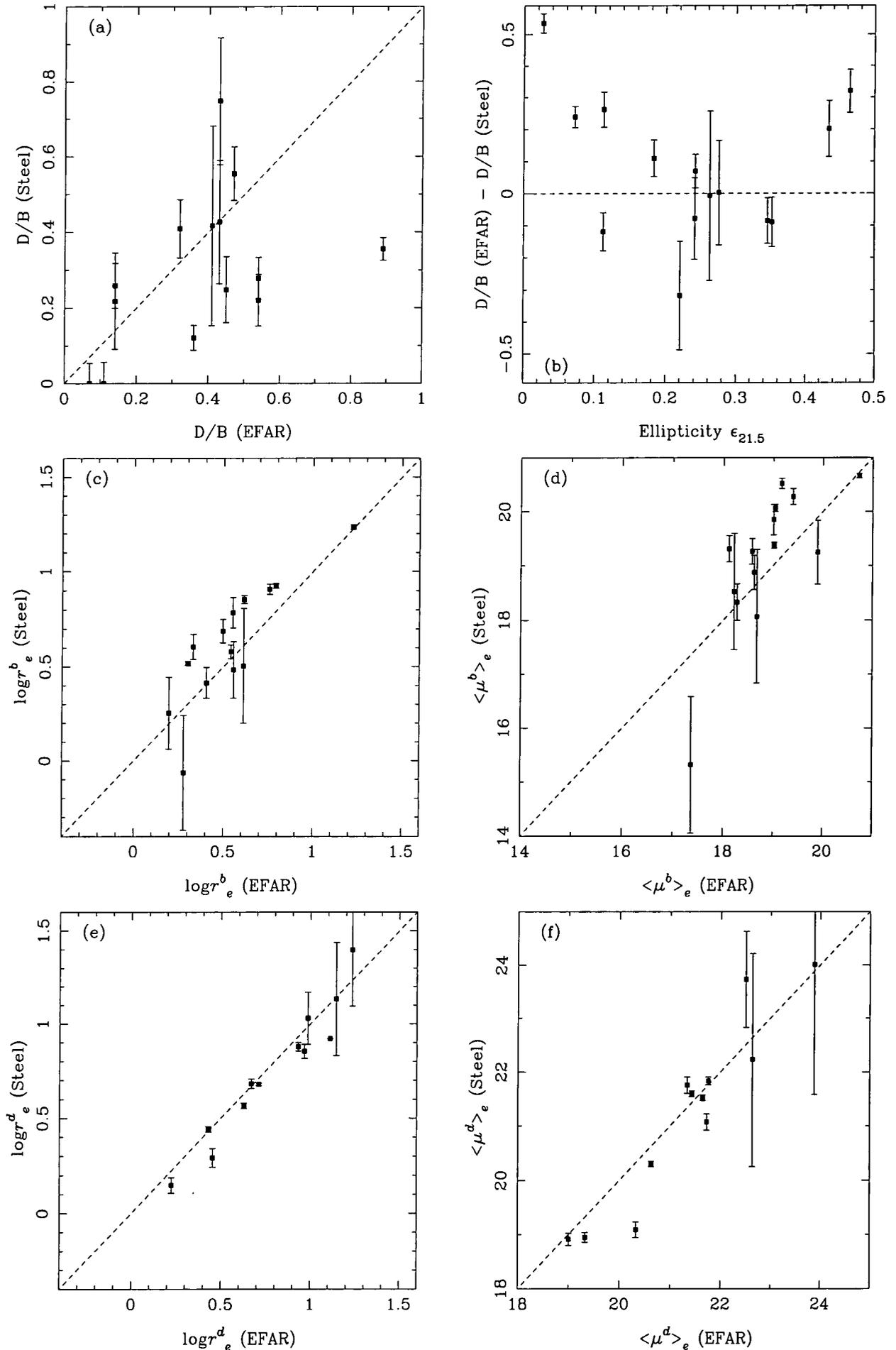
Figure 7.2: A comparison of disk and bulge parameters between Steel and the EFAR collaboration (Saglia *et al.* 1997). Plot (a) shows the direct comparison of D/B ratio, whilst (b) plots the residual of D/B versus ellipticity. The remaining plots (c)-(f) compare the parameters $\log r_e^b$, $\langle \mu^b \rangle_e$, $\log r_e^d$ and $\langle \mu^b \rangle_e$.

objects. The viewing angle is thought to be highly significant - van den Bergh (1990) pointed out the deficiency of face-on faint S0's in the RSA Catalogue (Sandage and Tammann 1981), arguing that many S0's have been, in fact, misclassified as ellipticals. Rix and White (1990) used idealized $r^{\frac{1}{4}}$-law bulge plus exponential disk models to demonstrate that a disk containing 20% of the total luminosity would be undetectable (in c_4) for more than half the possible viewing angles. Indeed, even brighter disks would be invisible for low inclination angles - such galaxies would inevitably be classified elliptical.

Jorgensen and Franx (1994, hereafter JF94) used ellipticity measured at isophote $gunn\ r = 21.85$ ($\epsilon_{21.85}$) to derive cumulative distributions of apparent ellipticities. It is immediately clear from their distribution plots that S0's are generally more flattened than ellipticals, and occupy a very differently shaped distribution - avoiding low apparent ellipticities. As a comparison (see Figure 7.3(a)), ellipticities have been measured for this study at the isophote $R = 21.5$ ($\epsilon_{21.5}$ - calculated by interpolating the ellipticity between the nearest 2 ellipses from the surface photometry). This is equivalent to $\epsilon_{21.85}$ in JF94. The ellipticity data agrees well with JF94, the RMS scatter between the two data-sets being 0.051. This scatter, together with an mean offset ($\epsilon_{21.5}$-$\epsilon_{21.85}$) of 0.037 are somewhat larger than would be expected from measurement errors (typically ±0.006 for Steel, JF94 quote ±0.014 for their data). The explanation almost certainly lies in seeing effects - the observations of JF94 were carried out with greater seeing ($\sim 2''$) than this study ($\sim 1.2''$), and therefore JF94 measures smaller ellipticities - with variations in seeing contributing to the scatter.

The ellipticity data has been used to derive distributions of the apparent ellipticities for the different morphological types. The division of the early-type (E) class into the classical 'Hubble' types or 'visual' classes (E and S0) is extended to the whole data-set. The types for Abell 1367 are taken from Butcher and Oemler (1985). The few early-type galaxies which remain without a type have been examined by the author and typed E or S0 depending on the visual existence of a disk. The resulting distributions are shown in Figures 7.3(b) and (c). Figure 7.3(b) shows a number distribution of ellipticity, sorted into ellipticals, lenticulars, and late-type (S+I) galaxies. The plot compares well with Figure 3(a) in JF94, and shows clearly the different ellipticity distributions of those early-type galaxies classed 'E' and 'S0' according to the normal morphological criterion (the late-type galaxies exist across a wide range in $\epsilon_{21.5}$, as expected). The absence of face-on lenticular galaxies is striking, and is demonstrated well in the plot of the cumulative distribution -
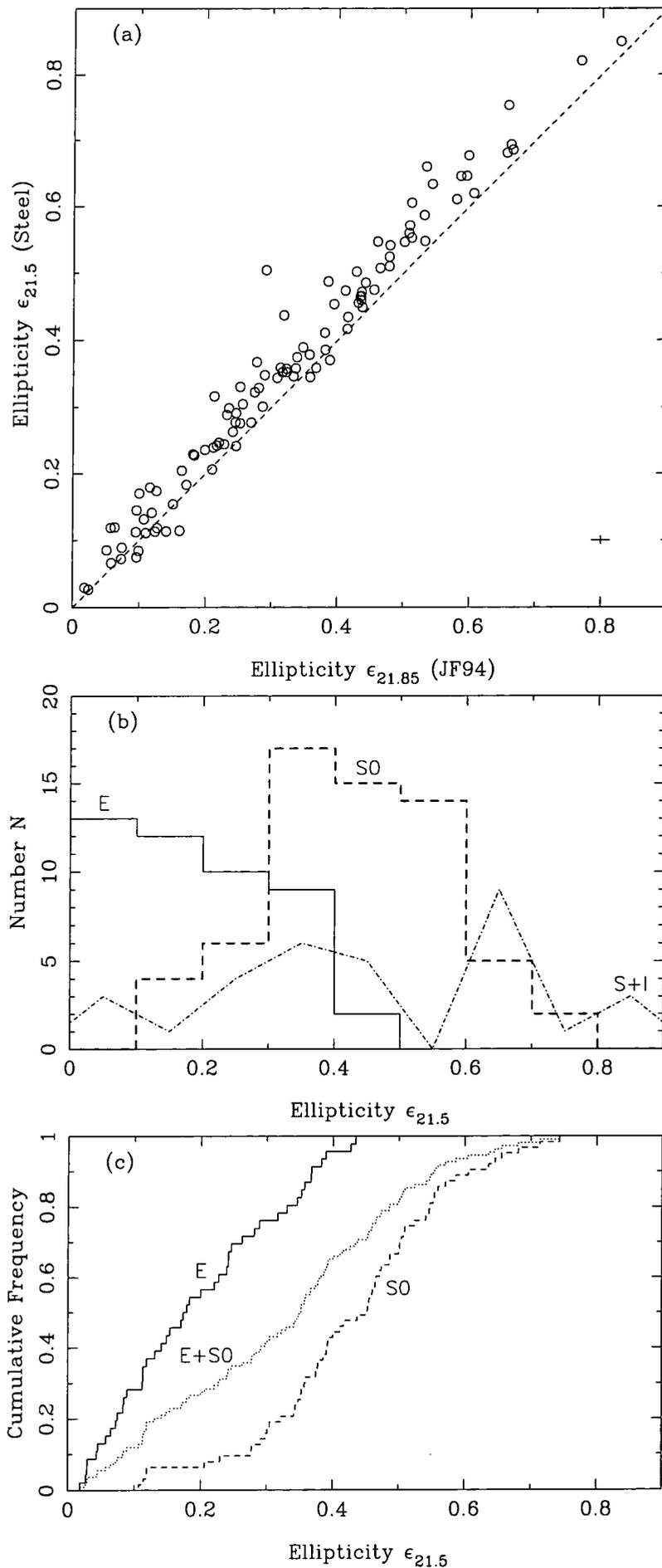
Figure 7.3: (a) Comparison of Steel's ellipticities ($\epsilon_{21.5}$) with those of JF94 ($\epsilon_{21.85}$). (b) Number distribution of apparent ellipticity, sorted by type, in bins of 0.1 mag. (c) Cumulative Distribution of apparent ellipticity - sorted into ellipticals, S0's and all early-type (E plus S0).

Figure 7.3(c) (c.f. fig. 3(b) in JF94). Whereas more than half of the ellipticals are more face-on than $\epsilon_{21.5} = 0.2$, this is true for less than 10% of the lenticulars. A Kolmogorov-Smirnov (KS) test rules out any possibility of the two classes having the same parent ellipticity distribution (the probability of getting the same or greater difference between the two cumulative distributions given the same parent is 3.2×10^{-10}!).

Clearly, the morphological criterion for distinguishing between elliptical and S0 galaxies is strongly dependent upon apparent ellipticity, and therefore inclination angle. The relative properties of elliptical and S0 galaxies could be studied in a more meaningful way if the criterion for separating them is *independent* of inclination angle. For instance, if an early-type galaxy possesses an exponential disk component contributing more than a particular fraction of the total light then regard this galaxy as an 'S0', whereas other galaxies can be classed 'E'. Although simplistic in the sense that only one criterion is used (other criterion might include c_4 or kinematic information) this approach has the strength that if the disk fraction is calculated by an inclination-independent method, the resulting morphological 'classes' will not be degenerate at low apparent ellipticities. An interesting exercise, therefore, is to use the values of disk fraction $(D/T = 1 - B/T)$ calculated in this study to divide the early-types into two classes. Despite the large measurement errors, and systematic errors arising from departures from an $r^{\frac{1}{4}}$ + exp law, the method of bulge-disk segregation outlined in Chapter 6 is independent of inclination. This is demonstrated in Figure 7.4, where the bulge fraction is plotted against the apparent ellipticity.
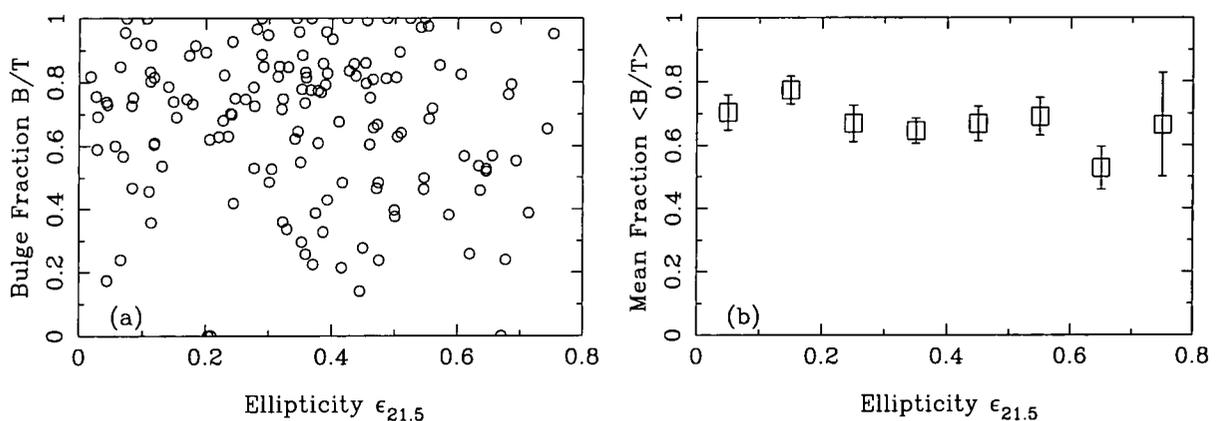
Figure 7.4: Plots showing the independence of bulge fraction (B/T) measurements as a function of ellipticity $(\epsilon_{21.5})$. (a) A scatter diagram for all galaxies - the correlation coefficient is -0.18. (b) Weighted-average B/T measurements (in ellipticity bins of 0.1) against $\epsilon_{21.5}$. The error bars show the standard error on the mean - $\langle B/T \rangle$ is almost constant (~ 0.65-0.7) with ellipticity.

All early-type galaxies are re-assigned 'morphological classes' according to disk luminosity fraction D/T. All galaxies with D/T greater than 24% are classed E+, while all galaxies with D/T smaller than 24% are classed E-. The labels E- and E+ are used instead of E and S0 to avoid confusion with the 'visual' classes. The value of 24% is not arbitrary - it is chosen so that the numbers of galaxies falling into 'photometric' classes E- and E+ are identical to the numbers of galaxies in the 'visual' classes E and S0 respectively (for this sample). The cumulative ellipticity distribution is then plotted for the new classes E+ and E- in Figure 7.5 (c.f. Figure 7.3). It can be clearly seen that the distributions for the two classes are very similar. In particular, there is no shortfall in the number of low ellipticity E+ galaxies (which are equivalent to S0's). There is a slight difference at the high-ellipticity end of the distributions where there are several E+ galaxies with $\epsilon_{21.5}$ greater than 0.6. This is not surprising, however, as at high inclinations the brighter disks of E+ relative to E- galaxies will have the effect of increasing the apparent ellipticities. Despite this small difference, a KS test on the two distributions shows that they are not statistically inconsistent with being drawn from the same parent ellipticity distribution (the probability of getting a larger difference between the E+ and E- distributions given the same parent is 60.7%).

Summarising, it has been shown that the distribution of ellipticity for visually-classed ellipticals and S0's is incompatible with the two classes having the same parent distribution, in agreement with the result of JF94. In particular, there is an almost complete lack of face-on galaxies traditionally classed as S0. This problem can be remedied by choosing an inclination-independent parameter - the disk-fraction D/T - to determine the morphology, rather than visual appearance of diskyness, which is biased by viewing angle.

7.4   Bulge-Disk Model versus Power-Law Model

The alternative profile shape for early-type galaxies to the $r^{\frac{1}{4}}$ plus exponential model is a generalised $r^{\frac{1}{n}}$ single power law (Sersic 1968). D'Onofrio et $al.$ (1994) demonstrated that a correlation exists between the size (r_e) of early-type galaxies and the index n of the best fit $r^{\frac{1}{n}}$-law for the Fornax and Virgo clusters, in the sense that smaller galaxies have shallower (smaller n) profiles. Is it not possible that the change in the $r^{\frac{1}{n}}$ profile shape is directly attributable to the varying strength of an exponential disk component? Generally,
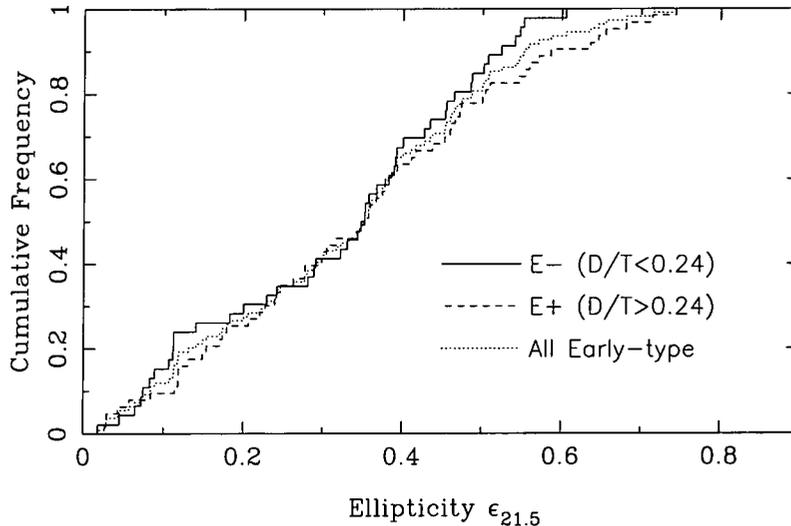
Figure 7.5: Cumulative distribution of apparent ellipticities for classes E+ and E-, selected from 109 early-type galaxies by a cut-off in measured disk luminosity fraction D/T.

a brighter disk will produce a shallower (lower n) overall profile - a pure bulge galaxy should have $n = 4$, while a pure exponential disk galaxy will have $n = 1$.

In order to make a comparison between the two models for the surface brightness profile shape, and their relation to galaxy morphology, the single-component power-law index n has been measured for all 153 galaxies in the sample. Two different methods have been employed, with the final value of n calculated as the average of the two values of n from each method.

Firstly, all galaxies are fitted by a single power law $r^{\frac{1}{n}}$, with n taking the values 1, 2, 3, 4 and 5. The three values of n which give the lowest χ^2 are then determined and a parabola is fitted to these values to approximately calculate the value of n which gives the lowest χ^2, i.e. the best fit. This a similar method as Caon et $al.$ (1993), although they perform a 3-parameter fit, allowing n to vary. The method which has been employed here is convenient because it uses the same software as the two-component fit.

Secondly, n can be determined from the difference between the effective surface brightness ($\langle\mu\rangle_e$) and the surface brightness at r_e (μ_e) as follows. Suppose the surface brightness's $\langle\mu\rangle_e$ and μ_e are equivalent to flux's $\langle I\rangle_e$ and I_e. Given that the effective radius and effective surface brightness represent the half-light values for a perfect fit, the total luminosity L can be given by:-

$$L = 2\pi\langle I\rangle_e r_e{}^2 \tag{7.1}$$
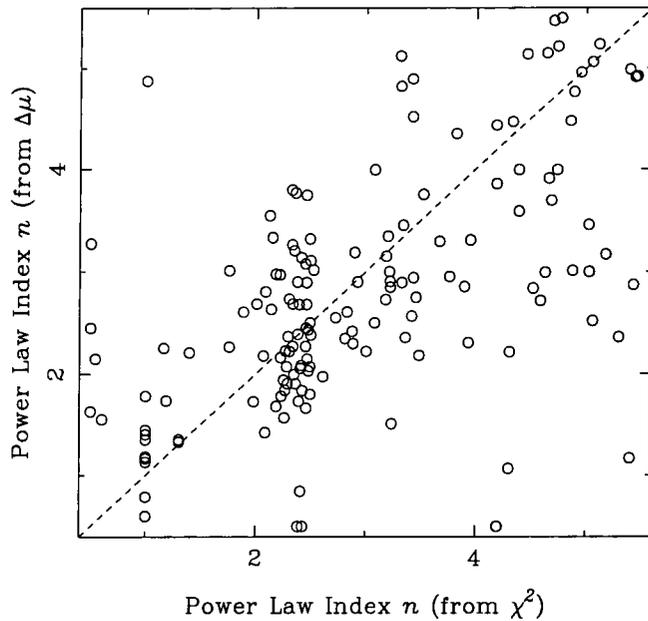
Figure 7.6: Graph showing the scatter between the two different measurements of power-law index n, using the two methods described in the text. The RMS scatter is 1.16.

Similarly, it is apparent that the total luminosity is proportional to I_e. The constant of proportionality is, however, dependent upon the shape of the surface brightness profile, i.e. the index n:-

$$L = k_n I_e r_e{}^2 \qquad (7.2)$$

Equating 7.1 with 7.2:-

$$\frac{I_e}{\langle I \rangle_e} = \frac{2\pi}{k_n} \qquad (7.3)$$

Converting from flux's to magnitudes:-

$$\mu_e - \langle \mu \rangle_e = 2.5 \left(\log k_n - \log 2\pi \right) \qquad (7.4)$$

The constant k_n can be calculated by integrating the surface brightness profile from $r = 0$ to $r = \infty$. Unfortunately, this can only be done algebraically for a few specific values of n. However, by calculating the integral numerically, Caon et $al.$ (1993) have shown that the following relation is appropriate in the range $0.5 < n < 16.5$:-

$$\log k_n = 0.030 (\log n)^2 + 0.441 \log n + 1.079 \qquad (7.5)$$

Substituting equation 7.5 into equation 7.4 and turning everything around to make n the unknown, we finally get a relation between power-index n and difference $\mu_e - \langle \mu \rangle_e$:-

$$\log n = -7.350 + \sqrt{44.661 + 13.333 \left(\mu_e - \langle \mu \rangle_e \right)} \qquad (7.6)$$
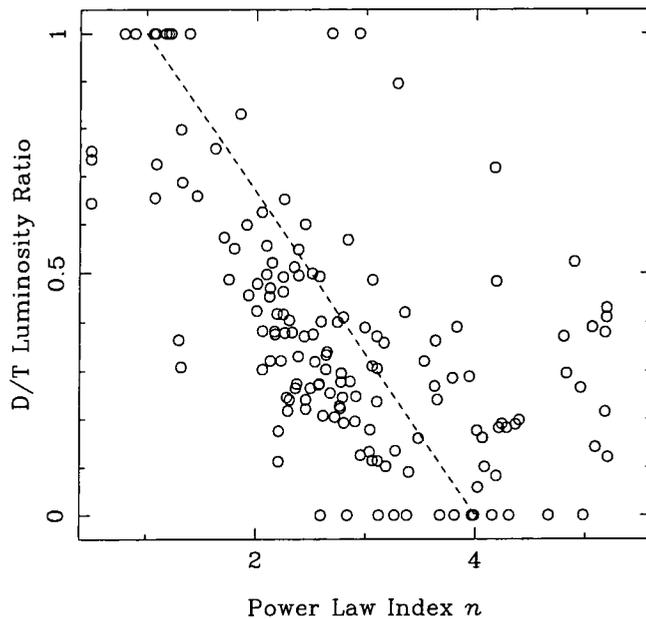
Figure 7.7: Graph showing the relation for the whole sample (all types) between the D/T luminosity ratio (characterising the two-component fit) against the power-law index n (characterising the single-component fit). The dotted line shows the general trend expected - pure bulges will have $n = 4$ while pure disks will have $n = 1$.

Each method of measuring n has advantages and disadvantages. The minimum-χ^2 method has the advantage that a large range of the profile is used for fitting, but is affected by seeing and sky subtraction errors in a similar way to the two-component fit. The surface brightness method (using difference $\mu_e - \langle \mu \rangle_e$) is critically dependent upon a single measurement of surface brightness (at r_e), which may suffer from a localised perturbation. However, it does also use $\langle \mu \rangle_e$ which is calculated from aperture photometry (which has high signal-to-noise). It can be seen from Figure 7.6 that the scatter between the two values of n is considerable ($RMS = 1.16$). It was therefore decided to reduce the scatter by averaging the two values for each galaxy. The resulting value of n will still have a typical error of at least ± 0.5. A minimum value of n is set at 0.5 (from the range of the relation taken from Caon *et al.* 1993) - only a few late-type galaxies exceed this. A maximum value of n is set at 5.5, as the profile shapes become degenerate for high n - in fact, no galaxies exceed this value.

If n characterises the single-component $r^{\frac{1}{n}}$-law fit and D/T characterises a two-component model fit, it is apparent that there should be a correlation between the two parameters, even if one or both of the model fits are wholly inappropriate. For instance, an $r^{\frac{1}{4}}$ plus

exponential model with $D/T = 1$ (i.e. a pure disk) is identical to an $r^{\frac{1}{n}}$-law model with $n = 1$, and similarly an $r^{\frac{1}{4}}$ plus exponential model with $D/T = 0$ (i.e. a pure bulge) is identical to an $r^{\frac{1}{n}}$-law model with $n = 4$. By plotting the calculated values of n against D/T, this trend is shown in Figure 7.7. The scatter in Figure 7.7 is considerable, but expected. For a given value of D/T the bulge and disk components can have a large variety of shapes depending on individual disk and bulge parameters, leading to a range of n values if this fit is chosen. However, it is apparent from the plot that a strong correlation exists between the two parameters, especially in the range $n = 2$ to $n = 3.5$, where the typical disk fraction decreases from about 55% to around 10%. The correlation of galaxy shape, as defined by n or $B/T = 1 - D/T$, with galaxy size, as defined by half-light radius or magnitude is investigated next, before making a final conclusion about which model gives the best representation of early-type galaxies.

Using the values of n calculated for each galaxy, it is possible to plot the correlation of index n against size r_e for the Coma and Abell 1367 clusters. This is shown in Figure 7.8, which is directly comparable to Figure 8 in D'Onofrio *et al.* (1994) which shows a similar plot for Virgo and Fornax. The sample is divided by type for clarity. Again, the early-type (E) class is divided into the 'visual' classes 'Elliptical' and 'S0'. The trend for ellipticals is similar to that of D'Onofrio *et al.* (1994), although there is no evidence for the bimodality in the distribution which those authors suggest. The magnitude range covered by the two studies is similar, although D'Onofrio *et al.* (1994) go slightly deeper - to $B = 14$ in Virgo (equivalent to $R{\sim}16$ in Coma) compared to $R = 15.6$ by this study. The conclusions are unaffected, however. The lenticulars cover more or less the same area as the ellipticals, although they seem to avoid values of n greater than 4. Predictably, late-type galaxies display smaller values of n at all sizes, due to their more dominant exponential disk component. Figure 7.9 shows the same data, but using total magnitude M_t rather than r_e as the measure of galaxian size. The same trend of increasing n with size is also seen here. It is clear from both figures that the universality of the de Vaucouleurs $r^{\frac{1}{4}}$-law does not hold for early-type galaxies, whether classed visually as elliptical or S0. Rather, the shape of the light profile seems to depend approximately upon the size of the galaxy.

Given that the light profile shapes of early-type galaxies seem to depend on size, are these profiles best described by a two-component or single-component model? In Figure 7.7, it was shown that the bulge-to-disk ratio derived from a two-component fit is correlated
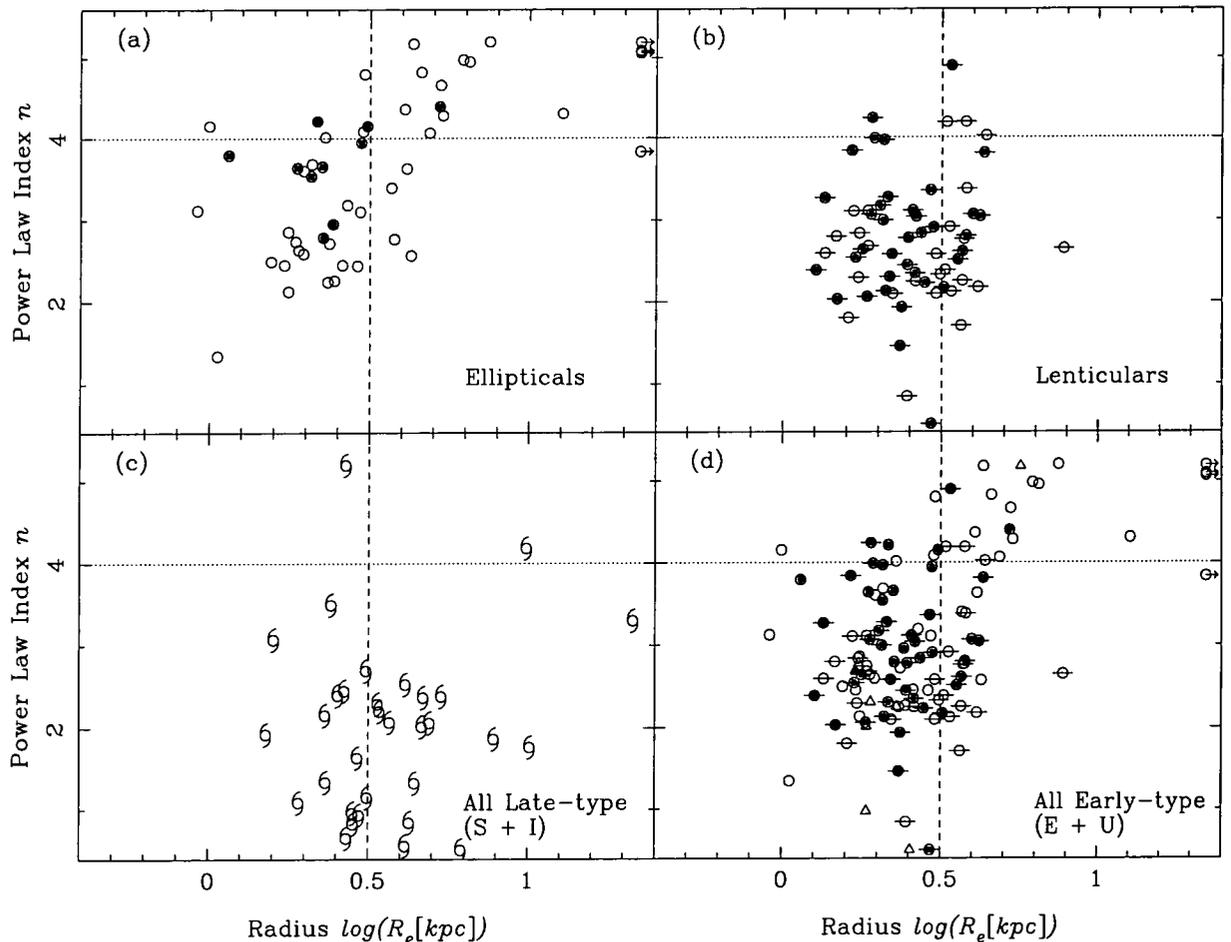
Figure 7.8: The distribution of power-law index n with non-parametric half-light radius r_e, separated into the different morphological types (c.f. fig 8, D'Onofrio et al. 1994). The symbols in (d) are the same as those in (a) and (b) for ellipticals and lenticulars, with the addition of triangles for the unclassified (U) galaxies. The filled symbols in (a),(b) and (d) represent positive (2σ) detections of c_4 parameter for early-type galaxies.

with the index n from a single-component $r^{\frac{1}{n}}$. Could the trend of n with galaxy size displayed in Figures 7.8 and 7.9, and in D'Onofrio et al. (1994), therefore, derive from a variation in disk fraction with size/luminosity, in the sense that smaller systems become progressively more disk-dominated. In addition to the shape of the surface brightness profile, a further indicator of the presence of two photometric components is a positive c_4 parameter. In Figures 7.8 and 7.9, the symbols for early-type galaxies are filled-in where there is a significant detection (2σ) of positive c_4 (see Section 7.5). Figure 7.8(a) clearly demonstrates that smaller galaxies are more likely to have two components - for ellipticals smaller than $\log r_e = 0.5$, 29% have detectable c_4, compared with only 1 out of 19 (5%) of those larger than $\log r_e = 0.5$ When the whole early-type (E) sample is
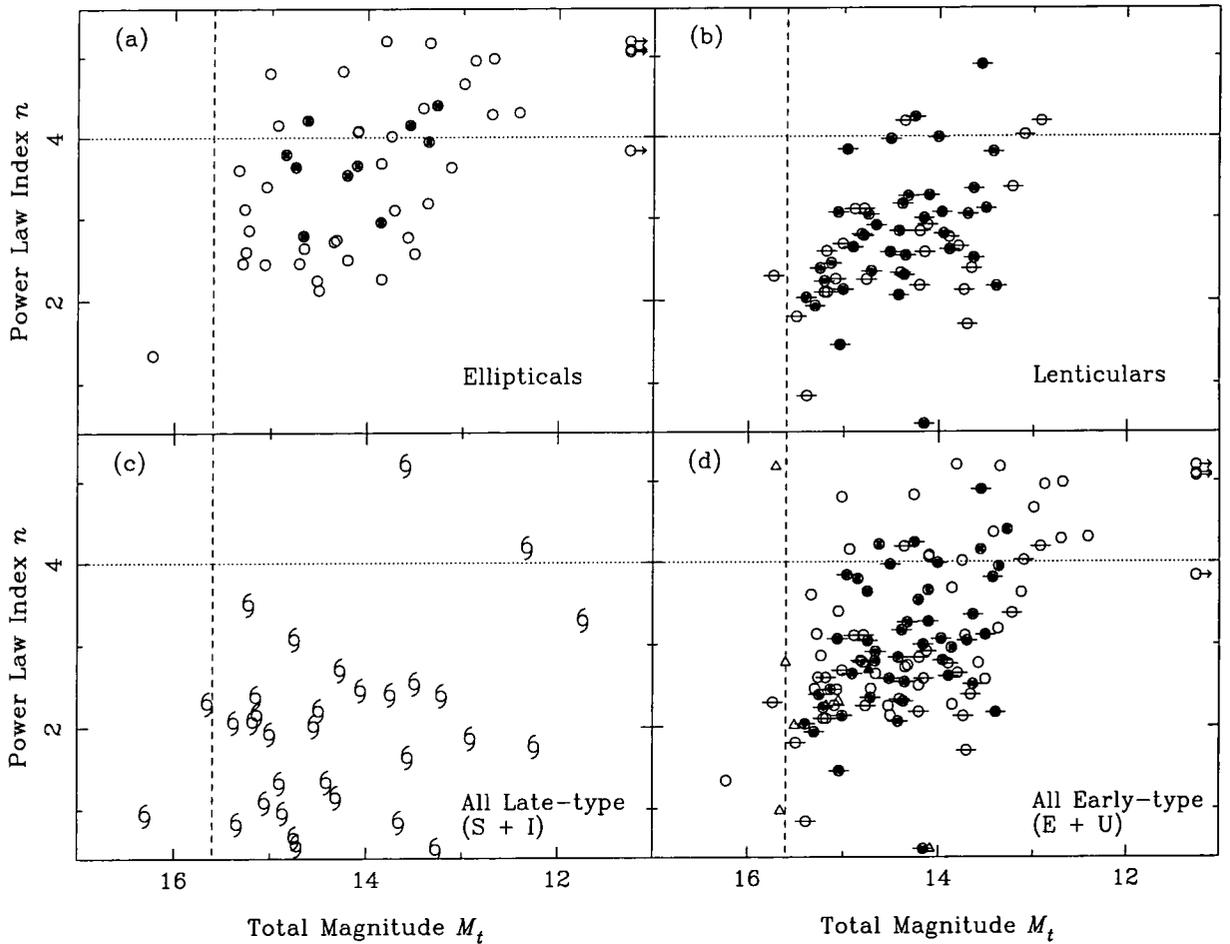
Figure 7.9: The distribution of power-law index n with asymptotic total magnitude M_t, separated into the different morphological types (c.f. fig 8, D'Onofrio *et al.* 1994). The magnitudes are corrected to Coma's redshift for Abell 1367 galaxies. The selection magnitude limit ($R{\sim}15.6$) is shown by the dotted line. The symbols in (d) are the same as those in (a) and (b) for ellipticals and lenticulars, with the addition of triangles for the unclassified (U) galaxies. The filled symbols in (a),(b) and (d) represent positive (2σ) detections of c_4 parameter for early-type galaxies.

examined (Figure 7.8(d), also including U galaxies), these proportions increase to 48% for $\log r_e < 0.5$, but still only 23% for $\log r_e > 0.5$. These figures do seem to indicate increasing evidence of disks for smaller r_e (and smaller n) galaxies.

Given the correlations of bulge-disk ratio with n, and n with galaxy size, one would expect a correlation between bulge-to-disk ratio (or bulge fraction) with galaxy size. Figures 7.10 and 7.11 are basically the same plots as Figures 7.8 and 7.9, but with B/T luminosity ratio rather than index n as the ordinate. The brightest galaxy in Abell 1367, NGC 3862, has not been included in these plots as it possesses a cD-like extended halo which photometrically mimics an exponential disk. It is apparent that B/T shows weaker

evidence of a trend with galaxy size than n. This is partly a result of observational scatter - a two-component model is harder to fit than a one-component fit. There is some degeneracy as the 4 parameters of the two-component model can produce similarly good fits to the profile from different combinations of values. This aside, it can be seen from the two figures is that smaller early-type galaxies do indeed become progressively more disk-dominated. At any given galaxy size or luminosity, there appears to be an upper limit on the relative size of the disk component, if this is how the light profiles are to be interpreted. This upper limit increases with decreasing size - for an $M = 13$ galaxy, the disk can account for up to 30% of the total luminosity, while for an $M = 15$ galaxy, this figure is increased to around 75%. The upper limit on disk fraction is larger at all magnitudes for galaxies visually classed S0 than those classed elliptical. This is not surprising, however, as early-type galaxies with very bright disks are more likely to be classed S0, whatever their inclination, whereas for less luminous disks it is the inclination angle which is the prime factor in deciding whether a galaxy is classed elliptical or S0.

Summarising, we have seen above that the universality of the de Vaucouleurs $r^{\frac{1}{4}}$-law does not hold for the vast majority of early-type galaxies. The exact shape of the light profile seems to be dependent at some level upon the luminosity or radial size of the galaxy. The two most commonly used forms for the light profiles of early-type galaxies are the two-component $r^{\frac{1}{4}}$ (bulge) plus exponential (disk) model and the Sersic single-component $r^{\frac{1}{n}}$ power law. By fitting both types of profile to early-type galaxies, it has been shown that the parameters of the profiles (n, B/T) correlate with the total magnitudes or effective radii of the galaxies, in the sense that smaller galaxies tend to have 'diskier' or 'shallower' profiles.

But which profile type is actually the better representation of the surface brightness profile of early-type galaxies? Figure 7.12 plots the difference between the χ^2 for the two-component fit and the minimum χ^2 for the $r^{\frac{1}{n}}$-law fit (using $n = 1, 2, 3, 4, 5$), against the total magnitude and half-light radius. The **reduced** χ^2 has been used to take into account the differences in the degrees of freedom between the different models. It is calculated as:-

$$\chi^2 = \frac{1}{n - m} \sum_{i=1}^{n} \frac{\left[\mu_{meas}(r_i) - \mu_{model}(r_i) \right]^2}{\Delta \mu_{meas}(r_i)^2} \qquad (7.7)$$

Where $n - m$ is the total degrees of freedom for the fitted model (number of points in the fit *minus* the number of free parameters in the model), while μ_{meas} and μ_{model} are respectively
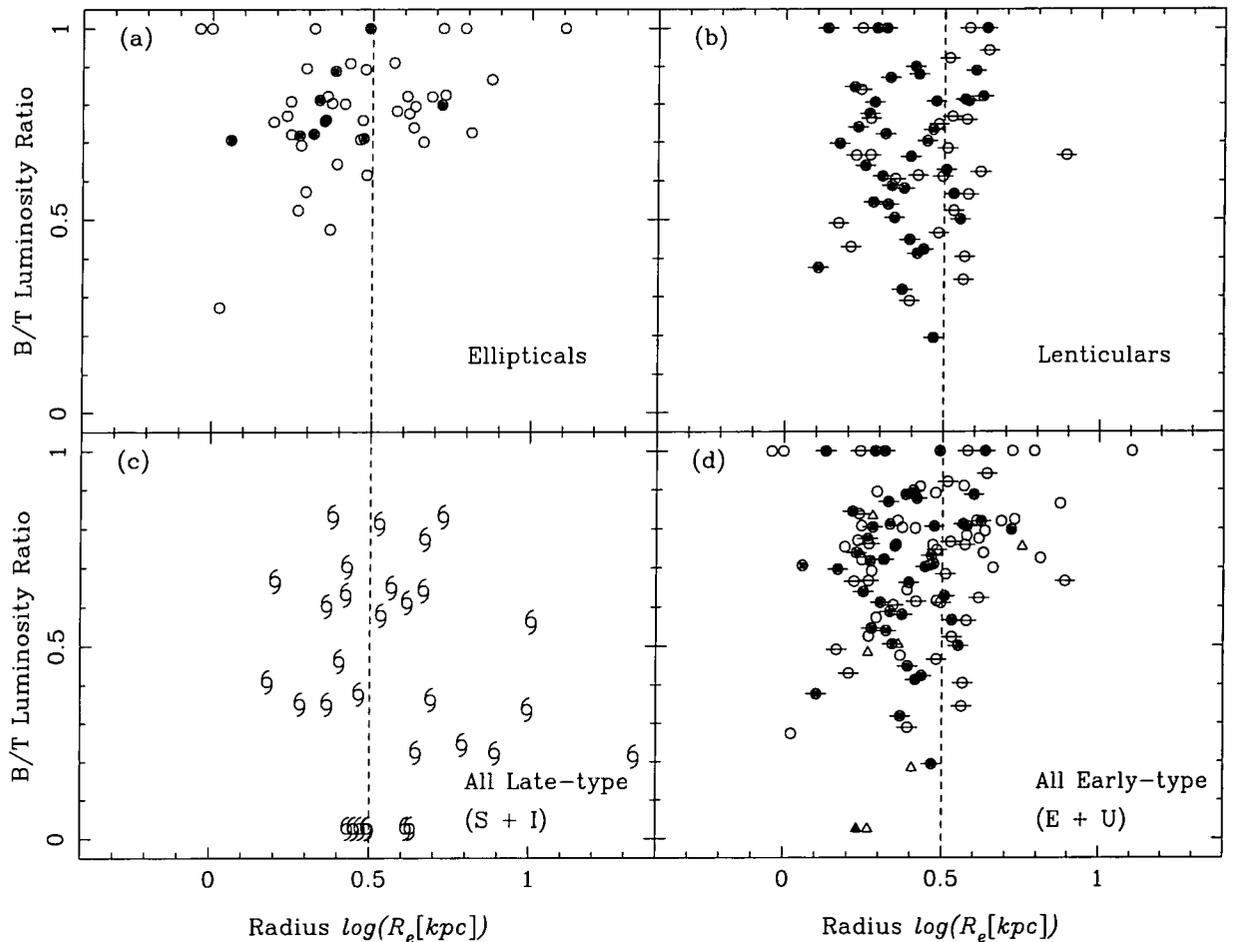
Figure 7.10: The distribution of bulge-total luminosity ratio B/T with non-parametric half-light radius r_e, separated into the different morphological types. The symbols in (d) are the same as those in (a) and (b) for ellipticals and lenticulars, with the addition of triangles for the unclassified (U) galaxies. The filled symbols in (a),(b) and (d) represent positive (2σ) detections of c_4 parameter for early-type galaxies.

the measured (i.e. seeing deconvolved) and fitted surface brightnesses at each point. The standard deviation on each point is taken as equal to $\Delta\mu_{meas}$ - the random measurement error from the profile-fitting routine (this includes a value equal to 0.2 times the seeing correction - this is added in quadrature to the measurement error, to account for errors in the deconvolution process, see Chapter 6).

It is apparent that for the majority of early-type galaxies, whether they have been previously classed elliptical or S0, an $r^{\frac{1}{4}}$ plus exponential model gives a fit with a lower χ^2 than an $r^{\frac{1}{n}}$-law model. In fact, 83% of those galaxies fitted with a two-component model generate a better quality fit than a single power-law model. Interesting, the few galaxies which show a much better fit for the $r^{\frac{1}{n}}$-law $(\Delta\chi^2 > 2)$ are all bright, extended objects. The suggestion of D'Onofrio *et al.* (1994) is that the large, high n, group of ellipticals
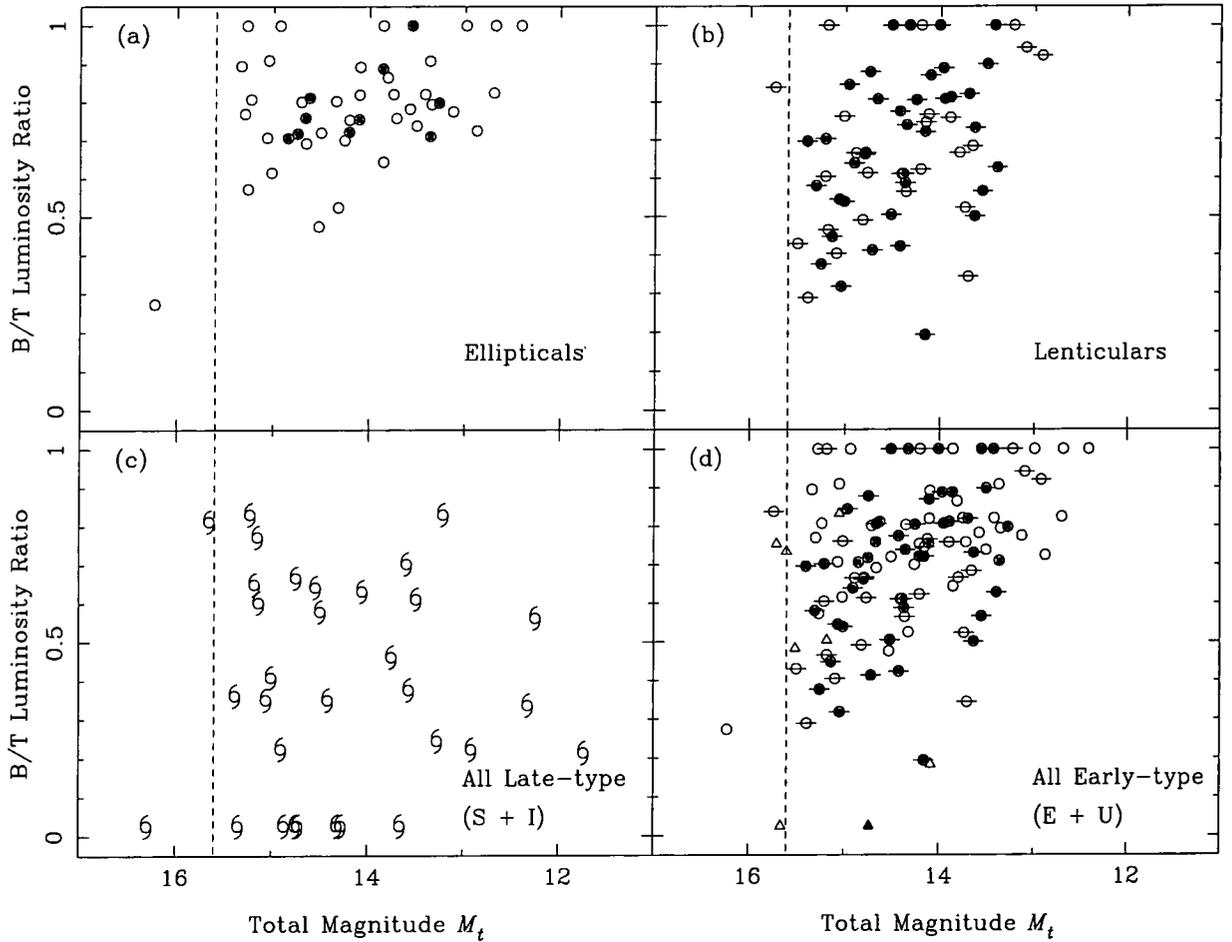
Figure 7.11: The distribution of bulge-total luminosity ratio B/T with asymptotic total magnitude M_t, separated into the different morphological types. The magnitudes are corrected to Coma's redshift for Abell 1367 galaxies. The selection magnitude limit ($R\sim15.6$) is shown by the dotted line. The symbols in (d) are the same as those in (a) and (b) for ellipticals and lenticulars, with the addition of triangles for the unclassified (U) galaxies. The filled symbols in (a),(b) and (d) represent positive (2σ) detections of c_4 parameter for early-type galaxies.

represents a bright family of merged objects. Certainly, this study does not contradict this assertion in any way. However, the evidence from the c_4 parameters and the relative quality (as measured by χ^2) of the profile fits does not support the assertion that the disk-less $r^{\frac{1}{n}}$ model for early-type galaxies can be extended to smaller ellipticals, which do not appear statistically distinguishable from those galaxies which have been traditionally classed S0.

The χ^2 statistic has been used here merely as an indication of relative quality-of-fit between the one and two component models. The actual values of χ^2 only have their usual statistical meaning if the measured data points are independent of each other and the errors are normally distributed. In this case, it is possible to use χ^2 (non-reduced) to calculate

the chi-square probability function $Q(0.5[n-m], 0.5\chi^2)$, which gives the probability that the minimised chi-square should exceed by chance the value χ^2. However, the measured data presented here has been through a seeing-deconvolution process which has had the effect of smoothing the data and reducing the errors. The χ^2 values obtained are therefore systematically smaller than the true values. The difference should be fairly independent of which profile model was fitted to the data. A rough estimate of what this difference should be can be calculated. Suppose that the deconvolution process has resulted in the random error amplitudes being reduced by 50%. One way of estimating the 'true' χ^2 is to add random errors back onto the measured data points. If we approximate all errors as normally distributed, then the standard deviation of the 'added' errors required to make up the difference will, by adding in quadrature, equal $\sqrt{0.75}$ times the standard deviation of the quoted errors (i.e. $\Delta\mu_{meas}$). Adding these errors into Equation 7.7:-

$$\chi_{true}^2 = \frac{1}{n-m}\sum_{i=1}^{n}\frac{[\mu_{meas}(r_i) - \mu_{model}(r_i) + A_i\Delta\mu_{meas}(r_i)]^2}{\Delta\mu_{meas}(r_i)^2} \qquad (7.8)$$

Where A_i is picked from a normal distribution of standard deviation σ_A equal to $\sqrt{0.75}$. Expanding Equation 7.8:-

$$\chi_{true}^2 = \frac{1}{n-m}\left(\sum_{i=1}^{n}\frac{[\mu_{meas}(r_i) - \mu_{model}(r_i)]^2}{\Delta\mu_{meas}(r_i)^2} + 2\sum_{i=1}^{n}A_i\left(\frac{\mu_{meas}(r_i) - \mu_{model}(r_i)}{\Delta\mu_{meas}(r_i)}\right) + \sum_{i=1}^{n}A_i^2\right) \qquad (7.9)$$

The middle term cancels out because the average of A_i is zero. The first term is just the calculated value of χ^2. The difference between the true and calculated χ^2 is thus:-

$$\chi_{true}^2 - \chi_{calc}^2 = \frac{1}{n-m}\sum_{i=1}^{n}A_i^2 \simeq \frac{\sum_{i=1}^{n}A_i^2}{n} = \sigma_A^2 = 0.75 \qquad (7.10)$$

In the impossible situation that the measurement errors in the deconvolved profiles are entirely (i.e. 100%) erased, then this difference between the true and calculated χ^2 values increases to 1.0. We can reasonably conclude that a correction constant between 0.75 and 1.0 needs to be added to every calculated value of χ^2. Provided that the number of points in the fit n is always large - this constant is not dependent on the model fit used. The comparison of χ^2 values for different models, as displayed in Figure 7.12, is therefore perfectly valid.

It could be argued that for the smaller galaxies, the reduced range between the *FWHM* and the sky background means fewer points in the profile fitting, and therefore little chance of distinguishing between the different types of profile. This resolution effect is clearly

visible in Figure 7.12, whereby the differences in the χ^2 are reduced for smaller and fainter galaxies. However, as a test of whether the profiles of small galaxies can be distinguished, a model single power-law profile was made-up ($r^{\frac{1}{2}}$-law, $r_e = 3''$ and $M_t = 14.3$) and fitted with the same one and two-component profiles as the real galaxies. The parameters of the model were chosen as being typical of a fainter elliptical in Coma. An $r^{\frac{1}{2}}$-law was chosen as it intermediate between an $r^{\frac{1}{4}}$ and exponential law and thus closely resembles a two-component fit. The reduced χ^2 for the $r^{\frac{1}{2}}$-law fit was 1.242 compared with $\chi^2 = 3.122$ for the $r^{\frac{1}{4}}$ plus exponential fit (the difference is plotted is Figure 7.12 with a star symbol). Although the difference is only 1.9, this is greater than the difference (in favour of the one-component fit) for any real galaxy smaller than $r_e = 4''$ or fainter than $M_t = 14.3$. One might expect, therefore, that if significant numbers of fainter galaxies (at least to $M_t = 14.3$, as faint as the model profile) were best fit by a single power-law, we would see more galaxies with a χ^2-difference of around 2 (just as can be seen for galaxies best-fit by a two-component profile).
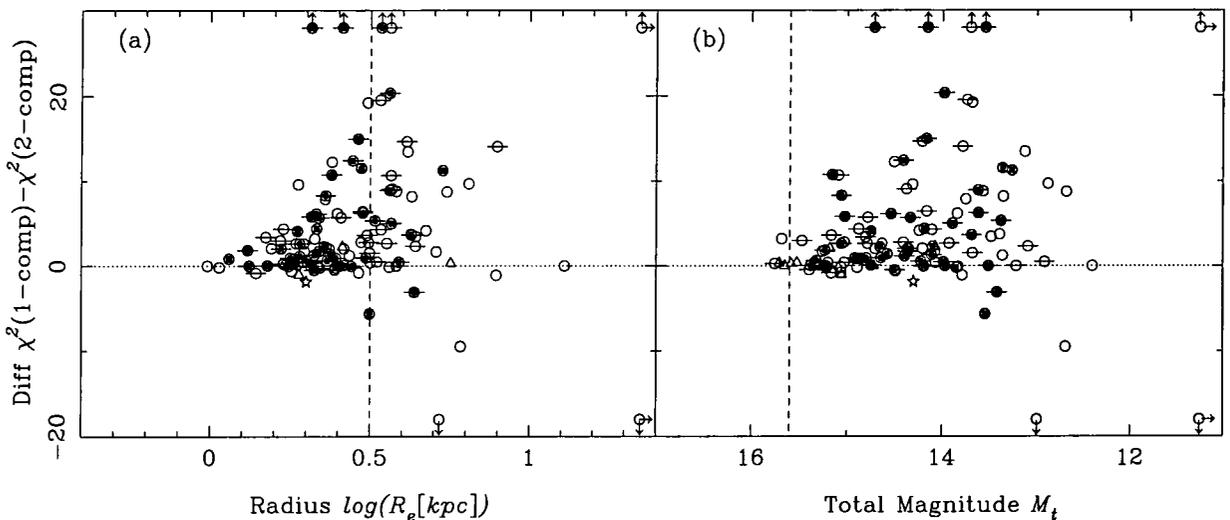
Figure 7.12: The difference between the quality-of-fit parameter χ^2 (**reduced**) for the two-component fit and the one-component fit, plotted against half-light radius (a) and asymptotic total magnitude (b), for all early-type (E) and unclassified (U) galaxies. The symbols are the same as those used in figures 7.8 to 7.11. The star symbol shows the χ^2 difference for a made-up model $r^{\frac{1}{2}}$ profile with $r_e = 3''$ and $M_t = 14.3$ (to demonstrate the resolution between different profiles for faint galaxies).
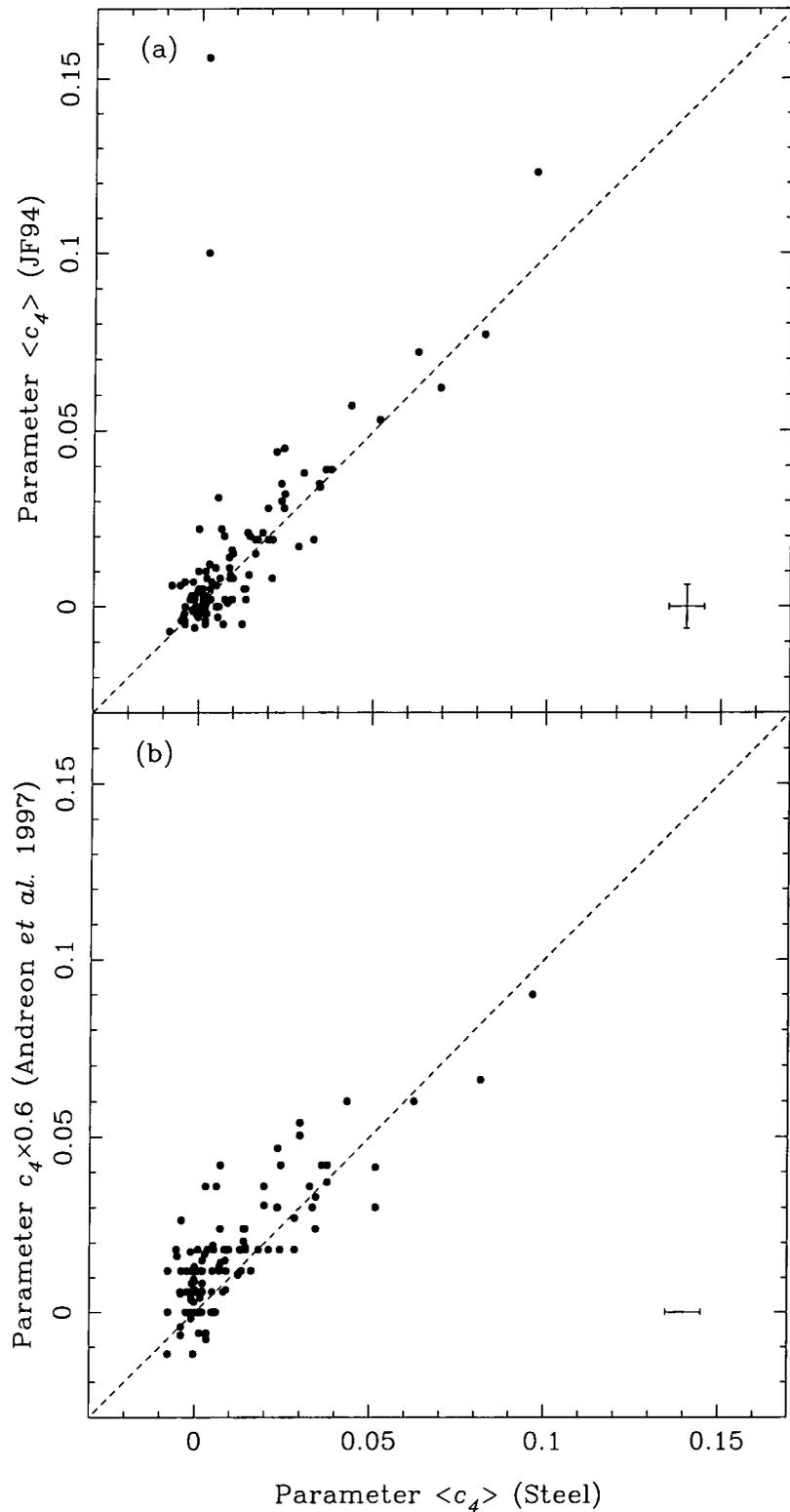
Figure 7.13: A comparison between the isophotal parameter $\langle c_4 \rangle$ measured by Steel for the Coma cluster, and those published by (a) JF94 and (b) Andreon *et al.* (1996). The error bars in the lower RH corner show the typical uncertainties for Steel and JF94 (Andreon *et al.* do not quote an uncertainty for their values). Note that the c_4 parameters published by Andreon *et al.* (1996) are extremum values rather than the intensity-weighted mean value $\langle c_4 \rangle$ computed by Steel and JF94.
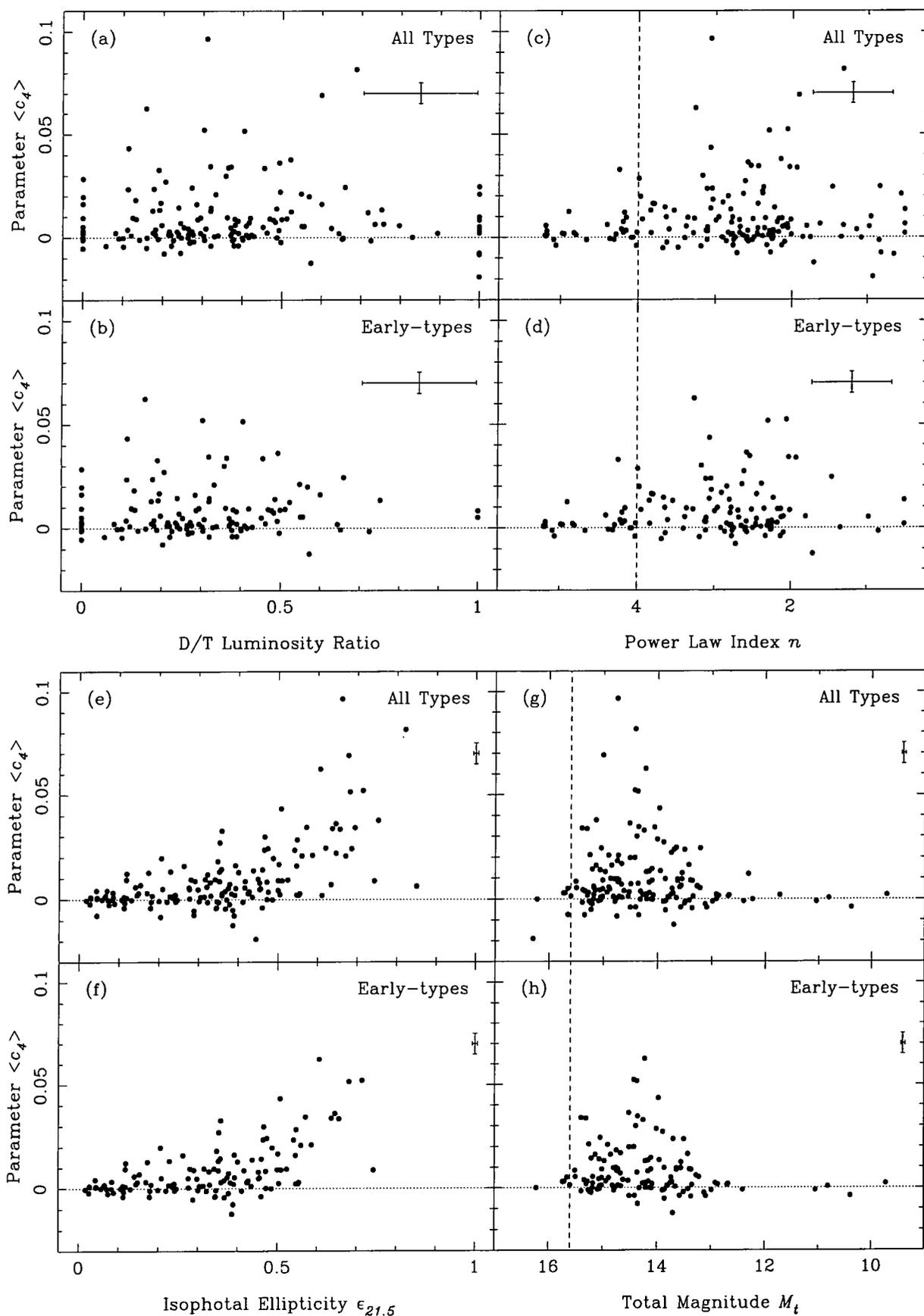
Figure 7.14: Isophotal parameter $\langle c_4 \rangle$ plotted against disk fraction D/T (a-b), power-law index n (c-d), apparent ellipticity $\epsilon_{21.5}$ (e-f) and total magnitude M_t (g-h). Each plot is shown twice - first will all 153 galaxies shown, then with just the early-type (E+U) galaxies. Typical uncertainties are shown by the error bars in the top RH corner.

7.5 Isophotal Shapes

This study has concentrated upon the detection of disks in early-type galaxies from the parameterisation of the surface brightness profile. An alternative method of disk detection comes from the measurement of deviations of the isophotes from a perfect ellipse (Carter 1987, Bender *et al.* 1989). The basis of this method is the quantification of the residuals of surface brightness along an elliptical isophote, in terms of the coefficients of a Fourier expansion (equation 7.11).

$$I(\theta, r) = I_0(r) + \sum_{i=1}^{N} (c_i \cos i\theta + s_i \sin i\theta) \tag{7.11}$$

A significantly positive 4th-order cosine term c_4 indicates a 'lemon'-shaped isophote. If a positive c_4 parameter persists across a range of isophotal radii, then the most likely explanation is that two photometric components of different apparent flattening (i.e. a bulge and a disk) are overlapping. The amplitude of the c_4 coefficient is highest where the two components are of similar surface brightness and the system is edge-on (thus giving the largest contrast in apparent ellipticity). In Section 7.3, it was shown that many face-on early-type galaxies, which had previously been regarded as disk-less ellipticals due to their lack of isophotal distortions, actually possessed relatively strong disks. This was predicted by Rix & White (1990), who demonstrated with models that galaxies with 20% disks would not show any significant c_4 for half the possible viewing angles.

Morphological studies of the Coma cluster, based on isophotal shapes, have been undertaken by JF94 and Andreon *et al.* (1996, hereafter A96). In order to compare with these two studies, and to add further morphological detail to this study, isophotal parameters have been measured for all 153 galaxies in the sample. Using the *GALPHOT*-based surface photometry routine (see Section 5.3), the higher-order terms c_3, s_3, c_4 and s_4 were measured as a function of isophotal radius for all the un-deconvolved galaxy images. As this study is comparing galaxies with a wide range of morphology (with greatly varying profile shapes for the high-order terms), it was decided to follow the method of JF94 in calculating an intensity-weighted mean value (and uncertainty) for c_4 and the other isophotal parameters, rather than the extremum value which is often used. Where repeat images of the same galaxy occur, the mean values for the parameters ($\langle c_3 \rangle$, $\langle s_3 \rangle$, $\langle c_4 \rangle$ and $\langle s_4 \rangle$) have been averaged.

Given that the isophotal parameters have been calculated by the author using virtually

the same software and averaging method as JF94, one would expect an excellent agreement between the two data-sets. The comparison is shown in Figure 7.13(a) and is indeed very good. There is strong disagreement for two objects, Dressler 90 and Dressler 146, which JF94 claim are both extremely pointed ($\langle c_4 \rangle$ equals 0.156 and 0.100 respectively), but Steel regards as having negligible c_4 ($\langle c_4 \rangle$ equals 0.002 for both objects). Given both the visual appearance of Dressler 90, which is not especially pointy, and the extremum value of 0.033 for c_4 quoted by JF94, one must conclude that the mean value of 0.156 is a mistype. The reason for the disagreement with Dressler 146, an SB0 galaxy, is less clear, but may result from an ID problem. These two galaxies aside, the agreement is good with an RMS scatter of only 0.008, which is comparable with the measurement uncertainties for both data-sets.

A more recent study of isophotal shapes of Coma galaxies, using R-band photometry, was published by A96. The comparison between the measurements of c_4 by the author and by A96 is displayed in Figure 7.13(b). Unfortunately, the c_4 parameter is measured differently by A96, who take the extremum value of c_4 (or the value of c_4 at r_e if the extremum is undefined), instead of the intensity-weighted average value ($\langle c_4 \rangle$) measured by Steel. The extremum value of c_4 is generally larger than the averaged value. According to JF94, the magnitude of $\langle c_4 \rangle$ is, in median, 60% of the magnitude of extremum c_4. In order to compare the c_4 data of A96 with the $\langle c_4 \rangle$ data of Steel, the values of c_4 have been multiplied by 0.6 in Figure 7.13(b) to approximate the averaged values. Despite the different definitions of c_4, the comparison is quite reasonable, with the RMS scatter not much greater than that between Steel and JF94 at 0.010. Part of the sample of A96 was taken from digitized photographic plates, and these objects only have c_4 quoted to the nearest 1% (0.01) - hence the quantisation of some of the c_4 values seen in Figure 7.13(b). A96 code their isophotal/photometric evidence for a disk component as *no* (none), *ft* (faint), *cl* (clear) and *st* (strong). Using the values of disk fraction D/T measured by Steel, it is possible to calculate the average disk fraction for each of the disk classes of A96 - this is summarised in Table 7.2.

It is clear that, despite the high scatter, the trend of the disk fraction is correlated with the A96 disk classes. However, it is significant that those galaxies regarded by A96 as having no detectable disk have a mean disk fraction of 24%, confirming the assertion of Rix & White (1990) that relatively strong disks can lie undetected in face-on galaxies.

In Figure 7.14, the isophotal parameter $\langle c_4 \rangle$ has been plotted against other parameters

Table 7.2: Comparison of the 'disk classes' of A96, calculated from isophotal shapes, with the average values of disk fraction D/T calculated by Steel.

Disk Class (A96)	Mean Disk Fraction D/T (Steel)	RMS Scatter about Mean D/T (Steel)
none	0.24	0.23
faint	0.30	0.13
clear	0.36	0.19
strong	0.44	0.28

measured from the data-set - the disk luminosity fraction D/T, the power-law index n, the isophotal ellipticity $\epsilon_{21.5}$ and the total asymptotic magnitude M_t. There are two plots for each parameter - one displaying the whole sample, the other with just the early-type galaxies (E, S0 and unclassified) shown. It is apparent from Figures 7.14(b) and (d) that while many early-type galaxies have an insignificant $\langle c_4 \rangle$ term, those with the greatest positive values of $\langle c_4 \rangle$ have intermediate values of shape parameters D/T ($\sim$0.4) and n ($\sim$2.5). This is precisely what is expected from a two component bulge and disk model, whereby the greatest isophotal deviations occur where the two components are of comparative brightness. In particular, plot (d) shows that for pure 'bulge' galaxies ($n \gtrsim 4$) and extremely 'disky' galaxies ($n \lesssim 1$), the $\langle c_4 \rangle$ parameter is not significantly different from zero for almost all objects.

For a fixed bulge-disk ratio, the biggest control on $\langle c_4 \rangle$ is the inclination, and hence the apparent ellipticity. Figures 7.14(e) and (f) show how the value of $\langle c_4 \rangle$ increases with apparent ellipticity, measured at isophote $R = 21.5$ (c.f. figure 5b in JF94, who use the $\langle c_4 \rangle$-ellipticity plane to define bulge-disk models). Figures 7.14(g) and (h) show how $\langle c_4 \rangle$ varies with total magnitude. Supporting the evidence from profile shapes, it is quite apparent that 'diskyness' increases considerably for fainter galaxies. Using $R = 14$ as a cut-off, brighter galaxies have an average $\langle c_4 \rangle$ of 0.0027±0.0003, while for those fainter than $R = 14$, this increases to 0.0104±0.0003. Once the disk begins to dominate over the bulge, c_4 will start to decrease again - this can be seen in Figure 7.14(b) where there are no galaxies with $\langle c_4 \rangle > 0.03$ for disk fraction D/T greater than a half. It is just possible that we are starting to see this effect in Figure 7.14(h). Fainter than $R \sim 14.5$, early-type

galaxies become so disky that the maximum possible value for $\langle c_4 \rangle$ at a given magnitude is decreasing (although the mean $\langle c_4 \rangle$ continues to increase). The plot hints at this possibility, but it would require a larger sample to prove statistically.

Summarising, isophotal parameters ($\langle c_3 \rangle$, $\langle s_3 \rangle$, $\langle c_4 \rangle$ and $\langle s_4 \rangle$) have been measured for all 153 galaxies in the sample, according to the prescription of JF94. Figure 7.13 demonstrates that the authors values agree well with the measurements of JF94 and A96. The relationship between the $\langle c_4 \rangle$ parameter, as an indicator of diskyness, and the profile shape parameters D/T and n is shown in Figures 7.14(a) to (d). Despite the large scatter (due largely to the difficulty in measuring the profile shape parameters), it is apparent that the *qualitative* behaviour of $\langle c_4 \rangle$ with shape is consistent with the commonly-asserted hypothesis that most elliptical and S0 galaxies comprise a population of two component (bulge and disk) systems with smoothly varying bulge-to-disk ratio, differentiated in visual appearance by viewing angle. It would be interesting to test this assertion *quantitatively* by investigating the relation between c_4, D/T and n using model galaxies. The dependence of profile shape on galaxy size (see Section 7.4) is also mirrored by the distribution of $\langle c_4 \rangle$ parameter with total magnitude, see Figures 7.14(g) and (h).

Chapter 8

Conclusions

The main aim of this project, outlined in Chapter 1, was to use surface brightness profiles to investigate the dichotomy between disky/non-disky ellipticals and the relationship between disky ellipticals and S0's. To this end, extensive software has been developed to deconvolve the effects of atmospheric seeing from $\mu(r)$ and fit parametric models to the profiles. Using model galaxies, it was shown that $\mu(r)$ can be reproduced to well within the *FWHM* of the seeing point-spread function (Chapters 5 and 6). With the imperfections of real data, the deconvolution is less reliable, but nonetheless the inner limit for profile-fitting can be extended to only 1 or 2 times the *FWHM*, representing a vast improvement on un-corrected data.

The seeing-deconvolution and profile-fitting software has been used on a magnitude-limited ($R{\sim}15.6$) sample of 153 galaxies in Coma and Abell 1367. For each galaxy, the surface brightness profile has been fitted with six different parametric shapes - the standard two-component $r^{\frac{1}{4}}$ plus exponential law, and the one-component Sersic $r^{\frac{1}{n}}$-law, with values of n equal to 1, 2, 3, 4 and 5. Additionally, non-parametric (i.e. model-independent) characteristics have been measured from both surface and aperture photometry, including total (asymptotic) magnitude, half-light radius/surface brightness and isophotal ellipticity (measured at $R = 21.5$). Although the aim of this study is to use the surface brightness profile to interpret morphology, the isophotal high-order terms (up to 4th order) have also been determined to provide additional morphological detail. This extensive data-set (see Tables A.1 and A.2 in Appendix A) has been used to look at various aspects of the morphology of early-type galaxies. The principle conclusions which have been reached by this study are outlined as follows:-

1. **A two-component $r^{\frac{1}{4}}$ plus exponential law fit is better than a single-component $r^{\frac{1}{4}}$-law fit at describing the profiles of early-type galaxies.** The evidence for this assertion is seen clearly in Figure 7.12, whereby 83% of early-type galaxies display a lower χ^2 (i.e. better fit) for the two-component model than the single power-law fit. Compare this to the 52% of early-type galaxies in the sample which are normally classified as S0. There are, however, two points here to consider. Firstly, the fact that there is generally a better fit for the two-component model does not necessarily mean that an $r^{\frac{1}{4}}$ plus exponential profile is absolutely correct. In fact, only a minority of objects have a χ^2 less than 2 and some (e.g. NGC 4919) are fitted very poorly. It is fair to say, though, that the two-component $r^{\frac{1}{4}}$ plus exponential profile fit is a reasonable approximation for a wide range of galaxies. Secondly, a good fit to an $r^{\frac{1}{4}}$ plus exponential profile does not, in isolation, indicate that there are two *physical* components, i.e. a bulge and a disk. This interpretation can only be confirmed by isophotal shape analysis and/or spectroscopy. The author's own measurements of isophotal parameter c_4 are plotted against profile shape parameters D/T and n in Figures 7.14(b) and (d). The c_4 parameter displays the greatest positive values for intermediate profile shapes ($D/T{\sim}0.4$, $n{\sim}2.5$), This is precisely where one would expect to locate two-component galaxies with components of similar brightness, and hence the greatest c_4 isophote deviations. This does suggest that the interpretation of a 'bulge' and 'disk' component model is the correct one.

2. **The traditional division of early-type galaxies into 'Elliptical' and 'S0' types is found to be a consequence of the viewing angle, rather than any physical difference in morphology.** The discovery of faint disks in many elliptical galaxies (Carter 1987, Bender *et al.* 1989), and the assertion by Rix & White (1990) that bright disks may lay undetected in elliptical galaxies, due to the viewing angle, has prompted much speculation over the relation between E and S0 galaxies. In particular, van den Bergh (1990) and JF94 have shown there is a deficit of face-on S0's and have concluded that many S0's have indeed been classified as ellipticals. In Section 7.3, the ellipticity distributions for this sample have been plotted, confirming the results of JF94 (who have a similar sample) that the distribution of ellipticals and S0's are totally inconsistent with having the same parent ellipticity distribution. As a test,

the early-type sample was separated into two classes on the basis of a viewing-angle independent parameter (disk fraction D/T, as measured by Steel) rather than on visual appearance (which is biased by viewing angle). Those with $D/T > 0.24$ were classed E+ (equivalent to S0) and those with $D/T < 0.24$ were classed E- (equivalent to ellipticals). Figure 7.5 shows the cumulative ellipticity distribution of classes E+ and E-. Clearly, there is no shortage of face-on disky early-type galaxies - the traditional segregation of early-type galaxies into elliptical and S0 classes is largely due to the change in visual appearance as a function of viewing angle. Further evidence that ellipticals and S0's are morphologically indistinguishable is seen from the plots of profile-shape parameters $(n, B/T)$ against galaxy size (M_t, r_e) - Figures 7.8 to 7.11. It is clear that there is considerable overlap in these plots between the distributions for ellipticals and S0's. The S0 galaxies do appear to extend into diskier regions (smaller B/T, smaller n), but this is not surprising - galaxies with brighter disks will appear disky over a greater range of viewing angle and will, therefore, be more likely to be classed S0 rather than elliptical. However, the prominence of the disk is only a secondary variable in the traditional classification of S0 and E - viewing angle is the prime variable. What is clear is that the vast majority of early-type galaxies possess an exponential component containing at least 10% of the total light.

3. **There is a general correlation (with much scatter) between the size of an early-type galaxy and its profile shape - the interpretation being that smaller galaxies are more disk-dominated than larger galaxies.** The correlations between the profile-shape parameters $(n, B/T)$ against galaxy size (M_t, r_e) are clearly displayed in Figures 7.8 to 7.11. In particular, Figure 7.8(d) - which shows n versus $r_{1/2}$ for all early-types - compares well with the relationship as found by Caon *et al.* (1993) and D'Onofrio *et al.* (1994). However, it has been argued that the best model profile for an early-type galaxy is not a Sersic $r^{\frac{1}{n}}$-law, but a two-component $r^{\frac{1}{4}}$ plus exponential law ('bulge' and 'disk'). The correlation of D/T versus size shows more scatter than the corresponding plots for n, largely due to the difficulty in measuring D/T. Despite this, it is still apparent that diskyness increases with decreasing galaxy luminosity. Confirmation of this trend is seen quite clearly in Figure 7.14(g) and (h), which shows the positive scatter in the $\langle c_4 \rangle$ values increasing dramatically

for galaxies fainter than $R \sim 13$.

What kind of scenario might have produced this correlation we see between the profile shapes of early-type galaxies with their luminosity or radius? For the densely-populated core of Coma, galaxy interactions, including mergers, must have been a highly significant factor in galaxy evolution. In a hierarchal model of galaxy evolution, is clear that larger galaxies are likely to have undergone more merging than smaller galaxies. D'Onofrio et al. (1994) suggests that the degree of merging experienced by a galaxy not only increases the size of the galaxy, it also re-distributes the matter such that the shape of the light profile is altered, changing from a low-n $r^{\frac{1}{n}}$-law to a high-n profile. However, it has been shown that the two-component $r^{\frac{1}{4}}$ plus exponential profile provides a much better fit to most early-type galaxies (although the index n of the Sersic law continues to be useful as an indicator of the profile shape). Clearly, we need a scenario whereby the degree of 'diskyness' is dependent upon the amount of merging which has taken place.

Such a scenario was proposed by Bender, Burstein & Faber (1992), who suggest that the characteristics of a galaxy are determined by the degree of gaseous dissipation occurring in the most recent merger. The first galaxies are formed by gaseous mergers, and are rapidly rotating and disky in their morphology. As the mergers proceed, each successive merger is increasingly stellar, resulting in larger systems which are slow-rotating and boxy (i.e. no disk). This is termed the gas/stellar (GS) continuum. In the core of a rich cluster like Coma, we should see galaxies which have merged along the whole range of GS continuum - from faint disky systems to bright disk-less systems. The correlations we see between profile shapes (and c_4) and the size of galaxies do seem to indicate that this is the case. The exact proportion of disk-less systems in the sample is hard to estimate, as the profile-fitting method in not sensitive to disks smaller than 10% of the total luminosity. The number of early-type galaxies in the Coma sample with no disks detected is 11, or 13 including the two cD galaxies - this is the maximum limit. The minimum limit is just the two cD galaxies. Thus the fraction of early-type galaxies in the core of Coma without a disk component is in the range 2% to 13%. This agrees with the estimation of JF94 that 10% of early-type systems are disk-less.

The evidence of a dichotomy between the disky and the bulk of the disk-less (or weak-disk) systems does not seem particularly strong, at least from the photometry. The distributions of profile shapes and galaxy sizes are continuous across the range of early-type

systems. There is, however, a break between the properties of the majority of disk-less or weak-disk systems which are fainter than $R{\sim}12$ and the few which are brighter. For this sample, of course, the brighter galaxies are the two cD's in Coma (NGC 4874 and NGC 4889) and the two brightest galaxies in Abell 1367 (NGC 3862 and NGC 3842). These objects are distinguished from all other early-type galaxies by their great luminosity and radial extent ($r_{1/2} > 200''$ for NGC 4874), and their unusual profile shapes. The light profiles of all four objects indicate vast extended halo's, which mimic a 'disk' component in the $r^{\frac{1}{4}}$ plus exponential fit, but are evidently not disks as they do not produce any positive deviation in the c_4 isophotal parameter. In any case, the position of these galaxies at the bottom of their clusters potential well indicates that their evolutionary history is likely to be very different from that of smaller galaxies.

An interesting extension to this project would be to extend the study to different environments - in the cluster halo's and field. Given the gas/stellar continuum scenario of Bender, Burstein & Faber (1992), one might expect lower density environments to display less evidence of a trend from faint/disky to bright/non-disky systems, as merging will not have proceeded to such a great extent. Unfortunately, the environmental baseline of this study was not great. Abell 1367 is a somewhat different environment to Coma, being less rich and less centrally concentrated - however, the sample for this cluster is too small (26 objects) to make any firm conclusions. In fact, the entire sample of galaxies observed with the INT in March 1994 (from which the sample used here is a small subset) includes a much wider range of environments, including fields out to over half the turnaround radius ($r{\sim}3°$) of Coma. At this distance, galaxies will not have yet visited the cluster core, and will therefore have had much less opportunity to interact, accrete material or merge. It is hoped that in the future, this study of light profiles of early-type galaxies will be extended to the remainder of the INT March 1994 dataset.

It is clear that the study of surface brightness profiles and isophotal parameters can provide important information about the morphological structure of early-type galaxies. In conjunction with data from other sources - including kinematics, stellar content and high-resolution studies of early-type cores - this information should help us build a picture of the evolutionary process, and how it is affected by the rich cluster environment.

References

Abell,G.O. (1958). *ApJS*, **3**, 211.

Abell,G.O. (1965). *Ann.Rev.Astr.Ap.*, **3**, 1.

Aguilar,L.A. & White,S.D.M. (1986). *ApJ*, **307**, 97.

Andreon,S., Davoust,E., Michard,R., Nieto,J.-L. & Poulain,P. (1996). *A&ASup*, **116**, 429. (A96)

Baggley,G. (1996). *Ph.D thesis, University of Oxford.*

Barnes,J.E. (1988). *ApJ*, **331**, 699.

Bender,R. (1988). *A&A*, **193**, L7.

Bender,R., Burstein,D. & Faber,S.M. (1992). *ApJ*, **399**, 462.

Bender,R., Surma,P., Doebereiner,S., Moellenhoff,C. & Madejsky,R. (1989). *A&A*, **217**, 35.

Bertola,F. & Capaccioli (1975). *ApJ*, **200**, 439.

Binggeli,B., Sandage,A. & Tammann,G,A. (1985). *AJ*, **90**, 1681.

Binggeli,B., Sandage,A. & Tarenghi,M. (1984). *AJ*, **89**, 64.

Boroson,T. (1981). *ApJS*, **46**, 177.

Bothun,G.D (1981). *Ph.D thesis, University of Washington (Seattle).*

Bower,R.G., Lucey,J.R. & Ellis,R.S. (1992). *MNRAS*, **254**, 589.

Burstein,D. (1979). *ApJ*, **234**, 829.

Burstein,D. & Heiles,C. (1984). *ApJS*, **54**, 33.

Butcher,H.R. & Oemler,A. (1978). *ApJ*, **226**, 559.

Butcher,H.R. & Oemler,A. (1985). *ApJS*, **57**, 665.

Caon,N. & Einasto,M. (1995). *MNRAS*, **273**, 913.

Caon,N., Capaccioli,M. & D'Onofrio,M. (1993). *MNRAS*, **265**, 1013.

Capaccioli,M. (1985). *Toulouse, New Aspects of Galaxy Photometry conf. proc.*, p.53.

Carter,D. (1978). *MNRAS*, **182**, 797.

Carter,D. (1987). *ApJ*, **312**, 514.

Cowie,L.L. & Songaila,A (1977). *Nature*, **226**, 501.

Davies,R.L., Efstathiou,G., Fall,S.M., Illingworth,G. & Schechter,P.L. (1983). *ApJ*, **266**, 41.

de Vaucouleurs,G. (1948). *Ann.Astrophys.*, **11**, 247.

Djorgovski,S. & Davis,M. (1987). *ApJ*, **313**, 59.

Doi,M., Fukugita,M., Okamura,S. & Tarusawa,K. (1995). *ApJS*, **97**, 77.

Dressler,A. (1980a). *ApJ*, **236**, 351.

Dressler,A. (1980b). *ApJS*, **42**, 565.

Dressler,A. (1984). *Ann.Rev.Astr.Ap.*, **22**, 185.

Dressler,A., Lynden-Bell,D., Burstein,D., Davies,R.L., Faber,S.M., Terlevich,R. & Wegner,G. (1987). *ApJ*, **313**, 42.

Faber,S.M. & Jackson,R.E. (1976). *ApJ*, **204**, 668.

Fall,S.M. (1983). *IAU symp.proc.*, **100**, 391.

Franx,M., Illingworth,G. & Heckman,T. (1989). *AJ*, **98**, 538.

Freeman,K.C. (1970). *ApJ*, **160**, 811.

Godwin,J.G. & Peach,J.V. (1977). *MNRAS*, **181**, 323.

Godwin,J.G., Metcalfe,N. & Peach,J.V. (1983). *MNRAS*, **202**, 113.

Gott,J.R. & Thuan,T.X. (1976). *ApJ*, **204**, 649.

Gunn,J.E. & Gott,J.R. (1972). *ApJ*, **176**, 1.

Hubble,E. (1936). *The Realm of the Nebulae.*

Hubble,E. & Humason,M.L. (1931). *ApJ*, **74**, 43.

Jedrzejewski,R.I. (1987). *MNRAS*, **226**, 747.

Jorgensen,I. & Franx,M. (1994). *ApJ*, **433**, 553. (JF94)

Kent,S.M. (1981). *ApJ*, **245**, 805.

Kent,S.M. (1986). *AJ*, **91**, 1301.

Kormendy,J. (1977). *ApJ*, **217**, 406.

Kormendy,J. (1980). *ESO Garching, 2D Photometry conf. proc.*, p.191.

Kormendy,J. (1982). *SAAS-FEE, Morphology & Dynamics conf. proc.*, p.115.

Landolt,A.U. (1992). *AJ*, **104**, 340.

Larson,R.B., Tinsley,B.M. & Caldwell,C.N. (1980). *ApJ*, **237**, 692.

Lobo,C., Biviano,A., Durret,F., Gerbal,D., Le Fevre,O., Mazure,A. & Slezak,E. (1997). *A&ASup*, **122**, 409.

Lucey,J.R., Bower,R.G. & Ellis,R.S. (1991). *MNRAS*, **249**, 755.

Lucey,J.R., Guzman,R., Carter,D. & Terlevich,R.J. (1991). *MNRAS*, **253**, 584.

Michard,R. (1985). *A&ASup*, **59**, 205.

Morgan,W.W. (1961). *Proc.Nat.Acad.Sci.*, **47**, 905.

Oemler,A. (1974). *ApJ*, **194**, 1.

Peebles,P.J.E. (1970). *ApJ(letters)*, **75**, 13.

Quintana,H. & Lawrie,D.G. (1982). *AJ*, **87**, 1.

Rix,H. & White,S.D.M. (1990). *ApJ*, **362**, 52.

Roddier,F. (1981). *Progress in Optics*, **19**, 281.

Rood,H.J. & Baum,W.A. (1967). *AJ*, **72**, 398.

Saglia,R.P., Bender,R. & Dressler,A. (1993). *A&A*, **279**, 75.

Saglia,R.P., Bertschinger,E., Baggley,G., Burstein,D., Colless,M., Davies,R.L., McMahan,R.K. & Wegner,G. (1997). *ApJS*, **109**, 79.

Sandage,A. & Tammann,G.A. (1981). *Revised Shapley-Ames Catalogue of Bright Galaxies*.

Sandage,A., Binggeli,B. & Tammann,G.A. (1985a). *AJ*, **90**, 395.

Sandage,A., Binggeli,B. & Tammann,G.A. (1985b). *AJ*, **90**, 1759.

Sandage,A. (1961). *The Hubble Atlas*.

Sandage,A., Freeman,K.C. & Stokes,N.R. (1970). *ApJ*, **160**, 831.

Schneider,D.P., Hoessel,J.G. & Schneider,D.P. (1983). *ApJ*, **268**, 476.

Schombert,J.M. & Bothun,G.D. (1987). *AJ*, **93**, 60.

Scorza,C. & Bender,R. (1990). *A&A*, **235**, 49.

Sersic,J.L. (1968). *Atlas de Galaxies Australes*.

Shaw,M.A. & Gilmore,G. (1990). *MNRAS*, **242**, 59.

Simien,F. & Michard,R. (1990). *A&A*, **227**, 11.

Spitzer,L. & Baade,W. (1951). *ApJ*, **113**, 413.

Strom,S.E. & Strom,K.M. (1979). *Scientific American*, **240**, 72.

Sullivan,W.T., Bates,B., Bothun,G.D. & Schommer,R.A. (1981). *AJ*, **86**, 919.

Terlevich,R., Davies,R.L., Faber,S.M. & Burstein,D. (1981). *MNRAS*, **196**, 381.

Toomre,A. & Toomre,J. (1972). *ApJ*, **178**, 623.

van Albada,T.S. (1982). *MNRAS*, **201**, 939.

van den Bergh,S. (1976). *ApJ*, **206**, 883.

van den Bergh,S. (1990). *ApJ*, **348**, 57.

White,S.D.M., Briel,U.G. & Henry,J.P. (1993). *MNRAS*, **261**, L8.

Appendix A

Tables of Photometric and Isophotal Parameters

This appendix contains tables of the photometric and isophotal parameters measured for all 153 galaxies in the sample. The data is separated in two tables. Table A.1, comprising columns (1) to (12), details the model-independent parameters, including the isophotal parameters. Table A.2, comprising columns (13) to (24), gives the parameters derived from profile-fitting. In all columns, the parenthesised value after each measurement represents the uncertainty on the *last significant digit* of the measurement (e.g. 0.785(22) means 0.785±0.022). The key for each column is as follows:-

1. The name of the galaxy. For Coma objects, either the Dressler (1980) number is given if available, or the Godwin, Metcalfe & Peach (1977) number otherwise. For Abell 1367 objects, the Butcher & Oemler (1985) number is given.

2. The broad morphological class of galaxy - E, S, I or U, as detailed in Chapter 2. For E galaxies, the letter in brackets gives the traditional (i.e. visual) classification of the object - E for ellipticals, L for lenticulars/S0's.

3. The half-light radius $r_{1/2}$, measured from the aperture photometry. Expressed as a log of the value in arc-seconds.

4. The half-light surface brightness $\langle\mu\rangle_{1/2}$ (i.e. average μ within $r_{1/2}$), measured from the aperture photometry.

5. The total asymptotic magnitude M_t, measured from extrapolation of the aperture photometry. *Erratum - the cosmological* $(1 + z)^4$ *surface brightness correction was wrongly included in these total magnitude values. Add 0.1 to each magnitude to remove this correction.*

6. The surface brightness $\mu(r_{1/2})$ measured *at* the half-light radius r_e from the surface photometry.

7. The logarithm of the photometric diameter $D_{19.23}$ - the effective diameter $(2\sqrt{ab})$ of the *ellipse* enclosing an average surface brightness of $R = 19.23$. This is equivalent to the photometric diameter D_V measured at $V = 19.8$ or D_n measured at $B = 20.75$. Where no value is entered, the galaxy does not reach a average μ of 19.23 at any radius, so no measurement is possible.

8. The isophotal ellipticity measured at $R = 21.5$, interpolated from the surface photometry. This is equivalent to the ellipticity of JF94, measured at $r = 21.85$.

9. The third-order cosine term of the Fourier expansion of the isophote deviations. Following the convention of JF94, these are intensity weighted-means, measured between radius limits of $2 \times FWHM$ and the equivalent radius where $\mu(r)$ falls to $R = 23.0$.

10. The third-order sine term of the Fourier expansion of the isophote deviations.

11. The fourth-order cosine term of the Fourier expansion of the isophote deviations.

12. The fourth-order sine term of the Fourier expansion of the isophote deviations.

13. The effective radius r_e of a pure exponential-law model fit (in arc-seconds). If the galaxy fitted this law perfectly, r_e would equal the half-light radius $r_{1/2}$.

14. The effective surface brightness $\langle\mu\rangle_e$ of a pure exponential-law model fit. If the galaxy fitted this law perfectly, r_e would equal the half-light surface brightness $\langle\mu\rangle_{1/2}$.

15. As (13) for a pure $r^{\frac{1}{2}}$-law fit.

16. As (14) for a pure $r^{\frac{1}{2}}$-law fit.

17. As (13) for a pure $r^{\frac{1}{4}}$-law fit.

18. As (14) for a pure $r^{\frac{1}{4}}$-law fit. Note that the effective parameters from the $r^{\frac{1}{3}}$-law and $r^{\frac{1}{5}}$-law fits can be found in the tables for individual galaxies in Appendix D.

19. The index n of the best-fitting single-component Sersic $r^{\frac{1}{n}}$-law. This is calculated from an average of two methods, described in Section 7.4.

20. The effective radius $r^{b}{}_{e}$ of the $r^{\frac{1}{4}}$ or 'bulge' component of the two-component $r^{\frac{1}{4}}$ plus exponential law fit. If no significant bulge, no value is shown.

21. The effective surface brightness $\langle\mu\rangle^{b}{}_{e}$ of the $r^{\frac{1}{4}}$ or 'bulge' component of the two-component $r^{\frac{1}{4}}$ plus exponential law fit. If no significant bulge, no value is shown.

22. The effective radius $r^{d}{}_{e}$ of the exponential or 'disk' component of the two-component $r^{\frac{1}{4}}$ plus exponential law fit. If no significant disk, no value is shown.

23. The effective surface brightness $\langle\mu\rangle^{d}{}_{e}$ of the exponential or 'disk' component of the two-component $r^{\frac{1}{4}}$ plus exponential law fit. If no significant disk, no value is shown.

24. The luminosity ratio D/B of the exponential (disk) component to the $r^{\frac{1}{4}}$ (bulge) component from the two-component fit. If the disk luminosity is zero, then the parenthesised number is an upper-limit on D/B.

Table A.1: Global (non-parametric) and isophotal parameters for Coma and Abell 1367 galaxies.

Name (1)	Type (2)	$\log r_{1/2}$ (3)	$\langle\mu\rangle_{1/2}$ (4)	M_t (5)	$\mu(r_{1/2})$ (6)	$\log D_{19.23}$ (7)	$\epsilon_{21.5}$ (8)	$\langle c_3\rangle$ (9)	$\langle s_3\rangle$ (10)	$\langle c_4\rangle$ (11)	$\langle s_4\rangle$ (12)
Abell 1656 (Coma)											
D62	E(L)	0.646(35)	19.887(120)	14.663(56)	21.184(125)	0.757(5)	0.5017(62)	0.0041(46)	-0.0048(45)	0.0168(46)	-0.0007(45)
D63	E(L)	0.563(6)	19.942(26)	15.134(19)	21.153(32)	0.639(5)	0.5461(37)	-0.0046(39)	-0.0037(39)	0.0161(39)	-0.0002(39)
D64	E(E)	0.739(43)	20.740(150)	15.050(68)	22.057(187)	0.571(5)	0.0180(111)	-0.0039(59)	-0.0039(60)	-0.0004(60)	0.0016(59)
D65	E(L)	0.667(12)	19.739(42)	14.407(27)	20.864(52)	0.804(5)	0.4597(54)	0.0029(37)	-0.0027(38)	-0.0039(38)	0.0040(37)
D68	E(L)	0.771(39)	19.822(131)	13.972(65)	21.051(159)	0.893(5)	0.5073(79)	0.0009(30)	-0.0002(30)	0.0434(30)	-0.0022(29)
D69	E(E)	0.806(63)	19.374(237)	13.350(79)	20.908(325)	1.068(4)	0.1120(80)	-0.0015(26)	-0.0001(26)	0.0013(26)	-0.0003(26)
D70	E(E)	0.650(43)	19.344(156)	14.098(60)	20.780(186)	0.920(4)	0.0722(76)	0.0019(41)	0.0021(41)	-0.0002(41)	0.0006(41)
D71	E(L)	0.545(11)	20.027(34)	15.304(28)	20.981(48)	0.560(6)	0.6554(50)	0.0022(52)	-0.0015(53)	0.0336(53)	0.0042(52)
D72	E(E)	0.522(14)	18.712(49)	14.109(28)	19.907(69)	0.970(4)	0.3570(59)	-0.0044(29)	0.0025(29)	0.0145(29)	-0.0020(28)
D78	E(E)	0.983(11)	19.787(43)	12.875(21)	21.292(50)	1.133(4)	0.2273(73)	-0.0005(23)	-0.0020(23)	0.0016(23)	-0.0001(23)
D79	E(L)	0.751(5)	18.971(23)	13.222(17)	20.191(21)	1.129(5)	0.4555(36)	-0.0007(27)	0.0011(27)	0.0052(27)	-0.0021(27)
D80	E(L)	0.748(25)	20.098(91)	14.362(38)	21.490(79)	0.803(5)	0.3781(84)	-0.0024(50)	0.0003(50)	0.0074(50)	-0.0014(50)
D81	E(E)	0.832(36)	20.414(132)	14.260(50)	21.898(163)	0.799(5)	0.2392(55)	0.0000(33)	0.0043(32)	0.0021(32)	-0.0028(33)
D82	S	1.178(13)	20.131(37)	12.245(33)	21.003(62)	1.095(6)	0.1107(116)	0.0257(88)	-0.0172(89)	-0.0001(89)	-0.0063(87)
D84	E(L)	0.507(11)	18.900(37)	14.370(26)	20.004(51)	0.908(5)	0.6807(50)	0.0073(50)	-0.0060(48)	0.0516(48)	0.0062(46)
D87	E(E)	0.417(21)	19.312(68)	15.232(40)	20.435(86)	0.692(5)	0.0889(65)	-0.0003(42)	0.0036(43)	-0.0019(43)	-0.0009(42)
D88	E(L)	0.459(17)	18.300(63)	14.010(30)	19.637(94)	1.007(4)	0.5474(32)	0.0000(32)	-0.0088(32)	0.0285(33)	0.0037(31)
D89	S	0.637(3)	18.750(17)	13.570(18)	19.372(25)	1.105(4)	0.8499(16)	0.0206(79)	-0.0113(80)	0.0064(80)	-0.0057(79)
D90	U	0.534(16)	19.843(53)	15.176(34)	20.937(56)	0.636(5)	0.5466(40)	0.0075(44)	-0.0008(46)	0.0022(45)	0.0036(45)
D91	E(L)	0.580(16)	18.401(55)	13.505(30)	19.628(82)	1.107(4)	0.5411(61)	0.0010(25)	-0.0003(25)	0.0235(25)	-0.0038(24)
D92	E(L)	0.452(10)	18.512(38)	14.255(22)	19.830(56)	0.948(4)	0.3577(73)	0.0005(46)	-0.0059(46)	0.0328(46)	-0.0052(46)
D97	S	1.502(4)	21.241(18)	11.734(19)	22.018(17)	1.128(5)	0.3584(139)	0.0010(56)	-0.0053(56)	0.0019(56)	0.0000(56)
D98	S	0.596(11)	19.038(38)	14.060(25)	20.166(57)	0.956(5)	0.6934(19)	0.0009(16)	-0.0007(16)	0.0343(16)	0.0030(15)
D99	S	0.624(6)	20.465(21)	15.348(22)	21.226(28)	0.409(7)	0.0442(109)	0.0014(52)	0.0000(51)	-0.0076(51)	-0.0064(52)
D100	S	0.454(3)	19.323(17)	15.058(17)	20.238(18)	0.721(6)	0.2441(42)	-0.0063(30)	-0.0077(29)	-0.0004(30)	0.0017(30)
D101	E(L)	0.477(7)	18.767(28)	14.387(19)	20.037(31)	0.909(4)	0.4658(73)	0.0019(24)	-0.0043(24)	0.0299(25)	-0.0013(24)
D102	I	0.554(19)	19.992(67)	15.228(33)	21.285(66)	0.627(5)	0.3857(51)	-0.0031(48)	-0.0017(45)	-0.0050(47)	0.0022(46)
D103	S	0.599(27)	18.587(103)	13.596(38)	20.095(127)	1.065(4)	0.2758(43)	-0.0053(27)	0.0005(27)	0.0057(27)	-0.0103(27)
D104	E(L)	0.501(15)	18.605(55)	14.106(28)	19.906(75)	0.975(4)	0.2910(34)	-0.0018(18)	-0.0018(18)	0.0089(18)	-0.0038(18)
D105	E(E)	0.787(11)	19.057(42)	13.125(23)	20.352(56)	1.137(4)	0.0745(55)	0.0006(16)	-0.0004(15)	-0.0025(16)	0.0001(15)
D106	E(L)	0.339(15)	18.506(55)	14.814(28)	19.794(70)	0.841(4)	0.3045(38)	0.0023(21)	0.0017(21)	0.0012(21)	0.0068(21)
D107	E(E)	0.586(29)	19.634(96)	14.710(54)	20.773(130)	0.755(5)	0.4346(25)	0.0026(17)	-0.0008(17)	0.0012(17)	-0.0003(17)
D108	E(L)	0.423(13)	19.018(47)	14.905(26)	20.246(50)	0.787(4)	0.5596(25)	0.0018(26)	0.0023(25)	0.0209(26)	0.0016(25)
D109	U	0.577(7)	18.966(28)	14.084(19)	20.256(28)	0.954(4)	0.0660(92)	0.0024(32)	-0.0025(32)	0.0018(32)	0.0012(31)
D110	E(L)	0.591(24)	19.695(84)	14.744(42)	20.914(116)	0.752(5)	0.3478(62)	-0.0002(38)	-0.0014(38)	0.0182(38)	0.0085(38)
D111	E(L)	0.743(15)	19.608(54)	13.896(29)	20.866(51)	0.935(4)	0.3222(57)	0.0035(30)	0.0016(30)	-0.0013(31)	-0.0029(30)
D112	U	0.452(9)	19.307(31)	15.050(23)	20.383(31)	0.729(5)	0.2356(48)	-0.0001(41)	-0.0005(41)	0.0009(41)	-0.0031(42)
D115	E(L)	0.566(15)	19.621(55)	14.794(29)	20.900(68)	0.753(4)	0.3414(55)	0.0003(31)	0.0012(30)	0.0096(31)	0.0041(30)
D116	E(L)	0.607(5)	19.453(23)	14.423(17)	20.784(21)	0.845(4)	0.2063(78)	0.0059(57)	0.0106(56)	0.0198(58)	0.0154(55)
D117	E(L)	0.589(4)	19.706(20)	14.766(17)	20.767(25)	0.728(5)	0.4717(45)	-0.0060(32)	0.0048(32)	0.0001(32)	0.0028(32)
D118	E(E)	0.748(12)	19.314(42)	13.578(24)	20.562(50)	1.024(5)	0.1127(65)	0.0012(23)	-0.0001(23)	-0.0040(23)	0.0031(23)
D119	U	0.404(8)	18.747(32)	14.732(18)	20.243(34)	0.833(4)	0.3287(48)	0.0025(25)	0.0010(25)	0.0082(25)	-0.0058(25)
D120	E(E)	0.418(6)	18.589(24)	14.505(19)	19.605(31)	0.911(4)	0.1791(69)	-0.0024(24)	-0.0023(24)	-0.0040(24)	0.0029(24)
D121	E(E)	0.601(6)	18.372(25)	13.369(18)	19.607(32)	1.138(4)	0.3672(49)	0.0004(17)	0.0034(17)	-0.0044(17)	0.0074(17)
D122	E(L)	0.515(15)	19.087(53)	14.517(30)	20.328(53)	0.858(5)	0.6455(41)	0.0062(35)	-0.0026(35)	0.0362(36)	0.0082(35)
D123	I	0.622(3)	19.972(17)	14.869(17)	20.837(18)	0.647(6)	0.4492(44)	0.0031(33)	0.0001(33)	0.0098(33)	-0.0237(33)
D124	E(E)	0.561(10)	18.654(34)	13.854(24)	19.747(48)	1.032(4)	0.3459(33)	0.0017(15)	0.0000(15)	-0.0009(15)	0.0018(15)
D125	E(E)	0.171(10)	17.785(38)	14.934(21)	19.283(38)	0.857(4)	0.1701(33)	0.0004(23)	0.0020(23)	0.0032(23)	-0.0016(23)
D126	E(L)	0.495(13)	19.481(42)	15.010(31)	20.479(65)	0.710(5)	0.5098(37)	-0.0042(31)	0.0072(31)	0.0090(32)	0.0015(32)
D127	E(L)	0.378(4)	19.379(20)	15.496(17)	20.469(21)	0.632(5)	0.3744(63)	0.0049(41)	-0.0005(41)	0.0054(41)	0.0043(41)
D128	E(L)	0.276(6)	18.626(25)	15.251(18)	19.873(26)	0.754(4)	0.5862(47)	0.0161(42)	-0.0056(40)	0.0211(41)	0.0118(41)
D129	E(E)	2.303(43)	23.228(145)	9.715(71)	24.352(216)	1.298(6)	0.1447(84)	-0.0019(15)	0.0016(15)	0.0021(15)	0.0015(15)
D130	E(E)	0.490(15)	18.302(54)	13.858(29)	19.519(69)	1.043(4)	0.2885(58)	-0.0020(24)	0.0012(24)	-0.0053(24)	-0.0016(24)
D131	E(L)	0.723(3)	19.247(19)	13.636(16)	20.436(19)	1.019(5)	0.4167(57)	-0.0005(30)	-0.0009(30)	0.0087(30)	-0.0019(30)
D132	E(L)	0.449(10)	19.303(38)	15.060(22)	20.665(42)	0.730(4)	0.4373(63)	-0.0015(43)	0.0028(43)	0.0139(43)	-0.0014(43)
D133	E(E)	0.531(21)	18.402(72)	13.751(36)	19.647(104)	1.056(4)	0.2414(42)	0.0007(16)	-0.0003(16)	0.0023(16)	0.0003(16)
D135	E(E)	0.464(14)	19.577(51)	15.261(28)	20.817(59)	0.661(5)	0.2206(69)	-0.0035(40)	-0.0051(41)	-0.0010(40)	-0.0003(41)
D136	E(E)	0.231(7)	18.000(26)	14.849(19)	19.157(35)	0.864(4)	0.2629(56)	-0.0002(23)	-0.0050(23)	0.0161(23)	0.0024(23)
D137	E(E)	0.663(7)	18.868(28)	13.556(19)	20.091(37)	1.067(4)	0.1182(51)	-0.0020(26)	-0.0010(26)	0.0095(26)	0.0030(26)
D142	E(E)	0.134(4)	17.939(19)	15.276(17)	19.051(19)	0.795(4)	0.1488(38)	0.0010(19)	-0.0005(20)	0.0031(20)	-0.0032(19)
D143	E(E)	1.277(59)	20.789(218)	12.411(80)	22.235(307)	1.102(5)	0.2421(60)	0.0001(24)	-0.0007(25)	-0.0010(24)	0.0016(24)
D144	E(L)	0.702(16)	19.056(64)	13.553(25)	20.581(83)	1.048(4)	0.1190(127)	-0.0034(27)	0.0014(27)	0.0124(28)	0.0007(27)
D145	E(L)	0.697(16)	19.606(57)	14.124(31)	20.834(76)	0.885(5)	0.4855(41)	0.0019(30)	-0.0005(30)	-0.0001(30)	-0.0055(30)
D146	E(L)	0.787(18)	20.138(57)	14.207(37)	21.196(58)	0.794(5)	0.5041(27)	-0.0029(24)	0.0007(24)	0.0024(24)	0.0042(24)
D147	S	0.706(21)	20.021(68)	14.497(43)	21.100(75)	0.753(5)	0.6335(36)	-0.0001(28)	-0.0041(28)	0.0072(28)	-0.0011(27)
D148	E(E)	1.777(32)	21.266(121)	10.386(45)	22.782(139)	1.494(5)	0.3448(33)	0.0014(10)	0.0014(10)	-0.0039(10)	0.0004(10)
D149	S	0.536(3)	19.810(18)	15.137(17)	20.798(19)	0.620(7)	0.7528(43)	0.0004(54)	0.0046(55)	0.0378(55)	0.0016(54)
D150	E(E)	0.540(14)	19.220(49)	14.526(29)	20.394(51)	0.844(5)	0.0841(72)	0.0000(25)	0.0030(25)	0.0034(25)	-0.0028(25)
D151	E(E)	0.801(11)	19.505(38)	13.506(24)	20.693(45)	1.018(5)	0.0267(95)	-0.0010(25)	0.0004(25)	-0.0021(25)	0.0005(25)
D152	E(L)	0.639(6)	19.348(25)	14.158(19)	20.491(23)	0.904(5)	0.3522(47)	0.0019(23)	-0.0001(23)	0.0133(23)	-0.0036(23)
D153	E(E)	0.449(19)	18.901(63)	14.660(36)	20.064(70)	0.848(4)	0.0293(89)	-0.0003(28)	0.0011(27)	0.0008(28)	0.0004(28)
D154	E(L)	0.737(26)	20.769(82)	15.090(54)	21.817(49)	0.496(6)	0.3009(84)	-0.0069(72)	0.0091(73)	-0.0008(72)	0.0010(72)
D155	E(L)	0.702(18)	19.243(60)	13.737(38)	20.326(75)	0.999(5)	0.2768(58)	0.0010(26)	0.0033(25)	0.0050(26)	0.0010(26)
D156	E(E)	0.405(25)	19.319(81)	15.296(48)	20.462(94)	0.679(5)	0.3304(51)	0.0023(36)	0.0021(36)	0.0018(36)	0.0013(36)
D157	E(L)	0.439(13)	18.977(47)	14.788(27)	20.222(69)	0.812(4)	0.4110(40)	0.0022(26)	-0.0026(26)	-0.0012(26)	-0.0020(26)
D158	E(L)	0.409(15)	19.779(46)	15.736(35)	20.813(74)	0.504(7)	0.5543(37)	0.0040(49)	0.0008(49)	0.0029(49)	0.0086(49)
D159	E(E)	0.893(42)	19.452(155)	12.990(59)	20.903(211)	1.133(4)	0.1130(61)	-0.0011(14)	0.0000(15)	-0.0012(14)	0.0007(15)
D160	E(L)	0.794(17)	19.665(59)	13.699(31)	20.941(68)	0.966(5)	0.4646(86)	-0.0001(29)	0.0014(29)	0.0236(29)	0.0057(29)
D161	E(E)	0.890(19)	19.721(71)	13.274(30)	21.171(85)	1.055(4)	0.1409(64)	-0.0015(18)	0.0001(18)	0.0060(18)	0.0011(18)
D162	I	0.643(17)	21.509(46)	16.298(46)	22.356(65)	—	0.4445(121)	-0.0435(147)	-0.0556(150)	-0.0190(148)	-0.0189(147)
D167	E(L)	0.812(28)	19.150(100)	13.095(42)	20.524(128)	1.135(4)	0.3436(39)	0.0010(13)	0.0002(13)	-0.0041(13)	-0.0011(13)
D168	E(E)	0.644(13)	18.578(47)	13.363(26)	19.825(73)	1.123(4)	0.3521(53)	-0.0010(17)	-0.0007(17)	0.0087(17)	-0.0006(17)
D169	I	0.664(8)	19.593(25)	14.276(25)	20.326(46)	0.775(11)	0.6105(48)	0.0487(76)	0.0111(74)	0.0020(74)	0.0144(76)
D170	E(L)	0.749(27)	19.695(91)	13.954(45)	20.958(110)	0.913(5)	0.2291(35)	0.0005(16)	-0.0009(16)	0.0134(16)	-0.0102(16)
D171	E(L)	0.394(21)	18.853(77)	14.886(34)	20.212(104)	0.798(4)	0.2983(60)	-0.0031(39)	-0.0032(39)	0.0048(39)	0.0010(39)
D172	E(E)	0.440(14)	18.520(52)	14.323(27)	19.819(57)	0.940(4)	0.1311(40)	-0.0016(16)	-0.0046(16)	-0.0002(16)	0.0005(16)
D173	E(L)	0.489(22)	18.949(83)	14.509(34)	20.405(95)	0.866(4)	0.4873(72)	-0.0030(34)	-0.0068(34)	0.0197(35)	0.0034(34)
D174	E(E)	0.364(4)	18.023(20)	14.208(17)	19.176(23)	0.999(4)	0.2464(47)	-0.0015(19)	0.0016(19)	-0.0001(19)	0.0043(19)
D175	E(L)	0.682(13)	19.065(45)	13.659(28)	20.195(59)	1.033(5)	0.2773(36)	0.0011(11)	-0.0004(11)	0.0005(11)	-0.0102(11)
D176	E(L)	0.400(11)	18.351(38)	14.355(24)	19.539(47)	0.948(4)	0.5710(26)	-0.0018(21)	-0.0050(21)	0.0345(22)	-0.0014(21)

Table A.1: *Continued...*

Name (1)	Type (2)	$\log r_{1/2}$ (3)	$\langle\mu\rangle_{1/2}$ (4)	M_t (5)	$\mu(r_{1/2})$ (6)	$\log D_{19.23}$ (7)	$\epsilon_{21.5}$ (8)	$\langle c_3\rangle$ (9)	$\langle s_3\rangle$ (10)	$\langle c_4\rangle$ (11)	$\langle s_4\rangle$ (12)
D177	E(L)	0.440(10)	19.209(37)	15.012(23)	20.436(52)	0.748(5)	0.4536(33)	0.0009(26)	-0.0020(26)	0.0049(25)	-0.0052(26)
D178	E(L)	0.563(11)	20.197(32)	15.388(33)	20.980(51)	0.509(5)	0.1140(65)	0.0028(43)	-0.0057(43)	-0.0016(43)	0.0044(43)
D179	E(L)	0.688(20)	18.356(70)	12.919(33)	19.708(102)	1.220(4)	0.5525(26)	-0.0022(11)	-0.0020(11)	0.0022(11)	0.0012(11)
D180	E(L)	1.062(20)	21.102(62)	13.798(44)	22.238(72)	0.741(5)	0.1184(85)	-0.0034(37)	0.0005(37)	0.0009(37)	-0.0018(37)
D181	S	0.375(9)	18.620(36)	14.750(21)	19.986(63)	0.841(4)	0.6601(98)	0.0003(84)	-0.0199(86)	0.0966(85)	-0.0235(85)
D182	E(L)	0.304(7)	18.700(27)	15.183(20)	19.810(38)	0.762(4)	0.1066(33)	0.0019(23)	-0.0015(23)	0.0000(23)	0.0003(23)
D183	I	0.839(4)	20.740(18)	14.547(17)	21.723(22)	—	0.0851(123)	-0.0323(95)	0.0027(94)	0.0012(94)	0.0073(95)
D184	S	0.738(9)	20.868(31)	15.182(26)	21.837(46)	—	0.3203(68)	0.0016(49)	-0.0051(50)	0.0061(49)	-0.0035(50)
D191	S	0.352(5)	18.764(20)	15.006(18)	19.684(22)	0.805(4)	0.6768(64)	0.0019(31)	-0.0035(32)	0.0690(33)	-0.0016(31)
D192	S	0.538(4)	19.101(18)	14.416(18)	19.948(23)	0.886(5)	0.8209(33)	0.0029(50)	-0.0054(50)	0.0817(51)	0.0023(49)
D193	E(E)	0.526(20)	19.292(66)	14.667(38)	20.445(93)	0.808(5)	0.1536(43)	-0.0015(25)	-0.0011(25)	0.0070(25)	0.0030(25)
D194	E(E)	0.963(26)	19.494(98)	12.683(36)	21.026(118)	1.193(4)	0.1832(64)	-0.0006(17)	0.0006(17)	0.0018(17)	0.0046(17)
D195	I	0.603(4)	19.764(18)	14.751(20)	20.354(20)	0.626(7)	0.2044(183)	0.0308(101)	0.0202(99)	-0.0083(100)	0.0084(100)
D196	E(E)	0.444(6)	18.965(26)	14.748(18)	20.325(33)	0.818(4)	0.3163(62)	-0.0018(35)	-0.0021(36)	0.0097(35)	-0.0016(35)
D197	S	0.576(9)	18.628(35)	13.751(22)	19.807(25)	1.060(4)	0.6458(31)	0.0025(19)	0.0017(19)	0.0221(19)	-0.0050(19)
D198	E(L)	0.540(5)	19.736(22)	15.042(19)	20.706(28)	0.655(6)	0.4738(73)	-0.0044(36)	0.0000(36)	0.0243(37)	0.0151(36)
D199	E(L)	0.654(8)	19.418(29)	14.154(21)	20.539(36)	0.895(5)	0.3588(62)	-0.0004(29)	0.0013(29)	0.0030(29)	-0.0221(30)
D200	E(L)	0.272(8)	17.583(31)	14.228(19)	18.833(26)	1.002(4)	0.6053(92)	0.0035(26)	-0.0030(27)	0.0625(27)	-0.0042(26)
D205	S	1.065(7)	20.232(24)	12.914(21)	21.200(24)	1.014(6)	0.3702(143)	0.0007(80)	-0.0042(80)	0.0000(81)	-0.0061(79)
D207	E(E)	0.545(16)	19.069(54)	14.349(32)	20.243(74)	0.894(4)	0.3892(43)	-0.0010(26)	-0.0011(26)	-0.0077(26)	-0.0032(26)
D208	E(L)	0.517(19)	19.787(59)	15.206(41)	20.803(65)	0.622(6)	0.3776(97)	0.0039(80)	0.0027(80)	-0.0023(80)	0.0025(81)
D210	E(E)	0.488(16)	18.649(59)	14.212(27)	20.041(81)	0.944(4)	0.1737(86)	-0.0015(27)	-0.0005(27)	0.0129(27)	-0.0050(27)
D211	S	0.800(20)	19.656(52)	13.661(52)	20.431(77)	0.924(6)	0.6194(67)	-0.0073(84)	-0.0093(84)	0.0245(84)	0.0011(84)
D212	S	0.668(2)	19.653(17)	14.318(17)	20.636(17)	0.823(5)	0.4750(50)	-0.0018(33)	0.0028(32)	0.0036(32)	0.0018(33)
D218	E(L)	0.637(10)	18.817(36)	13.636(22)	20.054(44)	1.057(4)	0.5240(74)	-0.0011(40)	0.0009(40)	0.0094(40)	-0.0015(39)
D220	I	0.900(15)	19.709(42)	13.216(37)	20.610(75)	0.977(9)	0.6854(54)	0.0020(195)	-0.0148(195)	0.0242(196)	0.0063(194)
D224	U	0.438(13)	19.843(37)	15.656(34)	20.723(38)	0.516(6)	0.2091(72)	0.0094(45)	-0.0054(46)	0.0051(45)	-0.0117(46)
D225	U	0.438(30)	19.695(96)	15.509(58)	20.798(145)	0.591(5)	0.4712(82)	0.0023(107)	0.0021(106)	0.0084(107)	-0.0068(107)
G2201	E(E)	0.654(29)	20.279(111)	15.016(40)	21.803(116)	0.669(4)	0.0286(86)	0.0009(52)	-0.0023(52)	0.0012(51)	0.0024(52)
G2778	E(L)	0.654(5)	20.443(22)	15.177(19)	21.468(23)	0.518(6)	0.3929(76)	-0.0025(50)	0.0011(51)	0.0054(51)	0.0031(50)
G2914	S	0.843(47)	21.363(144)	15.151(90)	22.467(206)	—	0.0698(112)	-0.0013(77)	-0.0056(77)	0.0043(76)	-0.0034(77)
G2960	E(L)	0.618(7)	20.290(25)	15.206(21)	21.344(30)	0.531(6)	0.4603(41)	0.0042(31)	-0.0007(30)	0.0143(30)	0.0016(31)
G3133	U	0.414(19)	19.665(68)	15.601(34)	20.933(100)	0.583(5)	0.3141(37)	-0.0005(34)	0.0011(35)	0.0014(34)	0.0052(35)
G3298	S	0.863(30)	21.693(86)	15.381(66)	22.692(112)	—	0.4994(63)	-0.0038(110)	0.0101(110)	0.0044(110)	-0.0110(111)
G3554	E(E)	0.197(1)	19.204(15)	16.224(16)	20.280(15)	0.506(5)	0.0571(82)	-0.0019(43)	-0.0004(43)	0.0000(43)	-0.0017(43)
G3640	U	0.925(145)	22.326(516)	15.707(211)	23.826(664)	—	0.4238(85)	0.0132(169)	-0.0053(168)	0.0030(169)	-0.0067(168)
G4281	S	0.700(12)	21.150(36)	15.655(29)	22.208(42)	—	0.2883(77)	0.0035(81)	-0.0040(83)	-0.0074(83)	-0.0024(81)
Abell 1367											
B1	E(E)	2.131(31)	23.309(106)	10.657(52)	24.810(108)	1.293(4)	0.0439(50)	-0.0008(13)	-0.0006(14)	0.0006(13)	-0.0012(13)
B2	E(E)	1.702(53)	21.399(198)	10.893(67)	22.956(219)	1.365(5)	0.1803(20)	-0.0005(11)	0.0006(11)	-0.0011(11)	-0.0010(11)
B3	S	1.197(2)	20.149(17)	12.167(16)	21.422(18)	1.220(5)	0.3223(104)	0.0009(66)	-0.0024(67)	0.0120(66)	-0.0108(66)
B10	E(E)	0.931(16)	19.195(58)	12.543(27)	20.576(67)	1.242(4)	0.0646(40)	0.0003(12)	-0.0011(12)	0.0014(11)	-0.0010(12)
B12	I	0.993(3)	20.076(18)	13.118(17)	21.015(21)	0.484(7)	0.8503(53)	-0.0324(231)	-0.0345(230)	0.0063(226)	-0.0376(235)
B17	E(E)	0.811(36)	19.316(133)	13.264(51)	20.708(186)	1.089(4)	0.2001(63)	-0.0001(17)	0.0005(18)	-0.0007(17)	0.0016(18)
B22	E(L)	0.837(11)	19.453(40)	13.272(23)	20.697(56)	1.072(5)	0.3922(60)	-0.0011(18)	0.0001(18)	0.0163(18)	0.0089(18)
B23	E(L)	0.709(7)	18.781(26)	13.240(20)	19.820(35)	1.145(4)	0.7432(61)	0.0020(22)	0.0017(22)	0.0089(23)	0.0033(22)
B25	S	0.818(4)	19.427(21)	13.341(17)	20.625(23)	1.060(5)	0.3503(32)	0.0009(13)	0.0004(13)	-0.0013(13)	-0.0006(13)
B27	E(L)	0.764(10)	19.365(34)	13.549(23)	20.465(37)	1.023(5)	0.3860(58)	0.0002(21)	0.0004(21)	-0.0123(21)	0.0043(22)
B28	E(E)	0.587(2)	18.639(17)	13.707(16)	19.836(18)	1.057(4)	0.2809(35)	-0.0001(16)	-0.0009(16)	0.0096(16)	0.0036(16)
B33	E(L)	0.768(12)	19.572(40)	13.738(27)	20.665(46)	0.959(5)	0.3529(59)	0.0028(24)	-0.0020(24)	0.0271(24)	0.0020(24)
B38	E(E)	0.672(16)	18.918(55)	13.564(31)	20.119(78)	1.063(4)	0.3824(31)	-0.0011(14)	0.0009(14)	0.0028(14)	-0.0030(14)
B41	E(E)	1.077(65)	21.037(248)	13.657(78)	22.609(306)	0.877(5)	0.0448(74)	0.0007(25)	-0.0014(26)	0.0010(25)	0.0027(26)
B45	E(L)	0.443(4)	18.257(20)	14.048(17)	19.341(27)	1.015(4)	0.3908(32)	0.0008(14)	-0.0013(14)	0.0021(14)	-0.0034(14)
B46	E(L)	0.517(3)	18.585(17)	14.006(16)	19.751(21)	0.997(4)	0.4530(53)	-0.0002(14)	-0.0012(14)	0.0080(14)	0.0111(14)
B52	E(E)	0.889(30)	20.389(113)	13.950(42)	21.879(121)	0.873(4)	0.0831(79)	-0.0021(37)	-0.0014(37)	-0.0001(37)	0.0011(37)
B58	S	0.817(1)	20.651(15)	14.570(16)	21.112(15)	—	0.6703(41)	0.0269(102)	0.0246(102)	0.0208(103)	0.0057(101)
B61	S	0.847(4)	20.978(18)	14.747(18)	21.817(22)	—	0.4157(168)	-0.0112(82)	0.0569(84)	0.0057(84)	0.0051(82)
B64	E(L)	0.467(3)	18.603(18)	14.272(17)	19.552(25)	0.958(4)	0.7136(44)	0.0023(26)	0.0044(27)	0.0522(27)	0.0029(26)
B69	E(E)	0.537(7)	19.152(30)	14.470(18)	20.674(33)	0.859(4)	0.3664(26)	-0.0022(19)	-0.0022(19)	0.0039(18)	0.0006(19)
B76	E(L)	0.618(8)	19.646(32)	14.560(21)	20.835(32)	0.793(5)	0.5002(20)	0.0006(18)	-0.0035(18)	0.0091(18)	-0.0097(18)
B81	E(E)	0.664(5)	20.228(23)	14.910(18)	21.374(27)	0.632(6)	0.0430(41)	-0.0025(23)	-0.0004(22)	0.0043(23)	0.0014(22)
B90	E(L)	0.419(12)	18.899(45)	14.810(24)	20.220(67)	0.811(4)	0.4003(30)	0.0017(22)	-0.0022(22)	0.0130(22)	-0.0017(22)
B107	E(E)	0.496(28)	19.654(95)	15.181(48)	20.900(128)	0.666(5)	0.4271(34)	0.0014(23)	0.0016(23)	0.0038(24)	-0.0004(23)
B117	E(L)	0.373(2)	19.103(17)	15.242(16)	20.056(18)	0.717(5)	0.6361(28)	-0.0013(26)	-0.0072(26)	0.0339(26)	0.0007(25)

Table A.2: Parameters derived from $\mu(r)$ profile fitting for Coma and Abell 1367 galaxies.

Name (1)	r^1_e (13)	$\langle\mu\rangle^1_e$ (14)	r^2_e (15)	$\langle\mu\rangle^2_e$ (16)	r^4_e (17)	$\langle\mu\rangle^4_e$ (18)	n (19)	r^b_e (20)	$\langle\mu\rangle^b_e$ (21)	r^d_e (22)	$\langle\mu\rangle^d_e$ (23)	D/B (24)
Abell 1656 (Coma)												
D62	6.10(49)	20.94(10)	5.66(40)	20.58(12)	5.67(39)	20.29(12)	2.91(41)	5.37(132)	20.53(36)	6.00(23)	22.33(14)	0.24(8)
D63	4.46(6)	20.65(1)	4.61(4)	20.47(1)	5.40(3)	20.49(1)	2.45(36)	1.06(62)	18.04(91)	5.38(19)	21.34(18)	1.24(35)
D64	5.77(62)	21.29(13)	5.52(45)	21.00(13)	6.08(44)	20.90(13)	3.40(6)	5.53(173)	20.86(49)	6.46(65)	23.72(36)	0.10(8)
D65	5.25(21)	20.30(6)	5.00(11)	19.98(3)	5.25(4)	19.78(1)	2.33(4)	4.97(103)	20.45(36)	5.03(19)	20.96(12)	0.64(6)
D68	6.56(41)	20.37(7)	6.04(34)	20.05(9)	5.95(34)	19.76(10)	3.06(16)	6.14(85)	20.02(24)	5.74(47)	22.12(26)	0.13(3)
D69	9.78(136)	20.83(20)	8.02(109)	20.25(24)	6.66(105)	19.58(31)	5.18(6)	3.19(224)	18.07(123)	25.08(1755)	24.01(243)	0.26(6)
D70	6.78(75)	20.83(17)	5.93(63)	20.31(19)	5.20(64)	19.72(24)	4.09(26)	4.03(62)	19.31(24)	10.72(347)	23.73(90)	0.12(3)
D71	4.02(12)	20.52(2)	3.49(11)	19.96(6)	2.84(12)	19.19(9)	1.93(25)	4.80(52)	21.21(17)	3.47(4)	20.85(9)	0.73(7)
D72	5.13(35)	20.09(12)	3.76(23)	19.20(13)	2.40(15)	17.86(15)	3.65(94)	4.16(5)	19.53(13)	2.54(6)	19.68(19)	0.32(12)
D78	12.17(29)	20.78(3)	11.21(23)	20.46(3)	11.92(28)	20.32(4)	4.96(0)	5.73(401)	19.05(84)	26.65(1865)	23.44(128)	0.38(30)
D79	8.47(23)	20.14(4)	7.08(14)	19.61(4)	5.82(12)	18.92(4)	3.38(52)	5.82(12)	18.92(4)	—	—	0.00(39)
D80	6.83(21)	20.93(5)	6.73(19)	20.69(4)	7.71(25)	20.68(6)	4.19(20)	1.53(107)	17.79(53)	10.49(734)	22.25(112)	0.77(66)
D81	8.31(57)	21.32(8)	7.99(43)	21.08(8)	8.92(51)	21.03(10)	4.83(6)	3.96(277)	19.65(76)	17.10(1197)	23.75(104)	0.43(36)
D82	14.23(20)	20.16(1)	17.89(16)	20.50(1)	36.25(36)	21.55(2)	1.75(33)	34.50(258)	22.45(13)	13.54(19)	20.68(3)	0.79(7)
D84	4.08(22)	19.67(6)	3.26(13)	19.00(8)	2.41(7)	18.02(6)	2.30(3)	3.30(116)	19.56(77)	3.47(25)	20.05(26)	0.70(16)
D87	3.55(21)	20.36(11)	2.96(16)	19.68(11)	2.23(14)	18.71(14)	2.86(50)	1.00(70)	17.05(122)	5.55(307)	22.34(103)	0.24(14)
D88	5.58(64)	20.34(20)	4.06(40)	19.38(22)	2.58(27)	18.00(25)	3.99(40)	2.58(27)	18.00(25)	—	—	0.00(12)
D89	5.02(16)	19.12(3)	3.28(10)	17.87(11)	1.67(4)	15.86(11)	1.63(78)	6.32(32)	20.43(15)	3.35(2)	18.49(5)	1.68(16)
D90	4.16(26)	20.61(10)	3.45(17)	19.93(10)	2.64(11)	19.00(9)	2.25(2)	5.87(20)	21.84(22)	3.43(10)	20.69(6)	0.99(20)
D91	5.78(32)	19.71(9)	4.58(24)	19.00(11)	3.29(18)	17.96(12)	3.11(22)	2.70(4)	17.66(19)	7.63(157)	22.28(91)	0.11(9)
D92	5.73(62)	20.72(21)	4.24(40)	19.78(21)	2.69(30)	18.39(26)	4.24(78)	4.08(44)	19.57(31)	2.00(9)	19.56(19)	0.24(10)
D97	21.13(35)	20.62(1)	26.19(21)	21.02(1)	57.49(20)	22.21(0)	3.29(212)	5.08(22)	18.81(8)	46.71(84)	22.20(3)	3.74(3)
D98	4.93(20)	19.68(5)	3.93(13)	19.10(6)	3.00(8)	18.24(6)	2.44(6)	5.54(64)	20.28(25)	3.37(6)	19.77(7)	0.59(3)
D99	4.34(7)	20.63(1)	5.03(2)	20.64(0)	7.43(5)	21.09(1)	0.82(32)	—	—	4.34(7)	20.63(1)	∞
D100	3.06(3)	19.64(3)	2.88(2)	19.27(1)	2.74(1)	18.85(0)	1.08(47)	1.74(85)	19.40(89)	3.14(15)	20.00(11)	1.87(33)
D101	4.92(23)	20.24(6)	3.79(16)	19.44(9)	2.59(13)	18.27(11)	3.17(2)	6.36(176)	21.02(69)	3.25(9)	20.06(19)	0.64(11)
D102	4.73(37)	21.16(12)	3.99(28)	20.53(14)	3.25(25)	19.75(16)	3.48(19)	5.15(4)	21.05(7)	2.66(8)	21.34(37)	0.21(9)
D103	7.97(34)	20.70(6)	7.35(36)	20.32(9)	7.21(35)	20.00(9)	5.19(21)	0.86(61)	15.32(127)	13.63(954)	22.23(198)	0.43(16)
D104	4.64(39)	19.88(13)	3.57(16)	19.07(10)	2.54(9)	17.99(8)	3.27(7)	2.70(45)	18.39(41)	3.81(60)	21.19(58)	0.15(6)
D105	9.23(22)	20.39(4)	7.95(16)	19.83(4)	6.60(15)	19.12(5)	3.63(32)	2.90(203)	17.52(100)	14.99(1050)	22.43(71)	0.29(25)
D106	3.35(23)	19.99(15)	2.48(18)	18.97(17)	1.47(13)	17.37(22)	2.80(47)	4.06(64)	20.86(21)	2.68(8)	19.92(7)	1.04(20)
D107	4.47(27)	20.28(10)	4.00(20)	19.79(9)	3.57(19)	19.22(11)	2.45(2)	3.04(105)	19.25(59)	4.81(27)	21.76(15)	0.25(9)
D108	3.85(18)	20.24(9)	3.04(11)	19.47(8)	2.16(7)	18.37(7)	2.64(26)	3.06(75)	19.91(54)	3.22(19)	20.63(21)	0.57(9)
D109	5.36(15)	20.07(5)	4.57(7)	19.43(3)	3.68(0)	18.61(1)	0.50(50)	7.08(414)	22.43(66)	5.18(0)	20.13(10)	4.48(247)
D110	5.23(15)	20.70(5)	4.64(14)	20.22(5)	4.19(16)	19.70(7)	3.04(19)	3.61(51)	19.58(23)	6.15(22)	22.88(33)	0.14(6)
D111	6.82(17)	20.50(4)	6.15(11)	20.04(3)	5.89(10)	19.64(3)	2.76(31)	6.47(45)	20.32(11)	6.01(16)	21.40(2)	0.32(3)
D112	3.81(9)	20.22(4)	2.94(5)	19.38(4)	1.87(4)	17.98(5)	2.31(16)	1.32(85)	17.45(129)	4.65(128)	21.93(66)	0.20(5)
D115	4.82(27)	20.70(9)	4.40(16)	20.23(7)	4.18(11)	19.80(5)	2.78(43)	4.12(96)	20.46(38)	4.58(18)	21.42(7)	0.51(9)
D116	5.88(10)	20.61(5)	5.77(6)	20.29(2)	6.24(4)	20.14(1)	2.84(71)	1.66(2)	18.47(5)	6.78(12)	21.19(8)	1.37(12)
D117	4.35(7)	20.17(2)	3.91(5)	19.75(2)	3.65(4)	19.31(2)	2.25(17)	7.47(53)	21.58(18)	3.31(3)	20.31(2)	0.63(2)
D118	7.09(30)	20.15(7)	6.24(15)	19.69(4)	5.83(7)	19.26(2)	2.77(25)	4.88(70)	19.26(24)	7.54(38)	21.60(5)	0.28(6)
D119	4.64(6)	20.46(2)	4.62(1)	20.13(1)	4.96(11)	19.95(6)	2.69(219)	—	—	4.64(6)	20.46(2)	∞
D120	3.38(8)	19.42(5)	2.71(4)	18.66(3)	1.90(2)	17.54(3)	2.13(23)	1.81(5)	18.00(7)	3.33(5)	20.35(6)	0.39(3)
D121	5.79(21)	19.51(7)	4.68(12)	18.86(5)	3.67(8)	18.04(5)	3.19(25)	3.12(82)	17.82(51)	7.77(347)	22.29(110)	0.10(2)
D122	4.34(16)	20.06(6)	4.07(9)	19.70(3)	3.99(5)	19.36(3)	2.58(40)	1.26(59)	17.77(74)	5.13(23)	20.83(16)	0.98(25)
D123	4.71(6)	20.34(7)	4.92(2)	20.19(1)	5.89(3)	20.26(1)	0.95(45)	—	—	4.71(6)	20.34(7)	∞
D124	4.59(17)	19.42(6)	3.93(8)	18.86(4)	3.34(3)	18.20(1)	2.26(4)	2.59(49)	18.33(34)	4.78(9)	20.30(5)	0.56(7)
D125	2.71(14)	19.71(13)	1.87(9)	18.52(12)	0.97(6)	16.55(16)	4.16(74)	0.97(6)	16.55(16)	—	—	0.00(13)
D126	3.54(22)	20.02(10)	2.84(14)	19.30(10)	2.05(10)	18.24(11)	2.13(29)	5.76(56)	21.46(28)	2.64(4)	19.93(5)	0.86(18)
D127	2.99(4)	20.18(2)	2.72(2)	19.68(2)	2.41(2)	19.08(1)	1.80(41)	1.35(77)	19.10(109)	3.15(17)	20.64(12)	1.33(31)
D128	2.74(3)	19.78(2)	2.10(2)	18.88(2)	1.33(2)	17.46(3)	2.38(63)	3.78(83)	21.34(64)	2.41(3)	19.81(8)	1.66(24)
D129	27.19(36)	20.01(1)	31.37(38)	20.46(1)	68.11(100)	21.70(2)	3.83(147)	19.36(23)	20.21(2)	97.38(244)	22.68(2)	2.61(6)
D130	4.89(20)	19.75(8)	3.83(12)	18.98(7)	2.71(10)	17.89(8)	3.68(84)	2.71(10)	17.89(8)	—	—	0.00(7)
D131	6.98(6)	20.15(1)	6.96(5)	19.91(1)	7.76(6)	19.84(1)	2.51(18)	2.87(8)	18.67(5)	8.37(11)	21.00(3)	1.00(2)
D132	4.34(16)	20.67(4)	4.16(17)	20.29(7)	4.15(16)	19.96(7)	3.06(70)	1.06(74)	17.77(100)	5.33(51)	21.47(42)	0.84(42)
D133	5.60(47)	20.02(16)	4.13(31)	19.14(16)	2.64(23)	17.81(21)	4.02(102)	3.80(32)	18.88(31)	1.96(22)	19.09(15)	0.22(13)
D135	3.84(17)	20.54(8)	3.46(9)	20.04(5)	3.18(4)	19.53(2)	2.59(38)	3.29(8)	20.52(9)	3.67(12)	21.07(15)	0.75(17)
D136	3.18(22)	20.13(16)	2.05(14)	18.76(17)	0.97(8)	16.52(23)	3.79(127)	1.79(79)	18.53(107)	1.41(13)	18.95(9)	0.42(26)
D137	9.45(27)	21.06(5)	8.01(23)	20.45(6)	6.35(24)	19.62(8)	4.15(128)	6.35(24)	19.62(8)	—	—	0.00(5)
D142	2.16(9)	19.50(13)	1.35(6)	17.97(13)	0.56(3)	15.32(17)	3.12(82)	0.56(3)	15.32(17)	—	—	0.00(11)
D143	12.40(107)	20.29(10)	12.19(49)	20.22(6)	17.16(49)	20.66(4)	4.31(12)	17.16(49)	20.66(4)	—	—	0.00(5)
D144	8.00(18)	20.52(2)	7.88(17)	20.25(4)	8.96(12)	20.22(2)	4.90(25)	1.09(76)	16.15(64)	11.59(811)	21.57(120)	0.77(64)
D145	6.18(27)	20.38(6)	5.61(16)	19.99(5)	5.56(11)	19.68(4)	2.91(1)	3.74(95)	19.22(39)	7.93(3)	22.13(37)	0.31(12)
D146	6.22(19)	20.49(4)	6.52(11)	20.36(3)	8.48(9)	20.59(2)	2.18(11)	9.95(157)	21.71(28)	5.56(20)	20.99(5)	0.61(6)
D147	5.68(25)	20.54(5)	5.81(16)	20.36(4)	7.13(10)	20.47(2)	2.19(3)	5.57(168)	20.84(42)	5.78(17)	21.25(5)	0.73(19)
D148	22.52(117)	19.66(5)	20.59(50)	19.60(3)	32.08(54)	20.26(2)	5.06(0)	18.02(1262)	19.48(48)	84.57(5920)	23.04(28)	0.83(78)
D149	3.64(3)	20.06(1)	3.69(3)	19.86(1)	4.09(4)	19.78(2)	2.15(35)	1.37(38)	18.08(48)	4.99(7)	21.33(11)	0.67(11)
D150	4.42(19)	20.07(7)	4.01(9)	19.58(4)	3.72(2)	19.10(1)	2.25(36)	2.77(37)	19.61(16)	4.50(12)	20.56(9)	1.11(28)
D151	7.65(10)	20.23(2)	7.66(8)	20.02(2)	8.97(8)	20.04(2)	2.57(11)	7.14(34)	20.07(6)	8.32(1)	21.52(5)	0.36(3)
D152	5.49(10)	20.04(3)	5.56(2)	19.78(0)	6.46(10)	19.77(4)	0.50(50)	2.13(70)	19.65(99)	5.73(6)	20.25(3)	4.18(66)
D153	4.02(24)	20.05(10)	3.20(19)	19.31(12)	2.28(17)	18.22(16)	2.64(9)	4.08(56)	20.13(20)	2.86(15)	20.23(5)	0.45(7)
D154	5.18(21)	20.90(5)	6.06(16)	20.99(3)	9.57(20)	21.58(3)	2.25(23)	1.33(53)	18.60(63)	7.25(38)	21.85(15)	1.48(20)
D155	5.95(20)	19.91(5)	5.59(13)	19.54(4)	5.68(10)	19.26(3)	2.12(5)	7.59(165)	20.90(62)	5.39(6)	20.25(5)	0.92(16)
D156	3.27(26)	20.27(14)	2.68(23)	19.54(17)	1.95(21)	18.47(23)	2.45(0)	2.45(3)	19.48(17)	2.77(3)	21.05(31)	0.30(15)
D157	3.83(37)	20.20(16)	3.01(25)	19.39(18)	2.15(18)	18.29(19)	3.11(11)	4.17(163)	20.42(81)	2.64(11)	20.18(24)	0.50(12)
D158	2.98(14)	20.37(8)	2.43(13)	19.66(11)	1.74(11)	18.57(14)	2.29(32)	1.26(70)	18.11(114)	3.71(129)	22.23(111)	0.19(7)
D159	9.57(60)	20.30(10)	8.13(47)	19.82(10)	7.29(49)	19.33(13)	4.67(19)	7.29(49)	19.33(13)	—	—	0.00(11)
D160	6.98(36)	20.22(6)	6.51(26)	19.94(6)	6.75(23)	19.76(6)	3.04(14)	6.10(112)	19.85(28)	7.13(62)	21.83(7)	0.22(7)
D161	9.55(48)	20.58(8)	8.53(23)	20.19(5)	8.63(17)	19.95(4)	4.40(6)	5.33(368)	19.17(88)	17.00(1190)	23.18(99)	0.25(21)
D162	4.64(12)	21.78(3)	4.88(10)	21.59(3)	5.67(13)	21.57(6)	0.93(43)	—	—	4.64(12)	21.78(3)	∞
D167	9.00(67)	20.27(11)	7.56(40)	19.74(10)	6.63(32)	19.18(10)	4.02(17)	7.58(85)	19.56(27)	4.25(46)	21.32(78)	0.06(6)
D168	6.72(42)	19.86(12)	5.07(22)	19.11(9)	3.63(15)	18.09(9)	3.95(94)	8.08(51)	20.28(15)	2.76(9)	18.91(11)	0.41(8)
D169	5.33(18)	20.04(9)	3.74(14)	18.91(10)	1.98(11)	17.01(14)	2.69(162)	—	—	5.33(18)	20.04(9)	∞
D170	6.92(41)	20.53(7)	6.29(33)	20.11(9)	6.15(31)	19.70(10)	2.80(30)	6.46(116)	20.24(29)	6.15(42)	21.68(12)	0.24(5)
D171	4.50(32)	20.72(13)	3.80(19)	20.06(10)	3.07(10)	19.25(7)	3.10(64)	0.96(1)	17.12(7)	5.75(36)	21.76(51)	0.50(21)
D172	4.23(24)	19.92(9)	3.43(11)	19.16(8)	2.54(2)	18.15(4)	2.74(59)	3.08(164)	19.65(104)	3.91(35)	20.27(33)	0.91(18)
D173	5.11(33)	20.58(11)	4.14(23)	19.90(11)	3.15(20)	18.98(14)	3.97(55)	3.15(20)	18.98(14)	—	—	0.00(7)
D174	3.50(10)	19.37(6)	2.40(6)	18.20(6)	1.27(3)	16.30(7)	2.50(0)	1.71(96)	17.60(137)	2.71(16)	19.82(54)	0.33(38)
D175	5.92(17)	19.77(5)	5.27(9)	19.32(3)	4.88(5)	18.87(2)	2.39(0)	4.14(50)	19.11(20)	6.03(17)	20.76(3)	0.46(6)
D176	3.86(22)	19.67(11)	3.01(14)	18.86(12)	2.03(9)	17.64(12)	2.54(14)	1.12(78)	16.70(165)	4.67(146)	20.94(106)	0.35(37)

Table A.2: *Continued...*

Name (1)	r^1_e (13)	$\langle\mu\rangle^1_e$ (14)	r^2_e (15)	$\langle\mu\rangle^2_e$ (16)	r^4_e (17)	$\langle\mu\rangle^4_e$ (18)	n (19)	r^b_e (20)	$\langle\mu\rangle^b_e$ (21)	r^d_e (22)	$\langle\mu\rangle^d_e$ (23)	D/B (24)
D177	3.79(14)	20.34(7)	3.32(10)	19.78(6)	2.79(10)	19.06(7)	2.68(22)	1.83(26)	18.56(25)	4.60(56)	21.81(16)	0.31(9)
D178	4.25(12)	20.79(6)	3.36(10)	19.91(6)	2.17(9)	18.50(9)	0.84(34)	0.64(42)	17.74(248)	4.36(14)	20.93(13)	2.47(1342)
D179	6.95(30)	19.61(9)	5.67(18)	18.97(7)	4.51(16)	18.18(8)	4.19(50)	3.58(221)	17.73(114)	18.96(1327)	24.02(294)	0.09(5)
D180	10.23(67)	21.15(7)	12.24(65)	21.32(6)	20.93(123)	22.05(8)	2.65(23)	11.43(589)	21.51(58)	13.89(89)	22.68(46)	0.50(38)
D181	3.93(18)	20.17(9)	2.96(10)	19.29(8)	1.93(5)	17.97(6)	3.06(74)	2.15(9)	18.94(22)	3.59(11)	20.79(17)	0.51(13)
D182	3.19(17)	20.27(12)	2.25(11)	19.10(12)	1.21(7)	17.20(15)	2.59(29)	1.21(7)	17.20(15)	—	—	0.00(11)
D183	6.86(9)	20.90(2)	7.12(7)	20.75(1)	8.81(8)	20.88(2)	2.01(23)	12.28(65)	22.30(8)	5.98(7)	21.36(4)	0.56(4)
D184	4.91(9)	20.87(2)	5.17(6)	20.74(2)	6.52(6)	20.90(1)	2.06(33)	3.95(69)	20.54(24)	5.75(7)	22.02(12)	0.54(12)
D191	2.63(7)	19.27(84)	1.87(5)	18.24(9)	1.03(2)	16.47(16)	1.91(35)	3.00(81)	20.36(41)	2.14(3)	19.21(18)	1.46(10)
D192	3.70(8)	19.35(2)	2.82(2)	18.52(2)	1.85(2)	17.23(2)	1.33(2)	2.17(6)	19.18(21)	3.56(4)	19.57(6)	1.88(34)
D193	4.47(39)	20.28(12)	3.56(26)	19.55(15)	2.58(19)	18.50(17)	2.79(29)	3.91(65)	19.90(41)	3.12(19)	20.66(39)	0.32(15)
D194	10.24(44)	20.19(7)	8.70(27)	19.70(6)	8.41(24)	19.38(6)	4.98(24)	8.41(24)	19.38(6)	—	—	0.00(6)
D195	3.95(7)	19.72(3)	3.29(2)	19.09(1)	2.53(2)	18.20(2)	0.65(15)	—	—	3.95(7)	19.72(3)	∞
D196	4.83(14)	20.73(6)	4.12(8)	20.11(4)	3.46(7)	19.41(4)	3.64(11)	0.85(60)	16.49(105)	7.15(501)	22.12(199)	0.39(19)
D197	5.32(26)	19.66(9)	3.73(13)	18.65(8)	2.09(3)	16.94(4)	2.39(25)	4.03(18)	19.72(20)	4.41(1)	19.73(5)	1.18(21)
D198	3.78(5)	20.10(2)	3.69(2)	19.80(1)	3.84(1)	19.57(1)	1.46(27)	3.97(222)	21.31(97)	3.72(14)	20.34(12)	2.15(42)
D199	5.38(15)	19.99(4)	4.66(8)	19.55(3)	4.20(5)	19.07(3)	2.58(23)	6.16(3)	20.34(2)	3.76(1)	20.43(3)	0.34(2)
D200	3.77(28)	19.49(12)	2.51(17)	18.43(15)	1.31(10)	16.58(18)	3.26(105)	1.71(63)	17.47(102)	1.50(27)	19.10(29)	0.17(26)
D205	11.36(13)	20.21(2)	13.61(1)	20.47(0)	23.41(20)	21.28(2)	1.85(13)	1.72(112)	17.67(97)	13.53(3)	20.77(9)	3.54(70)
D207	4.61(27)	20.02(19)	3.73(18)	19.33(9)	2.84(14)	18.41(12)	2.72(11)	3.55(44)	19.29(32)	3.46(23)	20.77(86)	0.25(33)
D208	4.05(9)	20.43(24)	3.86(11)	20.05(2)	3.64(13)	19.59(7)	2.10(19)	1.54(54)	18.44(53)	4.88(38)	21.40(13)	0.66(20)
D210	5.48(35)	20.46(12)	4.46(20)	19.74(10)	3.48(12)	18.86(8)	3.54(46)	1.26(21)	16.91(28)	7.52(72)	21.83(67)	0.39(19)
D211	6.44(25)	19.83(4)	6.73(10)	19.66(2)	8.23(5)	19.75(2)	0.83(33)	—	—	6.44(25)	19.83(4)	∞
D212	5.37(4)	20.15(1)	5.70(1)	19.98(0)	7.01(7)	20.08(2)	1.14(64)	—	—	5.37(4)	20.15(1)	∞
D218	5.39(9)	19.52(3)	4.59(4)	18.97(2)	3.78(3)	18.26(2)	3.36(41)	1.06(74)	15.61(106)	8.33(583)	21.18(130)	0.37(27)
D220	8.31(23)	19.96(6)	7.05(31)	19.31(9)	5.34(30)	18.35(12)	2.37(87)	3.25(228)	17.47(131)	11.68(638)	21.96(164)	0.21(2)
D224	2.90(8)	20.03(6)	2.37(6)	19.22(5)	1.63(3)	17.98(3)	0.97(47)	—	—	2.90(8)	20.03(6)	∞
D225	3.51(19)	20.58(9)	3.16(21)	20.04(12)	2.68(22)	19.33(17)	2.01(25)	2.94(49)	20.73(17)	3.44(12)	20.99(15)	1.08(66)
G2201	6.50(46)	21.61(10)	6.26(33)	21.33(8)	7.02(34)	21.28(8)	4.80(34)	2.09(146)	19.18(61)	10.74(751)	23.24(114)	0.63(53)
G2778	4.96(7)	20.87(2)	5.43(5)	20.81(1)	7.35(6)	21.11(1)	2.10(16)	2.56(45)	20.00(33)	5.99(7)	21.70(8)	1.15(16)
G2914	7.16(41)	21.62(6)	8.00(43)	21.68(7)	11.98(68)	22.18(8)	2.36(9)	10.42(252)	22.36(28)	7.29(35)	22.91(17)	0.30(14)
G2960	4.19(11)	20.56(118)	4.36(8)	20.42(60)	5.35(10)	20.54(21)	2.23(18)	4.06(51)	20.55(46)	4.54(5)	21.72(632)	0.43(30)
G3133	3.50(10)	20.71(5)	3.15(8)	20.19(5)	2.78(9)	19.59(6)	2.78(36)	2.27(9)	19.67(10)	3.74(21)	21.85(14)	0.36(7)
G3298	6.76(30)	21.77(3)	8.49(28)	21.98(4)	15.36(32)	22.78(2)	2.05(21)	3.49(91)	21.23(25)	8.41(51)	22.51(25)	1.79(92)
G3554	4.12(17)	21.02(31)	4.24(20)	20.78(5)	4.81(33)	20.72(9)	1.35(80)	1.45(102)	19.98(100)	4.39(48)	21.32(9)	2.66(156)
G3640	7.60(236)	22.63(24)	6.71(275)	22.11(48)	5.64(319)	21.41(89)	5.18(27)	1.83(128)	18.85(136)	23.29(1630)	25.59(250)	0.33(19)
G4281	4.70(15)	21.16(4)	5.27(13)	21.16(3)	7.40(21)	21.52(4)	2.28(21)	5.86(7)	21.43(3)	5.52(34)	22.89(15)	0.23(1)
Abell 1367												
B1	30.18(89)	21.23(3)	30.26(66)	21.18(3)	46.89(113)	21.78(4)	5.19(27)	10.23(716)	19.38(11)	93.96(6577)	23.44(35)	2.02(194)
B2	27.74(116)	20.62(5)	27.30(80)	20.55(4)	40.23(104)	21.07(4)	5.09(39)	34.62(983)	20.86(39)	135.27(9469)	25.67(71)	0.18(15)
B3	14.93(30)	20.16(2)	15.26(9)	20.25(1)	22.77(14)	20.83(1)	4.18(101)	1.82(51)	16.58(55)	23.40(81)	21.37(10)	2.00(3)
B10	11.28(37)	20.18(6)	9.72(23)	19.70(4)	9.25(21)	19.34(4)	4.29(38)	5.93(402)	18.58(93)	22.51(1576)	23.15(189)	0.21(12)
B12	7.78(20)	19.79(13)	7.22(76)	19.38(22)	7.98(321)	19.27(134)	0.50(50)	1.54(94)	17.63(100)	8.26(6)	20.03(8)	3.13(43)
B17	8.57(24)	20.33(5)	7.73(19)	19.93(4)	7.42(22)	19.58(6)	4.36(37)	4.54(318)	18.69(103)	19.24(1347)	23.49(185)	0.22(12)
B22	8.59(24)	20.16(4)	7.40(19)	19.79(4)	6.81(21)	19.40(6)	3.81(82)	6.81(21)	19.40(6)	—	—	0.00(34)
B23	6.31(17)	19.39(2)	5.32(11)	18.91(4)	4.61(6)	18.33(2)	2.17(18)	5.87(63)	19.56(21)	5.24(15)	19.88(7)	0.59(2)
B25	8.38(6)	20.29(1)	8.28(5)	20.03(1)	9.01(5)	19.91(1)	2.52(22)	6.41(38)	19.95(9)	9.07(5)	21.19(2)	0.64(4)
B27	6.86(21)	20.02(5)	6.05(7)	19.55(2)	5.60(2)	19.09(1)	1.71(54)	3.74(53)	19.72(19)	6.97(13)	20.37(5)	1.91(36)
B28	5.11(4)	19.61(2)	4.31(3)	19.00(1)	3.50(3)	18.23(2)	2.96(23)	3.12(10)	18.17(7)	5.78(24)	21.77(9)	0.13(1)
B33	7.45(12)	20.16(2)	6.64(12)	19.89(3)	6.25(16)	19.57(5)	2.61(39)	8.22(43)	20.43(9)	5.10(16)	20.98(5)	0.23(1)
B38	6.56(41)	20.01(11)	5.04(23)	19.26(10)	3.67(15)	18.27(9)	3.10(35)	5.92(18)	19.75(15)	3.72(8)	19.98(24)	0.32(10)
B41	11.36(103)	21.44(11)	10.35(68)	21.15(10)	11.49(74)	21.11(11)	5.20(43)	9.17(377)	20.74(61)	39.48(2764)	25.93(167)	0.16(10)
B45	5.54(30)	20.56(13)	3.71(20)	19.24(14)	1.79(13)	17.02(20)	2.83(65)	1.79(13)	17.02(20)	—	—	0.00(5)
B46	4.98(6)	19.79(2)	4.20(3)	19.22(1)	3.46(1)	18.51(1)	2.99(43)	1.01(70)	16.01(102)	7.56(529)	21.42(81)	0.39(32)
B52	10.96(72)	21.65(10)	10.29(46)	21.33(8)	10.85(40)	21.16(7)	4.07(75)	7.85(230)	20.76(42)	14.97(39)	23.80(71)	0.22(14)
B58	6.86(1)	20.70(20)	9.61(15)	21.08(16)	21.82(84)	22.24(31)	0.55(5)	—	—	6.86(1)	20.70(20)	∞
B61	6.99(7)	21.00(1)	8.70(3)	21.30(0)	15.92(1)	22.17(0)	1.32(1)	5.23(57)	21.95(13)	7.54(7)	21.38(5)	3.51(99)
B64	3.73(14)	19.21(5)	2.60(7)	18.26(6)	1.44(3)	16.57(6)	2.06(40)	1.44(26)	17.01(81)	3.49(34)	20.27(64)	0.29(39)
B69	7.09(23)	21.34(6)	6.08(16)	20.75(5)	4.93(16)	19.97(7)	4.22(91)	2.94(171)	19.07(94)	10.27(254)	23.37(35)	0.23(13)
B76	5.18(14)	20.46(5)	4.48(6)	19.92(3)	3.97(1)	19.34(1)	2.35(34)	7.64(92)	22.08(26)	4.45(2)	20.53(3)	1.43(13)
B81	5.28(7)	20.78(2)	5.09(4)	20.51(1)	5.55(3)	20.39(1)	2.45(2)	4.09(22)	20.29(8)	5.85(0)	22.02(5)	0.42(3)
B90	4.58(29)	20.68(12)	3.55(19)	19.86(12)	2.55(13)	18.80(12)	3.84(36)	1.47(103)	17.70(110)	7.55(528)	23.09(214)	0.18(7)
B107	3.94(29)	20.54(13)	3.25(19)	19.91(11)	2.56(16)	19.09(13)	3.60(60)	3.28(26)	19.81(22)	2.09(13)	21.16(48)	0.12(7)
B117	2.93(6)	19.76(13)	2.14(4)	18.82(5)	1.26(2)	17.23(7)	2.03(35)	1.52(106)	18.34(179)	2.59(26)	20.40(72)	0.44(84)

Appendix B

Aperture Photometry - Output

This appendix contains contour plots and graphs showing the aperture photometry and extrapolation for all galaxies in the Coma and Abell 1367 samples. See end of appendix for explanatory notes.

B.1   Early-Type Galaxies - Coma

Dressler 062
GMP 2393

Best-fit
$r^{\frac{1}{4}}$

Tot.Mag M_t
= 14.643
± 0.057

Dressler 063 (frame 1)
GMP 2615

Best-fit
Exp

Tot.Mag M_t
= 15.143
± 0.023

Dressler 063 (frame 2)
GMP 2615

Best-fit
Exp

Tot.Mag M_t
= 15.164
± 0.023

Dressler 064
GMP 2866

Best-fit
$r^{\frac{1}{4}}$

Tot.Mag M_t
= 15.06
± 0.072

Dressler 070
IC 3957

Best-fit $r^{\frac{1}{4}}$

Tot.Mag M_t
= 14.069
± 0.059

Dressler 071
RB 2,14

Best-fit $r^{\frac{1}{4}}$

Tot.Mag M_t
= 15.32
± 0.028

Dressler 072
IC 3947

Best-fit $r^{\frac{1}{4}}$

Tot.Mag M_t
= 14.099
± 0.027

Dressler 078
NGC 4923

Best-fit $r^{\frac{1}{4}}$

Tot.Mag M_t
= 12.878
± 0.021

Counts/Pixel (corrected)

Aperture Magnitude $R(<r)$

Radius $r('')$

Dressler 079
NGC 4919

Best-fit
Exp

Tot.Mag M_t
= 13.217
± 0.018

Dressler 080
GMP 2237

Best-fit
$r^{\frac{1}{4}}$

Tot.Mag M_t
= 14.374
± 0.039

Dressler 081 (frame 1)
GMP 2252

Best-fit
$r^{\frac{1}{4}}$

Tot.Mag M_t
= 14.24
± 0.032

Dressler 081 (frame 2)
GMP 2252

Best-fit
$r^{\frac{1}{4}}$

Tot.Mag M_t
= 14.247
± 0.067

Dressler 092
GMP. 4499

Best-fit
$r^{\frac{1}{4}}$

Tot.Mag M_t
= 14.222
± 0.032

Dressler 101 (frame 1)
RB 49

Best-fit
$r^{\frac{1}{4}}$

Tot.Mag M_t
= 14.334
± 0.036

Dressler 101 (frame 2)
RB 49

Best-fit
$r^{\frac{1}{4}}$

Tot.Mag M_t
= 14.333
± 0.054

Dressler 11Q
GMP 4626

Best-fit
$r^{\frac{1}{4}}$

Tot.Mag M_t
= 14.748
± 0.043

Dressler 104 (frame 1)
NGC 4875

Best-fit
$r^{\frac{1}{4}}$

Tot.Mag M_t
= 14.097
± 0.031

Dressler 104 (frame 2)
NGC 4875

Best-fit
$r^{\frac{1}{4}}$

Tot.Mag M_t
= 14.116
± 0.02

Dressler 105 (frame 1)

Best-fit
$r^{\frac{1}{4}}$

Tot.Mag M_t
= 13.116
± 0.023

Dressler 105 (frame 2)
NGC 4869

Best-fit
$r^{\frac{1}{4}}$

Tot.Mag M_t
= 13.128
± 0.019

Dressler 106 (frame 1)
RB 8

Best-fit $r^{\frac{1}{4}}$

Tot.Mag M_t = 14.796 ± 0.028

Dressler 106 (frame 2)
RB 8

Best-fit $r^{\frac{1}{4}}$

Tot.Mag M_t = 14.809 ± 0.021

Dressler 108 (frame 1)
RB 262

Best-fit $r^{\frac{1}{4}}$

Tot.Mag M_t = 14.885 ± 0.024

Dressler 108 (frame 2)
RB 262

Best-fit $r^{\frac{1}{4}}$

Tot.Mag M_t = 14.895 ± 0.023

Counts/Pixel (corrected)

Aperture Magnitude $R(<r)$

Radius $r('')$

Dressler 107 (frame 1)
RB 6

Best-fit $r^{\frac{1}{4}}$

Tot.Mag M_t
= 14.694
± 0.053

Dressler 107 (frame 2)
RB 6

Best-fit $r^{\frac{1}{4}}$

Tot.Mag M_t
= 14.701
± 0.048

Dressler 107 (frame 3)
RB 6

Best-fit $r^{\frac{1}{4}}$

Tot.Mag M_t
= 14.716
± 0.049

Dressler 107 (frame 4)
RB 6

Best-fit $r^{\frac{1}{4}}$

Tot.Mag M_t
= 14.7
± 0.036

Dressler 111
GMP 4653

Best-fit
$r^{\frac{1}{4}}$

Tot.Mag M_t
= 13.926
± 0.02

Dressler 115
GMP 1865

Best-fit
$r^{\frac{1}{4}}$

Tot.Mag M_t
= 14.797
± 0.036

Dressler 116
RB 113

Best-fit
Exp

Tot.Mag M_t
= 14.408
± 0.017

Dressler 117
RB 119

Best-fit
$r^{\frac{1}{4}}$

Tot.Mag M_t
= 14.78
± 0.018

Dressler 118
NGC 4906

Best-fit
$r^{\frac{1}{4}}$

Tot.Mag M_t
= 13.568
± 0.026

Dressler 120
NGC 4898B

Best-fit
$r^{\frac{1}{4}}$

Tot.Mag M_t
= 14.489
± 0.019

Dressler 121
NGC 4898A

Best-fit
$r^{\frac{1}{4}}$

Tot.Mag M_t
= 13.361
± 0.018

Dressler 122
NGC 4894

Best-fit
Exp

Tot.Mag M_t
= 14.537
± 0.03

Dressler 132
RB 13

Best-fit
Exp

Tot.Mag M_t
= 15.056
± 0.022

Dressler 133 (frame 1)
NGC 4867

Best-fit
$r^{\frac{1}{4}}$

Tot.Mag M_t
= 13.748
± 0.035

Dressler 133 (frame 2)
NGC 4867

Best-fit
$r^{\frac{1}{4}}$

Tot.Mag M_t
= 13.753
± 0.028

Dressler 135
RB 260

Best-fit
$r^{\frac{1}{4}}$

Tot.Mag M_t
= 15.257
± 0.029

Counts/Pixel (corrected)

Aperture Magnitude $R(<r)$

Radius $r('')$

Dressler 136
RB 257

Dressler 137
NGC 4850

Dressler 142
RB 133

Dressler 143
IC 4051

Dressler 144
IC 4042

Best-fit
Exp

Tot.Mag M_t
= 13.548
± 0.025

Dressler 145
IC 4041

Best-fit
$r^{\frac{1}{4}}$

Tot.Mag M_t
= 14.109
± 0.031

Dressler 146 (frame 1)
RB 110

Best-fit
$r^{\frac{1}{4}}$

Tot.Mag M_t
= 14.202
± 0.037

Dressler 146 (frame 2)
RB 110

Best-fit
$r^{\frac{1}{4}}$

Tot.Mag M_t
= 14.212
± 0.021

Counts/Pixel (corrected)

Aperture Magnitude $R(<r)$

Radius $r('')$

Dressler 150
IC 4011

Best-fit
$r^{\frac{1}{4}}$

Tot.Mag M_{ℓ}
= 14.505
± 0.028

Dressler 151
NGC 4886

Best-fit
$r^{\frac{1}{4}}$

Tot.Mag M_{ℓ}
= 13.483
± 0.024

Dressler 152 (frame 1)
IC 3998

Best-fit
Exp

Tot.Mag M_{ℓ}
= 14.166
± 0.02

Dressler 152 (frame 2)
IC 3998

Best-fit
Exp

Tot.Mag M_{ℓ}
= 14.167
± 0.016

Dressler 153
RB 45

Best-fit
$r^{\frac{1}{4}}$

Counts/Pixel (corrected)

Radius $r('')$

Aperture Magnitude $R(<r)$

Tot.Mag M_t
= 14.632
± 0.037

Radius $r('')$

Dressler 154
RB 38

Best-fit
$r^{\frac{1}{4}}$

Counts/Pixel (corrected)

Radius $r('')$

Aperture Magnitude $R(<r)$

Tot.Mag M_t
= 15.089
± 0.054

Radius $r('')$

Dressler 155
NGC 4873

Best-fit
$r^{\frac{1}{4}}$

Counts/Pixel (corrected)

Radius $r('')$

Aperture Magnitude $R(<r)$

Tot.Mag M_t
= 13.736
± 0.037

Radius $r('')$

Dressler 156
RB 18

Best-fit
$r^{\frac{1}{4}}$

Counts/Pixel (corrected)

Radius $r('')$

Aperture Magnitude $R(<r)$

Tot.Mag M_t
= 15.292
± 0.049

Radius $r('')$

Dressler 157
RB 14

Best-fit
$r^{\frac{1}{4}}$

Tot.Mag M_t
= 14.784
± 0.027

Radius $r('')$

Dressler 158
RB 7

Best-fit
$r^{\frac{1}{2}}$

Tot.Mag M_t
= 15.754
± 0.033

10"

Radius $r('')$

Dressler 159 (frame 1)
NGC 4864

Best-fit
$r^{\frac{1}{4}}$

Tot.Mag M_t
= 12.995
± 0.059

50"

Radius $r('')$

Dressler 159 (frame 2)
NGC 4864

Best-fit
$r^{\frac{1}{4}}$

Tot.Mag M_t
= 12.994
± 0.043

Radius $r('')$

Dressler 160
IC 3955

Best-fit
$r^{\frac{1}{4}}$

Tot.Mag M_t
= 13.689
± 0.031

Dressler 161 (frame 1)
RB 241

Best-fit
$r^{\frac{1}{4}}$

Tot.Mag M_t
= 13.262
± 0.029

Dressler 161 (frame 2)

Best-fit
$r^{\frac{1}{4}}$

Tot.Mag M_t
= 13.263
± 0.029

Dressler 168
IC 4045

Best-fit
$r^{\frac{1}{4}}$

Tot.Mag M_t
= 13.362
± 0.029

Dressler 167 (frame 1)
NGC 4908

50"

Best-fit
$r^{\frac{1}{4}}$

Tot.Mag M_t
= 13.093
± 0.04

Dressler 167 (frame 2)
NGC 4908

50"

Best-fit
$r^{\frac{1}{4}}$

Tot.Mag M_t
= 13.09
± 0.044

Dressler 171
RB 91

20"

Best-fit
$r^{\frac{1}{4}}$

Tot.Mag M_t
= 14.876
± 0.034

Dressler 173
RB 87

10"

Best-fit
$r^{\frac{1}{4}}$

Tot.Mag M_t
= 14.498
± 0.028

Counts/Pixel (corrected)

Aperture Magnitude $R(<r)$

Radius $r('')$

Dressler 170 (frame 1)
IC 4026

Best-fit $r^{\frac{1}{2}}$

Tot.Mag M_t = 13.979 ± 0.045

Dressler 170 (frame 2)
IC 4026

Best-fit $r^{\frac{1}{2}}$

Tot.Mag M_t = 13.98 ± 0.045

Dressler 170 (frame 3)
IC 4026

Best-fit $r^{\frac{1}{2}}$

Tot.Mag M_t = 13.983 ± 0.039

Dressler 170 (frame 4)
IC 4026

Best-fit $r^{\frac{1}{2}}$

Tot.Mag M_t = 13.981 ± 0.047

Dressler 172 (frame 1)
IC 4021

Best-fit
$r^{\frac{1}{4}}$

Tot.Mag M_t
= 14.311
± 0.027

Dressler 172 (frame 2)
IC 4021

Best-fit
$r^{\frac{1}{4}}$

Tot.Mag M_t
= 14.313
± 0.021

Dressler 174
IC 4012

Best-fit
$r^{\frac{1}{4}}$

Tot.Mag M_t
= 14.207
± 0.017

Dressler 178
RB 21

Best-fit
Exp

Tot.Mag M_t
= 15.393
± 0.032

Dressler 175 (frame 1)
NGC 4883

Best-fit
$r^{\frac{1}{2}}$

Tot.Mag M_t
= 13.677
± 0.028

Dressler 175 (frame 2)
NGC 4883

Best-fit
$r^{\frac{1}{2}}$

Tot.Mag M_t
= 13.68
± 0.021

Dressler 175 (frame 3)
NGC 4883

Best-fit
$r^{\frac{1}{2}}$

Tot.Mag M_t
= 13.682
± 0.025

Dressler 175 (frame 4)
NGC 4883

Best-fit
$r^{\frac{1}{2}}$

Tot.Mag M_t
= 13.681
± 0.028

Dressler 176 (frame 1)
RB 26

Best-fit $r^{\frac{1}{4}}$

Tot.Mag M_t
= 14.363
± 0.024

Dressler 176 (frame 2)
RB 26

Best-fit $r^{\frac{1}{4}}$

Tot.Mag M_t
= 14.369
± 0.029

Dressler 177 (frame 1)
RB 22

Best-fit $r^{\frac{1}{4}}$

Tot.Mag M_t
= 15.025
± 0.023

Dressler 177 (frame 2)
RB 22

Best-fit $r^{\frac{1}{4}}$

Tot.Mag M_t
= 15.03
± 0.035

Dressler 179 (frame 1)
NGC 4865

Best-fit
$r^{\frac{1}{4}}$

Tot.Mag M_t
= 12.913
± 0.033

Dressler 179 (frame 2)
NGC 4865

Best-fit
$r^{\frac{1}{4}}$

Tot.Mag M_t
= 12.912
± 0.036

Dressler 180 (frame 1)
RB 268

Best-fit
$r^{\frac{1}{4}}$

Tot.Mag M_t
= 13.791
± 0.043

Dressler 180 (frame 2)
RB 268

Best-fit
$r^{\frac{1}{4}}$

Tot.Mag M_t
= 13.778
± 0.032

Counts/Pixel (corrected)

Aperture Magnitude $R(<r)$

Radius $r('')$

Dressler 182 (frame 1)
RB 243

Best-fit $r^{\frac{1}{4}}$

Tot.Mag M_t = 15.181 ± 0.02

Dressler 182 (frame 2)
RB 243

Best-fit $r^{\frac{1}{4}}$

Tot.Mag M_t = 15.149 ± 0.018

Dressler 193 (frame 1)
RB 155

Best-fit $r^{\frac{1}{4}}$

Tot.Mag M_t = 14.652 ± 0.038

Dressler 193 (frame 2)
RB 155

Best-fit $r^{\frac{1}{4}}$

Tot.Mag M_t = 14.652 ± 0.036

Dressler 194
NGC 4860

Best-fit
$r^{\frac{1}{4}}$

Tot.Mag M_t
= 12.691
± 0.035

Dressler 196
GMP 3935

Best-fit
$r^{\frac{1}{4}}$

Tot.Mag M_t
= 14.747
± 0.018

Dressler 198
IC 839

Best-fit
$r^{\frac{1}{4}}$

Tot.Mag M_t
= 15.057
± 0.017

Dressler 199
NGC 4851

Best-fit
$r^{\frac{1}{4}}$

Tot.Mag M_t
= 14.163
± 0.023

Dressler 210 (frame 1) GMP 4648 — Best-fit $r^{\frac{1}{4}}$ — Tot.Mag $M_t = 14.191 \pm 0.026$

Dressler 210 (frame 2) GMP 4648 — Best-fit $r^{\frac{1}{4}}$ — Tot.Mag $M_t = 14.185 \pm 0.039$

GMP 2201 RB 129 — Best-fit $r^{\frac{1}{4}}$ — Tot.Mag $M_t = 15.028 \pm 0.054$

GMP 2778 RB 94 — Best-fit Exp — Tot.Mag $M_t = 15.162 \pm 0.019$

GMP 2960 (frame 1)
RB 74

Best-fit
$r^{\frac{1}{4}}$

Tot.Mag M_t
= 15.214
± 0.021

GMP 2960 (frame 2)
RB 74

Best-fit
$r^{\frac{1}{4}}$

Tot.Mag M_t
= 15.216
± 0.041

GMP 3554 (frame 1)
RB 271

Best-fit
Exp

Tot.Mag M_t
= 15.682
± 0.03

GMP 3554 (frame 2)
RB 271

Best-fit
Exp

Tot.Mag M_t
= 15.68
± 0.019

B.2 Late-Type Galaxies - Coma

Dressler 098 (frame 1)
RB 124
Best-fit $r^{\frac{1}{4}}$
Tot.Mag M_t = 14.029 ± 0.028

Dressler 098 (frame 2)
RB 124
Best-fit $r^{\frac{1}{4}}$
Tot.Mag M_t = 14.05 ± 0.024

Dressler 098 (frame 3)
RB 124
Best-fit $r^{\frac{1}{4}}$
Tot.Mag M_t = 14.037 ± 0.025

Dressler 098 (frame 4)
RB 124
Best-fit $r^{\frac{1}{4}}$
Tot.Mag M_t = 14.068 ± 0.03

Dressler 147 (frame 1)
RB 100

Best-fit
$r^{\frac{1}{4}}$

Tot.Mag M_t
= 14.497
± 0.043

Dressler 147 (frame 2)
RB 100

Best-fit
$r^{\frac{1}{4}}$

Tot.Mag M_t
= 14.489
± 0.042

Dressler 149
RB 77

Best-fit
Exp

Tot.Mag M_t
= 15.147
± 0.017

Dressler 181
RB 252

Best-fit
$r^{\frac{1}{4}}$

Tot.Mag M_t
= 14.759
± 0.022

Counts/Pixel (corrected)

Aperture Magnitude $R(<r)$

Radius $r('')$

Dressler 184
GMP 4779

Best-fit
$r^{\frac{1}{2}}$

Tot.Mag M_t
= 15.255
± 0.03

Dressler 191
RB 116

Best-fit
$r^{\frac{1}{4}}$

Tot.Mag M_t
= 14.996
± 0.018

Dressler 192
GMP 2584

Best-fit
$r^{\frac{1}{2}}$

Tot.Mag M_t
= 14.416
± 0.016

Dressler 205
NGC 4907

Best-fit
$r^{\frac{1}{4}}$

Tot.Mag M_t
= 12.897
± 0.023

Dressler 197 (frame 1)
IC 3943

20"

Best-fit
$r^{\frac{1}{4}}$

Tot.Mag M_t
= 13.751
± 0.021

Counts/Pixel (corrected)

Aperture Magnitude $R(<r)$

Radius $r('')$

Dressler 197 (frame 2)
IC 3943

20"

Best-fit
$r^{\frac{1}{4}}$

Tot.Mag M_t
= 13.746
± 0.021

Counts/Pixel (corrected)

Aperture Magnitude $R(<r)$

Radius $r('')$

Dressler 214

20"

Best-fit
$r^{\frac{1}{4}}$

Tot.Mag M_t
= 13.663
± 0.049

Counts/Pixel (corrected)

Aperture Magnitude $R(<r)$

Radius $r('')$

GMP 2914
RB 166

20"

Best-fit
$r^{\frac{1}{4}}$

Tot.Mag M_t
= 15.191
± 0.047

Counts/Pixel (corrected)

Aperture Magnitude $R(<r)$

Radius $r('')$

Dressler 212 (frame 1)
GMP 4866

Best-fit
$r^{\frac{1}{2}}$

Tot.Mag M_t
= 14.318
± 0.02

Dressler 212 (frame 2)
GMP 4866

Best-fit
Exp

Tot.Mag M_t
= 14.302
± 0.041

GMP 3298

Best-fit
$r^{\frac{1}{2}}$

Tot.Mag M_t
= 15.429
± 0.062

GMP 4281

Best-fit
Exp

Tot.Mag M_t
= 15.655
± 0.029

B.3   Irregular or Peculiar Galaxies - Coma

Dressler 162 (frame 1)
GMP 4570

10"

Best-fit
Exp

Tot.Mag M_t
= 16.349
± 0.027

Dressler 162 (frame 2)
GMP 4570

10"

Best-fit
Exp

Tot.Mag M_t
= 16.364
± 0.047

Dressler 169
IC 4040

20"

Best-fit
$r^{\frac{1}{4}}$

Tot.Mag M_t
= 14.269
± 0.025

Dressler 195
NGC 4858

20"

Best-fit
$r^{\frac{1}{4}}$

Tot.Mag M_t
= 14.742
± 0.02

Dressler 183 (frame 1)
GMP 4555

Best-fit $r^{\frac{1}{4}}$

Tot.Mag M_t
= 14.576
± 0.017

Dressler 183 (frame 2)
GMP 4555

Best-fit $r^{\frac{1}{4}}$

Tot.Mag M_t
= 14.593
± 0.054

Best-fit $r^{\frac{1}{4}}$

Tot.Mag M_t
= 13.133
± 0.035

Counts/Pixel (corrected)

Aperture Magnitude $R(<r)$

Radius $r('')$

B.4 Unclassified Galaxies - Coma

Dressler 119 (frame 1)
RB 99

Best-fit
Exp

Tot.Mag M_t
= 14.719
± 0.018

Dressler 119 (frame 2)
RB 99

Best-fit
Exp

Tot.Mag M_t
= 14.717
± 0.017

Dressler 224 (frame b)
GMP 4043

Best-fit
$r^{\frac{1}{4}}$

Tot.Mag M_t
= 15.656
± 0.032

Dressler 224 (frame 2)
GMP 4043

Best-fit
$r^{\frac{1}{4}}$

Tot.Mag M_t
= 15.64
± 0.035

Dressler 225
GMP 4235

Best-fit
$r^{\frac{1}{4}}$

Tot.Mag M_t
= 15.523
± 0.061

GMP 3133 (frame 1)
RB 55

Best-fit
$r^{\frac{1}{4}}$

Tot.Mag M_t
= 15.581
± 0.034

GMP 3133 (frame 2)
RB 55

Best-fit
$r^{\frac{1}{4}}$

Tot.Mag M_t
= 15.583
± 0.023

GMP 3640

Best-fit
$r^{\frac{1}{4}}$

Tot.Mag M_t
= 15.706
± 0.207

B.5   Early-Type Galaxies - Abell 1367

BO 017
NGC 3841

Best-fit
$r^{\frac{1}{2}}$

Counts/Pixel (corrected)

Radius $r('')$

Aperture Magnitude $R(<r)$

Tot.Mag M_t
= 13.237
± 0.05

Radius $r('')$

022

Best-fit
$r^{\frac{1}{2}}$

Counts/Pixel (corrected)

Radius $r('')$

Aperture Magnitude $R(<r)$

Tot.Mag M_t
= 13.266
± 0.032

Radius $r('')$

BO 023
NGC 3844

Best-fit
$r^{\frac{1}{4}}$

Counts/Pixel (corrected)

Radius $r('')$

Aperture Magnitude $R(<r)$

Tot.Mag M_t
= 13.223
± 0.022

Radius $r('')$

BO 027
NGC 3845

Best-fit
$r^{\frac{1}{4}}$

Counts/Pixel (corrected)

Radius $r('')$

Aperture Magnitude $R(<r)$

Tot.Mag M_t
= 13.547
± 0.023

Radius $r('')$

BO 028
IC 2955

Best-fit
$r^{\frac{1}{2}}$

Tot.Mag M_t
= 13.694
± 0.016

BO 033

Best-fit
Exp

Tot.Mag M_t
= 13.736
± 0.026

BO 038
NGC 3851

Best-fit
$r^{\frac{1}{4}}$

Tot.Mag M_t
= 13.528
± 0.034

BO 041

Best-fit
$r^{\frac{1}{4}}$

Tot.Mag M_t
= 13.633
± 0.079

BO 064

Best-fit
$r^{\frac{1}{4}}$

Tot.Mag M_t
= 14.24
± 0.017

Counts/Pixel (corrected)

Radius $r('')$

Aperture Magnitude $R(<r)$

Radius $r('')$

BO 069 (frame 1)

Best-fit
$r^{\frac{1}{4}}$

Tot.Mag M_t
= 14.421
± 0.018

Counts/Pixel (corrected)

Radius $r('')$

Aperture Magnitude $R(<r)$

Radius $r('')$

BO 069 (frame 2)

Best-fit
$r^{\frac{1}{4}}$

Tot.Mag M_t
= 14.421
± 0.038

Counts/Pixel (corrected)

Radius $r('')$

Aperture Magnitude $R(<r)$

Radius $r('')$

BO 090

Best-fit
$r^{\frac{1}{4}}$

Tot.Mag M_t
= 14.76
± 0.025

Counts/Pixel (corrected)

Radius $r('')$

Aperture Magnitude $R(<r)$

Radius $r('')$

20"

BO 076 (frame 1)

Best-fit $r^{\frac{1}{4}}$

Tot.Mag M_t = 14.564 ± 0.019

BO 076 (frame 2)

Best-fit $r^{\frac{1}{4}}$

Tot.Mag M_t = 14.565 ± 0.022

BO 081 (frame 1)

Best-fit $r^{\frac{1}{2}}$

Tot.Mag M_t = 14.905 ± 0.025

BO 081 (frame 2)

Best-fit $r^{\frac{1}{2}}$

Tot.Mag M_t = 14.907 ± 0.029

BO 107

20"

Best-fit

$r^{\frac{1}{4}}$

Counts/Pixel (corrected)

Radius $r('')$

Aperture Magnitude $R(<r)$

Tot.Mag M_t
$= 15.18$
± 0.042

Radius $r('')$

BO 117

20"

Best-fit

$r^{\frac{1}{2}}$

Counts/Pixel (corrected)

Radius $r('')$

Aperture Magnitude $R(<r)$

Tot.Mag M_t
$= 15.224$
± 0.017

Radius $r('')$

B.6   Late-Type Galaxies - Abell 1367

B.7 Irregular or Peculiar Galaxies - Abell 1367

NOTES on the figures:-

The left-hand figures show a contour plot of the individual images as subtracted from the main CCD fields - the areas shaded grey are ignored in the surface photometry fitting, and replaced by a model in the aperture photometry integrations. The contour interval is 1 mag, with the lowest contour representing 23 mag in all plots. The central figures show the surface photometry fit at large radii. The two vertical solid lines represent the limits of the fit - which is chosen by minimum χ^2 between an $r^{\frac{1}{4}}$, an $r^{\frac{1}{2}}$ and an exponential. The dashed line shows the radius of the largest *complete* ellipse (only if this is within the outer fitting limit). Beyond the outer fitting limit (or largest ellipse), the extrapolation from the aperture magnitude to total magnitude is calculated assuming the best-fit law continues outwards to infinity. The elliptical aperture photometry curve and total magnitude are shown in the right-hand figures (including the *half-light* fit). The errors are shown by dashed lines. *Erratum - the cosmological* $(1 + z)^4$ *surface brightness correction was wrongly included in the total magnitude values in the RH plots. Add 0.1 to each magnitude to remove this correction.*

Appendix C

Surface Photometry - Output

This appendix contains plots displaying the deconvolved surface photometry for each Coma and Abell 1367 galaxy image. These include the surface brightness profile, ellipticity profile, position angle profile and centroid profiles. Also shown is the shift from the un-deconvolved surface photometry profiles. The figures for repeat frames of individual galaxies are positioned adjacently for comparison. See end of appendix for more detailed explanatory notes. **Because of limited page space in this thesis, the pages of this appendix containing the plots have been stored as a postscript file (AppendixC.ps) on the CD-ROM attached to this thesis.**

C.1   Early-Type Galaxies - Coma

Contents:-

C.2   Late-Type Galaxies - Coma

<u>*Contents:-*</u>

C.3   Irregular or Peculiar Galaxies - Coma

<u>*Contents:-*</u>

C.4   Unclassified Galaxies - Coma

Contents:-

C.5 Early-Type Galaxies - Abell 1367

<u>*Contents:-*</u>

C.6   Late-Type Galaxies - Abell 1367

<u>*Contents:-*</u>

C.7 Irregular or Peculiar Galaxies - Abell 1367

<u>*Contents:-*</u>

NOTES on the figures:-

These plots display the deconvolved profiles derived from surface photometry, plus the seeing correction, for each Coma and Abell 1367 galaxy image. The plots for each galaxy are shown in vertical strips. Since the deconvolution is performed on all the images, there can be more than one set of plots for an individual galaxy - these figures are positioned adjacently for comparison (as near as possible). Each vertical strip contains five plots showing, from top to bottom, the radial profiles of surface brightness, ellipticity, position angle, central X-coordinate and central Y-coordinate. In each plot, the circles show the corrected profiles, with the attached 'tails' showing the seeing correction from the raw profiles. The dotted-lines surrounding each profile represent the error envelopes on the deconvolved profiles. The inner limit of the plot in each case is the measured *FWHM* of the seeing PSF, which is minimum possible radius where seeing corrections can be deemed reliable. The outer limits to the surface brightness plots is defined by the point where the intensity drops below 0.75 times the sky measurement error. For the ellipse parameter plots, the outer limit is the furthest point at which the surface photometry algorithm is able to fit ellipse parameters (from the original image) due to the falling S/N-ratio (beyond this limit, the ellipse parameters are fixed as a constant although the surface brightness continues to be measured).

Appendix D

Parameter Fitting - Output

This appendix contains plots of the deconvolved surface-brightness profiles for each of the Coma and Abell 1367 galaxies, overlaid with the best-fitting $r^{\frac{1}{4}}$ and $r^{\frac{1}{4}}+\exp$ functions (and residuals). Also shown is a table giving details of the best-fitting parameters for the above functions (plus $r^{\frac{1}{3}}$ and $r^{\frac{1}{5}}$ law fits). See end of appendix for more detailed explanatory notes.

Because of limited page space in this thesis, the pages of this appendix containing the plots have been stored as a postscript file (AppendixD.ps) on the CD-ROM attached to this thesis.

D.1   Early-Type Galaxies - Coma

<u>Contents:-</u>

D.2 Late-Type Galaxies - Coma

<u>*Contents:-*</u>

D.3   Irregular or Peculiar Galaxies - Coma

Contents:-

D.4   Unclassified Galaxies - Coma

<u>*Contents:-*</u>

D.5 Early-Type Galaxies - Abell 1367

Contents:-

D.6   Late-Type Galaxies - Abell 1367

<u>Contents:-</u>

D.7   Irregular or Peculiar Galaxies - Abell 1367

<u>Contents:-</u>

NOTES on the figures:-

The figures in this appendix show the results of the profile-fitting algorithms for each individual galaxy. Each galaxy was fitting by six different profile models - a combined $r^{\frac{1}{4}}$ plus exponential law and a range of single power-law fits ($r^{\frac{1}{n}}$, where $n = 1, 2, 3, 4, 5$).

The results of the two-component fit are shown in the top two plots. The top-left plot shows the surface brightness profile with the best-fit model. The solid line is the combined model surface profile, while the two dashed lines show the profiles of the individual components. Note that the abscissa is $r^{\frac{1}{4}}$, so an $r^{\frac{1}{4}}$ law will appear as a straight line, while an exponential law will appear as a convex curve. The ranges of the profile-fitting are also shown as dotted lines. The measurement error on each point is shown by the error bars (which include an estimated seeing-correction error at low radii equal to one-fifth of the seeing-correction). The crosses show the systematic error due to sky measurement error, which becomes significant at large radii. The top-right plot show the *residual* between the SB profile and the best-fit two-component model. The key is identical to the surface brightness profile plot, except that the individual component profiles (dashed lines) are not shown, as they would have little meaning on the residual plot. The scales are chosen such that if the galaxy is brighter than the model, the data will appear above the zero-residual line, and vice-versa.

The bottom-left plot also shows the seeing-corrected SB profile, this time overlayed by three of the best-fit single power-law profiles. The best-fit $r^{\frac{1}{4}}$ law is the solid line (straight). The best-fit $r^{\frac{1}{3}}$ law is the dot-dashed line (convex curve). The best-fit $r^{\frac{1}{5}}$ law is the dotted line (concave curve). For clarity, the best-fit single-exponential and $r^{\frac{1}{2}}$ laws are not shown here, but their parameters can be found in Table A.2 in Appendix A. The measured SB profile and the best-fit $r^{\frac{1}{3}}$ & $r^{\frac{1}{5}}$ are also plotted in the bottom-right graph as a residual from the best-fit $r^{\frac{1}{4}}$-law. It is clear from this plot that most early-type galaxies depart significantly from a perfect de Vaucouleurs law.

Finally, a table of the best-fit parameters for the two-component model and the three single power-law models is shown at the bottom of each page. In addition to the effective radii, effective surface brightnesses and total magnitudes for each model, two quality-of-fit parameters are shown - the RMS deviation from the fit and the reduced χ^2. Also shown for comparison purposes are the model-independent half-light parameters and asymptotic total magnitudes taken from the magnitude extrapolation (see Chapter 4). *Erratum - the cosmological $(1 + z)^4$ surface brightness correction was wrongly included in all total magnitude values. Add 0.1 to each magnitude to remove this correction.*